

Sediment Suspension Dynamics in Turbulent Unsteady, Depth-Varying Open-Channel Flow over a Gravel Bed

THÈSE N° 5168 (2012)

PRÉSENTÉE LE 13 JANVIER 2012

À LA FACULTÉ ENVIRONNEMENT NATUREL, ARCHITECTURAL ET CONSTRUIT
LABORATOIRE DE MÉCANIQUE DES FLUIDES DE L'ENVIRONNEMENT
PROGRAMME DOCTORAL EN ENVIRONNEMENT

ÉCOLE POLYTECHNIQUE FÉDÉRALE DE LAUSANNE

POUR L'OBTENTION DU GRADE DE DOCTEUR ÈS SCIENCES

PAR

Fereshteh BAGHERIMIYAB

acceptée sur proposition du jury:

Prof. F. Golay, président du jury
Prof. M. Parlange, Prof. U. Lemmin, directeurs de thèse
Prof. E. J. Hopfinger, rapporteur
Prof. G. Parker, rapporteur
Prof. F. Porte Agel, rapporteur



ÉCOLE POLYTECHNIQUE
FÉDÉRALE DE LAUSANNE

Suisse
2012

*To my parents, Parvin and Edris
and to my love Urs*

ABSTRACT

Even though flow in natural rivers and channels is generally unsteady, only a few studies on turbulent structures in unsteady open-channel flows have been carried out. In hydraulic engineering problems, unsteady flow is often approximated with concepts of steady flow, because the treatment of unsteady flow can be difficult. Many variables enter into the mathematical relationship and the differential equations cannot be integrated in closed form, except under very simplified conditions. The limited number of studies of unsteady flow may also be due to the lack of experimental equipment capable of capturing small-scale, unsteady open-channel flow dynamics. Therefore, it is important to know when unsteady flow can be approximated by steady flow concepts and which simplifications are acceptable. In most cases, especially when simulating unsteady flood flow by a steady flow approach, the calculations may not produce reliable results.

The mechanism of sediment transport in rivers and open channels is governed by complicated interactions between unsteady accelerating and decelerating turbulent flow, particle motion and bed configuration. Understanding the dynamics of unsteady sediment-laden water flows and characterizing the velocity of suspended particles is essential for enhancing the predictive accuracy of sediment transport and its impact on environmental processes in the water column.

In order to simulate fine sediment dynamics over an armored bed in a river during the passage of a flood wave, unsteady accelerating, and decelerating open-channel flow over a movable (but not moving) coarse gravel bed ($D_{50} = 5.5$ mm) first without and then with fine sediment were studied. A layer of fine sediment of mean particle size about $120\ \mu\text{m}$ was placed on the coarse gravel bed. The thickness of the fine sediment layer on the gravel bed was varied between 4 mm and 6 mm, but it was found that the thickness of the layer had no effect on the results. Quasi-instantaneous profiles of velocity and sediment concentration were taken simultaneously and co-located. An acoustic Doppler and imaging method, using an Acoustic Doppler Velocity Profiler (ADVP) was combined with an optical method, using Particle Tracking Velocimetry (PTV) for suspended sediment particle tracking. Measurements resolved turbulence scales. Unsteadiness strongly affects the profile shape of velocity and friction velocity, particularly in the final phase of the accelerating range. Flow in the decelerating range approaches steady flow. Systematically higher friction velocities were observed in the accelerating flow than in the decelerating flow for comparable flow depth. This indicates that for the same change of relative submergence, different flow dynamics are generated during accelerating and decelerating flows.

For the lowest unsteadiness (90 s hydrograph), the differences between velocity profiles in the accelerating and the decelerating ranges become small, indicating that for this unsteadiness, steady state conditions are approached.

During the accelerating flow range, fine sediment suspension from the bed started in bursts and in the final phase of the accelerating flow range, a ripple pattern is rapidly created that remained nearly stationary. Thereafter, vortex shedding produced most of the sediment suspension into the water column in the form of events, making suspension intermittent. Simultaneously, sediment particles rolled along the bed following the ripple structure, thus slowly advancing the ripple pattern in the direction of the flow. However, ripple geometry and ripple shape were not altered by this process, despite the fact that flow velocities

changed. Due to the ripple structure, high sediment suspension events continued to occur in bursts during the decelerating flow even though mean flow velocity and friction velocity decreased. The dynamics of sediment suspension observed in this study indicate that mean value concepts cannot be applied in unsteady flow.

Fine sediment particles and hydrogen bubbles were used individually and combined as flow tracers in the acoustic measurements. When used individually, hydrogen bubbles provided full depth flow and backscattering information, whereas sediment particles traced only the lower layers of the flow, indicating sediment suspension. When both tracers were combined, hydrogen bubbles could not be distinguished from sediment particles. The intermittency was observed in the backscattering of the acoustic system. The event structure in fine sediment suspension is seen by the PTV method. PTV velocity vectors varied in speed and orientation, but were organized in large coherent packets, mainly in the near-bed layers. They also extended well above the bed, supporting the concept that coherent structure events contribute to sediment suspension over ripples. The two methods provide complementary information. ADVP measurements allow long timeseries analysis, whereas the spatial details seen in the PTV results cannot be resolved in the ADVP measurements.

Keywords: *fine sediment, suspension, accelerating and decelerating flow, ripple formation, acoustic Doppler methods, PTV (Particle Tracking Velocimetry).*

RESUME

Alors que généralement, les écoulements naturels en rivières sont instationnaires, seulement peu d'études expérimentales ont été effectués dans ces conditions. Dans l'ingénierie hydraulique, les écoulements instationnaires sont souvent approchés grâce aux concepts développés en régime permanent car le traitement des écoulements instationnaires peut être difficile. Beaucoup de variables entrent en jeu dans leurs formulation mathématique et les équations aux dérivées partielles ne peuvent pas être résolues, excepté dans de rares et simples cas. Le nombre limité d'études du régime non permanent peut être aussi du au manque d'appareils de mesure capables de capturer la dynamique des petites échelles dans les écoulement transitoires. C'est pourquoi il est important de connaître quand les écoulements instationnaires peuvent être approximés par les concepts développés en régime permanent et quelles simplifications sont acceptables. Dans la plupart des cas, généralement lors de la simulation de crues par une approche permanente, les solutions obtenues peuvent ne pas être correctes.

Le mécanisme du transport de sédiment dans les rivières et les canaux est gouverné par des interactions compliquées entre l'accélération et la décélération de l'écoulement turbulent, ainsi que le mouvement des particules et la topographie du lit. La compréhension de la dynamique des écoulements chargés en particules et la caractérisation de la vitesse des particules en suspension sont essentielles pour améliorer la qualité de la prédiction du transport solide par suspension et son impact sur l'environnement.

Pour simuler la dynamique des sédiments fins sur un lit pavé dans une rivière pendant le passage d'une onde de crue, des écoulements instationnaires sur un lit de gravier grossiers ($D_{50}=5.5\text{mm}$) d'abord sans et ensuite avec sédiments fins furent étudiés. Une couche de sédiments fins de diamètre moyen $120\ \mu\text{m}$ fût placée sur le lit de gravier grossier. Différentes épaisseur de couche (4 à 6 mm) furent utilisées, mais sans influence notable sur les résultats. Des profils quasi-instantanés de vitesse et de concentration en sédiment furent obtenus simultanément et à la même position. Un Doppler acoustique et une méthode d'analyse d'image utilisant un Acoustic Doppler Velocity Profiler (ADVP) fut combiné avec une méthode optique, basée sur le suivi des particules de sédiment (Particle Tracking Velocity; PTV). Les mesures permirent de résoudre toutes les échelles turbulentes. Il est constaté que les effets instationnaires modifient fortement le profil de vitesse et la vitesse de frottement, particulièrement pendant la phase final de l'accélération. La phase de décélération est semblable au régime permanent. De plus grandes vitesses de frottement sont systématiquement observées durant la phase d'accélération plutôt que pendant la phase de décélération pour des hauteurs d'eau comparables. Cela montre que pour le même changement de submergence relative, différentes dynamiques d'écoulement sont générées durant la phase d'accélération et de décélération.

Pour les plus faibles instationnarités (hydrographe de 90s), la différence entre les profils de vitesses ascendant et descendant devient faible, indiquant que les conditions permanentes sont approchées.

Pendant la phase d'accélération, la mise en suspension des sédiments du lit commence par des poussées sporadiques et dans la phase finale de l'accélération, des ondulations quasi stationnaires du lit apparaissent. Ensuite, la propagation des vortex produit la plupart des sédiments en suspension, sous la forme d'événements intermittents. Dans le même temps, les particules de sédiment roulent le long du lit suivant les structures morphologiques, les faisant avancer régulièrement dans la direction de l'écoulement. Pourtant, la géométrie des ondulations et leur forme n'est pas altéré par ce processus, malgré le fait que les vitesses de

l'écoulement change. Due aux ondulations, des événements extrêmes de départ de sédiment en suspension continuent de se produire en poussées sporadiques pendant la phase de décélération de l'écoulement même si la vitesse moyenne de l'écoulement et sa vitesse de frottement diminue. L'observation de la dynamique des suspensions de cette étude indique que les concepts de valeurs moyennes ne peuvent pas être appliqués aux écoulements instationnaires.

Des particules fines de sédiment et des bulles d'hydrogène sont utilisées individuellement et combinées comme traceurs du fluide dans les mesures acoustiques. Utilisées séparément, les bulles d'hydrogène donnent une information sur toute la profondeur de l'écoulement, alors que les particules de sédiment suivent seulement la partie basse de l'écoulement, indiquant la concentration en particule de ce dernier. Quand les deux types de traceurs sont combinés, les bulles d'hydrogènes ne peuvent pas être distinguées des particules de sédiment. L'intermittence est observée dans le backscattering du système acoustique. La structure des événements dans la suspension de sédiment est observée par la méthode de PTV. Les vecteurs de vitesse de PTV varient en intensité et en direction, mais sont organisés en groupes larges et cohérents, surtout près du lit. Ils s'étendent aussi bien au-dessus du lit, supportant l'idée que les structures cohérentes contribuent à la suspension des sédiments au-dessus d'ondulations du lit.

Les deux méthodes donnent des informations complémentaires. Les mesures d'ADVP permettent une analyse de longues séries de données, tandis que la bonne résolution spatiale donnée par la PTV ne peut pas être donnée par les mesures d'ADVP.

Mots Clefs: *Sédiment fins, suspension, Écoulement instationnaire, formation des ondulations, Méthode Doppler Acoustique, PTV (Particle Tracking Velocimetry).*

ACKNOWLEDGEMENTS

This research project was only possible with the support of many people, whom I would like to thank here.

This study is supported by the European Commission (FP6; RII3; Contract no. 022441) HYDRALAB III–SANDS. I am very grateful for their support.

I am deeply grateful to my supervisors, professors Ulrich Lemmin and Marc Parlange, for giving me the opportunity to pursue my Ph.D under their supervision and for making my academic experience at EPFL truly enjoyable.

I owe my deepest gratitude to Professor Ulrich Lemmin for his supervision, advice, and guidance from the very early stage of my research work as well as giving me extraordinary insights throughout our collaboration. Above all and when I most needed it, he provided encouragement and support in various ways; he generously helped me adjust to my new life in Lausanne. His truly scientific intuition has made him a constant source of ideas and passion, which continues to inspire and enrich my growth as a student, a researcher and inspires me to become the scientist that I hope to be. I am indebted to him more than he knows. I am also grateful to his wife for the time she spent proofreading my thesis.

I would like to thank Professor Marc Parlange for giving me the opportunity to be a part of his laboratory, for his support and for his passion. I am thankful to Marc for being open to our discussions and I am looking forward to our continued collaboration.

I also thank the members of my committee, Emil Hopfinger, Gary Parker and Fernando Porté Agel, for the time they spent reviewing this thesis and for their constructive feedback on the manuscript. I thank François Golay for agreeing to be the president of my committee.

Many thanks go in particular to Navid Borhani. I am much indebted to Navid who helped me immensely. He provided the optical system and assistance to use it and shared his time with me, even to answer simple and naïve questions. Only with his help was I able to make my PTV measurements.

Special thanks go to Professor Willi Hermann Hager for his support and in particular for lending me the light sheet and PIV instruments from his hydraulics laboratory at the ETH in Zurich.

David Hurther and Mario Franca are well remembered, and I thank them for their discussions, encouragement and advice at conferences and when we met at EPFL.

I would like to thank our extraordinary secretaries, Barbara Tinguely and Marie-José Pellaud, whose doors were always open and who helped me in all possible ways.

Collective and individual acknowledgments are also owed to my colleagues at LHE and EFLUM labs for all the fruitful discussions and friendly moments: Joris, for being the best officemate, Martin and his family for their friendship, Ismail my first officemate, Philippe Aviolat and Bob de Graffenried, LHE technicians, the technical support of Claude Perrinjaquet is greatly appreciated. Thanks to my friends at EFLUM: Natalie, Megan, Holley and Susana, and my friends from LCH Lab: Marcelo and Michael.

A very special thank you goes to Shokoufeh for her indispensable help during my stay in Lausanne. I am grateful also to Ehsan and Mahdi for answering my questions about coding and Matlab anytime. I would like to thank all my friends in Lausanne, who made my stay

in Switzerland a very happy and pleasant experience and I am grateful to them for all the unforgettable moments we had together: Abbas, Atefeh, Azadeh, Azin, Azad, Banafsheh, Ehsan, Elham, Hesam, Hooman, Hossein, Laleh, Mahdi, Milad, Mona, Nicole, Parisa, Samira, Sara, Shokoufeh, Soheil, Tohid, Vahid, Yaser, Zahra, and many others.

It is a pleasure to express my gratitude wholeheartedly to Professor Salah Kouchakzadeh who was my master thesis supervisor at Tehran University in Iran for all his advice.

Great thanks go to my friend Atefeh Parvaresh who advised me to consider EPFL for graduate studies.

And I certainly owe a great thank you to my Uncle Mohammad, for all the love and his help and advice starting from before coming to Switzerland, from the beginning when I applied to EPFL and during my PhD and stay in Lausanne.

My parents have my special gratitude for their inseparable support and prayers. My Father, Edris, and my mother, Parvin, are the persons who put the foundation for my learning character, showing me the joy of intellectual pursuit ever since I was a child, who gave me all the love and passion of learning I would need to reach the present state. My Mother, Parvin, is the one who sincerely raised me with her caring and gentle love. I also thank my sister Katayoun, my brother Ali and my sister-in-law Roshanak, who filled my life with joy and happiness.

Words fail me to express my appreciation for my love Urs, for his encouragement, love and support.

Finally, I would like to thank everybody who was important to the successful realization of this thesis, as well as expressing my apologies that I could not mention everybody personally.

TABLE OF CONTENTS

CHAPTER 1

INTRODUCTION	1
1.1 Research motivation	3
1.1.1 Unsteady flow	5
1.1.2 Sediment transport	6
1.1.3 Suspended load	6
1.1.4 Bedforms	7
1.2 Objectives	9
1.3 Thesis outline	10
1.4 References	11

CHAPTER 2

THEORY	13
2.1 Introduction	15
2.2 Unsteady open-channel flow	19
2.2.1 Basic equations	22
2.2.1.1 Steady flow case	22
2.2.1.2 Unsteady flow case	23
2.2.2 Unsteadiness parameters	25
2.3 Flow characteristics	29
2.3.1 Definition of mean velocity component	31
2.3.2 Shear velocity	32
2.3.2.1 Logarithmic velocity profile method	32
2.3.2.2 Reynolds shear stress	34
2.4 Sediment transport and morphodynamics	37
2.4.1 Sediment transport	39
2.4.2 Bedload transport	41
2.4.3 Suspended load transport	42
2.4.4 Bedforms	44
2.5 References	49

CHAPTER 3

EXPERIMENTAL SET-UP, INSTRUMENTATION AND EXPERIMENTAL PROCEDURE	55
3.1 Introduction	57
3.2 Experimental set-up	57
3.3 Instrumentation	61
3.3.1 Acoustic methods	62
3.3.1.1 Acoustic Doppler Velocity Profiler (ADVP)	62
3.3.1.2 Acoustic Doppler Particle Flux Profiler	63
3.3.1.3 Ultrasonic Limnimeter	64
3.3.2 Particle Tracing Velocimetry (PTV)	65
3.4 Experimental procedure	68
3.5 References	72

CHAPTER 4

DATA ANALYSIS AND RESULTS	75
4.1 Introduction	77
4.2 Velocity distribution in unsteady rough-bed open-channel flow without sediment	79
4.2.1 Hydrographs	81
4.2.2 Mean velocities	82
4.2.3 Friction velocity	89
4.3 Fine sediment dynamics in unsteady open-channel flow studied with acoustic and optical systems	93
4.3.1 Acoustic measurements with low target concentration	95
4.3.2 Sediment suspension in unsteady flows	102
4.3.3 Sediment suspension characterization	106
4.3.4 Sediment suspension studies using PTV	110
4.4 Bedforms and particle interaction in unsteady suspended sediment-laden open-channel flow	137
4.5 References	141

CHAPTER 5

SUMMARY AND CONCLUSIONS	143
A. APPENDICES	149
A.1 Fine sediment dynamics in tidal open-channel flow studied with acoustic and optical systems (submitted to the Journal of Continental Shelf Research)	151
A.2 Shear velocity estimates in rough-bed open-channel flow (will be submitted)	177
A.3 Coherent structures in rough-bed open-channel flow observed in fluctuations of velocity profiles, shear velocity and pressure (will be submitted)	199
A.4 Curriculum Vitae	219

CHAPTER 1

INTRODUCTION

1.1 RESEARCH MOTIVATION	3
1.2 OBJECTIVES	9
1.3 THESIS OUTLINE	10
1.4 REFERENCES	11

1.1 RESEARCH MOTIVATION

1.1.1	Unsteady flow	5
1.1.2	Sediment transport	6
1.1.2.1	Suspended load	6
1.1.3	Bedforms	7

1.1 RESEARCH MOTIVATION

Floods are the most frequently occurring phenomena among natural disasters. They take place all over the world and affect a large segments of the population. They are devastating events causing human casualties and property damage, due to high water discharge which may be charged with debris and pollutants and due to extensive sediment erosion resulting from high velocities of flood waters. A flood has a discharge rate which exceeds an acceptable threshold value and is typically caused by excessive rainfall in the catchment basin. The variability of the intensity and duration of the rainfall will produce flood hydrographs of different forms. Most often a flood travels along a river reach as a wave characterized by unsteady flow with velocity and water depth continuously changing with time and distance. In order to minimize flood damage, it is essential to predict as accurately as possible the magnitude and the propagation of the flood wave along a river. The present study will focus on some aspects of flood wave dynamics and thus help improve flood prediction.

1.1.1 UNSTEADY FLOW

Even though flow in natural rivers and channels is generally unsteady, only a few studies on turbulent structures in unsteady open-channel flows have been carried out. In hydraulic engineering problems, unsteady flow is often approximated with concepts of steady flow, because the treatment of unsteady flow can be difficult. Many variables enter into the mathematical relationship and the differential equations cannot be integrated in closed form, except under very simplified conditions. The limited number of studies of unsteady flow may also be due to the lack of experimental equipment capable of capturing small-scale, unsteady open-channel flow dynamics. Therefore, it is important to know when unsteady flow can be approximated by steady flow concepts and which simplifications are acceptable. In most cases, especially when simulating unsteady flood flow by a steady flow approach, the calculations may not produce reliable results.

In unsteady open-channel flows over a smooth wall, Nezu and Nakagawa (1993) found that the log law of the mean velocity is still valid. This was confirmed by Afzalimehr and Anctil (2000) who studied spatially accelerating shear velocity in gravel-bed channels. Nezu and Nakagawa (1993) estimated the friction velocity u_* and the wall shear stress ρu_*^2 as a function of time in unsteady flows. In oscillatory closed-channel flows, Jensen and Sumer (1989) and Akhavan et al. (1991) observed that the mean velocity obeyed the log law distribution, except at the very early stages of the acceleration phase and the late stages of the deceleration phase. By measuring the turbulence structure over a smooth wall in unsteady depth-varying open-channel flows, Nezu et al. (1997) established that in the accelerating phase, the wall shear stress attains its maximum ahead of the flow depth. They also detected hysteresis loop properties of velocity and turbulence profiles in unsteady open-channel flows. These studies demonstrate that determining the structure of turbulence in unsteady flow without sediment is important in order to advance the understanding of sediment flux development.

1.1.2 SEDIMENT TRANSPORT

Sediments are transported as suspended load or bedload depending upon fundamental properties of water and sediment particle size, density, etc. The mechanism of sediment transport in rivers and open channels involves complicated interactions between turbulent unsteady (accelerating and decelerating) flow, particle motion and bed configuration. Turbulence plays an essential role in suspended sediment transport, and in turn, particle motion influences the velocity profiles. It is recognized that due to turbulent flow, and particularly due to the presence of coherent structures in the flow, some of the sand grains are moved from the bed up into the water column and are then transported as suspended sediment.

In nature, sediment is often transported by unsteady and non-uniform flows. There is an urgent need to understand sediment transport and river deformation in unsteady flows (Wang et al., 1997). Most intensive transport processes in rivers occur during the passage of a flood wave (Huygens et al., 2000; Rowinski and Czernuszenko, 1998). Such events in rivers with a high unsteady flow regime cause suspension and transport of deposited bottom sediments, release contaminants from the interstitial water of the sediments and cause land erosion. This creates important water quality and sediment quantity problems downstream.

Although bedload transport in unsteady flow has been the subject of much research, less attention has been paid to the suspension of sediment under unsteady flow. Most studies concerning sediment suspension reported in the literature have investigated steady flow situations. Rivers that generally present bedload transport can also experience suspended load when the water discharge is greater during flood events. Claudin et al. (2011) found that when suspended load is the dominant type of transport, the relaxation length (characteristic length L_{sat}) is typically four to five orders of magnitude higher than for bedload. Suspended transport thus prevents the formation of bedforms with a wavelength smaller than water depth. Under steady flow conditions, suspension may also be caused by secondary currents (Nezu and Nakagawa, 1993) or coherent structures (Nezu and Nakagawa, 1993; Cellino and Lemmin, 2004; Nezu, 2005). McLean et al. (1994) measured the turbulence structure over sand dunes and pointed out the importance of coherent eddies in lifting up sediment particles behind the dune crest.

When sediments are deposited in river basins, water level rises, which can result in ecological problems, such as flood disasters. Sediment particles in water may behave as a carrier for heavy metals, which have a tendency to attach to cohesive sediments. They become a major pollutant and can cause the disruption of ecosystems. Sediment particles, nitrogen, organic compounds, residues, pathogenic bacteria, pesticides and viruses, are carried into reservoirs, where they may cause the deterioration of water quality. Sediment transport reduces the reservoir's lifetime and the hydrodynamic potential of dams, and can contribute to the pollution of drinking water supplies. Since sediment deposition involves water and sediment particles, the physical properties of water and sediment particles should be studied to understand sediment transport mechanisms.

1.1.2.1 SUSPENDED LOAD

Suspended sediment transport occurs in many geophysical flows, which directly affects physical and biogeochemical processes in the whole water column. This phenomenon

occurs when the local bottom shear stress ρu_*^2 exceeds the critical value (Shields, 1936) and when the falling velocity of the particles is smaller than the turbulent velocity fluctuations. In that case, particles can remain suspended for a long time, trapped by turbulent eddies, before they eventually fall back to the bed due to gravity. In nature, one observes suspension in the downstream of rivers, where a large amount of fine particles may accumulate from the catchment basin. In tidal channels, estuaries and rivers, sediment erosion and deposition may lead to channel changes and relates to scour. It is therefore of great importance to understand suspended sediment transport dynamics and turbulent sediment fluxes, because geophysical flows are often turbulent. Most of these flows are unsteady and flow acceleration and deceleration during the unsteady phase may lead to the initiation or termination of sediment suspension, generate or modify bed forms and/or change bed and channel topography. Initiation of sediment motion due to unsteady turbulent water flows is an important aspect of river and coastal engineering.

Sediment transport studies in unsteady flow (De Sutter et al., 2001) indicate a hysteresis loop in sediment concentration, similar to the one observed in turbulence intensities by Nezu et al. (1997).

1.1.3 BEDFORMS

The interaction of flow and sediment transport often creates bedforms such as ripples, dunes, antidunes, and bars. These bedforms in turn can interact with the flow to modify the rate of sediment transport. Ripples and dunes are the most prominent small-scale features in the low Froude number range among bed forms in loose bed conditions with fine sediments. A detailed description of the creation, geometry and movement of bedforms is given in DuBuat (1786) who recognized that bedforms have a triangular geometry. He observed that sand grains move up a gentle slope, arrive at the summit and fall down a steep slope, whose angle is close to the angle of repose of sand grains. The current erodes the upstream face and deposits the eroded material on the downstream face. By this process of sand grain movement, the whole bedform advances slowly in the direction of the flow. Their mode of advancement is similar to that of aeolian (resulting from or caused by the motion of the wind) ripples. It is recognized that the characteristics of flow over alluvial bedforms has many similarities to flow over tidal and oceanic bedforms, as well as to flow over aeolian dunes (Bagnold, 1941). Therefore, the results from an open-channel study carried out here can also be applied to coastal ocean situations. Flow over ripples is dominated by shear layer instability resulting from separation zones on the lee side of the ripple. Turbulent coherent structures are able to penetrate further into the outer flow and induce return flows that are able to exert greater shear stress which influences the bed (Best, 2005). The shear stress on the bed can be considered the sum of flow-induced shear and form-induced shear by the ripples. In most cases, ripples will develop first during unsteady accelerating flow, followed by dunes in the long term. Reviews by Best (2005) and Garcia (2007) summarize recent developments in bedform research. Most studies concerning the dynamics of ripple formation reported in the literature have investigated steady flow situations. Therefore, a study of bedform dynamics in unsteady flow is needed to better understand river bed deformation in unsteady flows and thus avoid important water quality and sediment quantity problems downstream of rivers, especially during flood events.

Taking real time observations can explain real life systems better than flume experiments, because many simplifying assumptions are usually made in laboratory studies. It is

however difficult or even impossible, e.g., during a flood, to take real time data in the field. Therefore, laboratory studies are still important to understand basic concepts of river flow and sediment transport, and they can provide a detailed analysis for parameters related to the physics of the problem. Furthermore, many investigators have developed empirical methods to represent sediment transport phenomena using data obtained in the laboratory.

1.2 OBJECTIVES

In this research, we aim to understand when turbulent, unsteady accelerating and decelerating flow over a gravel bed follows steady flow concepts and when simulating unsteady flow by a steady flow approach is acceptable.

Most studies concerning the dynamics of ripple formation and sediment suspension reported in the literature have investigated steady flow situations. However, it appears that no detailed investigations of suspension dynamics taking place during unsteady flow exist. In order to advance the understanding of river deformation in unsteady flows and thus reduce water quality and sediment quantity problems downstream during the flood events the study of bedform dynamics in unsteady flow is necessary. Therefore, in this research, we investigate, in turbulent unsteady accelerating and decelerating flow, what the influence of different unsteadiness is on the suspension of sediment and on the dimension of the ripples. We will also try to determine whether there is any relationship between different unsteadiness and dimension of ripples.

This study focuses on detailed aspects of sediment suspension in unsteady open-channel flows by combining acoustic and optical methods. Ripple development in depth varying accelerating and decelerating flow will be investigated. The development from a flat sediment bed at rest to quasi-steady flow with suspended sediments and ripple formation will also be covered.

In tidal rivers and the coastal ocean, tracers for acoustic and optical studies may include gas bubbles, algae, detritus and sediment particles. In field studies, it is often difficult to determine a priori the nature of the acoustic scatterers in the flow field. Most often, they occur as a mixture of several or all of them. However, the transport of sediment particles is frequently of major interest because of its effect on bed and channel morphology. The presence and concentration of individual tracers should be known in order to correctly quantify the contribution by sediment particles.

Acoustic and optical methods will be applied, providing high spatial and temporal resolution profile data that allow determining velocity profiles and particle dynamics. The advantages of each method will be discussed. In particular, the case of low sediment particle concentration suspended over only part of the water column will be addressed. Due to the relatively low number of particles inside the acoustic beam, acoustic methods may have difficulty measuring velocity and sediment particle concentration correctly in low sediment concentration flows, which typically occur during the beginning of accelerating flow. Therefore, in this study, video image recordings will be synchronized with the acoustic measurements to visualize the sediment suspension process during the hydrograph, and thereby help to confirm the acoustic measurements.

1.3 THESIS OUTLINE

This Ph.D. thesis is composed of the following 6 chapters:

- The first chapter gives details of the research motivation and objectives.
- The second chapter briefly describes the theory of unsteady flow, sediment transport and morphodynamics
- The third chapter presents the experimental set-up and the instrumentation (ADVP and PTV).
- The fourth chapter presents the experimental results.
- The main conclusions of the research are summarized in the fifth chapter.

1.4 REFERENCES

- Afzalimehr, H., Anctil, F., 2000. Accelerating shear velocity in gravel-bed channels. *J. Hydrol. Sci.* 45, 113–123.
- Akhavan, R., Kamm, R. D., Shapiro, A. H., 1991. An investigation of transition to turbulence in bounded oscillatory Stokes flows. I: Experiments. *J. Fluid Mech.* 225, 395–422.
- Bagnold, R.A., 1941. *The physics of blown sand and desert dunes*. Methuen, New York.
- Best, J., 2005. The fluid dynamics of river dunes: a review and some future research directions. *J. Geophys. Res.* 110, F04S02, doi: 10.1029/2004JF000218.
- Cellino, M., Lemmin, U., 2004. Influence of coherent flow structures on the dynamics of suspended sediment transport in open-channel flow. *J. Hydr. Eng.* 130, 1077–1088.
- Claudin, P., Charru, F., Andreotti, B., 2011. Transport relaxation time and length scales in turbulent suspensions. *J. Fluid mech.* 1–16, doi: 10.1017/S0022112010005823.
- De Sutter R., Verhoeven, R., Krein, A., 2001. Simulation of sediment transport during flood events: laboratory work and field experiments. *Hydrol. Sci.* 46, 599–610.
- DuBuat, P., 1786. *Principes d’hydraulique*. L’imprimerie de monsieur, Paris, France.
- Garcia, M.H., 2007. Sediment transport and morphodynamics. In: M.H. Garcia (Ed.) *Sedimentation engineering*. ASCE Manuals and Reports on Engineering Practice No. 110, pp. 21–146.
- Huygens, M., Verhoeven, R., De Sutter, R., 2000. Integrated river management of a small Flemish river catchment. In: *The Role of Erosion and Sediment Transport in Nutrient and Contaminant Transfer (Proceedings of a symposium held at Waterloo, Canada, July 2000)*, 191–198. IAHS Publ. No. 263.
- Jensen, B.L., Sumer, B. M., 1989. Turbulent oscillatory boundary layers at high Reynolds numbers. *J. Fluid Mech.* 206, 265–297.
- McLean, S.R., Nelson, J.M., Wolfe, S.R., 1994. Turbulence structure over two dimensional bedforms: implications for sediment transport. *J. Geophys. Res.* 99, 12729–12747. doi: 10.1029/94JC00571.
- Nezu, I., 2005. Open-channel flow turbulence and its research prospect in the 21st century. *J. Hydr. Eng.* 131, 229–246.
- Nezu, I., Nakagawa, H., 1993. *Turbulence in open channel flows*. Balkema, Rotterdam, NL.
- Nezu, I., Kadata, A., Nakagawa, H., 1997. Turbulent structure in unsteady depth-varying open-channel flows. *J. Hydr. Eng.* 123, 752–763.
- Rowinski, P. M., Czernuszenko, W., 1998. Experimental study of river turbulence under unsteady conditions. *Acta Geophys. Polonica XLVI*, 461–480.
- Shields, I.A., 1936. *Anwendung der Aehnlichkeitsmechanik und der Turbulenzforschung auf die Geschiebebewegung*. Mitt. Preuss. Versuchsanstalt für Wasserbau, Berlin, Heft 26.
- Wang, Z., Lin, B., Nestmann, F., 1997. Prospects and new problems of sediment research. *Int. J. Sediment Res.* 12, 1–15.

CHAPTER 2

THEORY

2.1	INTRODUCTION	15
2.2	UNSTEADY OPEN-CHANNEL FLOW	19
2.3	FLOW CHARACTERISTICS	29
2.4	SEDIMENT TRANSPORT AND MORPHODYNAMICS	37
2.5	REFERENCES	49

2.1 INTRODUCTION

An open-channel is a waterway, canal or conduit with a free surface separating air and water. Open-channel flows are found in nature, as well as in man-made structures. These flows include rivulets flowing across a field, gutters along streets, partially filled closed conduits conveying waste water, irrigation and water supply canals, and rivers. In nature, torrential waters are encountered in mountain rivers, river rapids and flood waves. Open-channel flows are nearly always turbulent.

If the velocity at a given location changes with respect to time, then the flow in rivers and open-channels is called unsteady flow. Unsteady flow in open channels by nature is nonuniform as well as unsteady because of the free surface. Mathematically, this means that the flow dependent flow variables (e.g. velocity and depth or discharge and depth) are functions of both distance along the channel and time for one-dimensional applications. Problem formulation requires two partial differential equations representing the continuity and momentum principles in the two unknown dependent variables. The differential form of the energy equation could be used in cases where the flow variables are continuous, but the momentum equation is required where they are not continuous as in surges or tidal bores. The full differential forms of the two governing equations are called the Saint-Venant equations or the dynamic wave equations. Only in rather severe simplifications of the governing equations are analytical solutions available for unsteady flow.

A wave is a disturbance that propagates through space and time, transferring energy. It is defined as a temporal (i.e., with respect to time) or spatial (i.e., with respect to distance) variation of flow depth and rate of discharge. The wave length, L , is the distance between two adjacent wave crests or troughs and the amplitude, z , of a wave is the height of the maximum water level above the still water level. A wave is called a translatory wave if there is net mass transport. Flood waves are translatory. Translatory waves may be further classified as solitary or as a wave train. A solitary wave has a rising and a falling range and has a single peak. A wave train is a group of waves in succession. A translatory wave having a steep front is called a surge. Unsteady flow problems arise in hydraulic engineering in a variety of settings. They may be natural flood waves and dam-break surges in rivers, waves formed in irrigation channels by gate operation or in hydroelectric plant headraces and tailraces by turbine operation. Only shallow water waves are considered in which water movement occurs over the full depth and vertical velocity and acceleration can be neglected to allow the use of one-dimensional forms of the governing equations. In all the wave problems considered, the purpose of obtaining the solution of the governing equations is to describe the flow velocity and depth as functions of space and time. In other words the spatial shape and temporal development of the translatory wave are sought.

Even though the flow conditions in man-made systems usually vary with time, and the flows are turbulent and often unsteady, in some situations it is possible to transform unsteady flow into steady flow by considering a coordinate system with respect to a moving reference frame. This simplification is helpful in the visualization of flow and in the derivation of the governing equations. Therefore such a transformation is possible only if the wave shape does not change as the wave propagates. For example, the shape of a surge wave moving in a smooth channel does not change, and consequently the propagation of a surge wave in an otherwise unsteady flow may be converted into steady

flow by moving the reference coordinates at the absolute surge velocity. A typical example of such a situation is the movement of a flood wave in a natural channel, where the shape of the wave is modified as it propagates along the channel. The unsteadiness may be due to natural processes such as flood waves in streams, rivers, and drainage channels due to rain-storms and/or snow-melt or produced by the failure of dams, dikes, levees or other control structures or due to human activities. The analysis of unsteady flows is usually more complex than that of steady flows. Therefore, partial differential equations describe unsteady flows, since the dependent variables (flow depth and flow velocity) are functions of more than one independent variable (space and time). A closed-form solution of these equations is not available except in very simplified cases, and thus numerical methods are employed for their solution (Chaudhry, 2008).

Interactions between turbulent unsteady (accelerating and decelerating) flow, particle motion and bed configuration over a movable bed in rivers and open-channels is complicated. Turbulence plays an essential role in suspended sediment transport, and in turn, particle motion influences the velocity profiles (Cellino and Lemmin, 2004). Furthermore, understanding the dynamics of unsteady sediment-laden water flows and characterizing the velocity of suspended particles is essential for enhancing the predictive accuracy of sediment transport and its impact on environmental processes in the water column. The study of turbulence in unsteady flow is important in order to advance the understanding of sediment flux development because of its impact on physical, chemical, biological and ecological processes in the water column.

Sediment transport generally is the term used for the transport of material in rivers and streams. This transport is called the sediment load and may occur as bedload and suspended load. Bedload and suspended load have different characteristics. Bedload characterizes grains rolling along the bed, whereas suspended load refers to grains maintained in suspension by turbulence. This distinction, however, sometimes appears to be arbitrary when both loads are of the same material.

The study of sediment transport is important, because in tidal channels, estuaries and rivers, sediment erosion and deposition may lead to channel changes, and relates to scour. The planning of hydraulic structures such as dams and canals, is practically impossible without sediment dynamics information. Sediment deposition in stream or river channels can cause flooding. Although bedload transport in unsteady flow has been the subject of much research, less attention has been paid to the suspension of sediment under unsteady flow.

The movement of sediment is linked with the turbulence associated with natural flows. It is recognized that due to the turbulent flow, and particularly the presence of coherent structures in the flow, some of the sand grains are moved from the bed up into the water column and are then transported as suspended sediment. Turbulent coherent structures can penetrate further into the outer flow and induce return flows that are able to exert greater shear stress as they impact on the bed (Best, 2005). Therefore, it is of great importance to understand suspended sediment transport dynamics and turbulent sediment fluxes, because geophysical flows are often turbulent. Most of these flows are unsteady and flow acceleration and deceleration during the unsteady phase may lead to the initiation or termination of sediment suspension, and generate or modify bed forms, and change bed and channel topography. Initiation of sediment motion due to unsteady turbulent water flows is an important aspect of river and coastal engineering.

In this chapter, aspects of the unsteady flow theory, flow characteristics on rough-bed open-channel flow, sediment transport, and morphodynamics which relate to the present study are reviewed briefly.

2.2 UNSTEADY OPEN-CHANNEL FLOW

2.2.1	Basic equations	22
2.2.1.1	Steady flow case	22
2.2.1.2	Unsteady flow case	23
2.2.2	Unsteadiness parameters	25

2.2 UNSTEADY OPEN-CHANNEL FLOW

Steady-state flow refers to the condition where flow properties such as depth and velocity at a point in the system does not change over time. Otherwise the flow is called unsteady. Whether a particular flow is steady or unsteady depends on the chosen frame of reference. For instance, laminar flow over a sphere is steady in a frame of reference that is stationary with respect to the sphere. In a frame of reference that is stationary with respect to a background flow, the flow is unsteady. Turbulent flows are unsteady by definition. However, a turbulent flow can be statistically stationary. Steady flows are often more tractable than unsteady flows under similar conditions. The governing equations of a steady problem have one dimension less (time) than the governing equations of an unsteady problem. In two- or three-dimensional steady flows, the time variation of all components of velocity is zero.

A fluid flow is unsteady if any of the variables that describe the flow change with respect to time. Mathematically, a flow would be determined to be unsteady if any of the partial derivations of any variable that describes the flow such as depth, velocity, or cross-sectional area, with respect to time is different from zero. Generally if one variable changes with respect to time, all variables do.

A significant feature of unsteady open-channel flow is the presence of a free surface. The water surface pressure is equal to the atmospheric pressure. The physics of open-channel flow is basically governed by the interaction between inertial forces, gravity forces and friction forces. The gravity forces result in the variation of water surface or flow depth, h , in open-channel flows (Fig. 1), and friction forces apply as a shear force along the boundary (channel bed and walls).

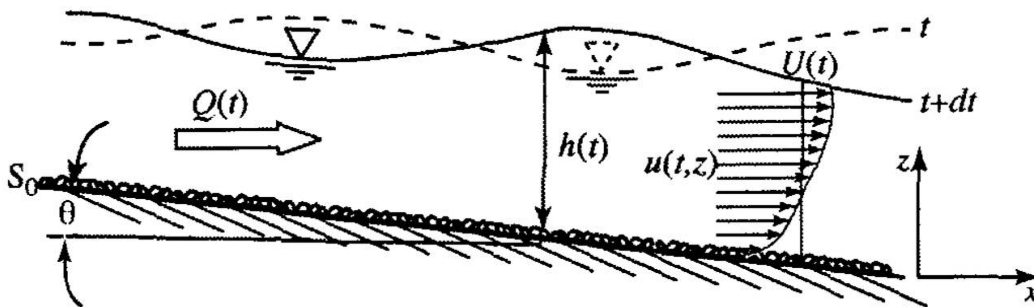


Fig. 1 Schematic of unsteady open-channel flows (Qu, 2003)

The Reynolds number, Re , (eq. 1) is a dimensionless number that gives a measure of the ratio of inertial forces to viscous forces and consequently quantifies the relative importance of these two types of forces for a given flow condition. The dimensionless Froude number, Fr , (eq. 2) is traditionally used in hydraulic engineering to express the relative importance of inertial and gravity forces, and is applied throughout open-channel hydraulics. It is only relevant if the water has a free surface. These two dimensionless numbers, especially the Froude number, play a significant role in the study of open-channel flows.

$$\frac{\mu(u/D_h^2)}{\rho u^2/D_h} = \frac{\nu}{uD_h} = Re^{-1} \Rightarrow Re = \frac{uD_h}{\nu}, \quad (1)$$

$$\frac{\rho g}{\rho u^2/D_h} = \frac{gD_h}{u^2} = Fr^{-2} \Rightarrow Fr = \frac{u}{\sqrt{gD_h}}, \quad (2)$$

where u is the mean flow velocity, D_h is the hydraulic depth, h is the flow depth, ρ is the fluid density, g is the gravity, constant μ is the dynamic viscosity, and ν is the kinematic viscosity of flow.

In (eq. 1) and (eq. 2) the hydraulic depth, D_h , is equal to the flow depth, h , for rectangular channels. Consequently, a combination of the Reynolds number, Re , and Froude number, Fr , gives the following regimes of flow:

Subcritical-laminar flow	$Fr < 1$ and $Re < 500$
Subcritical-turbulent flow	$Fr < 1$ and $Re > 2000$
Supercritical-laminar flow	$Fr > 1$ and $Re < 500$
Supercritical-turbulent flow	$Fr > 1$ and $Re > 2000$
Critical flow	$Fr = 1$
Transition flow	$500 < Re < 2000$

In the present study, we investigate subcritical turbulent flow in an open-channel with zero bed slope, $\theta = 0$, a Reynolds number that has a magnitude of the order of $O(10^4)$, $Re \gg 2000$ and a Froude number, $Fr < 1$.

2.2.1 BASIC EQUATIONS

Three conservation laws for mass, momentum, and energy are used to describe open-channel flows. Two flow variables, such as the flow depth and velocity, or the flow depth and rate of discharge, are sufficient to define the flow conditions at a channel cross section. Therefore, two governing equations may be used to analyze a typical flow situation. The continuity equation and the momentum or energy equation are used for this purpose.

2.2.1.1 STEADY FLOW CASE

The continuity equation (conservation of mass)

For any volume during the small time interval, δt , the principle of conservation of mass implies that the mass of flow entering the control volume minus the mass of flow leaving the control volume equals the change of mass within the control volume.

If the flow is steady and the fluid incompressible, the mass entering is equal to the mass leaving, so there is no change of mass within the control volume.

For the time interval, δt , Mass flow entering = mass flow leaving.

If ρ is the fluid density and Q is the volume flow rate then the mass flow rate is ρQ and the continuity equation for steady incompressible flow can be written as

$$\rho Q_{\text{entering}} = \rho Q_{\text{leaving}} \quad (3)$$

Since Q , the volume flow rate is the product of the area and the mean velocity at the upstream face, where the mean velocity is u_1 and the cross-section area is A_1

$$Q_{\text{entering}} = u_1 A_1 \quad (4)$$

Similar at the downstream face, where the mean velocity is u_2 and the cross-section area is A_2

$$Q_{\text{leaving}} = u_2 A_2 \quad (5)$$

Therefore the continuity equation for steady flow can be written as

$$u_1 A_1 = u_2 A_2 \quad (6)$$

The momentum equation (conservation of momentum)

The law of conservation of momentum states that a moving body cannot gain or lose momentum unless acted upon by an external force, Newton's Second law of motion : Force = rate of change of momentum.

Consider the control volume during the time δt

$$\text{momentum entering} = \rho \delta Q_1 \delta t u_1 \quad (7)$$

$$\text{momentum leaving} = \rho \delta Q_2 \delta t u_2 \quad (8)$$

By the continuity principle, $\delta Q_1 = \delta Q_2 = \delta Q$ and by Newton's Second law, Force = rate of change of momentum:

$$\delta F = \frac{\text{momentum leaving} - \text{momentum entering}}{\delta t} = \rho \delta Q (u_2 - u_1) \quad (9)$$

It is more convenient to write the force on a control volume for each of the three axes directions, x , y , and z , e.g. in the x -direction

$$\delta F_x = \rho \delta Q (u_{2x} - u_{1x}) \quad (10)$$

Integration over a volume gives a total force in the x -direction as

$$F_x = \rho Q (V_{2x} - V_{1x}) \quad (11)$$

as long as flow velocity, V , is uniform over the whole cross section. This is the momentum equation for steady flow for a region of uniform velocity.

2.2.1.2 UNSTEADY FLOW CASE

The governing equations of continuity and momentum in the x -direction for an unsteady open-channel are

The continuity equation

$$\frac{\partial u}{\partial x} + \frac{\partial w}{\partial z} = 0 \quad (12)$$

The x momentum equation

$$\frac{\partial u}{\partial t} + u \frac{\partial u}{\partial x} + w \frac{\partial u}{\partial z} = -\frac{1}{\rho} \frac{\partial p}{\partial x} + \frac{\partial}{\partial z} \left(\frac{\tau_{zx}}{\rho} \right) \quad (13)$$

where u and w are the mean velocity components in the x and z directions respectively, ρ is the fluid density, g is the gravity, ν the kinematic turbulent viscosity, τ is the total shear stress and p is the mean pressure.

Saint-Venant equations

The equations that describe unsteady flows in open-channels are called the Saint-Venant equations. These equations consist of two partial differential equations, one that satisfies mass conservation (the continuity equation), and one that is obtained from Newton's second law which is the momentum equation for one-dimensional hydraulics. The two independent variables in these equations are x (for position) and t (for time).

The present study focuses on open-channel flows in a channel with a rectangular cross section having a free water surface and unsteady accelerating and decelerating flow. The bed slope, S_0 is 0.07, the discharge with unit width is given by $q = uh$, where u is the mean flow velocity component in the x direction and h is flow depth. Under those conditions one can obtain the Saint-Venant equations by integrating the basic equations of continuity and momentum over the whole water depth. One of the assumptions in the derivation of the governing equations is that the head losses in unsteady flow may be simulated by using the steady state resistance laws, such as the Manning or Chezy equation, i.e., head losses for a given flow velocity during unsteady flow are the same as that during steady flow.

The continuity equation

$$\frac{\partial q}{\partial x} + \frac{\partial h}{\partial t} = 0 \quad (14)$$

Replacing q by uh , eq. 14 can be written as

$$\frac{\partial h}{\partial t} + u \frac{\partial h}{\partial x} + h \frac{\partial u}{\partial x} = 0 \quad (15)$$

The momentum equation

$$\frac{\partial q}{\partial t} + \frac{\partial}{\partial x} \left(\frac{q^2}{h} + \frac{1}{2} gh^2 \right) + gh \frac{\partial z}{\partial x} = -ghS_f \quad (16)$$

where the friction slope, S_f is related to the flow depth, h and velocity, u . It can be expressed as

$$S_f = \frac{u_*^2}{gh} \quad (17)$$

where u_* is shear velocity, g is gravity and h is water depth.

By replacing $q = uh$ and the continuity equation, one can obtain the momentum equation as a function of u and h as

$$\frac{\partial u}{\partial t} + u \frac{\partial u}{\partial x} + g \frac{\partial h}{\partial x} + g \frac{\partial z}{\partial x} = -gS_f. \quad (18)$$

The continuity and momentum equations form a set of nonlinear partial differential equations. A closed form solution of these equations is not available except for very simple cases. Therefore numerical methods are used for their integration.

The Saint-Venant equations were developed for one-dimensional flows with hydrostatic pressure distributions, small bed slopes, constant water density, no sediment motion and assuming that the flow resistance is the same as for a steady uniform flow for the same depth and velocity. Limitations of the Saint-Venant equation applications include two- and three-dimensional flows, shallow-water flood plains where the flow is nearly two-dimensional, wavy flows, and the propagation of sharp discontinuities.

2.2.2 UNSTEADINESS PARAMETERS

Various non-dimensional parameters for characterizing the unsteady open-channel flows have been defined in previous studies. Nezu et al. (1997) proposed a parameter, α , that characterizes the effects of unsteadiness on velocity profiles and turbulence in unsteady open-channel flow over smooth bed:

$$\alpha = \frac{1}{u_c} \frac{\partial h}{\partial t} \cong \frac{1}{u_c} \frac{h_p - h_b}{T_d}, \quad (19)$$

where u_c is the convection velocity of turbulent eddies and is approximately $(u_b + u_p)/2$, T_d is the duration from the base discharge to the peak discharge in the hydrograph. The subscripts b and p denote the "base" and "peak" values, respectively. In their experiments, $\alpha \ll 1$, with typical order of magnitude being $O(10^{-3})$.

Qu (2003) proposed an alternative parameter, Ω , as an unsteadiness parameter over a mobile bed

$$\Omega = \frac{1}{u_{*b}^2} \frac{h_p u_p - h_b u_b}{T_d}. \quad (20)$$

Unsteadiness affects sediment transport and bed deformation in rivers and open-channels. Regression relations for bed profile, variation of sediment size, and the total amount of sediment discharge were established in terms of the unsteady flow parameter. De Sutter et al. (2001) discussed the effectiveness of this parameter and concluded that the unsteadiness parameter should include only the duration of the accelerating part of the hydrograph. Hayashi et al. (1988), using a hot-film anemometer, suggested that turbulence is stronger in the accelerating stage than in the decelerating stage of unsteady flow. Nezu et al. (1997) detected hysteresis loop properties of velocity and turbulence profiles in unsteady open-channel flows. Under steady uniform flow conditions, a one-to-one relationship exists between water discharge, and flow depth or stage, and between sediment discharge and water discharge. However, for unsteady flow, there is no one-to-one relationship between

sediment and flow discharge. The existence of hysteresis means that, in general, the sediment discharge under unsteady flow conditions cannot be approximated by quasi-steady conditions. Therefore, in this study, we investigated the effects of the five symmetrical hydrographs with different unsteadiness on suspended sediment.

2.3 FLOW CHARACTERISTICS

2.3.1	Definition of mean velocity component	31
2.3.2	Shear velocity	32
2.3.2.1	Logarithmic velocity profile method	32
2.3.2.2	Reynolds shear stress	34

2.3 FLOW CHARACTERISTICS

2.3.1 DEFINITION OF MEAN VELOCITY COMPONENT

In unsteady flow, an important aspect to investigate in turbulent structures is how to determine the mean velocity component $u(t)$ from the instantaneous velocity $\tilde{u}(t) \equiv u(t) + u'(t)$. Three different methods are proposed in the literature to determine the mean velocity $u(t)$: (1) the ensemble-average method, (2) the moving time-average method, and (3) the Fourier-component method. Method 1 is often used in investigations in oscillatory flows in pipes, closed-channels, and unsteady boundary layer flows (Brereton and Mankbadi, 1995). Nezu and Nakagawa (1991) examined the applicability of these three methods to unsteady open-channel flows and concluded that the Fourier-component method was the most suitable for free surface flows. The Fourier component method uses a discrete Fourier transform (DFT). The instantaneous velocity \tilde{u}_i [$i = 0, 1, 2, \dots, (N - 1)$] is transformed into the frequency domain. Only the frequency components lower than $f_c = (m - 1)/(2T_h)$ are used as representations of the mean velocity component, u_i , as follows:

$$u_i = \frac{1}{2}a_0 + \sum_{k=1}^{(m-1)/2} (a_k \cos \omega_{ik} + b_k \sin \omega_{ik}), \quad (21)$$

where

$$a_k = \frac{2}{N} \sum_{i=0}^{(N-1)} \tilde{u}_i \cos \omega_{ik}, \quad b_k = \frac{2}{N} \sum_{i=0}^{(N-1)} \tilde{u}_i \sin \omega_{ik}, \quad (22)$$

$$\omega_{ik} = 2\pi \left(\frac{i}{N} \right) k, \quad k = (0, 1, 2, \dots, (m - 1)/2), \quad (23)$$

where T_h is time period of the measurement of the hydrograph. The cut-off frequency, f_c , of the Fourier components for mean velocity is reasonably chosen so as to be much smaller than the burst frequency of turbulence. Nezu et al. (1997) using 7 Fourier components, m , found that the Fourier component method is applicable to the wall region near the bed, and to the depth-varying zone near the free surface.

The discrete Fourier transform (DFT) method is widely used for the data treatment of phenomenon where the signal is time-varying and difficult to repeat. Suszka (1987) and Tu (1991) used the moving average method for filtering their measurement signals. Song (1994) chose the method of transforming the instantaneous signal values into a frequency domain by applying a Fourier transform (DFT) and inverse-transforming it by retaining only those frequencies that are smaller than a given cut-off frequency. Qu (2003) also applied a Fourier transform (DFT) for treatment of his experimental data where the signal was time-varying and difficult to repeat, using only the frequency components lower than a certain frequency representing mean values. Filtering techniques such as the moving average and Fourier transformations, used by Tu and Graf (1992), Song and Graf (1996), Nezu et al. (1997), and Qu (2003), revealed some difficulties in decomposing the measured signals into their time-varying mean value and the fluctuating component.

Each technique has its advantages and disadvantages. The method to be used in a particular application must be carefully selected by taking into account the nature of signals being studied. The use of an unsuitable technique not only can introduce false oscillations in the

time-varying mean value, but it can also cause errors and create false time lags between the peak values of different signals.

Hurther and Lemmin (2001) proposed a direct correction method by which most of the noise in turbulence measurements taken with four-receiver ADVP instruments can be eliminated. A four-receiver configuration gives redundant information on one velocity component which allows estimating the noise level. The noise level is subsequently subtracted from the other components. Blanckaert and Lemmin (2006) proposed another method by changing the geometric configuration of the ADVP to de-noise the ADVP data and compared the results with those of Hurther and Lemmin (2001).

In this study, the method proposed by Hurther and Lemmin (2001) and a new de-noising method based on wavelet analysis were applied to ADVP data. By using the SWT (stationary wavelet analysis tool) of the Matlab Wavelet tool box, 1D denoising was carried out.

In Chapter 4, we explain how we treat the velocity data.

2.3.2 SHEAR VELOCITY

Shear velocity was initially defined within concepts of boundary layer flow. Commonly employed techniques are based on the assumption of the presence of a constant shear layer. In open-channel flow, a constant shear layer does not exist and therefore those concepts should not be used. However, as will be shown below, they have been applied in some open-channel flow studies. For open-channel flow over rough beds, Nezu and Nakagawa, (1993) suggest four methods to calculate shear velocity and bed shear stress: the logarithmic law method, the Reynolds stress method, a bulk method using the channel slope, also called the reach average method, and direct measurements.

To compare the methods presented below, a bulk shear stress or shear velocity estimate based on a force balance over a control section of the open-channel is often used as a reference. This can be expressed as

$$u_* = \sqrt{g R S_0} \quad , \quad (24)$$

where g is the gravitational acceleration, R is the hydraulic radius, and S_0 is the bed slope of the channel. However, in fully rough flows, local estimates of the shear velocity may strongly deviate from this section mean, because of significant bed irregularity. This method cannot be applied in the present case, since the bed slope is zero. Direct measurements can be made using a hot-film sensor. However, for rough-bed flows, an in situ calibration is necessary (Albayrak et al., 2008; Albayrak, 2008). Therefore, this is not an independent method, and it was not included in the present analysis.

2.3.2.1 LOGARITHMIC VELOCITY PROFILE METHOD

Shear velocity can be calculated by assuming an equation for the vertical profile of streamwise velocity. In rough bed flows, Katul et al. (2002) suggest that if $h > 10D$, a logarithmic velocity profile may exist in the inner layer of the flow, covering the lowest

20% of the water depth. The logarithmic velocity distribution is described by the von Kármán-Prandtl equation with the following form (Schlichting, 1987):

$$\frac{u}{u_*} = \frac{1}{\kappa} \ln \left(\frac{z}{z_0} \right), \quad (25)$$

where z_0 describes the characteristic hydraulic roughness length (or roughness), and u is the mean longitudinal velocity at height z above the bed. Monin and Yaglom (1971) define z_0 as the height at which the mean velocity of the flow would become zero, if the logarithmic law would be applicable down to this height. For 2D uniform flow without sediment transport, it is well established that von Kármán's constant, κ , is 0.4. In rough bed flows, the relative magnitude of z_0 and a representative length scale for the roughness elements are important for the determination of the lower limit of the validity of the log-law. For homogeneous sand roughness, Monin and Yaglom (1971) established $z_0/D_{50} = 1/30$ between the roughness length z_0 and bed roughness parameter D_{50} . For irregular roughness, the proportionality coefficient may vary and is often larger: $z_0/D_{50} \approx 1/10$ or even $z_0/D_{50} \approx 1/5$ (Monin and Yaglom, 1971; Townsend, 1976). These authors stress that this coefficient may not strictly be a constant for a set of irregularities, since it also depends on the form of the roughness element.

This method is widely used in open-channel flow and river studies (Nezu and Nakagawa, 1993). To provide estimates for z_0 and u_* , measured data $u = f(z)$ are plotted in semi-logarithmic form. The procedure involves fitting a straight line with an ordinary least-square regression to the profile and calculating the values of u_* and z_0 from the slope and interception of the computed regression equation. This procedure requires that the level of the profile origin ($z = 0$) is known. In rough bed flows, a logarithmic profile will develop above the roughness layer. Townsend (1976) indicated that the log law can only be valid at heights of $z/z_0 > 50$. According to Wilcock (1996), a logarithmic profile is found between $3 D_p < z < h/5$ (D_p being the grain size, for which p percent are finer; often taken as D_{84}), but it may actually extend higher into the outer region. Smart (1999) suggested a range of $0.05 h < z < h/2$.

Nezu and Nakagawa (1991, 1993, 1993b) found that the log law is still valid in unsteady open-channel flows over a smooth wall. Afzalimehr and Anctil (2000) studied spatially accelerating shear velocity in gravel-bed channels. They showed that the logarithmic law is valid for gravel-bed channels, as long as it is applied to the inner layer of the flow ($y/h \leq 0.2$). Nezu et al. (1993) verified that the values of wall shear stress estimated from the aforementioned log law coincide reasonably well with those evaluated from the momentum equation. In oscillatory closed-channel flows, Jensen and Sumer (1989) and Akhavan et al. (1991) observed that the mean velocity obeyed the log law distribution, except at the very early stages of the acceleration phase and the late stages of the deceleration phase. By measuring the turbulence structure over a smooth wall in unsteady depth-varying open-channel flows, Nezu et al. (1997) established that in the rising stage, the wall shear stress attains its maximum before the flow depth. This strongly suggests that sediment transport in unsteady flood flows become stronger in the accelerating stage than in the decelerating stage.

Where velocity data follow the log law, plotting $\kappa u = f[\ln(z)]$ will indicate a straight line with gradient u_* and intercept $-u_* \ln(z)$, thus allowing calculations of u_* and z_0 from a measured profile (Fig.2).

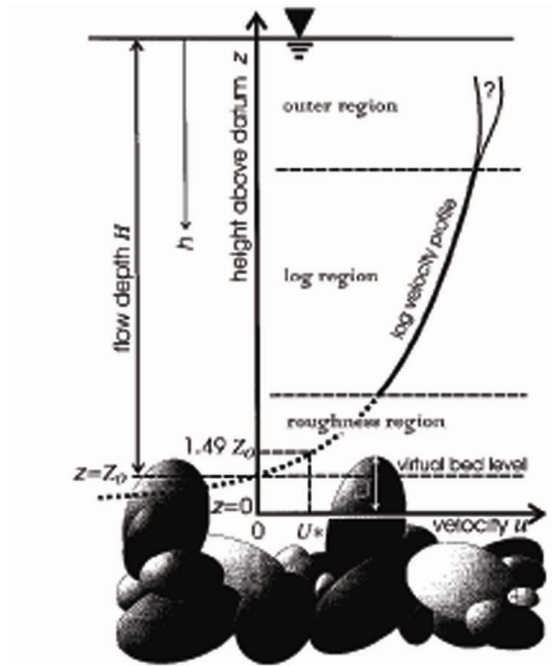


Fig. 2. Illustration of velocity profile extrapolated into bed and showing nomenclature (not to scale) (Smart, 1999).

We applied this method in the present study. In Chapter 4, we discuss the validity of this method in the inner layer of unsteady accelerating and decelerating flow.

2.3.2.2 REYNOLDS SHEAR STRESS

When turbulence measurements are available, local mean shear velocity can be determined from the measured Reynolds stress distribution in the constant stress layer, which is found at the lower end of the logarithmic profile layer. It can be expressed as

$$u_* = \sqrt{-\overline{u'w'}} \quad , \quad (26)$$

where u' and w' are the velocity fluctuations of the longitudinal (streamwise) and vertical components, respectively. The overbar denotes time mean values. Recently, instruments, which can measure the two components of turbulent velocity fluctuations with sufficient temporal resolution, have become available, allowing to calculate shear velocity in rough bed flows by this method when it may be difficult to apply the logarithmic profile method. However, the Reynolds stress method is sensitive to any deviation from 2D uniform flow (Nezu and Nakagawa, 1993; Kim et al., 2000; Nikora and Goring, 2000; Albayrak, 2008) and a precise sensor alignment is required to obtain reliable data for the two velocity components.

Shear velocity, u_* , can be calculated from turbulence measurements at a single depth within the constant stress layer at the bottom of the logarithmic profile layer, if the thickness of the roughness layer and the level of the constant stress layer are known. However, acoustic Doppler instrument measurements are less reliable in strong velocity gradient layers such as the one close to the bed due to internal shear within the measuring volume (Lhermitte and Lemmin, 1994; Dombroski and Crimaldi, 2007). Kim et al. (2000)

measured with an ADV at 14 cm above a silt bed and estimated the height of the logarithmic layer as 44 cm.

In rough-bed open-channel steady flow, Reynolds stress varies linearly from the bed to the free surface (Nezu and Nakagawa, 1993). Therefore, Nezu and Nakagawa (1993) and Nikora and Goring (2000) suggested using the extrapolation of the Reynolds stress profile to the bed,

$$u_* = \sqrt{\left(-\overline{u'w'}\right)_{z \rightarrow 0}} . \quad (27)$$

In addition, this method allows verifying the 2D flow conditions with a linear distribution of the Reynolds stress above the maximum. Nezu and Nakagawa (1993) favour this method.

Nezu and Nakagawa (1993) estimated the friction velocity u_* and the wall shear stress ρu_*^2 as a function of time in unsteady flows.

In the present study, it is shown that the assumption of a constant stress layer on which the calculation by eq. (26) is based, is not valid in open-channel flow.

2.4 SEDIMENT TRANSPORT AND MORPHODYNAMICS

2.4.1	Sediment transport	39
2.4.2	Bedload transport	41
2.4.3	Suspended load transport	42
2.4.4	Bedforms	44

2.4.1 SEDIMENT TRANSPORT

Sediment transport is the movement of solid particles (sediment), typically due to a combination of the force of gravity acting on the sediment, and/or the movement of the fluid, in which the sediment is entrained. Sediment transport is important in the fields of sedimentary geology, geomorphology, civil engineering and environmental engineering. Knowledge of sediment transport dynamics is often required in order to determine whether erosion or deposition will occur, the magnitude of this erosion or deposition, and the time and distance over which it will occur.

In natural systems, sediment particles are boulders, gravel, sand, clay, or mud; the fluid is air, water, or ice; and the force of gravity acts to move the particles due to the sloping surface on which they are resting. Sediment transport occurs in rivers, oceans, lakes, seas, and other bodies of water, due to currents and tides; in glaciers as they flow, and on terrestrial surfaces under the influence of wind. The volume of sediment transport is determined by the strength of the flow that carries it and the particle size, volume, density, and shape. Stronger flows will increase the lift and drag on the particles, causing them to rise. Larger or denser particles will be transported closer to the bed.

Rivers and streams carry sediment in their flows. This sediment transport can occur at a variety of locations within the flow depth, depending on the balance between the upwards velocity on the particle (drag and lift forces), and the settling velocity of the particle.

When a grain settles down in still water, it reaches a constant velocity when the upward fluid drag force, $F_D = \frac{1}{2}\rho C_D \frac{\pi D_s^2}{4} V_s^2$, on the grain is equal to the downward submerged weight of the grain, $F_g = (\rho_s - \rho)g \frac{\pi D_s^3}{6}$. This constant velocity is defined as the settling velocity (fall velocity) of the grain.

The force balance between the drag force and the submerged weight is given as follows:

$$\frac{1}{2}\rho C_D \frac{\pi D_s^2}{4} V_s^2 = (\rho_s - \rho)g \frac{\pi D_s^3}{6}. \quad (28)$$

Therefore the settling velocity of the spherical particle is

$$V_s = \sqrt{\frac{4RgD_s}{3C_D}}, \quad (29)$$

where ρ is the water density, ρ_s is sediment particle density, C_D is the dimensionless drag coefficient, g is the gravity, D_s is the sediment particle diameter, and $R = (\rho_s - \rho)/\rho$ is the submerged specific gravity of the sediment.

Dimensional analysis implies that the drag coefficient is a function of the Reynolds number and the particle shape

$$C_d = f\left(\frac{V_s D_s}{\nu}, \text{ particle shape}\right), \quad (30)$$

where ν is the kinematic viscosity of water.

This relation is not explicit in V_s ; one must compute fall velocity by trial and error.

At low particle Reynolds number ($\frac{V_s D_s}{\nu} < 1$), the flow around the particle is laminar. At large particle Reynolds number ($\frac{V_s D_s}{\nu} > 10^3$), the flow around the spherical particle is turbulent, and the drag coefficient is nearly constant. Sediment particles have irregular shapes and their drag coefficient differs from that of spherical particles. Their shape is often angular, sometimes disc shaped, and the drag coefficient can be expected to be larger than that of spheres. Other useful relations to estimate sediment fall velocity can be found in the literature (Dietrich, 1982; Garcia, 2007).

The settling velocity of a single particle is modified by the presence of surrounding particles. Experiments have shown that thick homogeneous suspensions have a slower fall velocity than that of a single particle. Furthermore, the fall velocity of the suspension decreases with increasing volumetric sediment concentration. This effect, called hindered settling, results from the interaction between the downward fluid motion induced by each particle on the surrounding fluid and the return flow (i.e., upward fluid motion) following the passage of a particle. As a particle settles down, a volume of fluid equal to the particle volume is displaced upwards. In thick sediment suspension, the drag on each particle tends to oppose the upward fluid displacement (Chanson, 2004).

The Rouse number is a ratio of sediment fall velocity to upwards velocity from lift and drag forces (Rouse, 1939)

$$Rouse = \frac{V_s}{\kappa u_*}, \quad (31)$$

where V_s is the fall velocity, κ is the von Kármán constant and u_* is the shear velocity.

If the upwards velocity approximately equals the settling velocity, sediment will be transported downstream entirely as suspended load. If the upwards velocity is much less than the settling velocity, but still high enough for the sediment to move, it will move along the bed as bedload by rolling, sliding, and saltating (jumping up into the flow, being transported a short distance, then settling again). If the upwards velocity is higher than the settling velocity, the sediment will be transported high in the flow as wash load. Since there is generally a range of different particle sizes in the flow, it is common for material of different sizes to move through all areas of the flow for a given stream condition.

Yang (1996) pointed out the importance of fall velocity in the study of sediment transport by applying the unit stream power on the data of Schumm and Khan (1972). He showed that a close relationship between total sediment concentration and unit stream power exist in straight channels, in those channels that are in the process of changing their patterns from straight to meandering, and in braided channels. He concluded that among all the parameters used in the determination of sediment transport rate, stream power and unit stream power have stronger correlation with sediment transport rate or concentration. Based on theoretical derivations and measured data, unit stream power or dimensionless unit stream power are preferable to other parameters for the determination of sediment transport rate or concentration. The lack of a well-defined strong correlation between sediment load or concentration and a dominant variable selected for the development of a sediment transport equation may be the fundamental reason for discrepancies between computed and measured results under different flow and sediment conditions. He applied this method only to steady flow conditions.

Unit stream power is defined as: $\frac{u S}{V_s}$, where u is mean flow velocity, S is energy or surface

slope, and V_s is fall velocity.

Unit stream power is not applicable for zero bed slope situations. In the present study, we could not use this method because the slope of the channel was zero.

During a flood, the relation between the stream flow discharge and the instantaneous sediment concentration may not be unique. This tendency of sediment concentration to have different values at identical stream discharges, namely the hysteresis effect, is the primary drawback to the application of transport curves during floods.

Croley (1982) described unsteady flow and sedimentation in overland rills by continuity equations and approximations for flow, entrainment and transport capacity. The solution of these equations with the method of characteristics for the unsteady flow case results in three analytical expressions describing sediment concentrations: the first one for the accelerating stage of the hydrograph, the second one for the initial phase of the steady-state part of the hydrograph, and the third one for the remaining portion of the steady-state part of the hydrograph. Sediment equilibrium occurs well after flow equilibrium and suggests a mechanism for the time lag observed in hydrographs between the flood peak and the sediment peak. This time lag is also found in routing when there are no lateral inflows. The initial concentration may be smaller than or greater than the amount suggested by steady-uniform transport capacity relations and reaches an equilibrium value which also may not be consistent with steady-uniform transport capacity due to the presence of lateral inflow.

2.4.2 BEDLOAD TRANSPORT

The term bedload describes particles in a flowing fluid (usually water) that are transported along the bed. Bedload moves by rolling, sliding, and/or saltating. Generally, bedload downstream will be smaller and more rounded than bedload upstream. This is due in part to attrition and abrasion, which results from the stones colliding with each other and against the river channel, thus removing the rough texture (rounding) and reducing the size of the particles. However, selective transport of sediments also plays a role in relation to downstream fining: smaller-than-average particles are more easily entrained than larger-than-average particles, since the shear stress required to entrain a grain is linearly proportional to the diameter of the grain. However, the degree of size selectivity is restricted by the hiding effect described by Parker et. al. (1982). Larger particles protrude from the bed, whereas small particles are shielded and hidden by larger particles, with the result that nearly all grain sizes become entrained at nearly the same shear stress. Thus bedload must be determined in relation to the effective shear stress that acts directly on the grain surface and bedload transport occurs when the bed shear stress exceeds a critical value. It is reasonable to assume that the volume bedload transport rate per unit width (sliding, rolling, saltating), q_b , increases with a depth-averaged flow velocity, u , or boundary shear stress, τ_b .

Several researchers (e.g., Meyer-Peter and Muller, 1948; Shields, 1936; Einstein, 1950; Nielsen, 1992; Parker, 1979) attempted to predict the rate of bedload transport, and they proposed formulae to estimate the characteristics of the bedload layer. Some commonly quoted bedload transport relations with good data bases are given below (Parker, 2004; Garcia, 2007)

$$\frac{1}{\sqrt{\pi}} = \int_{-\left(\frac{0.143}{\tau^*}\right)^{-2}}^{\left(\frac{0.143}{\tau^*}\right)^{-2}} e^{-t^2} dt = \frac{43.5q_b^*}{1+43.5q_b^*} \quad \text{Einstein (1950)} \quad (32)$$

$$q_b^* = 17(\tau^* - \tau_c^*)(\sqrt{\tau^*} - \sqrt{\tau_c^*}), \tau_c^* = 0.05 \quad \text{Ashida and Michiue (1972)} \quad (33)$$

$$q_b^* = 18.74(\tau^* - \tau_c^*)(\sqrt{\tau^*} - 0.7\sqrt{\tau_c^*}), \tau_c^* = 0.05 \quad \text{Engelund and Fredsoe (1976)} \quad (34)$$

$$q_b^* = 5.7(\tau^* - \tau_c^*)^{1/2}, \tau_c^* = 0.037 \sim 0.0455 \quad \text{Fernandez Luque and van Beek (1976)} \quad (35)$$

$$q_b^* = 11.2(\tau^*)^{1.5} \left[1 - \frac{\tau_c^*}{\tau^*}\right]^{4.5}, \tau_c^* = 0.03 \quad \text{Parker (1979) fit to Einstein (1950),} \quad (36)$$

where q_b^* is the volume bedload transport rate per unit width, q^* is the dimensionless Einstein bedload number, τ^* , is the Shields stress, and τ_c^* , is the critical Shields stress.

Ouriemi et al. (2009) proposed a continuum approach to describe bedload transport in the laminar viscous regime. They addressed a situation in which bedload can be considered as a mobile granular medium where the particles mainly interact through contact forces. In nonuniform flows like those on the stoss sides of typical bed forms, for example, spatially separated near-bed points at the same height above the bed that have the same local bed shear stress can have significantly different turbulence intensities. In unsteady or nonuniform flows such as those over typical bed features Nelson et al. (1995) explained that the magnitude and frequency structure of the turbulence near the bed can vary dramatically, and hence result in considerable change in the bedload transport processes with little or no variation in bed shear stress. Thus in many important cases, including but not limited to flow over bed forms, bed shear stress is not a suitable parameter from which to predict mean sediment flux if the objective is to address the subtle interactions between flow and bed that govern the morphology of erodible beds and its response to changing flow conditions.

2.4.3 SUSPENDED LOAD TRANSPORT

Suspended load is the term used for sediment particles that settle slowly enough to be carried in flowing water (such as in a stream or coastal area), either without touching the bed, or while only intermittently touching it. These particles are generally the size of fine sand, silt and clay, although larger particles may be carried as well, depending on the intensity of the flow. The initiation of sediment motion is related to shear velocity or to bed shear stress. Suspension of sediment particles occurs when the local bottom shear stress, ρu_*^2 , exceeds the critical value (Shields, 1936). Under steady flow conditions, suspension may also be caused by secondary currents (Nezu and Nakagawa, 1993) or coherent structures (Nezu and Nakagawa, 1993; Cellino and Lemmin, 2004; Nezu, 2005).

Considering a particle in suspension, particle motion in the direction normal to the bed is related to the balance between the particle fall velocity component ($V_s \cos \theta$) and the turbulent velocity fluctuation w' in the direction normal to the bed. Turbulence studies suggest that the turbulent velocity fluctuation is of the same order of magnitude as shear velocity (Chanson, 2004).

Several researchers proposed criteria for the onset of suspension and their formulae are summarized by Chanson (2004). Suspended sediment load occurs when the flow

turbulence is strong enough to balance the particle weight. In a first approximation, it takes place when

$$\frac{u_*}{V_s} > 0.2 \text{ to } 2, \quad (37)$$

where u_* is the shear velocity and V_s is the settling velocity. Julien (1995) proposed that in turbulent water flow over a rough bed, suspended sediment load occurs when $\frac{u_*}{V_s} > 0.2$.

For sediment to be maintained in suspension to any significant degree, some measure of the characteristic velocity of the turbulent fluctuations of the flow must be at least of the same order of magnitude as the fall velocity V_s of the sediment itself (Parker 2004).

Parker (2004) obtained the following criterion for the onset of significant suspension:

$$\tau_s^* = \frac{u_{*sus}^2}{RgD_s} = \frac{V_s^2}{RgD_s} = R_f^2(Re_p), \quad (38)$$

where $R = (\rho_s - \rho)/\rho$ is the submerged specific gravity of the sediment, ρ is the water density, ρ_s is the sediment particle density, g is the acceleration of gravity, D_s is the sediment particle diameter, $R_f = R_f(Re_p)$ defines the functional relationship for fall velocity, $Re_p = \frac{\sqrt{RgD_s}D_s}{\nu}$, and u_{*sus} is the shear velocity of suspension sediment.

Suspended sediment concentration can be calculated with the Rouse distribution which is one of the milestones in the mechanics of sediment transport (Vanoni, 1984) as

$$\frac{\bar{c}}{\bar{c}_b} = \left[\frac{(h-z)/z}{(h-b)/b} \right]^{\frac{V_s}{\kappa u_*}}, \quad (39)$$

where \bar{c}_b is a near bed reference concentration measured at a distance $z = b$ from the bed, b is a position near the bed elevation, such that $b/h \ll 1$, where the volume concentration of suspension sediment is c_b ; (Garcia and Parker, 1991) use a reference height $b = 0.05 h$; h is the water depth, u_* is the shear velocity, V_s is the settling velocity, and κ is the von Kármán constant.

Depth-averaged volume suspended sediment concentration, \bar{C} , is defined by Garcia (2007):

$$\bar{C} = \frac{1}{h} \int_b^h \bar{c}(z) dz, \quad (40)$$

where $\bar{c}(z)$ is a concentration measured at a distance z from the bed, and h is the water depth.

Liu et. al. (2007) showed that in open-channel flow two types of sediment concentration profiles are possible. In type one, which is explained with the traditional diffusion theory, the sediment concentration always decreases from the bed to the water surface. In type two, which cannot be explained by the diffusion theory, sediment concentration increases at first, then begins to decrease when the height from the bed reaches a critical value. They found that both the gradient of the vertical fluctuation intensity of particles and the flow uplift force may cause the reverse distribution of sediment concentration. Therefore the rapid decrease of the gradient of the particle fluctuation intensity with height from the bed

and the flow uplift force in the region near the bed are the key factors leading to a type two profile of sediment concentration. They also showed that the momentum transport caused by the vertical fluctuation of particles is the most significant factor leading to sediment particle suspension in water flow.

The different velocities of flood waves and stream flow can have a major effect on the relation of stream discharge to suspended sediment concentrations. Flood waves move downstream faster than the flow velocity, thus leaving the original floodwaters and their entrained sediments lagging progressively further behind with increasing distance downstream. Therefore understanding the suspension sediment dynamics during flood events is important to predict the effects of sedimentation and the loss of storage capacity of reservoirs, to control changes in river morphology and to find the best solution for problems in rivers.

2.4.4 BEDFORMS

Moving sediment can generate a variety of different forms depending on the characteristics of the material and its substrate, which ultimately effect transport and bed morphology. The interaction of flow and sediment transport often creates bedforms. In general, bedforms are generated at a constant rate starting from flat bed conditions. The rate of bedform generation increases with increasing sediment transport rate. Bedforms, such as ripples, dunes, antidunes, and bars, in turn can interact with the flow to modify the rate of sediment transport. Ripples and dunes move in the downstream direction. Antidunes and step-pools are observed with supercritical flows, and they migrate in the upstream flow direction. The typical beforms are summarized in Fig. 3.

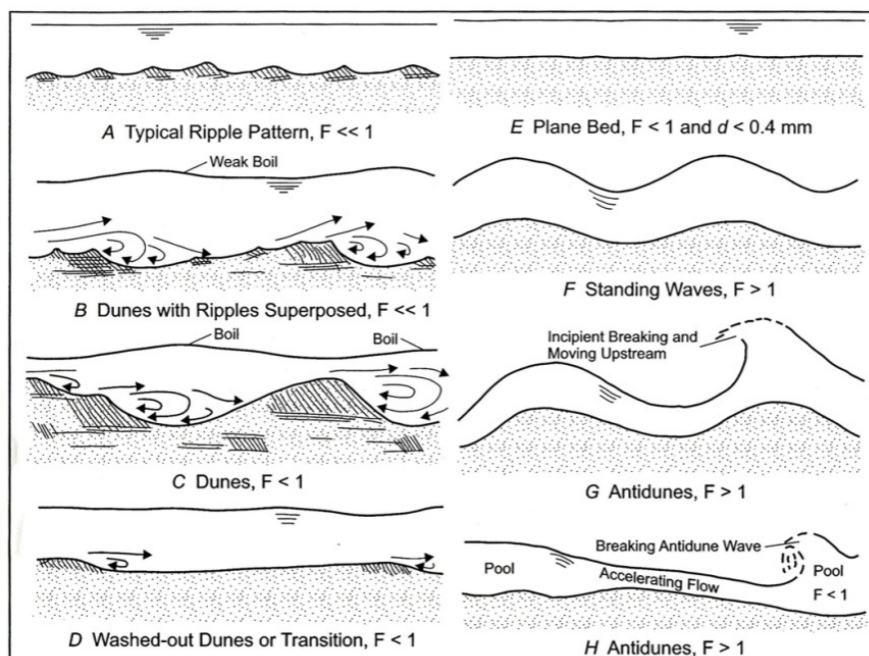


Fig. 3. Schematic of different bedforms, F = Froude number, d = Sediment size (Garcia, 2007)

Coleman and Melville (1994) determined that the bedform propagation speed decreases with increasing bedform height. The mechanisms of bedform coalescence and bedform throughpassing are found to be central to bed evolution processes. They observed that the rate of bedform development from flat bed conditions increases with increasing bed shear stress and decreasing sand size. Coleman and Melville (1996) described wavelength of the bedform by the empirical formula

$$\frac{l}{d_g} R_{*c}^{0.2} = 10^{2.5} \quad (41)$$

where l is sand wavelet length, d_g is geometric mean sediment size $= (d_{84} d_{16})^{0.5}$, d_{84} is sediment size for which 84% by weight of sediment is finer, d_{16} is sediment size for which 16% by weight of sediment is finer, R_{*c} is critical grain Reynolds number $= d_g u_{*c} / \nu$, u_{*c} is critical shear velocity and ν is fluid kinematic viscosity.

This formula shows that sand wave length is relatively insensitive to applied bed shear stress and is primarily a function of sediment size. They argue that sand-wavelet generation is predicted to begin with the occurrence of a random pile-up of sediment on the bed. This pile-up subsequently grows as more sediment is trapped by the pile-up. When the height of the pile-up approaches the order of the bed roughness height, further pile-ups are generated downstream of the initial sediment pile-up. The rate of generation of these latter pile-ups is the function of the rate of sediment transport for the fluid-sediment flow system being considered.

Ripples occur mainly in sands with diameters < 0.6 mm and are steeper and shorter than dunes. Their length depends on particle diameter (length of the ripples $\ll 1000D$ and height of the ripples $< 100D$). Most often, the wavelength of ripple crests is given as an indicator characterizing ripples. Typical wavelengths, λ , are of the order of tenths of centimeters and wave heights, $\Delta\eta$, are of the order of centimeters. Equations for equilibrium ripple dimensions are suggested by Baas (1999). However, he indicated that the observed dimensions are much smaller than the equilibrium ripple dimensions. Ripples migrate downstream and are asymmetric with a gentle stoss (upstream) side and a steep lee (downstream side).

In rivers, a viscous sublayer can exist only when the flow is very slow and well below flood conditions. Because of the viscous sublayer, ripples do not interact with the water surface. Formation of ripples by primary linear instability studies by Fourrière et al. (2010) showed that the evolution of the ripple wavelength and amplitude on short time scales is consistent with a linear instability. Ripple wavelengths grow and saturate just after crossing the resonance condition of surface waves and in the course of this pattern coarsening, the bedforms are in quasi equilibrium between erosion and deposition.

Parker (2004) used the modified Brownlie (1981) relation to yield a maximum value of Re_p (Reynolds number of particle) for ripple formation. The value he obtained was 91, corresponding to a grain size of 0.8 mm with $\nu = 0.01$ cm²/s and $R = 1.65$. In practice, ripples are observed only for $D < 0.6$ mm. Ripples can coexist with dunes (Fig. 4).

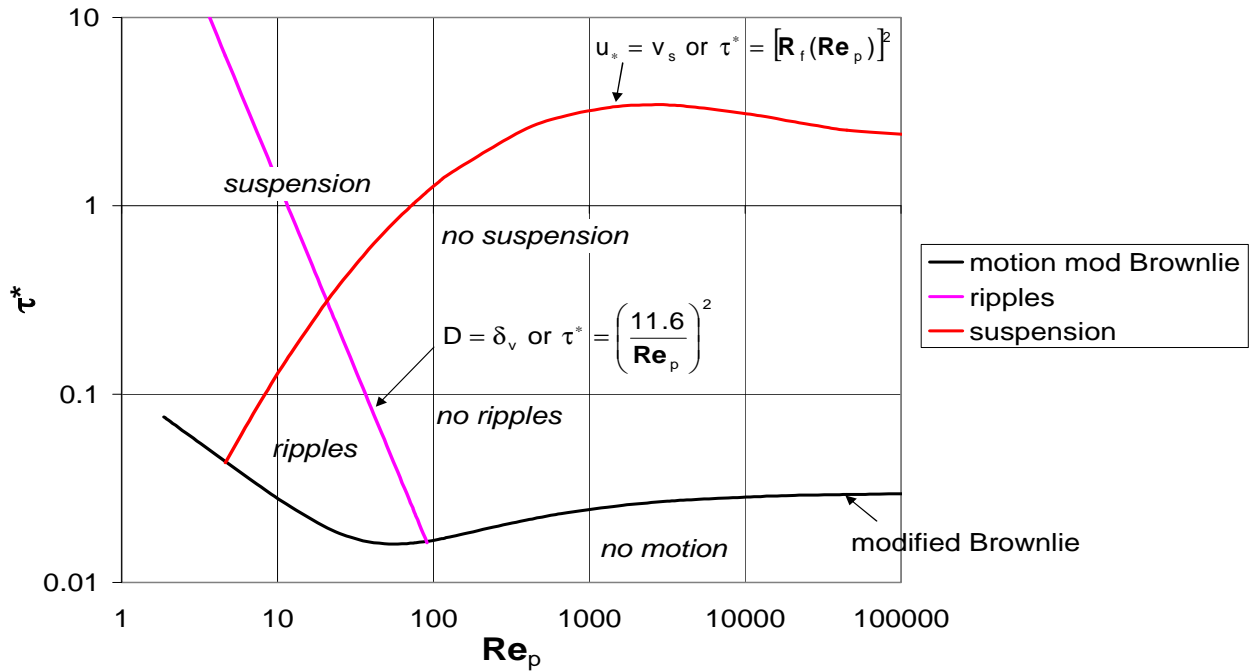


Fig. 4. Shields diagram with criterion for ripples, δ_v is thickness of the viscous sublayer (Parker, 2004)

In the present study, we will focus on the initial development of ripples.

Dunes are the most common bedforms in sand-bed rivers; they can also occur in gravel-bed rivers. Dune length may scale with water depth and dunes often generate a corresponding deformation of the free water surface, such that the flow accelerates over the crests, where water surface elevation is slightly reduced. Wavelength, λ , can range up to hundreds of meters, and wave height, $\Delta\eta$, can range up to 5 m or more in large rivers. Dunes are usually asymmetric, with a gentle stoss (upstream) side and a steep lee (downstream) side. They are characteristic of subcritical flow (Froude number sufficiently below 1). Dunes migrate downstream. In pipe flow, Ouriemi et al. (2009) observed that small dunes are present with small amplitudes and only exist in laminar flow. Vortex dunes are characterized by the existence of vortices at their front and are found either in laminar or turbulent flow. Sinuous dunes, showing a double periodicity, appear in turbulent flow. While the threshold for incipient motion is determined by the Shields number, the one dune formation appears to be described by the Reynolds number and not by the Shields number. Moreover, the dune instability is not a long-wave instability at threshold but does present a finite wavelength of the order of the fluid thickness (Ouriemi et al., 2009).

Antidunes occur in rivers with sufficiently high (but not necessarily supercritical) Froude numbers. They can also occur in sand-bed and gravel-bed rivers. The most common type of antidune migrates upstream and shows little asymmetry. The water surface is strongly in phase with the bed. A train of symmetrical surface waves is usually indicative of the presence of antidunes (Parker, 2004).

Trains of cyclic steps occur in very steep flows with supercritical Froude numbers. They are long-wave relatives of antidunes. The steps are delineated by hydraulic jumps (immediately downstream where the flow is locally subcritical). The steps migrate

upstream. Cyclic steps form in the field when slopes are steep, the flow is supercritical, and there is an abundance of sediment (Parker, 2004).

In streams with sufficient width B , the bed of the channel does not remain plane, but instead is subject to bar instability. The governing parameter here is the ratio of width- to -depth B/h . When this number exceeds a value between 12 and 20, the flow becomes unstable and creates single-row alternate bars. Alternate bars migrate downstream, and often have relatively sharp fronts. They are often precursors to meandering. Alternate bars may coexist with dunes and/or antidunes (Parker, 2004).

Multiple-row bars (linguoid bars) occur when the width-depth ratio, B/h , is even larger than that for alternate bars. These bars migrate downstream. They may co-exist with dunes or antidunes (Parker, 2004).

Coleman and Melville (1996) observed that both ripples and dunes, sand waves of different characteristics, are found to develop from the same sand wavelets. Colombini and Stocchino (2011) found that in the smooth and transitional regimes both ripples and dunes appear as a primary instability. Although ripple formation is also controlled by the viscous scale, the latter cannot be used alone to determine the characteristic wavelengths, since, as with the case of dunes, flow depth plays a role. Their results showed that dunes form at larger values of the Shields parameter, whereas ripples form at smaller values. At intermediate values of the Shields parameter, they may coexist. A study of the effects of flow separation on sediment dynamics over bedforms and ultimately on their hydraulic stability by Mazumder et. al. (2009) showed that the waveform with a sharply sloping lee-face has a thicker separation bubble with flow reversal, whereas there is flow separation only over a limited portion of the lee slope for a symmetric structure of equal stoss and lee sides. Experimental results of Doucette and O'Donoghue (2006) in oscillatory flow showed that equilibrium ripple geometry is independent of initial bed morphology whenever the time needed to reach equilibrium is largely independent of the initial bed and the equilibrium ripple size. The time needed to reach equilibrium depends strongly on the mobility number $\left(\frac{2u_{rms}^2}{(s-1)gD_{50}}\right)$ where u_{rms} is the root-mean-square horizontal water particle velocity, s is sediment specific gravity (2.65 for sand), g is gravity and D_{50} is the sediment size for which 50% of the sediment sample is finer).

McLean et al. (1994) measured the turbulence structure over sand dunes and pointed out the importance of coherent eddies in lifting up sediment particles behind the dune crest. Flow over ripples is dominated by shear layer instability resulting from separation zones in the lee side of the ripple. Turbulent coherent structures are able to penetrate further into the outer flow and thus induce return flows that are able to exert greater shear stress as they impact on the bed (Best, 2005). The shear stress on the bed can be considered as the sum of flow-induced shear and form-induced shear by the ripples. Best (2005) also indicated that differences in unsteady flow may affect the scales of bedforms. Flow unsteadiness was primarily expressed in a change of superimposed bedform type. The flow and sediment transport conditions on the back of the bedform control the superimposed bedform type and sorting (Reesink and Bridge, 2009).

In most cases, ripples will develop first during unsteady accelerating flow, followed by dunes in the long term. Reviews by Best (2005) and Garcia (2007) summarize recent developments in bedform research. It is recognized that the characteristics of the flow over alluvial bedforms has many similarities to flow over tidal and oceanic bedforms, as well as flow over aeolian dunes (Bagnold, 1941). Therefore, the results from an open-channel study carried out here can also be applied to coastal ocean situations.

Most studies concerning the dynamics of ripple formation and sediment suspension reported in the literature have investigated steady flow situations. In the present study, ripple development in depth-varying accelerating flow will be explored. We will cover a situation developing from a flat sediment bed at rest to quasi-steady flow with suspended sediments and ripple formation.

This study focuses on some hydrodynamic aspects of unsteady acceleration and decelerating open-channel flow without and with sediment transport to advance the understanding of sediment flux development and ripple formation under unsteady flow condition. We will apply acoustic and optical methods providing high spatial and temporal resolution profile data to determine velocity profiles and particle dynamics, and we will also consider the advantages of each method.

2.5 REFERENCES

- Afzalimehr, H., Anctil, F., 2000. Accelerating shear velocity in gravel-bed channels. *J. Hydrol. Sci.* 45, 113–123.
- Akhavan, R., Kamm, R. D., Shapiro, A. H., 1991. An investigation of transition to turbulence in bounded oscillatory Stokes flows. I: Experiments. *J. Fluid Mech.* 225, 395–422.
- Albayrak, I., 2008. An experimental study of coherent structures, secondary currents and surface boils and their interrelation in open-channel flow. Ph.D. Thesis, No 4112, Ecole Polytechnique Fédérale (EPFL), Lausanne, Switzerland.
- Albayrak, I., Hopfinger, E.J., Lemmin, U., 2008. Near-field flow structure of a confined wall jet on flat and concave rough walls. *J. Fluid Mech.* 606, 27–49.
- Ashida, K., Michiue, M., 1972. Study on hydraulic resistance and bedload transport rate in alluvial streams, *Transactions, Japan Society of Civil Engineering*, 206: 59-69 (in Japanese).
- Baas, J.H., 1999. An empirical model for the development and equilibrium morphology of current ripples in fine sand. *Sedimentology* 46, 123–138.
- Bagnold, R.A., 1941. *The physics of blown sand and desert dunes*. Methuen, New York.
- Best, J., 2005. The fluid dynamics of river dunes: a review and some future research directions. *J. Geophys. Res.* 110, F04S02, doi: 10.1029/2004JF000218.
- Blanckaert K., Lemmin U., 2006. Means of noise reduction in acoustic turbulence measurements. *J. Hydr. Res., IAHR*, 44: 3–17.
- Brereton, G.J., Mankbadi, R. R., 1995. Review of recent advances in the study of unsteady turbulent internal flows. *Appl. Mech. Rev.*, 48, 189–212.
- Brownlie, W. R., 1981. Prediction of flow depth and sediment discharge in open-channels, Report No. KH-R-43A, W. M. Keck Laboratory of Hydraulics and Water Resources, California Institute of Technology, Pasadena, California, USA, 232 p.
- Cellino, M., Lemmin, U., 2004. Influence of coherent flow structures on the dynamics of suspended sediment transport in open-channel flow. *J. Hydr. Eng.* 130, 1077–1088.
- Chanson, H., 2004. *The hydraulics of open-channel flow: an introduction basic principles, sediment motion, hydraulic modelling, design of hydraulic structures*. Second Edition, Elsevier Butterworth-Heinemann.
- Chaudhry, M.H., 2008. *Open-channel flow*. Second edition, Springer Science+Business Media, LLC.
- Coleman, S.E., Melville, B.W., 1994. Bed-form development. *J. Hydraulic engineering*, 120 (4), 544–560.
- Coleman, S.E., Melville, B.W., 1996. Initiation of bedforms on a final sand bed. *J. Hydraulic engineering*, 122 (6), 301–310.
- Colombini, M., Stocchino, A., 2011. Ripple and dune formation in rivers. *J. Fluid Mech.* 673, 121–131.
- Croley II, T.E., 1982. Unsteady overland sedimentation. *J. Hydrol.*, 56: 325–346.
- De Sutter, R., Verhoeven, R., Krein, A., 2001. Simulation of sediment transport during flood events: laboratory work and field experiments. *Hydrol. Sci.* 46, 599–610.
- Dietrich, W.E., 1982. Settling velocities of natural particles. *Water Resour. Res.* 18(6), 1615–1626.
- Doucette, J.S., O’Donoghue, T., 2006. Response of sand ripples to change in oscillatory flow. *Sedimentology*, 53, 581-596.

- Dombroski, D.E., Crimaldi, J.P. 2007. The accuracy of acoustic Doppler velocimetry measurements in turbulent boundary layer flows over a smooth bed. *Limnol. Oceanogr.: Methods*, 5: 23–33.
- DuBuat, P., 1786. *Principes d'hydraulique*. L'imprimerie de monsieur, Paris, France.
- Einstein, H.A., 1950. The bed-load function for sediment transportation in open-channel flows. Technical Bulletin 1026, U.S. Dept. of the Army, Soil Conservation Service.
- Engelund, F., Fredsoe, J., 1976. A sediment transport model for straight alluvial channels, *Nordic Hydrology*, 7, 293–306.
- Fernandez Luque, R., van Beek, R., 1976. Erosion and transport of bedload sediment, *Journal of Hydraulic Research*, 14(2): 127–144.
- Fourrière, A., Claudin, P., Andreotti, B., 2010. Bedforms in a turbulent stream: formation of ripples by primary linear instability and of dunes by nonlinear pattern coarsening. *J. Fluid Mech.*, 649, 287–328.
- Garcia, M.H., 2007. Sediment transport and morphodynamics. In: M.H. Garcia (Ed.) *Sedimentation engineering*. ASCE Manuals and Reports on Engineering Practice No 110, 21–146.
- Garcia, M.H., Parker, G., 1991. Entrainment of bed sediment into suspension. *Journal of Hydraulic Engineering*, ASCE, 117(4), 411–435.
- Hayashi, T., Ohashi, M., Oshima, M., 1988. Unsteadiness and turbulence structure of a flood wave. *Proc., 20th Symp. on Turbulence*, 154–159 (in Japanese).
- Hurth D., Lemmin U., 2001. Discussion of “Equilibrium near-bed concentration of suspended sediment” by Z. Cao. *J. Hydraul. Eng.* 127: 430–433.
- Jensen, B.L., Sumer, B. M., 1989. Turbulent oscillatory boundary layers at high Reynolds numbers. *J. Fluid Mech.* 206, 265–297.
- Julien, P. Y., 1995. *Erosion and sedimentation*. Cambridge university press, Cambridge, U.K.
- Katul, G., Wiberg, P., Albertson, J., Hornberger, G., 2002. A mixed layer theory for flow resistance in shallow streams. *Water Resour. Res.*, 38, 1250, doi: 10.1029/2001WR000817.
- Kim, S.C., Friedrichs, C.T., Maa, J.P.Y., Wright, L.D., 2000. Estimating bottom stress in a tidal boundary layer from acoustic Doppler velocimeter data. *J. Hydraulic Engineering*, ASCE, 126, 399–406.
- Lhermitte, R., Lemmin, U., 1994. Open-channel flow and turbulence measurement by high-resolution Doppler sonar. *J. Atm. and Ocean. Tech.* 11, 1295–1308.
- Liu, Q.Q., Shu, A.P., Singh, V.P., 2007. Analysis of the vertical profile of concentration in sediment-laden flows. *J. Engineering Mechanics*, ASCE, 133(6), 601–607.
- Mazumder, B.S., Pal, D.K., Ghoshal, K., 2009. Turbulence statistics of flow over isolated scalene and isosceles triangular-shaped bedforms. *Journal of hydraulic research*, 47 (5), 626–637.
- McLean, S.R., Nelson, J.M., Wolfe, S.R., 1994. Turbulence structure over two dimensional bedforms: implications for sediment transport. *J. Geophys. Res.* 99, 12729–12747. doi: 10.1029/94JC00571.
- Meyer-Peter, E. Müller, R., 1948, Formulas for bed-load transport, proceedings, 2nd Congress, International Association of Hydraulic Research, Stockholm: 39-64.
- Monin, A.S., and Yaglom, A.M., 1971. *Statistical fluid mechanics*. 1, MIT Press, Cambridge, Mass.
- Nelson, J.M., Shreve, R.L., McLean, S.R., Drake, T.G., 1995. Role of near-bed turbulence structure in bed load transport and bed form mechanics. *Water resources research*, 31(8), 2071–2086.

- Nezu, I., 2005. Open-channel flow turbulence and its research prospect in the 21st century. *J. Hydr. Eng.* 131, 229–246.
- Nezu, I., Nakagawa, H., 1991. Turbulent structures over dunes and its role on suspended sediments in steady and unsteady open-channel flows. *Int. Symp. on Transport of Suspended Sediments and Its Mathematical Modeling*, IAHR, Firenze, Italy, 165–190.
- Nezu, I., Nakagawa, H., Ishida, Y., Kadota, A., 1993. Bed shear stress in unsteady open-channel flows. *Proc., 1993 Hydr. Conl.*, ASCE, New York, N.Y., 1458–1463.
- Nezu, I., Nakagawa, H., 1993. *Turbulence in open-channel flows*. Balkema, Rotterdam, NL.
- Nezu, I., Nakagawa, H., 1993b. Basic structure of turbulence in unsteady open-channel flows. *Proc., 9th Symp. on Turbulent Shear Flows*, Kyoto, Japan, 7.1.1–7.1.6.
- Nezu, I., Kadota, A., Nakagawa, H., 1997. Turbulent structure in unsteady depth-varying open-channel flows. *J. Hydr. Eng.* 123, 752–763.
- Nielson, P., 1992. *Coastal bottom boundary layers and sediment transport*. World Scientific, River Edge, N.J.
- Nikora, V.I., Goring, D., 2000. Flow turbulence over fixed and weakly mobile gravel beds. *J. Hydraulic Engineering*, ASCE, 126, 679–690.
- Ouriemi, M., Aussillous, P., Guazzelli, E., 2009. Sediment dynamics. Part 1. Bed-load transport by laminar shearing flows. *J. Fluid Mech*, 636, 295–319.
- Ouriemi, M., Aussillous, P., Guazzelli, E., 2009. Sediment dynamics. Part 2. Dune formation in pipe flow. *J. Fluid Mech*, 636, 321–336.
- Parker, G., 1979. Hydraulic geometry of active gravel rivers, *Journal of Hydraulic Engineering*, 105(9), 1185–1201.
- Parker, G., 2004. *1D Sediment transport morphodynamics with applications to rivers and turbidity currents*. E-book.
- Parker, G., Klingeman, P. C., Mclean, D. G., 1982. Bedload and size distribution in paved gravel-bed streams. *Journal of Hydraulic Engineering*, ASCE, 108(4), 544–571.
- Qu, Z., 2003. *Unsteady open-channel flow over a mobile bed*. Ph.D. thesis No. 2688, Ecole Polytechnique Fédérale (EPFL), Lausanne, Switzerland.
- Reesink, A.J.H., Bridge, J.S., 2009. Influence of bedform superimposition and flow unsteadiness on the formation of cross strata in dunes and unit bars, part 2, further experiments. *Sedimentary Geology*, 222 (3-4), 274-300.
- Rouse, H., 1939, Experiments on the mechanics of sediment suspension, *Proceedings 5th International Congress on Applied Mechanics*, Cambridge, Mass, 550-554.
- Schlichting, H., 1987. *Boundary-layer theory*. McGraw-Hill, New York.
- Shields, I.A., 1936. *Anwendung der Aehnlichkeitmechanik und der Turbulenzforschung auf die Geschiebebewegung*, Mitt. Preuss Ver.-Anst., 26, Berlin, Germany.
- Shumm, S.A., Khan, H. R., 1972. Experimental study of channel patterns. *Geological Society of America*, 83, 407.
- Smart, G.M., 1999. Turbulent velocity profiles and boundary shear in gravel bed rivers. *J. Hydraulic Engineering*, ASCE, 125, 106–116.
- Song, T., 1994. *Velocity and turbulence distribution in non-uniform and unsteady open-channel flow*. PhD thesis, No. 1324, Ecole Polytechnique Fédérale (EPFL), Lausanne, Switzerland.
- Song, T., Graf, W. H., 1996. Velocity and turbulence distribution in unsteady open-channel flows. *Journal of Hydraulic Engineering*, 122(3), 63-71.
- Suszka, L. 1987. *Sediment transport at steady and unsteady flow: a laboratory study*. PhD thesis, No. 704, Ecole Polytechnique Fédérale (EPFL), Lausanne, Switzerland.
- Townsend, A.A., 1976. *The structure of turbulent shear flow*. Cambridge Univ. Press, New York.

- Tu, H. 1991. Velocity distribution in unsteady flow over gravel beds. PhD thesis, No. 911, Ecole Polytechnique Fédérale (EPFL), Lausanne, Switzerland.
- Tu, H., Graf, W. H., 1992. Velocity distribution in unsteady open channel flow over gravel beds. *Journal of Hydraulic Research*, 31 (1) 99-110.
- Vanoni, V.A. 1984. Fifty years of sedimentation, *Journal of hydraulic Engineering*, ASCE, 110(8), August, 1021-1050.
- Wilcock, P.R., 1996. Estimating local bed shear stress from velocity observations. *Water Resources Research*, 32, 3361–3366.
- Yang, C.T., 1996. *Sediment transport theory and practice*. McGraw-Hill, New York.

CHAPTER 3

EXPERIMENTAL SET-UP, INSTRUMENTATION AND EXPERIMENTAL PROCEDURE

3.1	INTRODUCTION	57
3.2	EXPERIMENTAL SET-UP	57
3.3	INSTRUMENTATION	61
3.4	EXPERIMENTAL PROCEDURE	68
3.5	REFERENCES	72

3.1 INTRODUCTION

To simulate fine sediment dynamics over an armored bed in a river during the passage of a flood wave, unsteady (first accelerating, then decelerating) laboratory open-channel flow over a movable (but not moving) coarse gravel bed ($D_{50} = 5.5$ mm) was studied. Quasi-instantaneous profiles of velocity and sediment concentration were taken simultaneously and co-located using acoustic Doppler and imaging methods. Flow visualization and PTV measurements were made in parallel.

The measurement techniques used in this research and the experimental procedure will be described. The results will then be discussed in the following chapters.

3.2 EXPERIMENTAL SET-UP

The measurements were carried out in a glass-walled open-channel at the Laboratoire d'Hydraulique Environnementale (LHE) of the Ecole Polytechnique Fédérale de Lausanne (EPFL), that is 17 m long and has a rectangular cross section 0.6 m wide and is 0.8 m deep. The bottom is covered with a 0.1 m thick gravel layer with $D_{50} = 5.5$ mm (Fig.1). The channel is operated in closed circuit mode. Water is stored in 2 tanks (1 and 2 in Fig. 2), from where it is pumped into the head tank of the channel via a supply pipe (3 in Fig. 2). An electromagnetic flowmeter (4 in Fig. 2) is installed in the pipe to measure the supply discharge. Discharge is modified by changing the rotational speed of the pump (P1 in Fig. 2) by computer. A shallow weir at the end of the channel controls the water level. The weir is strongly inclined in the flow direction and covered with coarse open cell foam and coarse gravel in order to damp oscillations which may be produced by changes in discharge. The water level in the channel is measured with three ultrasonic limnimeters (L1, L2 and L3 in Fig. 2) spaced along the channel axis. The bed of the channel is horizontal.

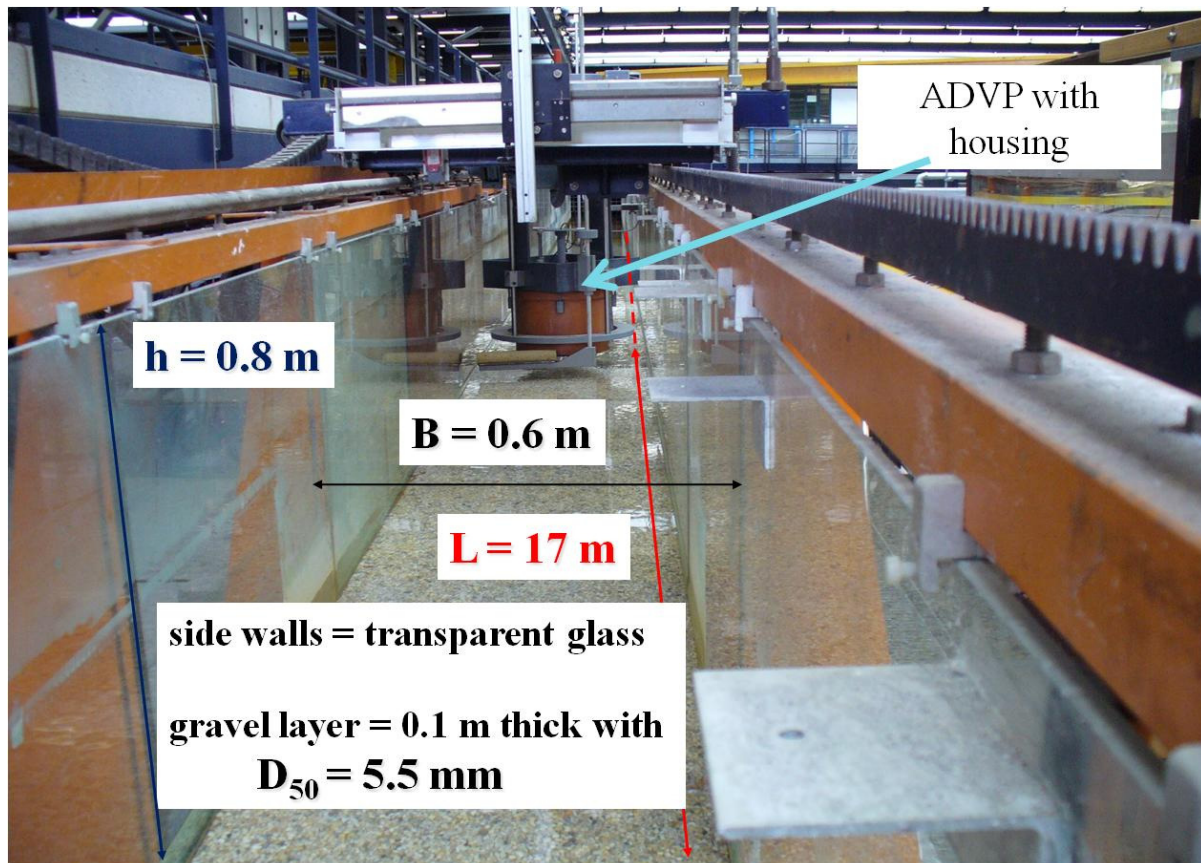


Fig. 1 Open-channel test section with Acoustic Doppler Velocity Profiler (ADVP)

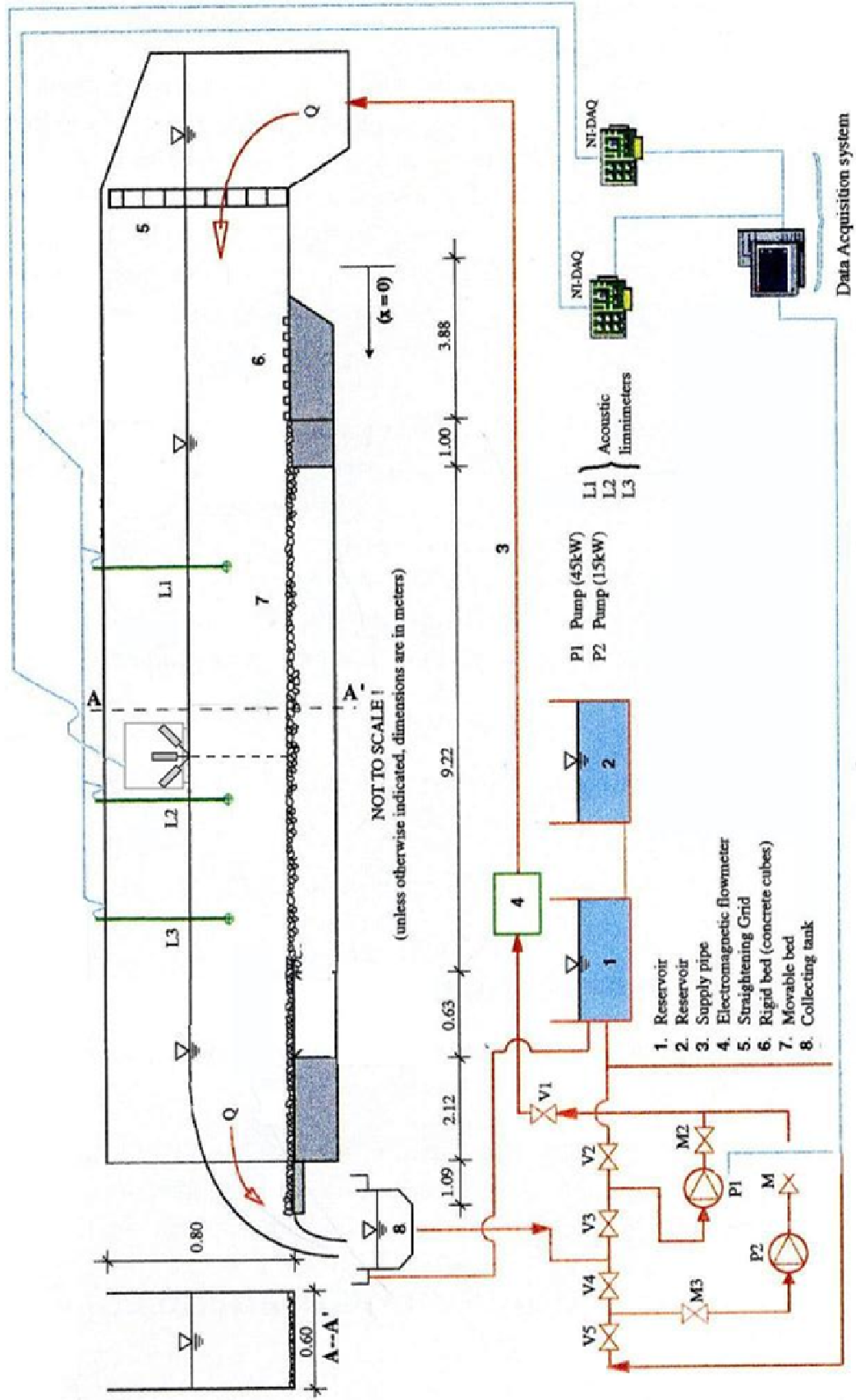


Fig. 2 General view of the experimental set-up

3.3 INSTRUMENTATION

3.3.1	Acoustic methods	62
3.3.1.1	Acoustic Doppler Velocity Profiler (ADVP)	62
3.3.1.2	Acoustic Doppler Particle Flux Profiler	63
3.3.1.3	Ultrasonic Limnimeter	64
3.3.2	Particle Tracking Velocimetry (PTV)	65

3.3 INSTRUMENTATION

3.3.1 ACOUSTIC METHODS

To capture the dynamics of unsteady sediment-laden flow, instrumentation is required that can simultaneously measure hydrodynamics, sediment concentration in the whole water column and bed morphology with sufficient spatial and temporal resolution to resolve turbulent scales. Acoustic methods based on the backscattering of sound are well suited to fulfill these requirements. Acoustic Backscattering Systems (ABS) can capture the Doppler phase angle and the intensity of the backscattered signal from which flow velocity and sediment concentration, respectively, can be obtained. Thorne and Hanes (2002) summarized the development of ABS techniques and instrumentation that allow extracting this information. At present, velocity and sediment concentration are most often obtained separately (Harris et al., 2003; VanderWeft et al., 2007; Thorne et al., 2009). With this approach, sediment flux can only be resolved for scales that are larger than the separation of the instruments. To resolve sediment fluxes on smaller scales, velocities and sediment concentration have to be measured in the same scattering volume.

3.3.1.1 ACOUSTIC DOPPLER VELOCITY PROFILER (ADVP)

An instrument that is capable of taking co-located measurements with the resolution of turbulent scales was developed at our laboratory and has evolved over the past twenty years. It is based on the work of Lhermitte (1983) who showed the feasibility of a pulse-to-pulse coherent system in resolving turbulence scales in tidal channel flows. Acoustic Doppler Velocity Profiler (ADVP) measurements are based on the backscattered echo produced when an ultrasonic signal is scattered by moving targets. The quality of the signal obtained with the ADVP measurement is closely related to the nature of scattering targets and their capability to follow the fluid motion. In an ADVP, quasi-instantaneous velocity profiles resolving turbulence scales in space and time are obtained from the Doppler phase angle (Lhermitte and Lemmin, 1994) by applying the pulse-pair algorithm (Lhermitte and Serafin, 1984). This system was extended to full 3D instruments (Rolland and Lemmin, 1997). These were further improved in the hardware (Hurther and Lemmin, 1998) and software (Hurther and Lemmin, 1998, 2008; Franca and Lemmin, 2006) domain to reduce noise contributions. Today the ADVP is a flexible and reliable instrument used in the laboratory (Hurther et al., 2007a), in rivers (Franca et al., 2008), in lakes (Lemmin and Jiang, 1999), and in the shore zone of oceans (Hurther et al., 2007b).

The ADVP, which was developed at the LHE-EPFL, measures quasi-instantaneous profiles of 3D velocity components over the entire water depth of an open-channel flow (Lhermitte and Lemmin, 1994; Hurther and Lemmin, 1998, 2001). The instrument consists of a central emitter and four wide-angle receiver transducers placed symmetrically around the emitter. The transducers are arranged in two perpendicular planes, each of which allows resolving profiles of one horizontal and the vertical velocity component. The redundancy of the vertical component allows controlling the quality of the geometrical alignment of the transducers. This transducer arrangement provides velocities along a single straight vertical

line of consecutive scattering volumes (Fig. 3). All velocity components are evaluated from phase information coming from the same scattering volume, because sound is only emitted from the central transducer. The typical spatio-temporal resolution (3.3 mm and 0.032 s, respectively) is sufficient to quantitatively estimate turbulence parameters in the productive and inertial ranges of the spectral space.

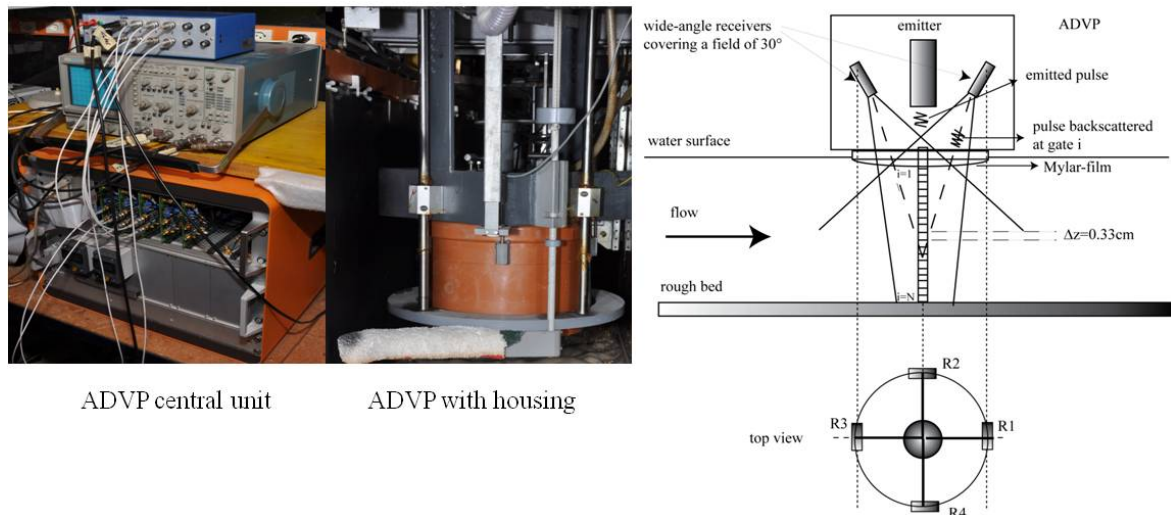


Fig. 3 Optimized four-receiver configuration of the Acoustic Doppler Velocity Profiler (ADVP) developed at the LHE, EPFL Lausanne

3.3.1.2 ACOUSTIC DOPPLER PARTICLE FLUX PROFILER

Backscattered intensity can be inverted into particle concentration after calibration (Thorne and Hanes, 2002). An iterative inversion method has been proposed by Thorne et al. (1993), and an explicit inversion method by Lee and Hanes (1995). However, both methods suffer from errors propagating through the profile (Shen and Lemmin, 1998). Thus, even a small error at one point in the profile generates errors in all of the following points. This is particularly severe when an error is made at the first point, where attenuation is assumed to be negligible, because it causes errors over the entire profile. Therefore, these methods are not well suited for attenuating media found in highly turbulent benthic suspension flows.

This problem, however, was overcome by combining backscattered and forward scattered profile signals, thus providing proper attenuation compensation even in high particle concentrations, as long as multiple scattering is avoided. By integrating this approach into the existing ADVP, an Acoustic Doppler Particle Flux Profiler was developed (Shen and Lemmin, 1996) which determined the 3D velocity field and the suspended particle concentration field co-located in the same scattering volumes of the full depth profile. It provided new insight into the dynamics of suspended particle transport (Hurther and Lemmin, 2001), and particularly demonstrated the importance of coherent structures in sediment transport (Shen and Lemmin, 1999; Cellino and Lemmin, 2004).

The inconvenience of this solution for field applications of the system was overcome by a new approach based on the exploitation of backscattering intensity at two (or more) emitted frequencies (Hay and Sheng, 1992; Hurther et al., 2006; Bricault, 2006). The advantage of this solution is that two relatively close frequencies (such as 1.25 MHz and 2 MHz) completely resolve the concentration field of fine particles typically found in benthic boundary layer applications. This frequency range can be handled by a single emitter transducer. Therefore, a two-frequency backscattering intensity profiler can easily be integrated into the existing ADV that was initially conceived to work with pulse interleaving at different frequencies. This provides a particle flux profiler that is unlimited in its application in the laboratory and field studies in rivers, estuaries, oceans and lakes, and, different from optical systems, it also functions well with high particle concentration. It has the important advantage that 3D velocity and particle concentration profile information is obtained simultaneously, co-located in the same scattering volumes within the profile, and resolves turbulence scales in time and space. Although the velocity determined from the Doppler phase does not require any calibration, an initial calibration of the backscattering intensity for a given particle size distribution has to be established. This can be obtained by suction sampling or from ABS systems in the same flow (Thorne and Hanes, 2002). A description of the most recent software developments of this Acoustic Doppler Particle Flux Profiler, showing in particular the advantage of a multi-frequency approach and its application under breaking waves in the shore zone of a wave flume, is given in Hurther et al. (2011). Smyth et al. (2002) also demonstrated the possibility of co-located velocity and concentration profiling using an ABS.

In low suspended particle concentrations, the number of sediment particles may not be sufficient to extract velocity and backscattering information, unless there are other tracers in sufficient quantity in the water. If this is not the case, particles may only be tracked occasionally through two consecutive pulses to obtain a velocity estimate. The rest of the time, no velocity data will be available. Mean value estimates over a whole time series may then be wrong. Such low particle density inside the scattering volume does not allow a calibration to obtain sediment concentration from backscattering intensity. Therefore, in this study no sediment flux estimates can be presented.

The location of the bed is easily extracted from the ADV or the Particle Flux Profiler by the strong echo of the backscattering intensity or from the zero velocity in the Doppler phase. For coarse beds, it is found (Bagherimiyab et al., 2008) that the bed level detected from the velocity profiles is located at about $0.2 D_{50}$ of the bed particles, which corresponds to the definition of reference bed level in rough flows.

3.3.1.3 ULTRASONIC LIMNIMETER

Ultrasonic limnimeters are placed above the water surface pointing down. They emit a sonic wave pulse which is reflected by an object of different density (e.g., flow surface, bed), back to the transducer. The time elapsed between emitting and receiving is proportional to the distance of the object from the sensor. For each experiment, the distance between the surface of the limnimeter transducer and the gravel bed is first measured. When the flow passes through the channel during experiments, the distance between the transducer and the water surface is obtained. The difference between both

gives the flow depth, which is verified by a manual limnimeter for the steady flow parts (Fig. 4). In this study, the water level in the channel is measured with three ultrasonic limnimeters spaced along the channel axis during the whole hydrograph.

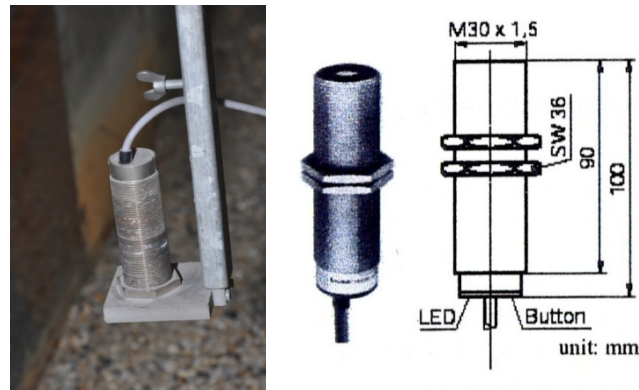


Fig. 4 Schematics of the Ultrasonic limnimeter. Left side: limnimeter in the channel, right side: limnimeter with its dimensions

3.2.2 PARTICLE TRACKING VELOCIMETRY (PTV)

Methods of fluid velocity measurements include Particle Image Velocimetry (PIV) and Particle Tracking Velocimetry (PTV), molecular tagging velocimetry, laser-based interferometry, ultrasonic Doppler methods, Doppler sensors, and new signal processing methodologies. Temporal integration of velocimetric information can be used to totalize fluid flow. In general, velocity measurements are made in the Lagrangian or Eulerian frames of reference.

In fluid dynamics, the Lagrangian specification of the flow field is a way of looking at fluid motion where the observer follows an individual fluid parcel as it moves through space and time. Plotting the position of an individual parcel as a function of time gives the pathline of the parcel. This can be visualized as sitting in a boat and drifting down a river.

In the Eulerian specification of the flow field, a fluid motion is observed at specific locations in space through which the fluid flows as time passes. This can be visualized as sitting on the bank of a river and watching the water pass a fixed location. Particle Tracking Velocimetry (PTV) is a Lagrangian approach which determines the velocity of individual flow tracer particles, whereas Particle Image Velocimetry (PIV), the average velocity within a sub-region of the field of view (Eulerian). In general, velocimetry can be traced back to the days of Leonardo Da Vinci, who would float grass seeds on a flow and sketch the resulting trajectories of the seeds that he observed (a Lagrangian measurement). Today, the basic idea is the same; the flow must be seeded with particles that can be observed by the method of choice. Prandtl and Tietjens (1929) already used particles to study fluid dynamics in a systematic manner. Later, Laser Doppler Velocimeters were developed using high particle concentrations. With the availability of fast, high-resolution

digital cameras, Particle Image Velocimetry (PIV) and PTV became standard measurement methods using lower particle concentrations (Adrian, 2005).

The principle of PTV is that tracer particles are added to the flow which are assumed to move with the local flow velocity. The flow with the illuminated tracer particles is recorded with cameras. Local flow velocities are reconstructed by determining the displacement of the tracer particles between two subsequent images over the time delay between the recordings of the images. Such an optical measurement technique provides flow velocity information of a large area of the flow simultaneously with the best resolution in any situation, and with no need of a probe which disturbs the flow. The PTV technique is flexible with respect to the experimental conditions, e.g., non-uniform particle density and moving boundaries, because it provides measurements only at a tracer's location. Furthermore, it allows studying the spatial distribution of the instantaneous velocity field, including the detection of spatial structures (even in highly unsteady conditions). Surface velocities, velocities within the water body, and the velocity of sediment suspension in the water column can also be measured by only illuminating tracer particles in the plane of interest within the water body by an appropriate plane light sheet. Since light is scattering from the particles in all directions, they become point light sources and thus are visible in the image. The Lagrangian approach of PTV is able to provide valuable information for the investigation of multiphase flows (Stitou and Riethmuller, 2001). They applied PTV under PIV imaging conditions to increase the spatial resolution of the measurements, especially in highly seeded flows where the implementation of PTV is not straightforward.

In PTV, each individual particle is recognized and identified separately and tracked in the second image. The determination of the displacement is possible, if a given particle belongs to a characteristic group (called a 'neighborhood'), which has a specific local distribution pattern (Sokoray-Varga and Józsa, 2008). For a comparison of neighborhoods in the evaluation procedure, most algorithms use cross-correlation analysis between a referenced neighborhood in the first image and a possible candidate neighborhood in the second image. The displacement of each individual particle is effectively determined using the information of the neighborhood. This means that PTV provides a displacement vector for each particle, which is efficient in terms of processing time at lower particle numbers. The vectors obtained by PTV are, however, not regularly placed, so it can be more difficult to eliminate false vectors. The resulting vector fields enable the tracking of particles that can then be used to calculate interesting Lagrangian features. In addition, the PTV particles do not have to be homogeneously distributed, and the extent of the displacement is no longer limited by the size of the interrogation area. However the degree of the deformation of the flow field may no longer be similar, if the deformations are too large for the neighborhoods. This prohibits the correlation (Sokoray-Varga and Józsa, 2008). The nature of seeding particles depends on many factors, including the type of fluid, the sensing method, the size of the measurement domain, and at times the expected accelerations in the flow. With the right choice of particle size and with a specific density, it is assured that tracer particles accurately follow the flow.

In the present study, measurements taken by the Particle Flux Profiler will be complemented by optical methods using Particle Tracking Velocimetry (PTV). PTV works well with low particle seeding, and can thus avoid pairing ambiguities. Since the

particle density is low and the particle distribution within a frame is rather inhomogeneous during the initial phase of sediment suspension and ripple formation in accelerating flow, this technique is well suited for the present study. PTV algorithms are generally more accurate than correlation-based PIV algorithms, because they are less affected by displacement gradients (Cowen and Monismith, 1997). We will therefore apply PTV in this study. Furthermore we developed a laser distance meter on top of the water surface which can move along the channel with a carriage system for ripple measurements.

3.4 EXPERIMENTAL PROCEDURE

For studies in steady, uniform flows, the acoustic emitter of the ADVP and its receivers are placed in a water-filled housing that is typically installed above the water surface and that slightly touches the flow. This is done to avoid measurements in the nearfield of the emitter transducer, where acoustic wave fronts are perturbed and turbulence measurements cannot be carried out correctly (Lhermitte and Lemmin, 1994).

In unsteady flows, where the flow depth changes between the base flow and the peak flow, the ADVP, installed in the housing above the water surface, has to follow the surface in the depth varying region of the hydrograph (Fig. 5). Therefore, in this study, the ADVP height changes automatically with water depth, so that the ADVP always touches the water

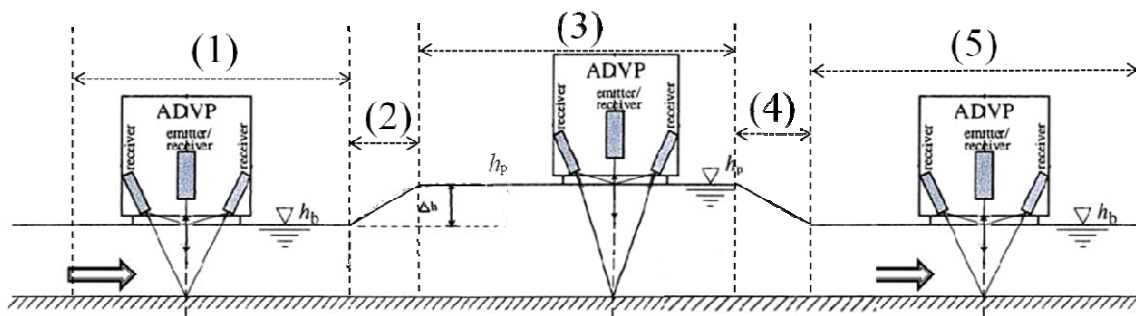


Fig. 5 Schematics of the ADVP instrument in unsteady flow

The ADVP used in this study, measures full depth 2D quasi-instantaneous velocity profiles in the streamwise and the vertical direction. The instrument works optimally at an acoustic frequency of 1 MHz. The transducers still function correctly at 2 MHz, however with reduced efficiency.

ADVP profiling was carried out on the centerline of the channel approximately 15 m from the entrance, where turbulence is well developed. A 1 cm thick layer of the water column near the water surface was omitted from the analysis, because the flow in this layer is slightly perturbed by the instrument. This does not affect the present analysis which focuses on the near-bed layer.

In this research to determine the effect of suspended sediment concentration on the flow field, experiments were first carried out without sediment and then repeated with a sediment load. The hydrograph for the experiments (without and with sediment) consists of 5 parts. The flow is first maintained at the base discharge with $h = h_b$ for 30 s (1 in Fig. 5), followed by the rising stage of the unsteady flow (accelerating) (2 in Fig. 5), where the discharge is linearly increased. Then, the peak discharge is kept steady at $h = h_p$ for 90 s (3 in Fig. 5). Thereafter, the discharge is linearly decreased during the falling stage of the unsteady flow (decelerating) (4 in Fig. 5) to the initial base discharge (5 in Fig. 5). Four different accelerating and decelerating times, 20 s, 30 s, 45 s, 60 s and 90 s, were investigated. The discharge, ADVP, and limnimeter data are simultaneously recorded

during the hydrograph. Since the experiment is computer-controlled, the deviations between individual experimental runs were less than 3%.

Table 1 gives the variations of discharge, water depth, mean velocity and Reynolds number at the base and peak flow for the hydrographs investigated here. With a channel width of 60 cm, the aspect ratio for base flow is 5.8 and for peak flow it is 3.65. Flow is therefore clearly 2D for base flow conditions. For peak flow, the ratio falls below 5, a limiting value for 2D flow suggested by Nezu and Nakagawa (1993). However, bed roughness was not included in their evaluation.

Table 1 Range of variations of discharge, water depth, mean velocity and Reynolds number during unsteady flow

Hydrograph			Base	Peak
Pump discharge	Q	(l sec ⁻¹)	10	35
Water depth	h	(cm)	10.3	16.4
Mean velocity	U _{mean}	(cms ⁻¹)	15	34
Reynolds Number	Re		1.6 × 10 ⁴	4.4 × 10 ⁴

To improve the performance of the ADVP under these low particle concentration conditions, the acoustic frequency of the emitter was varied and hydrogen bubbles were used as additional flow tracers as described in Blanckaert and Lemmin (2006). It had previously been shown (Shen and Lemmin, 1997) that small gas bubbles or clusters of gas bubbles are ideal flow tracers, because they follow the fluid motion with negligible inertial lag. In fully turbulent flow, as in the present case, buoyancy forces of the small bubbles are sufficiently small so as not to affect the measurements. Hydrogen bubbles and sediment particles are two tracers with completely different backscattering characteristics. This will allow investigating whether one can distinguish between the contribution of the two tracers to the backscattering and the velocity distribution.

The acoustic measurements were complemented by simultaneously taking high-speed videos with a light sheet (30 cm long and 8 - 10 mm thick) in the center of the channel, just upstream of the ADVP location (Fig. 6). White light was passed through a series of optical fibers aligned along the light sheet axis. A cylindrical lens focused the light into a light sheet with homogeneous light distribution. The velocity vectors within this sheet were determined. This allowed visualizing the dynamics of particle suspension during the unsteady flow and the formation of bedforms. Thus, ADVP and optical measurements were synchronized. A camera with 640 x 480 pixels was used with a frame rate of 80 Hz. Images of an area 9 cm high by 11.5 cm wide were taken through the glass wall of the channel for flow visualization and PTV analysis. The fine sediment particles that serve as flow tracers are near the upper limit of the particle size suitable for tracking the flow dynamics. The recording system of the camera did not allow recording images during the whole hydrograph. Therefore, the beginning of the image recording period was triggered by the ADVP recording system. The point of the trigger can be selected along the whole hydrograph. In the present experiments, image recording was started in the early part of the

accelerating flow in order to cover the full period of sediment suspension and ripple formation.



Fig. 6 The camera with a light sheet upstream of the ADVP

The water in the recirculating installation of the channel was permanently filtered to minimize the number of floating particles in the water. In recirculating open-channel systems, gas bubbles are often produced by the pump and the water cascade from the weir at the end of the channel. However, it was observed that in the discharge range used in the present experiments almost no gas bubbles were entrained into the water during the experiments. Therefore, under conditions of no fine sediment suspension, the water in the channel was nearly free of any flow tracers for acoustic and optical flow measurements.

To investigate the suspension of fine sediment particles, a layer of sand with $D_{50} = 0.12$ mm was spread on top of the coarse bed on a surface area of the channel extending about 1 m upstream from the location of the ADVP (Fig. 6). For the present study, 4 mm and 6 mm-thick layers were installed. They were carefully levelled by a carriage moving along the channel. This layer was thick enough to fully cover the coarse bed, and it smoothed out gravel bed roughness in that area. The range of velocities and the diameter of the fine sand of the present study correspond well to the area of ripples designated in the bedform stability diagram of Southard and Boguchwal (1990).

The rising time of the hydrograph was changed to determine the effect of flow acceleration on the formation of ripples. For all experimental conditions, the experiments were repeated 20 times and combined for the analysis. All ADVP data were de-aliased (Franca and Lemmin, 2006) and de-noised (Blanckaert and Lemmin, 2006) to improve data quality. In the present experiments, the channel slope is zero.

In order to measure the dimension of ripples, we installed a laser instrument on top of the water surface (Fig. 7). It was attached to a carriage which moved along the channel at constant speed for a distance of 1.5 m. The resolution of the laser beam was 0.4 mm which is higher than the size of the particles. At the beginning of the each experiment when no ripples appeared on the bed, we measured the level of the sediment as a zero reference level (Fig. 7a). At the end of the each experiment we measured the longitudinal profile of the ripple height over 1.5 m as it is shown in Fig. 7b.

a)

b)



Fig. 7. The laser instrument on top of the water surface a) measurement of zero level b) measurement of ripple dimensions

Combining acoustic and optical methods allow studying the long-term developments in timeseries obtained by the ADV in a single profiler location and the details of the 2D velocity field by PTV in the vicinity of the ADV location over shorter periods. This provides for a better interpretation of the data and the underlying processes (Bagherimiyab and Lemmin, 2010).

Results of the experiments without and with sediment transport will be presented in the following chapter.

3.5 REFERENCES

- Adrian, R.J., 2005. Twenty years of particle image velocimetry. *Exp. in Fluids* 39, 159 – 169.
- Bagherimiyab, F., Lemmin, U., 2010. Aspects of turbulence and fine sediment resuspension in accelerating and decelerating open-channel flow. In: *Proceedings of Riverflow 2010*, 8 – 10 September 2010, Braunschweig, Germany. 1, 121 – 127.
- Bagherimiyab, F., Albayrak, I., Lemmin, U., 2008. Bed shear velocity estimates in rough open-channel flow obtained from Acoustic Doppler Velocity Profiler data and direct bed shear stress measurements. In: *Proceedings of Riverflow 2008*, Izmir, Turkey. 2, 151 – 159.
- Blanckaert, K., Lemmin, U., 2006. Means of noise reduction in acoustic turbulence measurements. *J. Hydr. Res.* 44, 3 – 17.
- Bricault, M., 2006. Rétrodiffusion acoustique par une suspension en milieu turbulent: application à la mesure de concentration pour l'étude de processus hydro-sédimentaires. PhD thesis, Grenoble Institut National Polytechnique, Grenoble.
- Cellino, M., Lemmin, U., 2004. Influence of coherent flow structures on the dynamics of suspended sediment transport in open-channel flow. *J. Hydr. Eng.* 130, 1077 – 1088.
- Cowen, E.A., Monismith, S.G., 1997. A hybrid particle tracking velocimetry technique. *Exp. in Fluids* 22, 199 – 211.
- Franca, M.J., Lemmin, U., 2006. Eliminating velocity aliasing in acoustic Doppler velocity profiler data. *Meas. Sci. Technol.* 17, 313 – 322.
- Franca, M.J., Ferreira, R.M.L., Lemmin, U., 2008. Parameterization of the logarithmic layer of double-averaged streamwise velocity profiles in gravel-bed river flows. *Advances in Water Resources* 31, 915 – 925.
- Harris, K., Butman B., Traykovski P., 2003. Winter-time circulation and sediment transport in the Hudson Shelf Valley. *Cont. Shelf Res.* 23, 801 – 820.
- Hay, A.E., Sheng, J., 1992. Vertical profiles of suspended sand concentration and size from multifrequency acoustic back-scatter. *J. Geophys. Res.* 97, 15661 – 15677.
- Hurther, D., Lemmin, U., 1998. A constant beam width transducer for 3D acoustic Doppler profile measurements in open channels. *Meas. Sci. Tech.* 9, 1706 – 1714.
- Hurther, D., Lemmin, U., 2001. A discussion of equilibrium near-bed concentration of suspended sediment, *J. Hydraul. Eng.* 16, 430 – 433.
- Hurther, D., Lemmin U., 2008. Improved turbulence profiling with field adapted acoustic Doppler velocimeters using a bi-frequency Doppler noise suppression method. *J. Atmos. Oceanic Technol.* 25, 452 – 463.
- Hurther, D., Lemmin, U., Bricault, M., 2006. Multistatic acoustic Doppler profilers for fine-scale studies of velocity and particle flux processes. *Proceedings UAM07*, Heraklion, Greece.
- Hurther, D., Lemmin, U., Terray, E.A., 2007a. Turbulent transport in the outer region of rough-wall open-channel flows: the contribution of Large Coherent Shear Stress Structures (LC3S). *J. Fluid Mech.* 574, 465 – 493.
- Hurther, D., Michallet, H., Gondran, X., 2007b. Turbulent measurements in the surf zone suspension. *J. Coast. Res.* S150, 297 – 301.
- Hurther D., Thorne, P.D., Bricault, M., Lemmin, U., Barnoud, J.M., 2011. A multi-frequency acoustic concentration and velocity profiler for boundary layer measurements of fine-scale flow and sediment transport processes. *Coastal Engineering* in press.

- Lee, T.H., Hanes, D.M., 1995. Direct inversion method to measure the concentration profile of suspended particles using backscattered sound. *J. Geophys. Res.* 100, 2649 – 2657.
- Lemmin, U., Jiang, R., 1999. Vertical velocity structure and eddy scale distribution in the water column of the stratified Lake of Geneva. In: P.A. Davies (Ed.), *Mixing and dispersion in stratified flows*. Oxford University Press, Oxford, 123 – 144.
- Lhermitte, R., 1983. Doppler sonar observation of tidal flow. *J. Geophys. Res.* 88, 725 – 742.
- Lhermitte, R., Serafin, R., 1984. Pulse-to-pulse coherent Doppler signal processing techniques. *J. Atmos. Oceanic Technol.* 20, 429 – 442.
- Lhermitte, R., Lemmin, U., 1994. Open channel flow and turbulence measurement by high-resolution Doppler sonar. *J. Atm. and Ocean. Tech.* 11, 1295 – 1308.
- Nezu, I., Nakagawa, H., 1993. *Turbulence in open channel flows*. Balkema, Rotterdam, NL.
- Prandtl, L., Tietjens, O., 1929 und 1931. *Hydro- und Aerodynamik* (2 vol.), Berlin.
- Rolland, T., Lemmin, U., 1997. A two-component acoustic velocity profiler for use in turbulent open-channel flow. *J. Hyd. Res.* 35, 545 – 561.
- Shen, C., Lemmin, U., 1996. Ultrasonic measurements of suspended sediments: A concentration profiling system with attenuation compensation. *Meas. Sci. Tech.* 9, 1191 – 1194.
- Shen, C., Lemmin U., 1997. Ultrasonic scattering in highly turbulent clear water flow. *Ultrasonics* 35, 57 – 64.
- Shen, C., Lemmin, U., 1998. Improvements in acoustic sediment concentration profiling using an LMS compensation algorithm. *IEEE J. Oceanic Eng.* 23, 96 – 104.
- Shen, C., Lemmin, U., 1999. Application of an acoustic particle flux profiler in particle-laden open-channel flow. *J. Hydraul. Res.* 37, 407 – 419.
- Smyth, C.E., Zedel, L., Hay, A.E., 2002. Coherent Doppler profiler measurements of near-bed suspended sediment fluxes and the influence of bedforms. *J. Geophys. Res.* 107, C8, 19.1 – 19.20.
- Sokoray-Varga, B., Józsa, J., 2008. Particle tracking velocimetry (PTV) and its application to analyse free surface flows in laboratory scale models. *J. Civil Engineering* 52/2, 63 – 71 doi: 10.3311/pp.ci.2008-2.02.
- Southard, J.B., Boguchwal, L.A., 1990. Bed configuration in steady unidirectional water flows. *J. Sedim. Petrol.*, 60, 658 – 679.
- Stitou, A., Riethmuller, M L., 2001. Extension of PIV to super resolution using PTV. *J. Meas. Sci. Technol.* 12, 1398 – 1403.
- Thorne, P.D., Hanes, D.M., 2002. A review of acoustic measurement of small-scale sediment processes. *Cont. Shelf Res.* 22, 603 – 632.
- Thorne, P.D., Davies, J.S., Bell, P.S., 2009. Observations and analysis of sediment diffusivity profiles over sandy rippled beds under waves. *J. Geophys. Res.* 114, C02023, doi:10.1029/2008JC004944.
- Thorne, P.D., Hardcastle, P.J., Soulsby, R.L., 1993. Analysis of acoustic measurements of suspended sediments. *J. Geophys. Res.* 98, 899 910.
- VanderWeft, J.J., Doucette, J.S., O'Donoghue, T., Ribberink, J.S., 2007. Detailed measurements of velocity and suspended sand concentration over full-scale ripples in regular oscillatory flow. *J. Geophys. Res.* 112, F02012.

CHAPTER 4

DATA ANALYSIS AND RESULTS

4.1	INTRODUCTION	77
4.2	VELOCITY DISTRIBUTION IN UNSTEADY ROUGH-BED OPEN-CHANNEL FLOW WITHOUT SEDIMENT	79
4.3	FINE SEDIMENT DYNAMICS IN UNSTEADY OPEN-CHANNEL FLOW STUDIED WITH ACOUSTIC AND OPTICAL SYSTEMS	93
4.4	BEDFORMS AND PARTICLE INTERACTION IN UNSTEADY SUSPENDED SEDIMENT-LADEN OPEN-CHANNEL FLOW	137
4.5	REFERENCES	141

4.1 INTRODUCTION

In this chapter, results of unsteady accelerating and decelerating laboratory open-channel flow over a movable (but not moving) coarse gravel bed first without and then with fine sediment added are compared for five different accelerating and decelerating time scales. Table 1 gives the variations of discharge, water depth, mean velocity and Reynolds number at the base and peak flow for the hydrographs investigated here. With a channel width of 60 cm, the aspect ratio for base flow is 5.8 and for peak flow it is 3.65. Flow is therefore clearly 2D for base flow conditions. For peak flow, the ratio falls below 5, a limiting value for 2D flow suggested by Nezu and Nakagawa (1993). However, bed roughness was not included in their evaluation.

Table 1 Range of variations of discharge, water depth, mean velocity and Reynolds number during unsteady flow

Hydrograph		Base	Peak
Pump discharge	Q (l sec ⁻¹)	10	35
Water depth	h (cm)	10.3	16.4
Mean velocity	U _{mean} (cms ⁻¹)	15	34
Reynolds number	Re	1.6 × 10 ⁴	4.4 × 10 ⁴
Froude number	Fr	<1	<1

4.2 VELOCITY DISTRIBUTION IN UNSTEADY ROUGH-BED OPEN-CHANNEL FLOW WITHOUT SEDIMENT

4.2.1	Hydrographs	81
4.2.2	Mean velocities	82
4.2.3	Friction velocity	89

4.2 VELOCITY DISTRIBUTION IN UNSTEADY ROUGH-BED OPEN-CHANNEL FLOW WITHOUT SEDIMENT

4.2.1 HYDROGRAPHS

Figures 1 and 2 show the depth variation $\Delta h/\Delta h_p = (h - h_b)/(h_p - h_b)$ and discharge against water depth respectively near the ADVP for three parts of the five symmetrical hydrographs with different unsteadiness (20 s, 30 s, 45 s, 60 s and 90 s) for the experiments without and with sediment. These curves are representative for all experiments discussed in this chapter. As seen in Fig. 1, the transition from the accelerating range to the peak flow range is gradual and is particularly evident for the 20 s hydrograph. In this hydrograph, steady state during peak flow is only attained at the very end of the peak flow range. Even though the pump discharge is varied linearly in the course of the accelerating and decelerating stages, water depth changes non-linearly during parts of these periods. Figure 2 indicates that five different hysteresis loops are formed during the accelerating and decelerating ranges of the five hydrographs. In each loop, water depth for the accelerating range is different from the decelerating range for the same discharge. It shows that during the accelerating range, discharge for hydrographs 20 s, 30 s and 45 s increases until $Q = 23 \text{ lit s}^{-1}$ and 125 mm water depth at nearly the same rate and after that, the hydrographs change differently. The hydrograph with 20 s unsteadiness for the same discharge shows the lowest value for water depth and it increases until the peak discharge (35 lit s^{-1}). It reaches peak discharge at 145 mm water depth, whereas the 30 s, 45 s and 60 s hydrographs reach peak discharge at greater water depth. When the pump discharge was already constant at peak flow, water depth still slowly increased and did not reach steady state (Fig. 1). For the decelerating ranges, depth decreases at nearly the same rate until $Q = 23 \text{ lit s}^{-1}$ and the hydrographs again behave differently until the base discharge. It is observed that for the same discharge, all hydrographs have higher water depth than in the accelerating range. The hydrograph with the highest unsteadiness (20 s) has greatest water depth in the decelerating phase of the hydrograph. During the accelerating and decelerating ranges, the hydrograph with lowest unsteadiness (90 s) behaves differently. It increases rapidly and shows higher water depth for the same discharge as the other hydrographs. It remains in steady state during the peak steady flow and then it decreases again with a different slope during the decelerating range. For the same discharge as in the other hydrographs, it reaches a lower water depth. The discrepancy between the variation of the discharge and the observed water level over time indicates that along the channel, flow adjustment over the rough bed takes place. Furthermore, this adjustment is not the same for the accelerating and the decelerating ranges. This behavior is also different from depth variation during comparable hydrographs reported in the literature (Nezu et al., 1997; Song et al., 1994). In the present experiments, the channel slope is 0.07 and the velocities are smaller than in those studies.

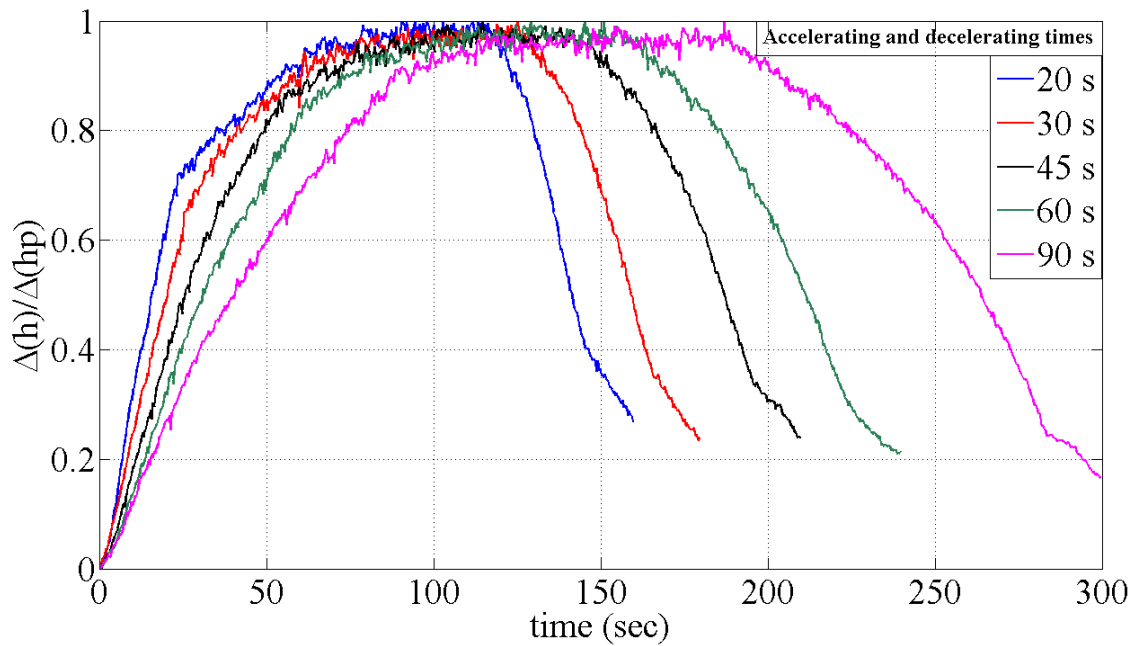


Fig. 1. Depth variation $\Delta h/\Delta h_p = (h - h_b)/(h_p - h_b)$ near the ADVP for three parts of the five hydrographs

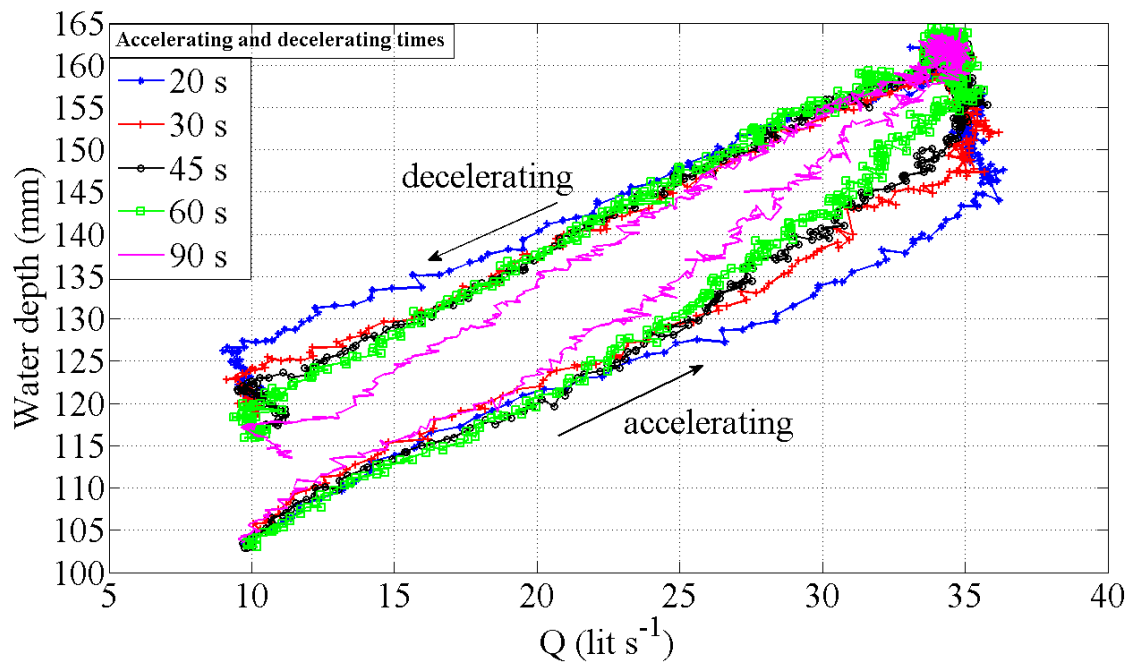


Fig. 2. Discharge against water depth near the ADVP for three parts of the five hydrographs

4.2.2 MEAN VELOCITIES

In this section, we will present the results of experiments without a layer of fine sediment on the bed. Hydrogen bubbles were added as flow tracers during these experiments.

From the instantaneous velocity profile data measured by the ADV instrument for twenty identical runs for each hydrograph, mean profiles over ten individual profiles are calculated for each run. Subsequently, the corresponding mean profiles are averaged over all twenty runs, thus subdividing the whole data set into a series of time slices for the following analysis (for the horizontal velocity component, this is denoted by u). U_{mean} in this chapter is the depth average over the time-averaged and ensemble-averaged velocity for each time slice.

The mean velocity development during the unsteady flow ranges of five hydrographs is given in Fig. 3. A hysteresis loop is formed during the accelerating and decelerating ranges. In Fig. 3 initially, mean velocity in the accelerating range increases steeply, then more slowly for all five hydrographs. The mean velocity of these five hydrographs increases by the same amount until water depth, $h = 112$ mm. Above this level, the velocities increase with different slopes and values, and higher unsteadiness reaches a higher mean velocity for the same water depth. The 20 s unsteadiness reaches 32 cm s^{-1} at water depth, $h = 140$ mm, whereas the 30 s unsteadiness reaches 29 cm s^{-1} at the same depth. The 45 s, 60 s and 90 s unsteadiness hydrographs reach this value of greater depth. They all come to the same mean velocity value at the peak flow end of the unsteady flow ranges. The decrease in the decelerating range is smoother for all hydrographs. Mean velocities decrease almost linearly during the decelerating flow ranges. The highest unsteadiness (20 s), shows smaller mean velocity at the same water depth compared to the other unsteadiness. The five different loops in Fig. 3 indicate the strong effect of unsteadiness in the accelerating range and this shows that flow in the decelerating range approaches steady flow.

The overall pattern of the mean velocity distribution reflects the water depth pattern shown in Fig. 2. During the final phase of the accelerating range, velocities decrease in the same way as water depth increases with constant discharge. Water depth for all hydrographs is greater in the decelerating range for a given discharge, and as a consequence, mean velocities are smaller in the decelerating range than in the accelerating range for comparable depth. The difference between water depths for the different hydrographs in the two unsteady ranges is also seen in the corresponding mean velocity differences in Fig. 3. It should be noted, however, that in particular for the highest unsteadiness, mean velocity in the final phase of the accelerating range starts to decrease (above $h \approx 135$ mm for the 20 s hydrograph) before discharge reaches its peak value (at $h \approx 145$ mm). The depth-discharge ratio did not change during this time interval.

To understand the behavior of unsteady flow as compared to the steady flow, ADV measurements were carried out for six different steady flows with different flow discharges, which cover the whole range of the hydrograph (base and peak discharges and 4 ranges in between). Mean velocity profiles of these six different steady flow experiments were also plotted in the same figure (Fig. 3).

The mean velocities for steady flows closely follow the curve of the decelerating range for the lowest unsteadiness hydrograph. With increasing unsteadiness, mean velocities in the decelerating range become progressively smaller with respect to the steady flow cases. However, the general slope of velocity decrease is similar during this range. Velocities in the accelerating range are significantly higher than the steady flow values for all hydrographs. This indicates that unsteadiness has a much stronger effect on the mean flow pattern during the accelerating flow range than during the decelerating one.

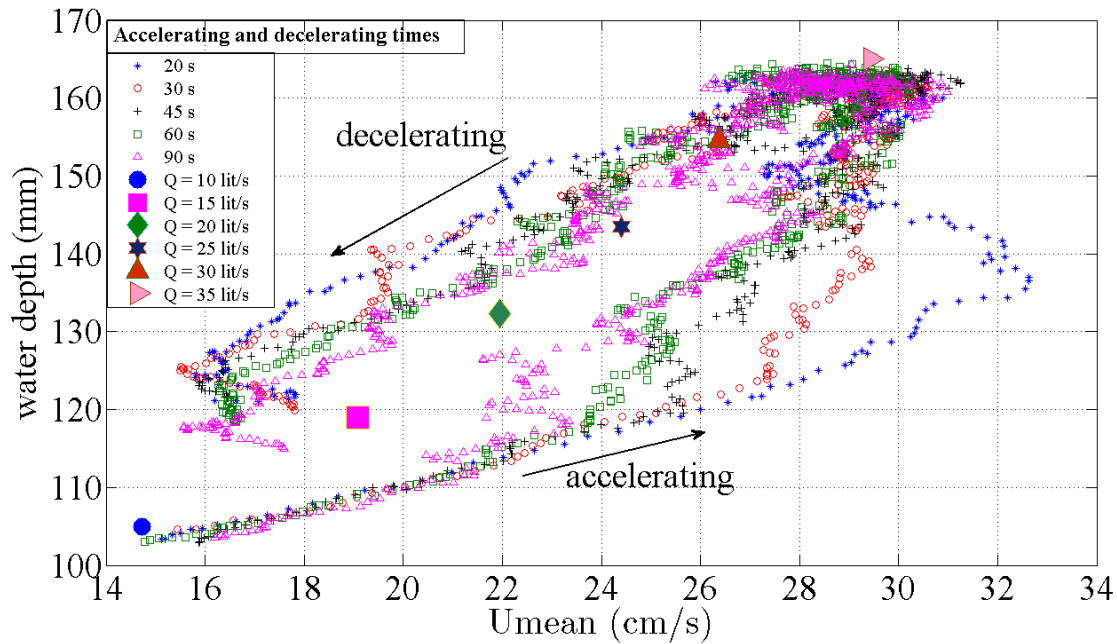


Fig. 3. Mean longitudinal velocity distribution for the unsteady range of five hydrographs and six steady flows

Figures 4, 5, 6, 7 and 8 show the distribution of longitudinal velocity against depth variation $\Delta h / \Delta h_p$ for different depth levels representative of the near-wall region, the intermediate region and the outer region of the 20 s, 30 s, 45 s, 60 s and 90 s accelerating and decelerating ranges, respectively. These figures indicate that the velocity increases more in the accelerating range than in the decelerating range at the same flow depth for the five hydrographs, forming a loop, as found by Nezu et al. (1997). The loop is wider for the 20 s unsteadiness because of the greater unsteadiness, and is tighter for the 90 s unsteadiness. This indicates that unsteadiness strongly affects the profile shape. The spreading of the curves for the different levels in the profiles shows that velocity profiles in accelerating ranges have much steeper angles than in the decelerating ones. Initially, velocity in the accelerating range increases steeply, then more slowly, particularly for the 20 s hydrograph. During the accelerating stage of all five hydrographs, velocities at $\frac{\Delta h}{\Delta h_p} = 0.2$ attain the same velocity value. The velocity for the hydrograph with 20 s unsteadiness then increases rapidly until $\frac{\Delta h}{\Delta h_p} = 0.6$, whereas velocities for 30 s, 45 s and 60 s unsteadiness increase rapidly only until $\frac{\Delta h}{\Delta h_p} = 0.3$ and until $\frac{\Delta h}{\Delta h_p} = 0.2$ for 90 s unsteadiness during the accelerating range of the hydrographs. The decrease in the decelerating range is smoother for all hydrographs. Therefore the velocity profiles in 20 s, 30 s, 45 s, 60 s and 90 s, in the accelerating ranges are quite different, but they are similar in the decelerating ranges. This is the effect of unsteadiness which is the strongest in the 20 s hydrograph and it is weakest in the 90 s one. For the 90 s hydrograph, profile gradients change little along the unsteady ranges and are similar in the two unsteady ranges. This indicates that steady state flow conditions are approached in this case.

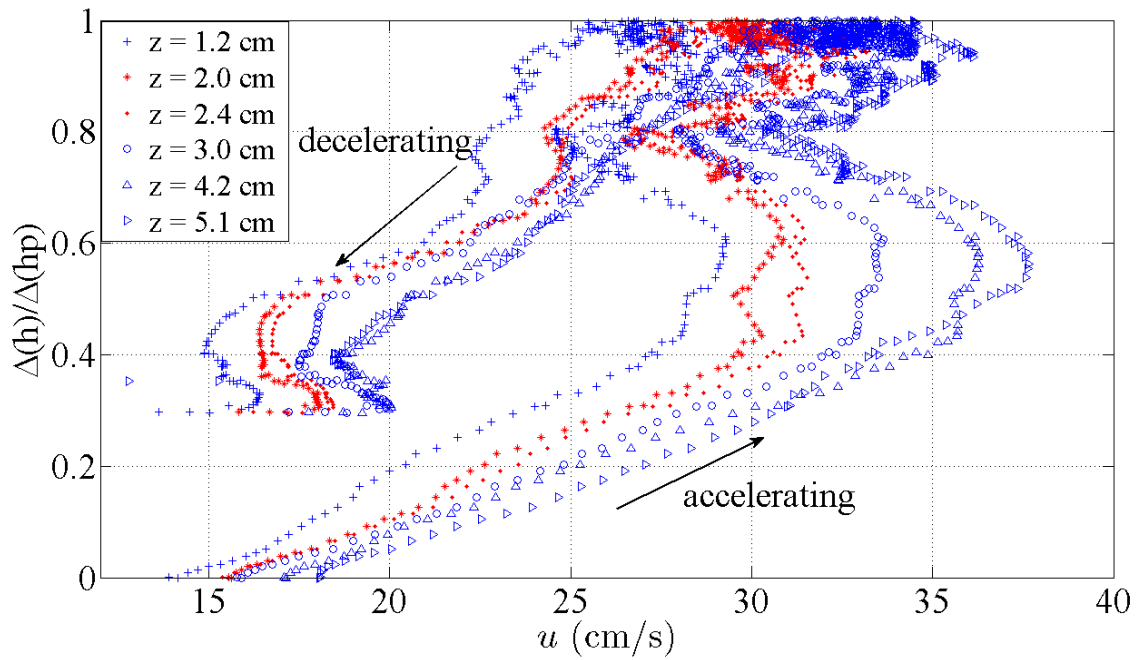


Fig. 4. Longitudinal velocity at different depths for accelerating and decelerating time of 20 s; z is the vertical coordinate measured upwards from the bed

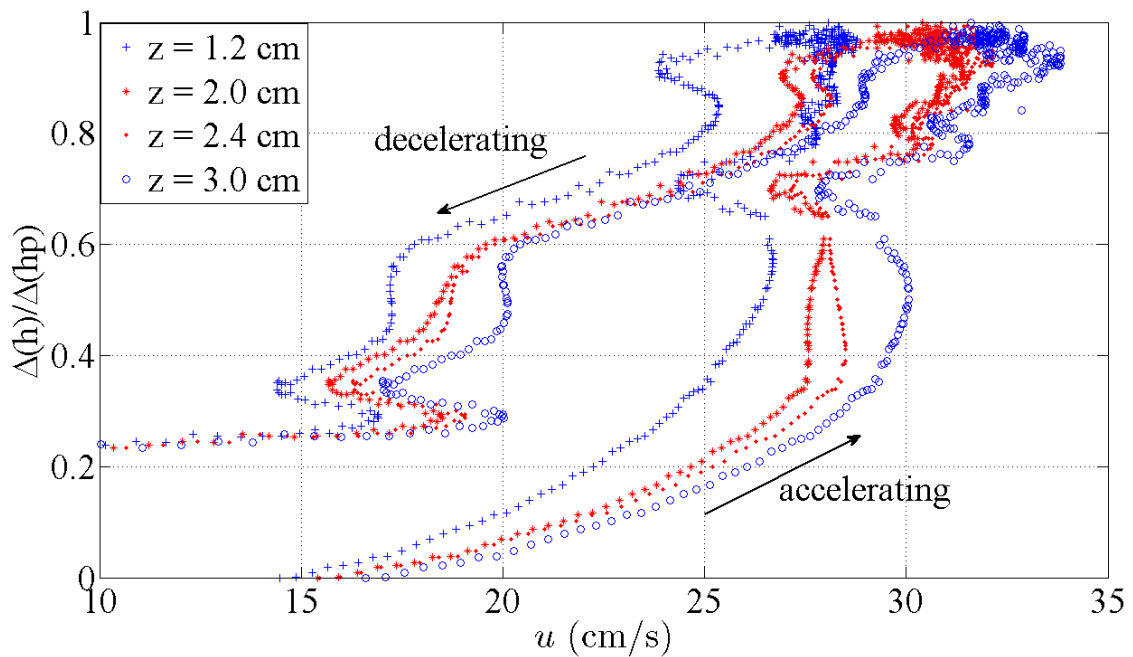


Fig. 5. Longitudinal velocity at different depths for accelerating and decelerating time of 30 s; z is the vertical coordinate measured upwards from the bed

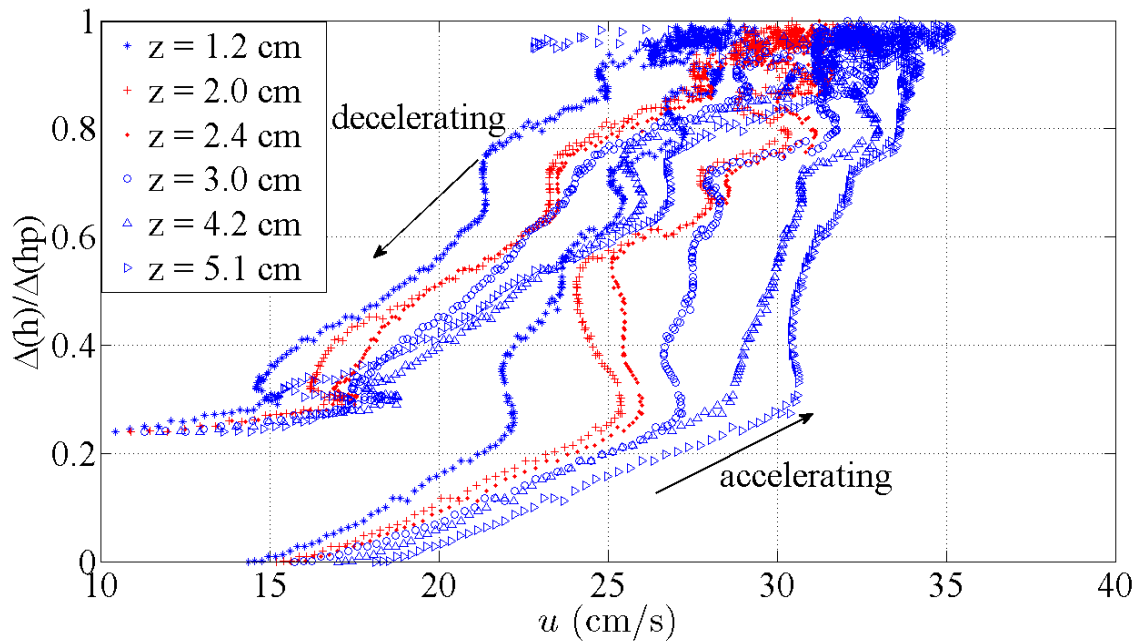


Fig. 6. Longitudinal velocity at different depths for accelerating and decelerating time of 45 s; z is the vertical coordinate measured upwards from the bed

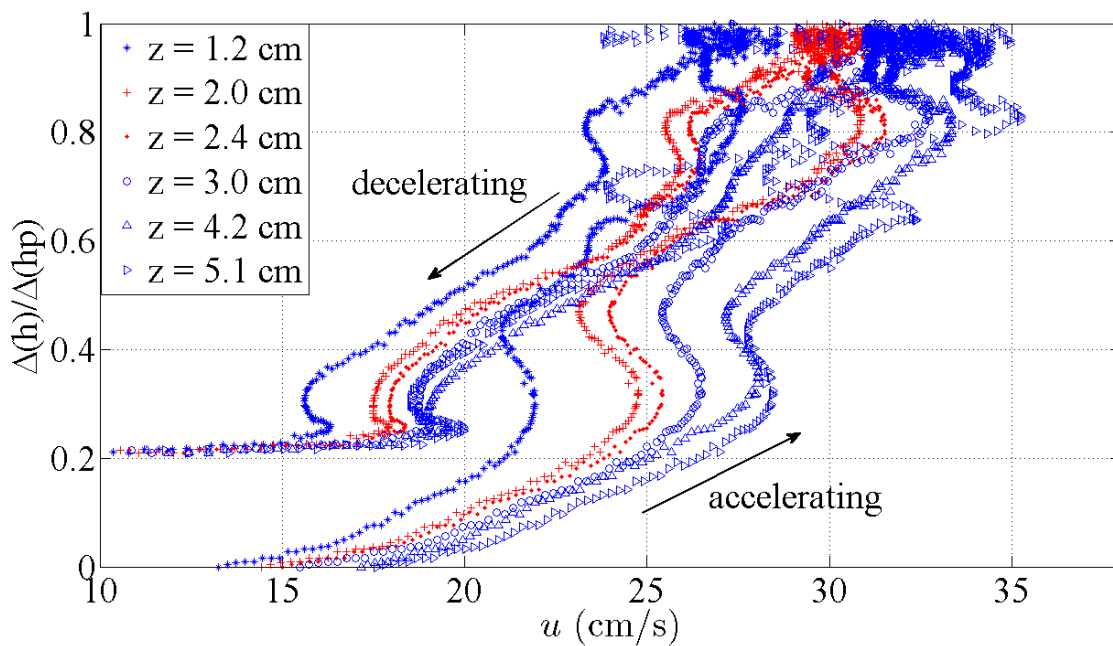


Fig. 7. Longitudinal velocity at different depths for accelerating and decelerating time of 60 s; z is the vertical coordinate measured upwards from the bed

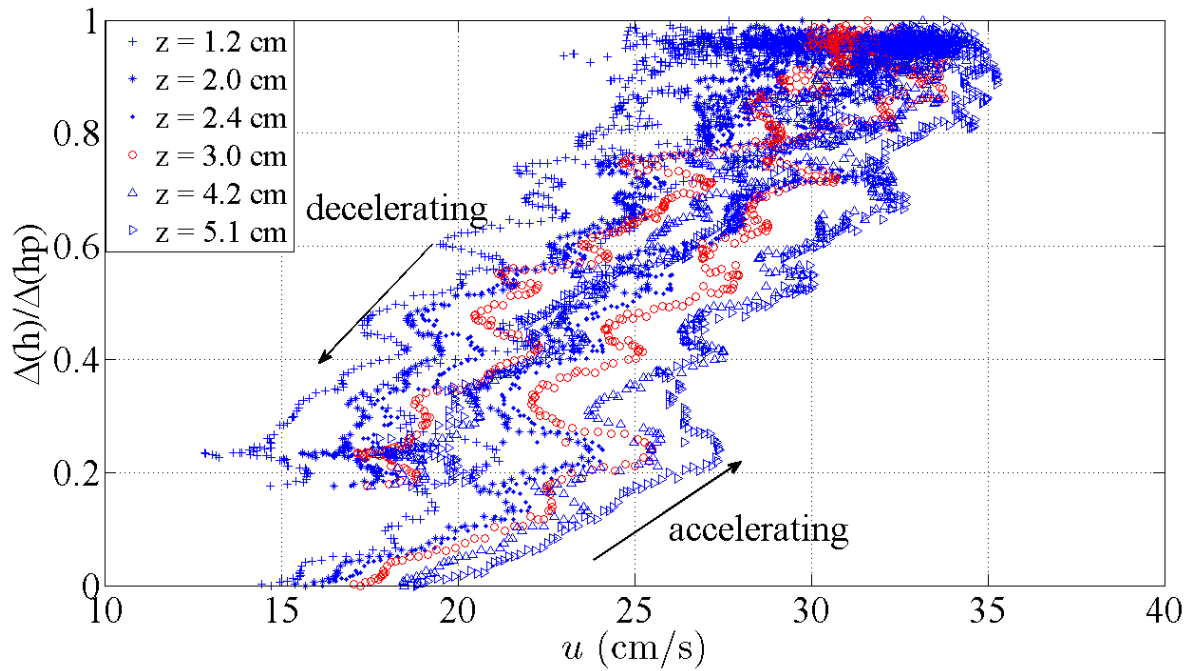


Fig. 8. Longitudinal velocity at different depths for accelerating and decelerating time of 90 s; z is the vertical coordinate measured upwards from the bed

Since logarithmic profiles were expected in the inner layer (Bagherimiyab and Lemmin 2010; Nezu and Nakagawa 1993), mean longitudinal velocity profiles were investigated by fitting the measured profiles to a logarithmic profile. The profile origin was taken at the level where the recorded velocity was zero. All profiles showed a roughness layer right above the rough bed which was between 0.8 and 1.2 D_{50} thick. In this layer, individual roughness elements determine the local flow structure and the flow may become 3D. This layer was therefore omitted from the fitting. It was found that during unsteady flow, all mean velocity profiles followed the logarithmic law in the inner layer, confirming observations in the literature. However, differences in the profile form were observed. Mean velocity profiles over the logarithmic part of the profile of accelerating and decelerating unsteady flow for the 30 s accelerating and decelerating time and for one of the steady flow cases with $Q = 15$ lit/s are shown in Fig. 9 for the same water depth. The accelerating flow profile gradient is much steeper than the decelerating one. Velocities during the accelerating flow range are significantly higher than during the decelerating range and the steady flow range in between. This confirms the above observations.

Figure 10 shows the distribution of the mean of the measured longitudinal velocities and mean velocities that were calculated from the logarithmic fit against the depth variation $\Delta h / \Delta h_p$ during the unsteady flow ranges for the hydrograph with 20 s accelerating and decelerating time. It is seen in Fig. 10 that the difference between measured velocities and mean velocities from the logarithmic fit is less than 3%. This confirms that the logarithmic fit is a good approximation for the velocity profiles in the inner layer (as shown in Fig. 9). Figure 10 indicates that a hysteresis loop is formed during the accelerating and decelerating ranges confirming the observations by Nezu et al. (1997) for a smooth bed. For a given water depth, the velocity significantly increases in the accelerating range than

in the decelerating stage. Initially, up to $\Delta h/\Delta h_p = 0.4$, velocity in the accelerating range increases steeply, then more slowly. The decrease in the decelerating range is smoother.

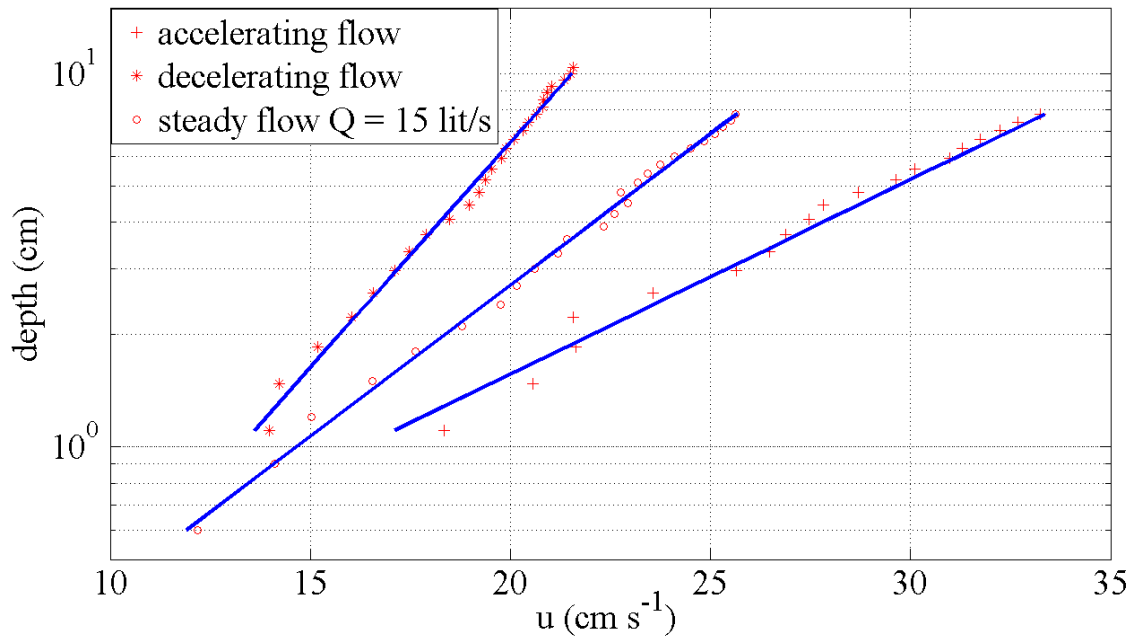


Fig. 9. Examples of longitudinal velocity profiles for accelerating and decelerating time of 30 s and for steady flow with $Q = 15$ lit/s; solid line: logarithmic profile approximation

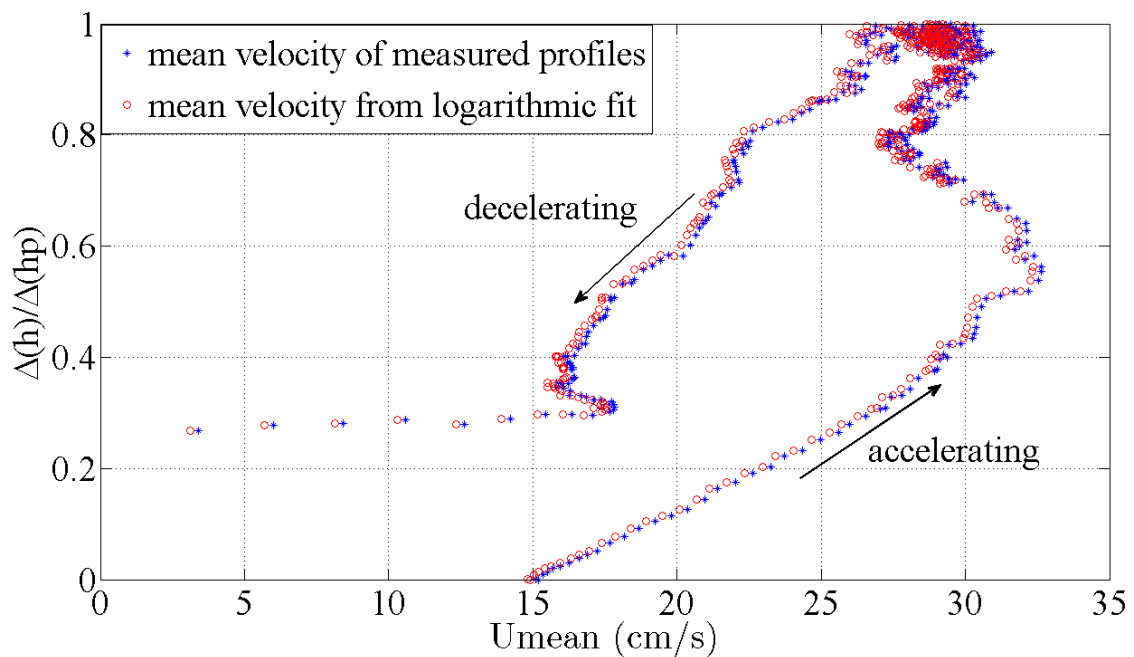


Fig. 10. Longitudinal mean velocity and mean velocity from the log law fit during the unsteady flow stages against depth changes for accelerating and decelerating time of 20 s

Mean velocity normalized by the maximum velocity for each profile (U_{max}) of the 30 s hydrograph is presented in Fig. 11, where two different hysteresis loops are seen above and below $\Delta h / \Delta h_p = 0.8$. For accelerating and decelerating flow in the loop below $\Delta h / \Delta h_p = 0.8$ which corresponds to the increasing and decreasing discharge stages (Fig. 2), the hysteresis loops in Fig. 10 and Fig. 11 turn in opposite directions. This indicates that profiles during the accelerating range have stronger gradients than during the decelerating range. Thus, not only the velocities are different in the two ranges, as seen in Fig. 10, but also in the velocity profile forms. Above $\Delta h / \Delta h_p = 0.8$, during the constant peak discharge range, the direction of the loop is reversed. The slow increase and the faster decrease in water depth during this range (Fig. 2) affect the profile dynamics in a different way. The profile gradient changes continuously throughout the hydrograph, even during the range of constant peak flow.

The same normalization was also carried out for the six steady flow cases and the results are plotted in Fig. 11. For lower steady flows, the gradients fall into the range of accelerating flows. For higher steady flows, they are found between accelerating and decelerating flows. In Fig. 3, mean velocities of steady flows were observed in the range of decelerating flows. Therefore, profile shapes of unsteady flows and thus flow characteristics of unsteady flows are not comparable to those of steady flows for the same water depths.

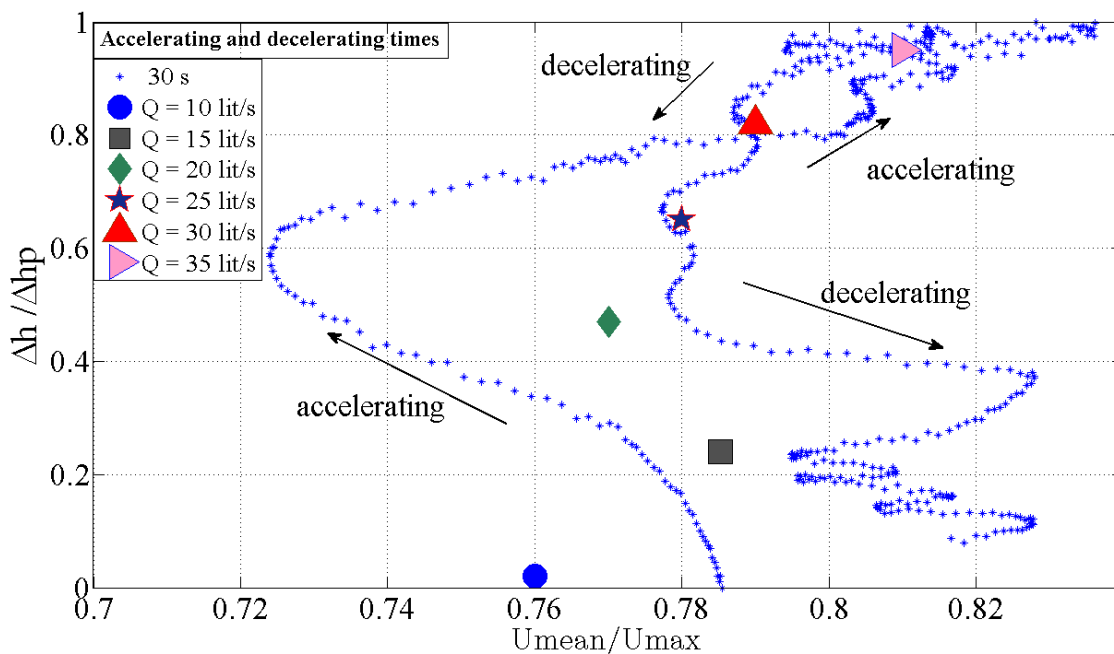


Figure 11. U_{mean}/U_{max} during the unsteady flow ranges

4.2.3 FRICTION VELOCITIES

Figure 12a shows friction velocities for the four hydrographs (20 s, 45 s, 60 s and 90 s) which were determined using the logarithmic mean velocity profile method in the inner layer for all time slices against the depth variation $\Delta h / \Delta h_p$. In this case, the friction

velocity in the accelerating and decelerating flow ranges have been included in order to show the effect of unsteadiness. In the accelerating range, the peak of the friction velocity is attained before the maximum of the water level, as was found by Nezu et al. (1997). Again, friction velocity forms a loop and changes differently in the accelerating and decelerating flow ranges. Friction velocity, u_* , does not return to the initial value of the base flow after the decelerating ranges, because water depth continues to slowly decrease past the end of the decelerating ranges and reaches base flow depth much later (Fig. 12a). This was already seen in the velocity profiles above, where it decreased linearly in the decelerating flow range and was similar for the 20 s, 45 s, 60 s and 90 s hydrographs. For comparable mean velocities in the accelerating and decelerating flow ranges, friction velocities are different. It should be noted that during the initial phase of acceleration, all four curves closely follow each other. As with velocity, friction velocity increases steeply to a higher value of $\Delta h / \Delta h_p$ ($= 0.6$) for 20 s unsteadiness compared to the others, and $\Delta h / \Delta h_p$ changes from 0.3 to 0.6 for the maxima from the lowest to highest unsteadiness. Therefore the large difference between the four hydrographs in the later phase of the unsteady accelerating ranges illustrates the effect of the difference in unsteadiness. It indicates that unsteadiness strongly affects the friction velocity in the final phase of the accelerating range. During this later phase, the value of the friction velocity for the 90 s hydrograph (the lowest unsteadiness) attains the value it has during the following steady peak flow. Thus, for the 90 s hydrograph, acceleration only affects the initial phase of the friction velocity. The friction velocity pattern follows that of the mean velocity. Similar to the flow velocities, the friction velocities come to the same value at the peak flow end of the unsteady flow ranges. For the 20 s hydrograph (the highest unsteadiness), friction velocities strongly increase during the last two-thirds of the accelerating range, and the maximum values are significantly larger than those during the steady peak flow. This shows that mean flow adjustment during the peak flow phase is different in the 20 s hydrograph (the highest unsteadiness) compared to the other hydrographs. Friction velocity, u_* , which affects sediment suspension changes significantly during acceleration in the different hydrographs.

The friction velocity was also calculated for the six steady flow cases. The results which are given in Fig. 12a indicate that friction velocities for steady flow fall into the range of accelerating flow. It was seen in Fig. 11 that steady flow profile gradients tend towards those for accelerating flows, whereas the mean velocities clearly follow decelerating flow (Fig. 3). This analysis shows that the hydrodynamics of unsteady flow and of steady flow are different.

As it was shown in Fig. 12a for the unsteady flow with 20 s accelerating and decelerating time, a similar loop behavior is seen for the friction velocity that was determined using the logarithmic mean velocity profile method for all time slices (Fig. 13). The peak of the friction velocity is attained at about $\Delta h / \Delta h_p = 0.6$, well before the maximum of the water level is reached, as was found by Nezu et al. (1997). This maximum coincides with the level of the minimum in U_{mean}/U_{max} in the accelerating range (Fig. 11). For the 20 s accelerating and decelerating flow range between $\Delta h / \Delta h_p = 0.4$ and $\Delta h / \Delta h_p = 0.8$, mean velocity changes little (Fig. 10), but shear velocity varies strongly. This difference is due to the change in profile form as seen in Fig. 12a.

Shear velocity normalized by the mean velocity for each profile of all hydrographs is presented in Fig. 12b, where different hysteresis loops are seen. This indicates that profiles during the accelerating range have stronger gradients than during the decelerating range.

The profile gradient changes continuously throughout the hydrograph, and the lowest unsteadiness (90 s accelerating and decelerating time) shows a higher gradient at $\Delta h / \Delta h_p = 0.3$. The same normalization was also carried out for the six steady flow cases and the results are plotted in Fig. 12b. For all steady flows, the gradients change between 0.073 and 0.095. Therefore, u_* / U_{mean} of the peak steady flows and six steady flows fall into the range given in the literatures for rough steady flow.

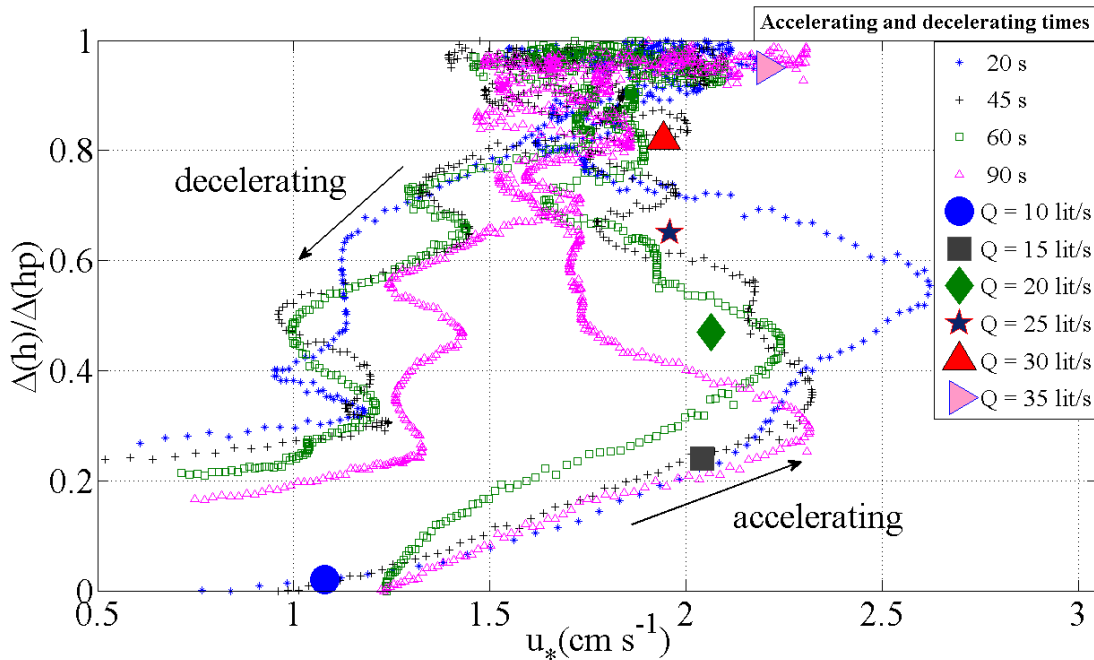


Fig. 12a. Friction velocity u_* distribution during the unsteady flow stages against depth changes for accelerating and decelerating times of 20 s, 45 s, 60 s and 90 s and six steady flows

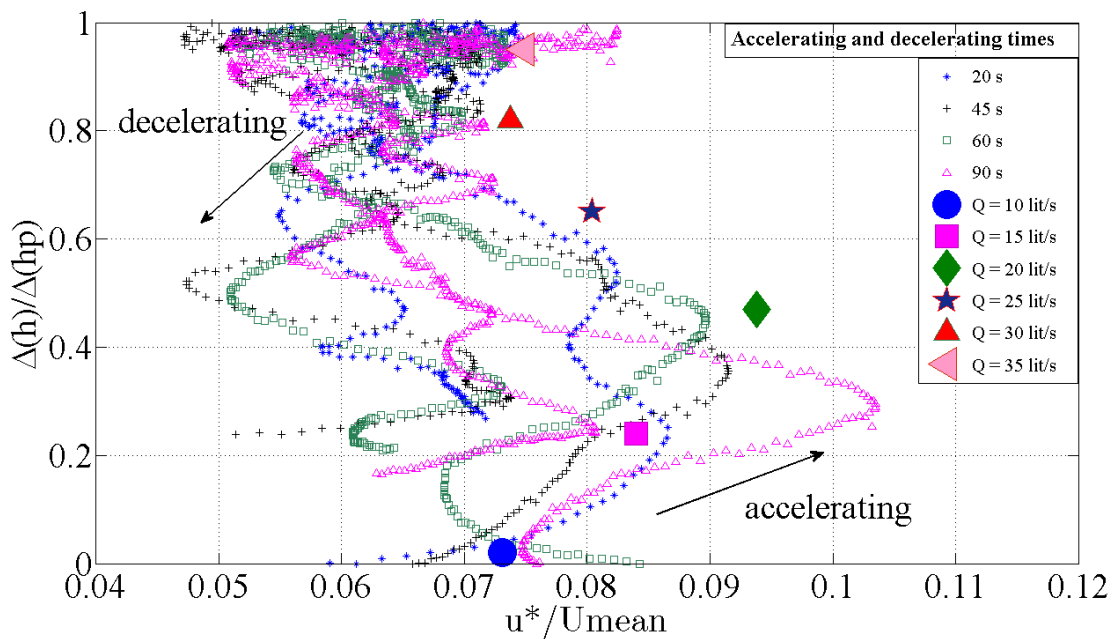


Fig. 12b. Friction velocity u_* normalized by the mean velocity during the unsteady flow stages against depth changes for accelerating and decelerating times of 20 s, 45 s, 60 s and 90 s and six steady flows

The friction velocity was also determined from Reynolds stress data using $u_* = (-\overline{u'w'})^{1/2}$ over the logarithmic range. For comparison, the results are included in Fig. 13. It can be seen that the shape of the hysteresis loop is similar to the one obtained from the logarithmic profile method. The turning point in the loop is again at $\Delta h/\Delta h_p = 0.6$. However, the numerical values are significantly different. This is to be expected, since the assumption of a constant stress layer on which the calculation by $u_* = (-\overline{u'w'})^{1/2}$ is based, is not valid in open-channel flow. Nevertheless, a comparison of the two curves indicates a correlation between the dynamics of the Reynolds stress and the friction velocity during all ranges of the hydrograph.

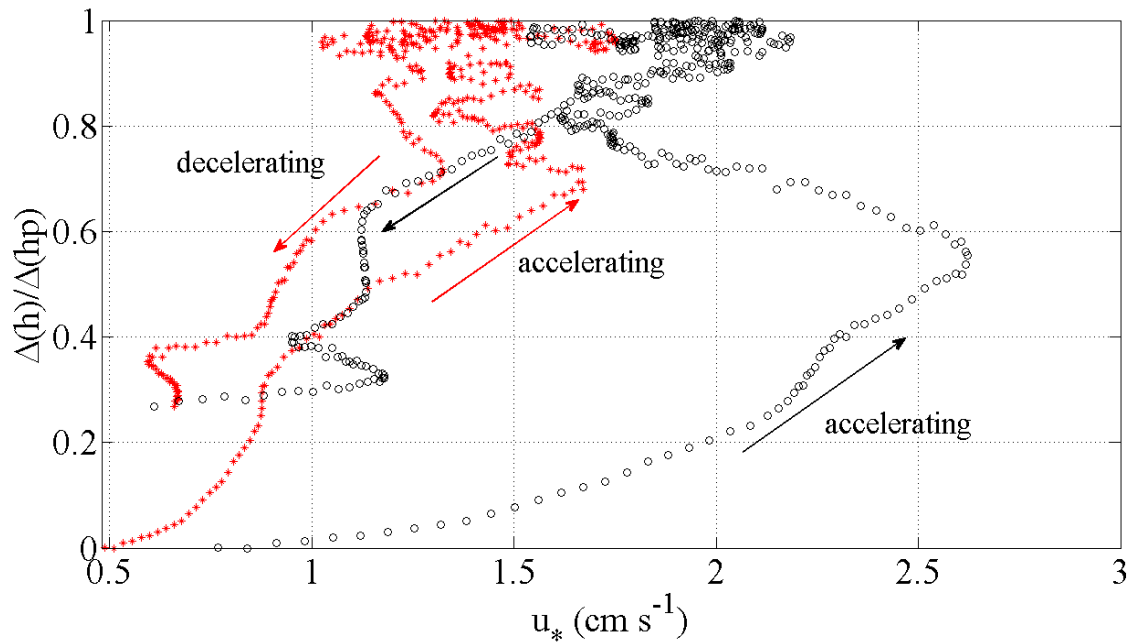


Fig. 13. Friction velocity u_* distribution for the hydrograph 20 s. Right side: o = logarithmic profile method and left side: * = $u_* = (-\overline{u'w'})^{1/2}$

4.3 FINE SEDIMENT DYNAMICS IN UNSTEADY OPEN-CHANNEL FLOW STUDIED WITH ACOUSTIC AND OPTICAL SYSTEMS

4.3.1	Acoustic measurements with low target concentration	95
4.3.2	Sediment suspension in unsteady flows	102
4.3.3	Sediment suspension characterization	106
4.3.4	Sediment suspension studies using PTV	110

4.3 FINE SEDIMENT DYNAMICS IN UNSTEADY OPEN-CHANNEL FLOW STUDIED WITH ACOUSTIC AND OPTICAL SYSTEMS

In this chapter, the initiation of sediment suspension and the subsequent increase in suspension concentration during accelerating flow will be investigated.

In low sediment concentration flows, acoustic methods may have difficulty determining the sediment particle concentration correctly, due to the relatively low number of particles inside the acoustic beam. This is the case of the present study where no sediment particles were suspended during base flow. During the accelerating range, suspended sediment particles progressively contribute to the acoustic targets. In order to investigate the recorded data correctly, the sensitivity and the limits of the ADV under these conditions will be determined first. Hydrograph measurements will be presented thereafter.

4.3.1 ACOUSTIC MEASUREMENTS WITH LOW TARGET CONCENTRATION

To investigate the performance of the ADV under low particle concentration conditions, nine sets of experiments for the same hydrograph which was shown in Fig. 1, were carried out. The acoustic frequency of the emitter was varied and hydrogen bubbles were used as additional flow tracers, as described in Blanckaert and Lemmin (2006). It had previously been shown (Shen and Lemmin, 1997) that small gas bubbles or clusters of gas bubbles are ideal flow tracers, because they follow the fluid motion with negligible inertial lag. In fully turbulent flow, as in the present case, buoyancy forces of the small bubbles are sufficiently small and do not affect the measurements. Hydrogen bubbles and sediment particles are two tracers with completely different backscattering characteristics. This allows investigating whether one can distinguish between the contribution of the two tracers to the backscattering and the velocity distribution. The experimental conditions for all experiments are summarized in Table 2.

Figures 14 and 15 show the distribution of mean velocity and backscattering intensity, respectively, against the water depths that were obtained by averaging over the peak steady flow range. Starting with measurements at 1 MHz, it can be seen that there are hardly any background tracers in the water. The mean velocity profile for E1 with no particles in the water is the result of averaging over data with mostly no velocity detection by the ADV and some rare velocity data when occasional particles allowed velocity calculations during the recording. This indicates that it is useful to analyze the recorded time series in detail when nothing is known about the tracer concentration in the water, in order to avoid an incorrect interpretation of the data.

In E2, the hydrogen bubbles that were added are seen to be good tracers to obtain an open-channel flow profile over the whole water depth that corresponds to the measured discharge. No fine sediment was placed on the bed in this experiment. When a fine sediment layer is added to the bed in E3 and hydrogen bubbles are turned off, velocity data are only obtained in the lower half of the water depth, due to the suspended sediment particles. In the upper half of the water depth, the backscattering situation corresponds to

E1 and no reliable velocity is recorded. A strong velocity gradient in the vertical near the bed with a maximum at around $0.25 h$ is found. It rapidly decreases above and falls to zero at about $0.6 h$. This indicates that no sediment transport is detected by the ADVP above this level. It may be mentioned that during the initial phase of the acceleration range where no particle suspension occurred, no velocity data could be obtained with the ADVP. When this experiment is repeated with hydrogen bubbles added (E4), a full depth profile is once again obtained. The velocities are slightly higher than in E2, because bottom roughness is decreased by the presence of the fine sediment layer.

When unsteadiness is increased in E5, and all other conditions are kept constant, the velocity profile changes compared to E3. Strong velocities are now detected throughout the water column. However, except for the near bottom layer, these are not the velocities corresponding to the discharge, because the profile is significantly different from E4. Therefore, this profile is an indication that due to the greater unsteadiness, sediment particles are now transported higher into the water column when compared to experiment E3. The two experiments, E3 and E5 were repeated by using the alternative sediment layer thickness. This did not affect the results. Therefore, the thickness of the sediment layer has no effect on the flow dynamics in our experiments, because during this early stage of ripple development, the sediment layer did not erode down to the gravel bed.

Table 2. Experimental conditions

Experiment	ADVP frequency (MHz)	Hydrogen bubbles	Rising time (s)	Fine sediment layer thickness (mm)
E1	1	no	60	no
E2	1	yes	60	no
E3	1	no	60	4
E4	1	yes	60	4
E5	1	no	30	6
E6	1.66	no	60	6
E7	1.66	yes	60	6
E8	2	no	60	6
E9	2	yes	60	6

In order to investigate whether the contribution of two different tracers, as made evident above, is dependent on the acoustic characteristics of the instrument, the above experiments were repeated at different acoustic frequencies. The frequency dependence of backscattering has been demonstrated before (Lhermitte and Lemmin, 1993) and the resonance effect for gas bubbles has been pointed out. Therefore, the acoustic frequency was increased in two steps, first to 1.66 MHz and then to 2 MHz. The ADVP hardware allows to work with frequencies up to 3 MHz. However, the drop in efficiency of the present transducer set with frequency increase was too strong to investigate even higher

frequencies. At 1.66 MHz, the profile of E6 that corresponds to E3 at 1 MHz, is close to that of E3. Similarly, E7 and E4 correspond well for the lower half of the profile. The deviation of E7 from the expected profile is difficult to explain. One may consider that at that level, E6 goes back to the background noise profile. In the upper half of the profile, hydrogen bubbles are the essential tracers and the deviation from the true profile is the effect of reduced backscatter from hydrogen bubbles with increased acoustic frequency. At 2 MHz, once again E8 is close to E3. E9 shows a continuation of the trend from E4 to E7 in that a deviation from the expected velocity profile occurs already in the inner layer. The upper part of the E9 profile cannot be explained. It can be expected that a further increase of the acoustic frequency may suppress backscattering from the hydrogen bubbles and thus produce a profile that corresponds to the one obtained only from sediment particles (E3), even in the presence of hydrogen bubbles.

All velocity profiles for experiments with fine sediment added have a similar gradient near the bed. This indicates that the profile form in this layer is determined by suspended sediment particle transport. By comparing E3 and E4, it appears that sediment does not affect the mean flow characteristics. During steady peak flow, it was found that mean flow velocity profiles for experiments E2, E4, E5 and E7 followed a logarithmic law in the inner layer.

The corresponding backscattering intensity profiles are plotted in Fig. 15. For the two experiments with hydrogen bubbles (E2 and E4), backscattering intensity is clearly dominated by the presence of the bubbles and it shows the same profile values for both experiments. Therefore, from these backscattering profiles it cannot be determined whether suspended sediment particle transport occurred or not. All experiments, except in clean water with no flow tracers (E1), show that sediment transport is concentrated in the near bottom layer (Fig. 15). For E5, backscattering intensity greatly increases in the central layers of the water column, mainly due to the ripples which are formed on the bed and which influence sediment suspension. A comparison of the results of E3 in Figs. 14 and 15 shows that backscattering intensity decreases more rapidly than mean particle velocity with distance from the bed. This indicates that sediment transport above $\sim 0.2 h$ is no longer a reliable tracer for mean velocity determination. Therefore, the upper part of the velocity profile above $z = 2$ cm for E3 in Fig. 14 should be interpreted with caution. From the backscattering intensity profile, it has to be expected that particle presence in this layer is strongly intermittent. This affects the mean velocity calculation, as discussed above. Actual velocities in this layer may be higher and the mean value over the whole profile shown here is not representative, even though the profile is smooth. This indicates that more sophisticated techniques than long-term averaging should be applied for determining the actual velocity profile. This example shows that only the simultaneous analysis of velocity and backscattering allows determining the correct interpretation. The higher acoustic frequency data are also included in this figure. However, these profiles do not provide reliable velocity information. This is due to the low transducer efficiency at these acoustic frequencies.

In order to relate backscattering intensity to particle density in the water column, the number of particles in the water was determined from PTV images taken in parallel. Two different tendencies can be observed when comparing the backscattering intensity which was measured by the ADV (Fig. 15) and particle numbers which were calculated by the PTV technique (Fig. 16). First, hydrogen bubbles do not contribute to the particle numbers indicated in Fig. 16. This shows that hydrogen bubbles cannot be detected by the camera system used in this study. Therefore, hydrogen bubbles are much smaller than the fine

sediment particles. Secondly, in the layer just above the bed, particle numbers are similar for E3 and E4 and are higher for E5. The lowest point in the profiles has to be interpreted with some caution, since the determination of the bed level is difficult in the PTV images. In E5, the layer of high particle numbers also extends upward into the water column. This confirms the ADV results discussed above. However, it also shows that mean particle numbers and mean backscattering decrease more sharply than mean velocity. The low particle numbers found in the PTV analysis confirm that the present experiments are carried out in a low particle density environment. Under these conditions, no attenuation compensation is needed for the ADV.

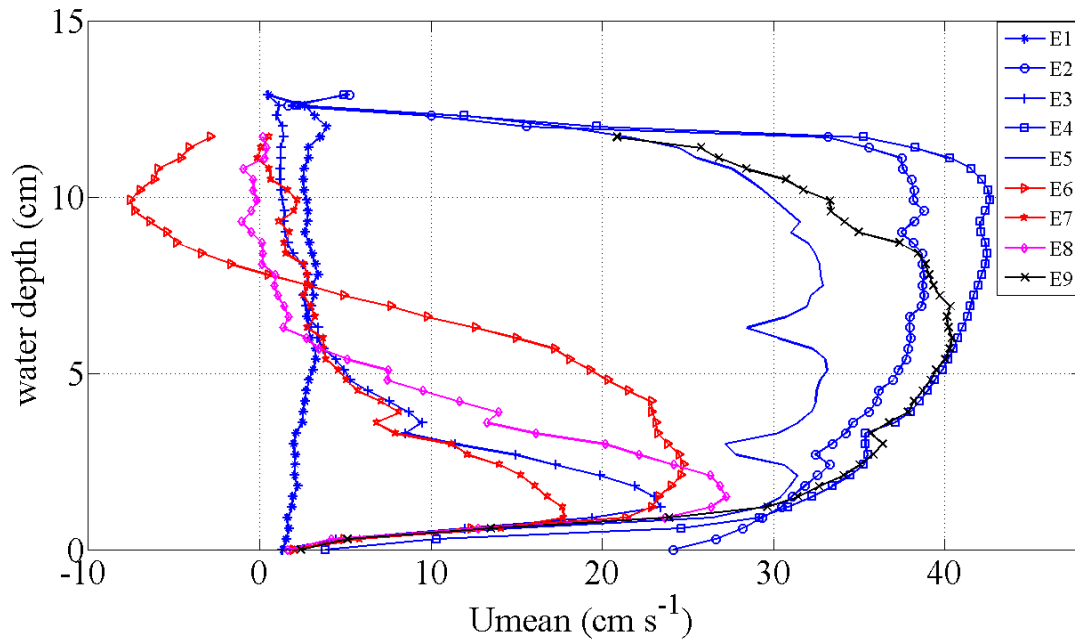


Fig. 14. Mean velocity profiles during steady peak flow for all experiments. For details on the legend, see Table 2.

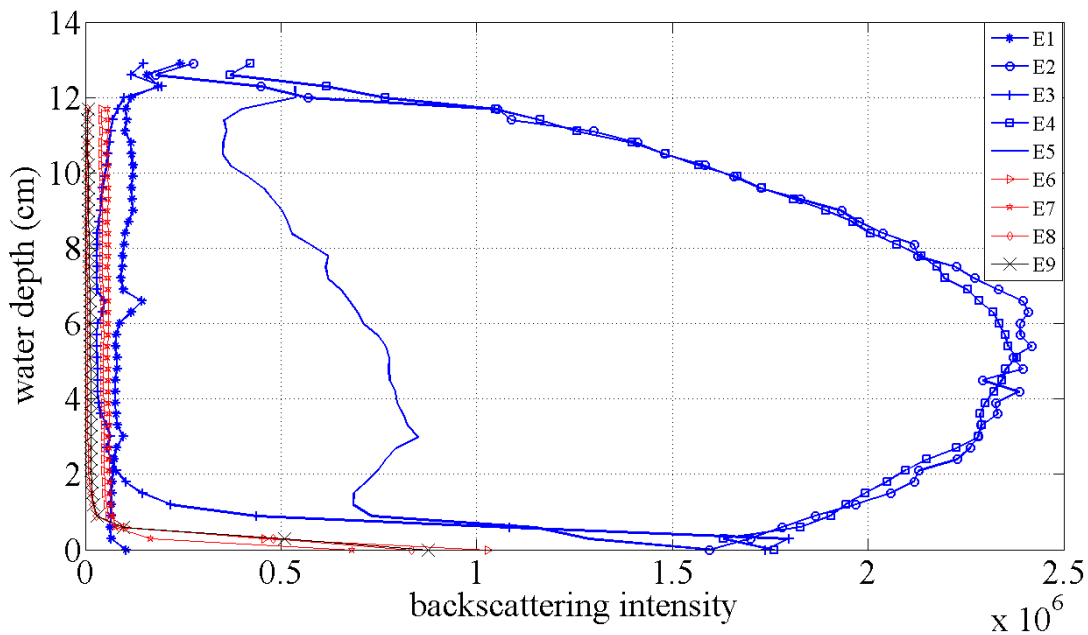


Fig. 15. Backscattering intensity profiles during steady peak flow for all experiments. For details on the legend, see Table 2.

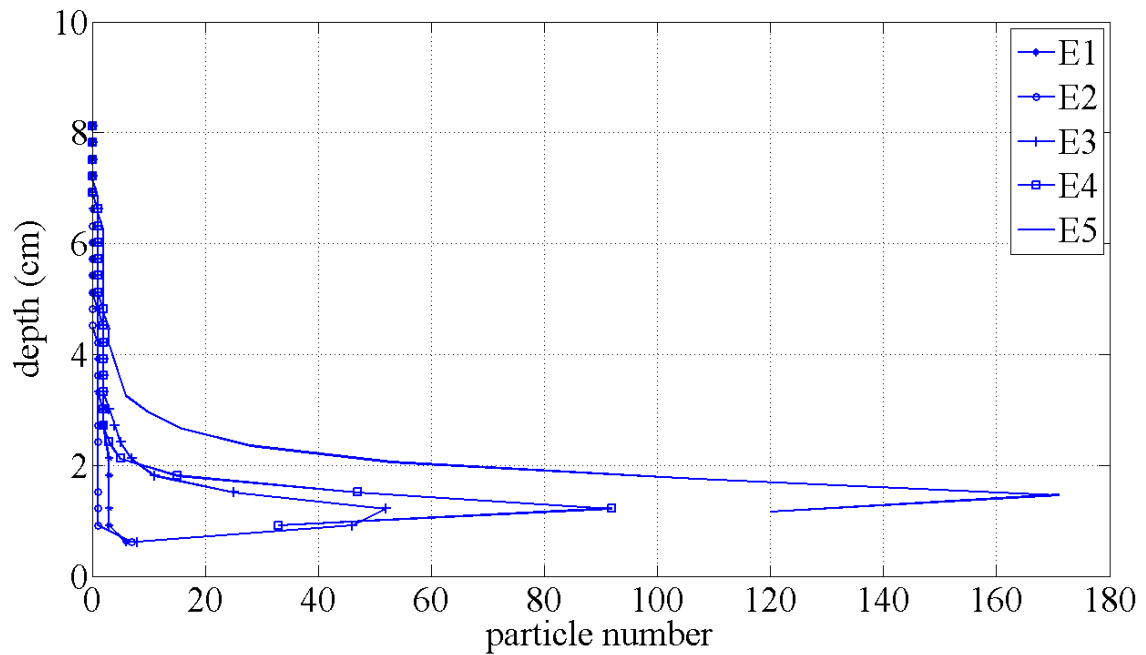


Fig. 16. Mean particle number for 1MHz experiments obtained from PTV images

In order to further investigate the time stability of velocity and backscattering profiles, mean profiles over ten consecutive profiles were calculated for both data sets. This corresponds to a 3 Hz resolution that is indicative of coherent structure scales. The results for E3, E4 and E5 are presented in Figs. 17, 18 and 19, respectively. In each case, velocity and backscattering data are presented. All three velocity profile time series show a rapid increase in the vertical velocity profile gradient in the layers near the bottom all along this section of the hydrograph. Over time, velocity profiles change little from the bottom to a depth of 2 cm. In all three experiments, velocities vary little between individual time slices, indicating that sufficient tracer particles are present at all times. Above this level, differences between the experiments can be seen. In E3 (Fig. 17a), velocity rapidly falls to zero in the upper part of the water column, because no sediment is suspended into this part of the water column. For E4 (Fig. 18a), smooth velocity profile time series over the whole water column are seen. In E5 (Fig. 19a), strong, but variable velocity profiles are observed for the different time slices in the upper layers. Variability occurs along the profiles and also between profiles.

The backscattering time series explain the observed differences in the velocity distribution. For E3 (Fig. 17b), significant backscattering only occurs directly above the bed. Although the velocity time series was rather smooth, strong variability in time is seen in the backscattering intensity in the near bottom layer. This indicates that backscattering and thus sediment suspension is strongly event-structured. As expected, backscattering in E4 (Fig. 18b) is more homogeneous in time. The maximum of the backscattering intensity is found in the mid-depth range of the profile. In the case of strong unsteadiness, E5 (Fig. 19b), the near bottom backscattering time development is similar to that observed in E3. However, significant backscattering, once again organized in events, also occurs in the remaining water column. When sediment particles are the only flow tracers, individual peaks in the backscattering intensity document a strong temporal and spatial variability and an event structure of the particle suspension process.

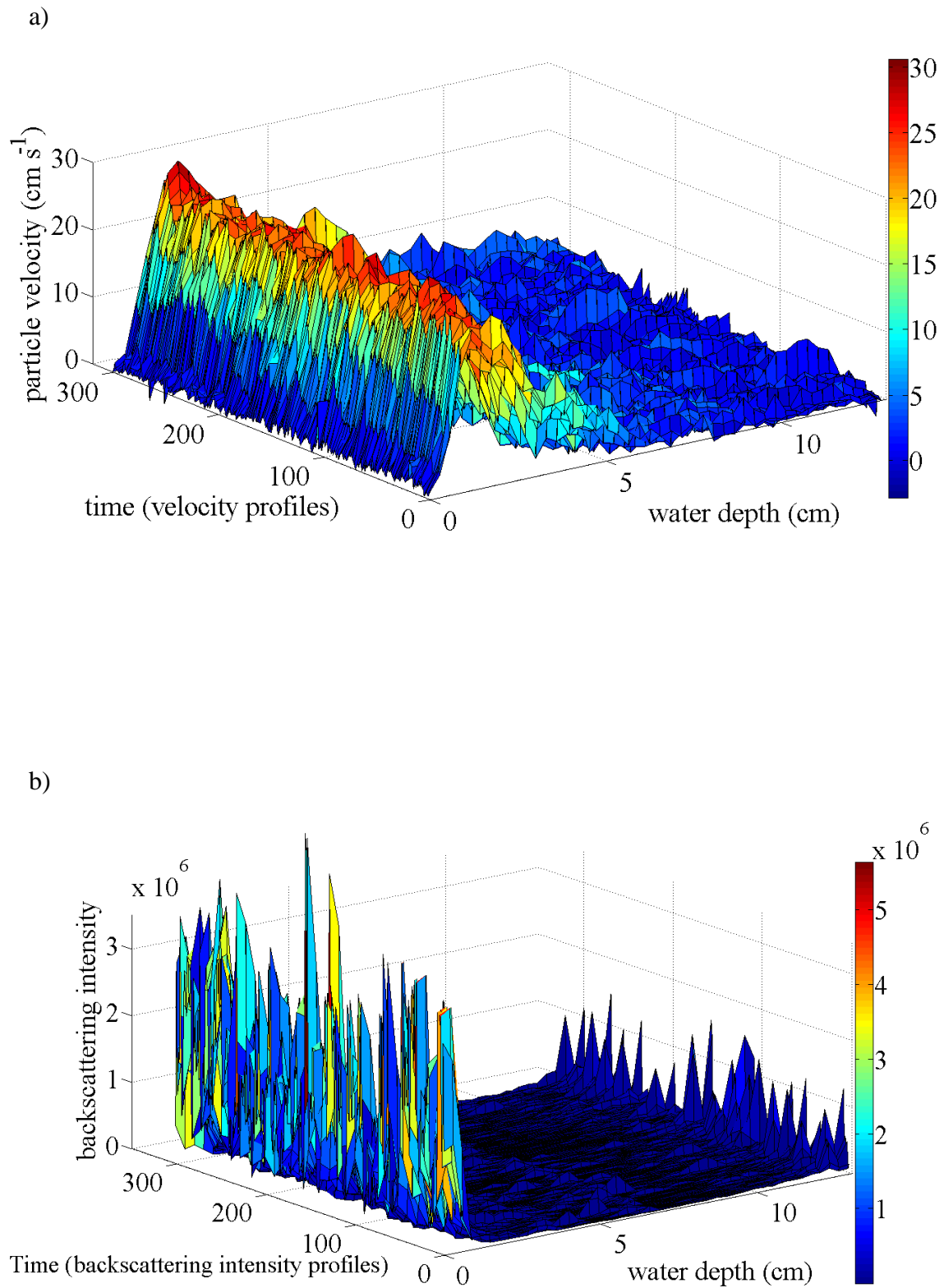


Fig. 17. Particle velocity and backscattering intensity during steady peak flow range for E3

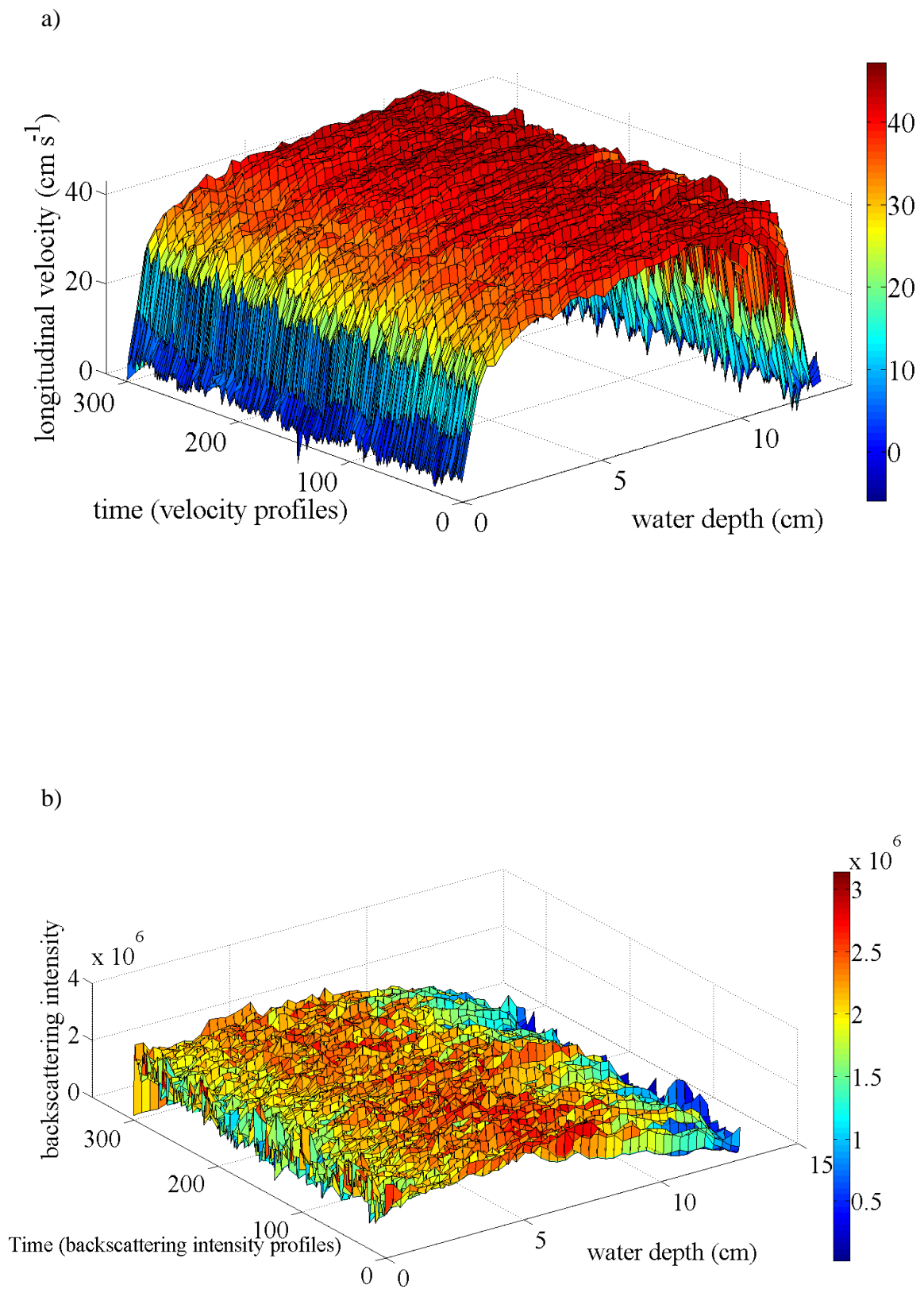


Fig. 18. Velocity and backscattering intensity profiles during steady peak flow for E4

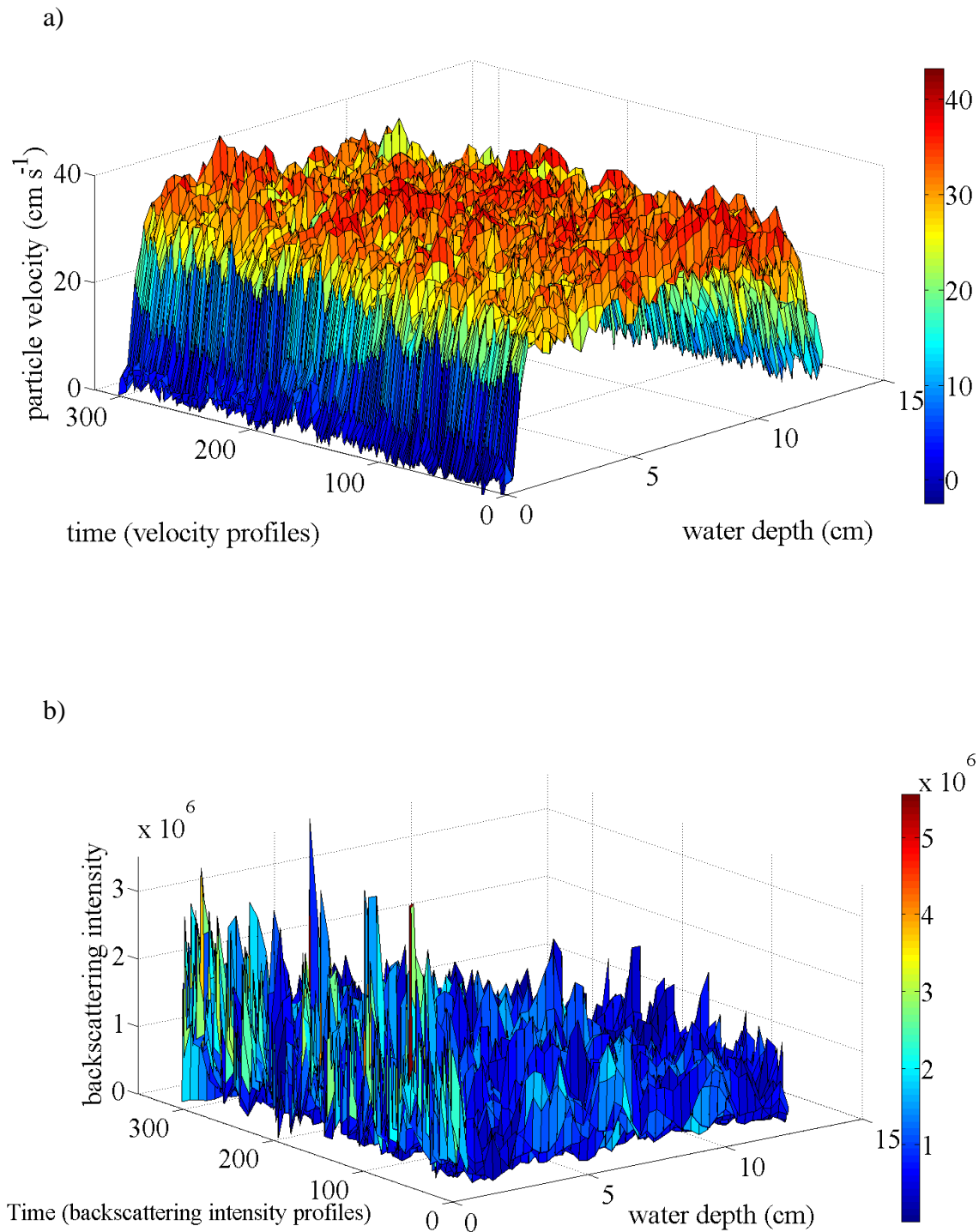


Fig. 19. Particle velocity and backscattering intensity during steady peak flow range for E5

4.3.2 SEDIMENT SUSPENSION IN UNSTEADY FLOWS

The results for the particle velocity profiles during the hydrographs 20 s and 90 s which cover the accelerating range, the steady peak flow and the decelerating ranges are presented in Figs. 20 and 21, respectively. These figures show a rapid velocity increase in

the vertical near the bottom all along this section of the hydrographs. Suspended particles are concentrated in the near bottom layer. The particle velocity remains nearly constant during the three central ranges of the hydrograph even though the mean flow velocity changes (Fig. 3). In the upper part of the water column, particle velocity rapidly falls to zero due to low particle concentration. Velocities above the velocity maximum can therefore not be interpreted as being indicative of the flow dynamics. This was discussed in detail in Section 4.3.1 (p. 96).

When the results for E3 (Fig. 17) and E5 (Fig. 18) and the results for highest unsteadiness (20 s in Fig. 20) and lowest unsteadiness (90 s in Fig. 21) are compared, the effect of unsteadiness on the accelerating flow is apparent: More particles are transported into the upper layers for higher unsteadiness. Therefore a stronger unsteadiness produces particle suspension into higher depth levels that allows tracing the velocity distribution over a wider depth range. However, as indicated above, velocities in the upper part of the water column are not representative of the flow dynamics. From these results, it appears that the sediment flux time series calculation will be strongly variable due to the variability of the particle density and not because of the variability of the velocities.

Some individual profiles covering the whole range of the hydrograph for 30 s accelerating and decelerating range, are shown in Fig. 22 for particle velocity and in Fig. 23 for the corresponding backscattering intensity, in order to present the suspension dynamics during the accelerating, peak flow and decelerating ranges of the hydrograph. The form of all of the velocity profiles is similar (Fig. 22) with a strong velocity gradient near the bed. The maxima of the profiles are found at around $0.25 h$. Velocities then rapidly decrease and fall to zero at about $0.6 h$. This indicates that no sediment transport can be detected by the ADVP above this level. Sediment particle velocities are similar, even though the flow velocities change during this part of the hydrograph (Fig. 3). The corresponding backscattering intensity profiles are plotted in Fig. 23. In the accelerating flow range, sediment transport is concentrated in the near bottom layer. In time, backscattering intensity progressively increases in layers further away from the bed. During decelerating flow, backscattering intensity greatly increases in the central layers of the water column, mainly due to the ripples which are formed on the bed and which influence sediment suspension as will be seen for the PTV results.

Figure 24 presents maximum particle velocities in each time slice profile for the 20 s and 90 s hydrographs against the depth variation, covering the whole range of this part of the hydrograph. They were extracted from Fig. 20 and Fig. 21 in order to present suspension dynamics during accelerating and peak flow and decelerating ranges of the hydrographs. Figure 24 indicates that two different hysteresis loops are formed during the highest unsteadiness (20 s) and lowest unsteadiness (90 s) for maximum particle velocity. It is seen in Fig. 24, that initially, maximum particle velocity in the accelerating range increases steeply, then more slowly. The decrease in particle velocity during the decelerating range is smoother. During both hydrographs, maximum particle velocity decreases linearly in the decelerating flow range and both hydrographs come to the same value at the peak flow end of the unsteady flow ranges. The two different loops in Fig. 24 indicate the strong effect of unsteadiness on particle velocity in accelerating range. Therefore the particle velocity pattern follows that of the mean velocity (Fig. 3).

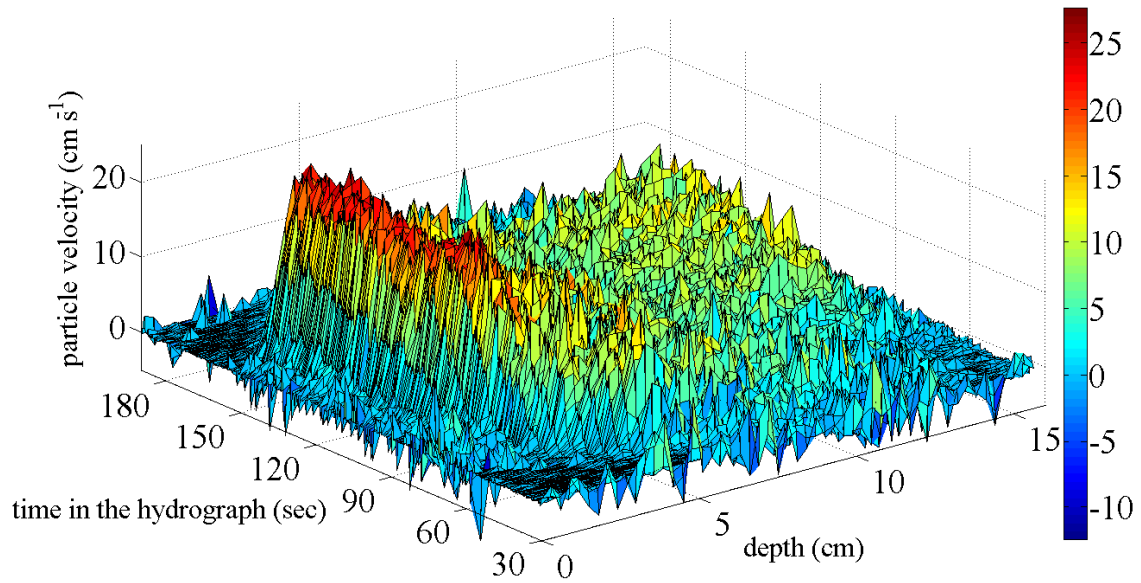


Fig. 20. Particle velocity during the unsteady flow ranges of accelerating and decelerating time of 20 s

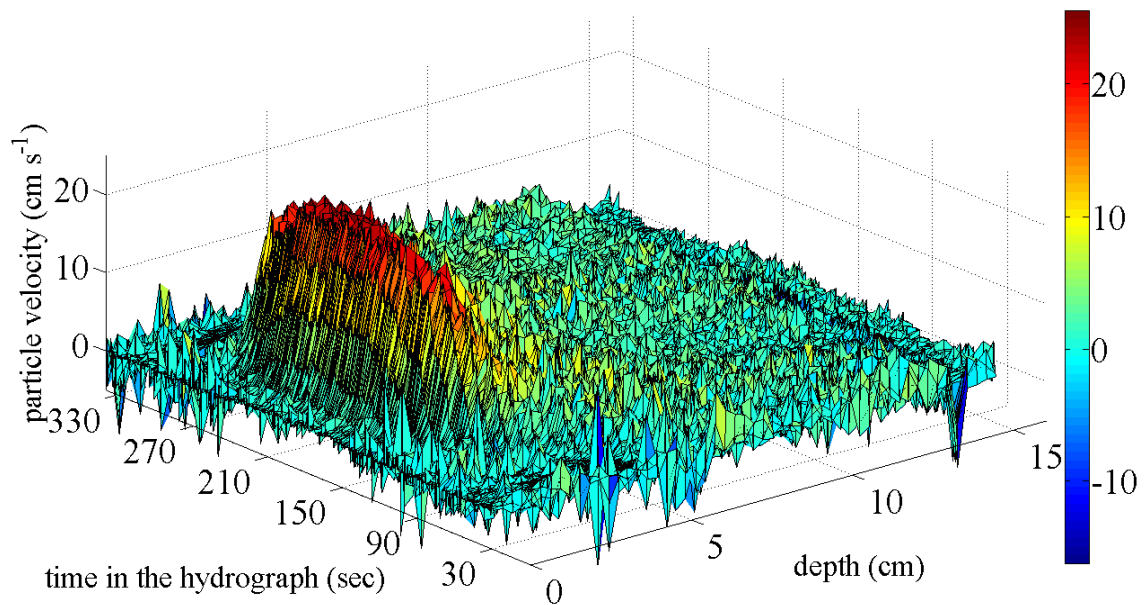


Fig. 21. Particle velocity during the unsteady flow ranges of accelerating and decelerating time of 90 s

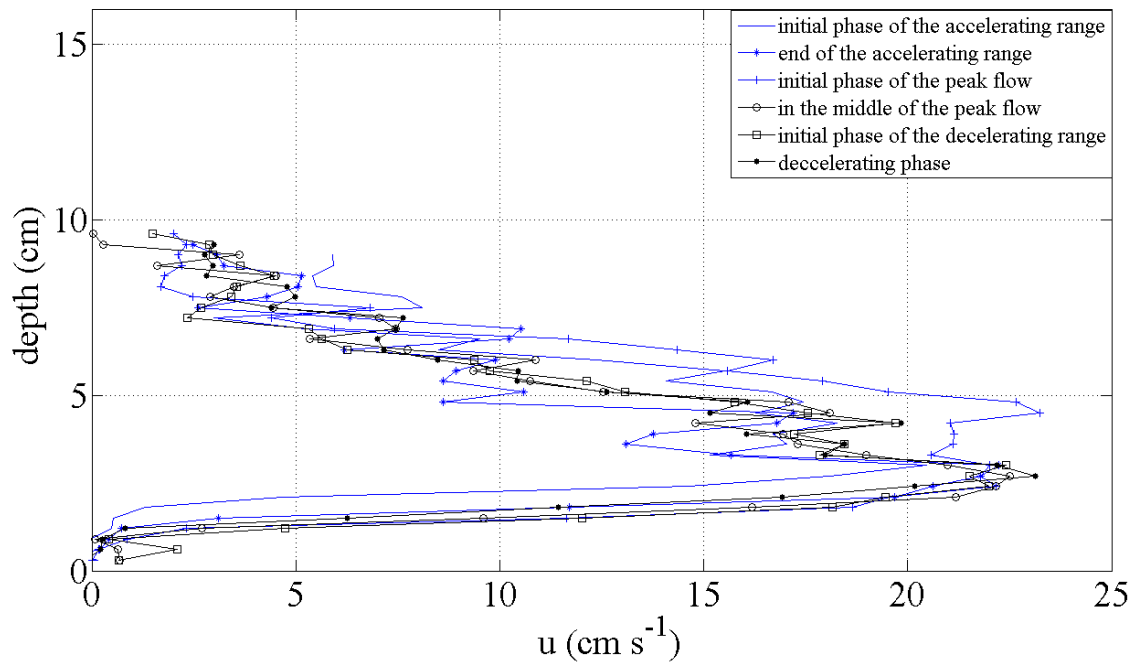


Fig. 22. Velocity profiles during unsteady flow

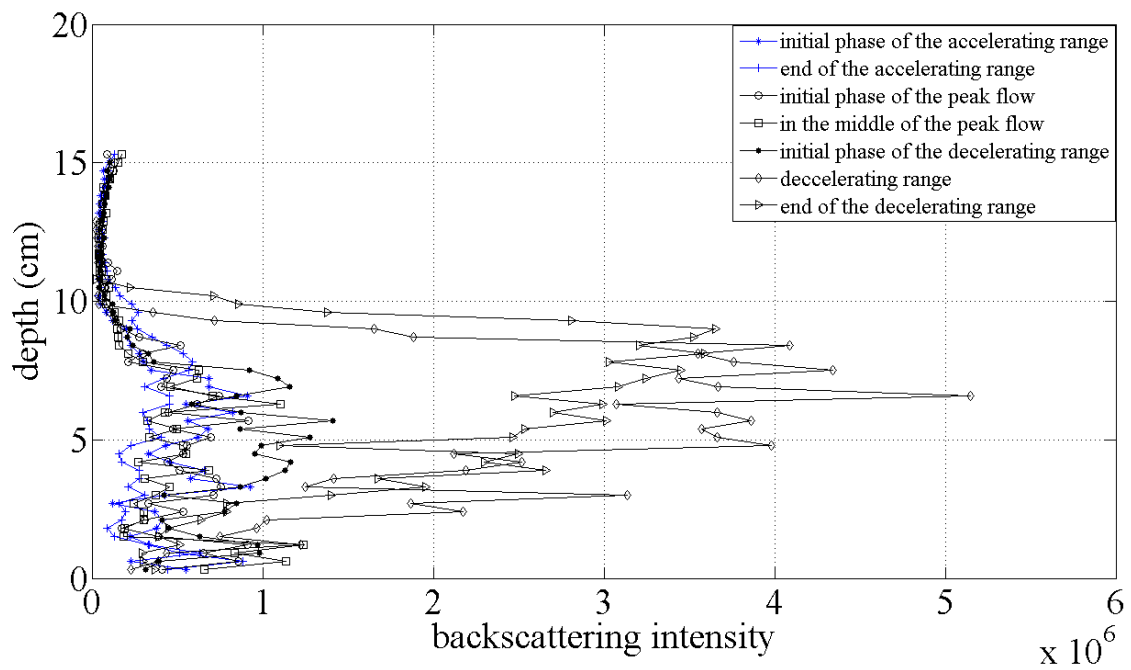


Fig. 23. Backscattering intensity profiles during unsteady flow

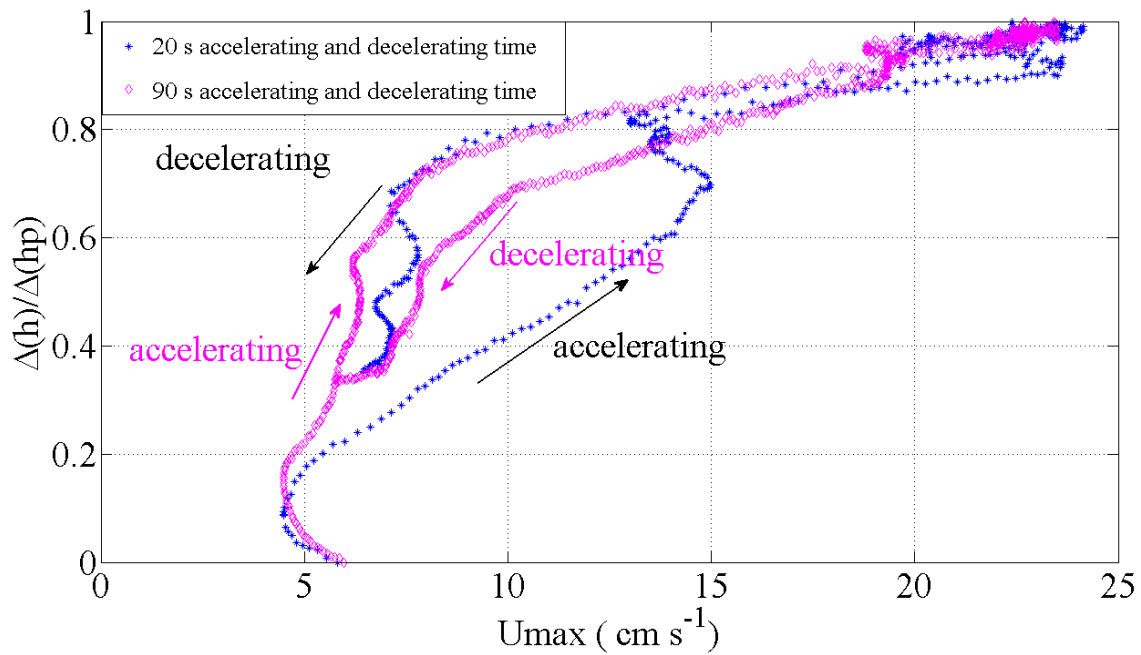


Fig. 24. Maximum particle velocity distribution during the unsteady flow stages against depth changes for accelerating and decelerating times 20 s and 90 s

4.3.3 SEDIMENT SUSPENSION CHARACTERIZATION

The Rouse number ($Rouse\ number = \frac{V_s}{\kappa u_*}$) is a non-dimensional number which is used in fluid dynamics to define a concentration profile of suspended sediment and which also determines how sediment will be transported in a flowing fluid. It is the ratio between the sediment fall velocity V_s and the upwards velocity on the grain as a product of the von Kármán constant κ and the shear velocity u_* as explained in Chapter 2. In order to understand how sediment will be transported in accelerating and decelerating unsteady flow and what the effect of the different unsteadiness is on sediment suspension, Rouse number distributions against depth variation were plotted for all five hydrographs and the results are presented in Fig. 25. In these experiments, the fall velocity of fine sediment is taken as $V_s = 0.75$ (cm s^{-1}).

The Rouse numbers characterizing transport as bedload, suspended load, and wash load, are given in Table 3.

Figure 25 shows that the Rouse number follows the shear velocity dynamics discussed above, forms a loop and changes differently in the accelerating and decelerating flow ranges. It indicates that during the accelerating range of the hydrographs, suspension strongly increases, whereas in the decelerating ranges of hydrograph, only 50% of particles are transported as suspended load. However, the Rouse number for all hydrographs changes between 0.73 and 2.1. Comparing the Rouse number for different unsteadiness shows that at the beginning of the accelerating phase of unsteady flow for the 20 s unsteadiness, less particles go into suspension than for the other hydrographs, but after that, up to $\Delta h / \Delta h_p = 0.2$ during the accelerating range of the hydrographs, the rate of reduction in Rouse number is similar for all of them. Above $\Delta h / \Delta h_p = 0.2$, it changes differently. The Rouse number reaches 0.73 for highest unsteadiness (20 s) in the accelerating phase of unsteady flow and

remains around this value with further depth increase, whereas it increases more rapidly for the 30 s, 45 s, 60 s and 90 s hydrographs during that phase of the hydrograph. It indicates that higher unsteadiness has a stronger effect on suspension in the water column during the accelerating range (as will be shown by PTV measurements). Again all hydrographs maintain the same value in peak steady flow, which is in the range where 100% suspension is predicted. During the decelerating flow, the lowest unsteadiness shows the lowest value for the Rouse number. Therefore, during the decelerating flow, less unsteadiness results in more suspended particles in the water column.

Table 3. Required Rouse numbers for transport as bedload, suspended load, and wash load

Mode of Transport	Rouse Number
Bed load	>2.5
Suspended load: 50% Suspended	>1.2, <2.5
Suspended load: 100% Suspended	>0.8, <1.2
Wash load	<0.8

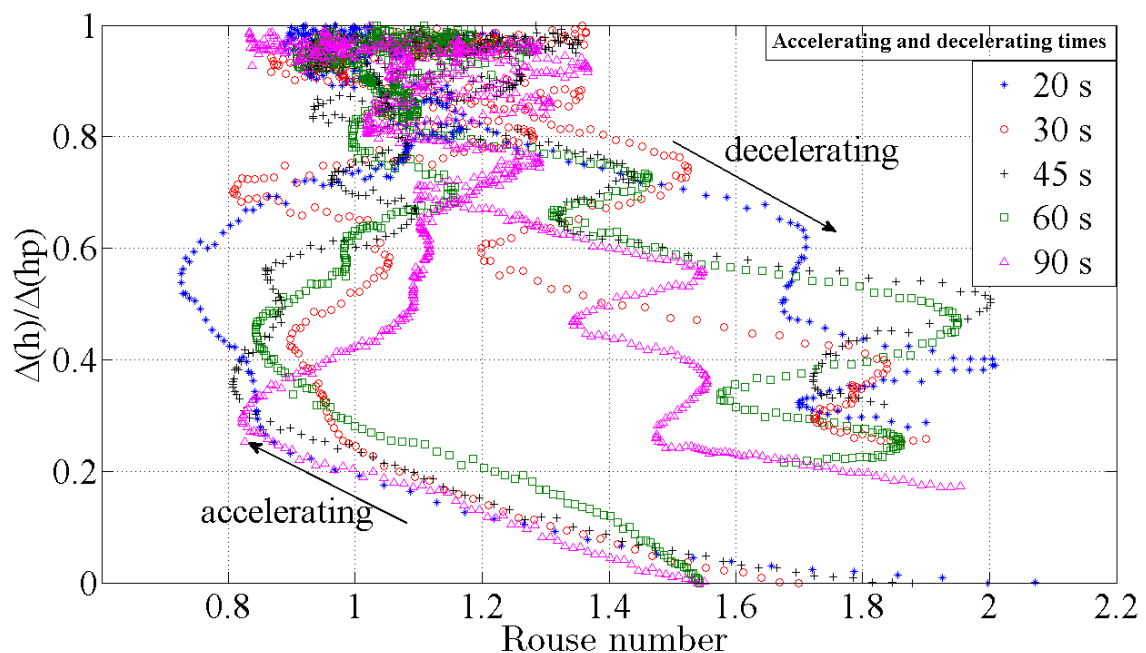


Fig. 25. Rouse number distribution during the unsteady flow stages against depth variation for accelerating and decelerating times of 20 s, 30 s, 45 s, 60 s and 90 s

The Shields parameter, also called the Shields criterion or Shields number, is a nondimensional number used to calculate the initiation of motion of sediment in a fluid flow. It can be considered as a nondimensionalized shear stress. Bed shear velocities u_*

were used to calculate the Shields parameter $F_s = u_*^2 / R g D_s$ for each of the five hydrographs; D_s is particle diameter, g is gravitational acceleration, $R = \rho_s / \rho_w - 1$, where ρ_s and ρ_w are densities of sediment and water respectively. Results, plotted in Fig. 26a against depth variation, show a steep increase in the early phase of the unsteady accelerating flow, but a less steep increase during the remainder of the unsteady accelerating flow, followed by a peak steady range. Different loop shapes are observed for the 20 s, 30 s, 45 s, 60 s and 90 s accelerating and decelerating ranges of the hydrographs with a particularly strong increase during accelerating phase of the hydrograph with 20 s accelerating and decelerating time. The highest values are found at around $\Delta h / \Delta h_p = 0.6$. These results were combined with the shear Reynolds number, $Re_* = D_s u_* / \nu$, where ν is fluid kinematic viscosity, and plotted against depth variation for all five hydrographs (Fig. 27). Figures 26a and 27 show that during the accelerating range of unsteady flow at around $\Delta h / \Delta h_p = 0.2$, the Shields parameter changes between 0.15 and 0.2 and the Shear Reynolds number changes between 2 and 2.5, with respect to the line separating the zones of particle motion from no particle motion (Graf 1971; Yalin and da Silva 2001). In these ranges, the accelerating ranges of all hydrographs fall into the particle motion zone in the suspension region. This behavior has even been observed for the region very close to the bed ($\Delta h / \Delta h_p < 0.2$) during the accelerating stages. However, as will be discussed later, particle motion starts as bedload during the initial phase of the accelerating range of the hydrographs and is followed by suspended load. With respect to the Shields parameters and shear Reynolds numbers for the decelerating range of all hydrographs, particles during this range of the hydrographs fall in the no particle motion zone even at $\Delta h / \Delta h_p = 0.6$. However, PTV results, which will be discussed later, show that particles stay in suspension during the decelerating range of the hydrographs. This process cannot be parameterized by the critical Shields parameter.

For the fine sediment ($D_{50} = 0.12$ mm) which is used in the present study and with $\nu = 0.01$ cm² s⁻¹ and $R = 1.65$, a particle Reynolds number ($Re_p = \frac{\sqrt{RgD_{50}D_{50}}}{\nu} = 5.27$) and a shear stress $\tau_* = \left[\frac{11.6}{Re_p} \right]^2 = 4.85$ for ripple formation were calculated. The Reynolds number of the fine sediment and the corresponding shear stress indicate that sediment suspension will occur. These values and the bed shear stress for each of the five hydrographs were incorporated in Fig. 4 of Chapter 2 and are presented in Fig. 26b. The blue points in Fig. 26b show the range of the shear stress values for all five hydrographs. It can be seen that for each hydrograph in the initial part of the accelerating range, shear stress falls into the range of no particle motion. Subsequently, it increases to values where ripple formation combined with sediment suspension is predicted. This is in agreement with the observations and the ADVP and PTV results.

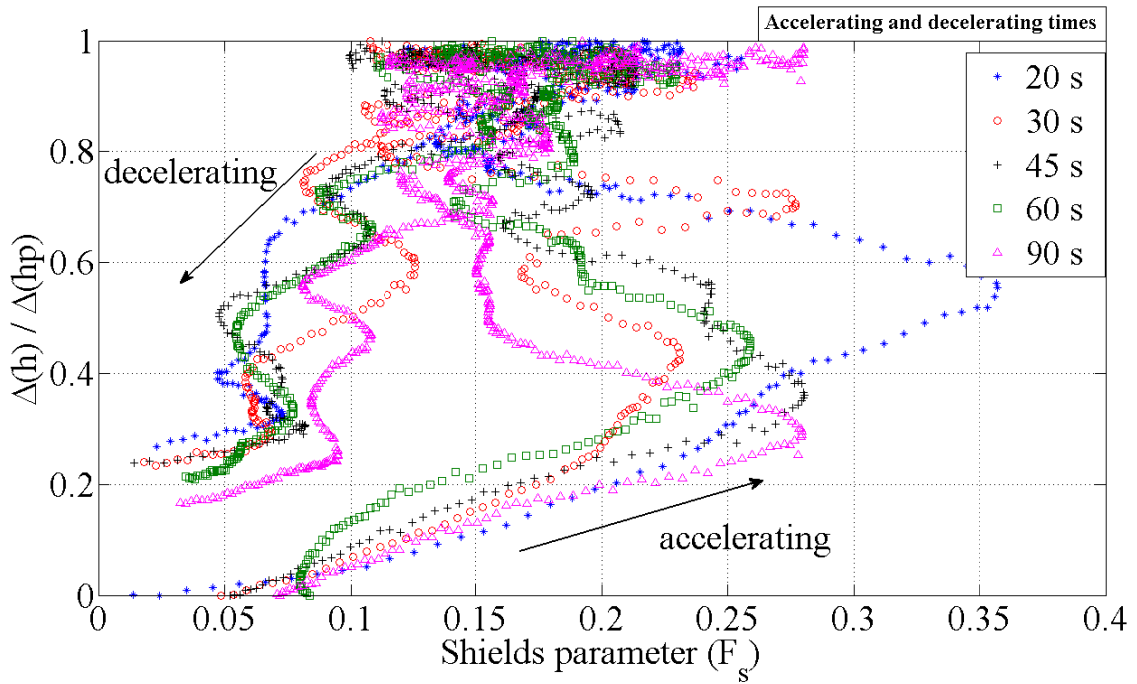


Fig. 26a. Shields parameter during the unsteady flow stages against depth variation for accelerating and decelerating times 20 s, 30 s, 45 s, 60 s and 90 s

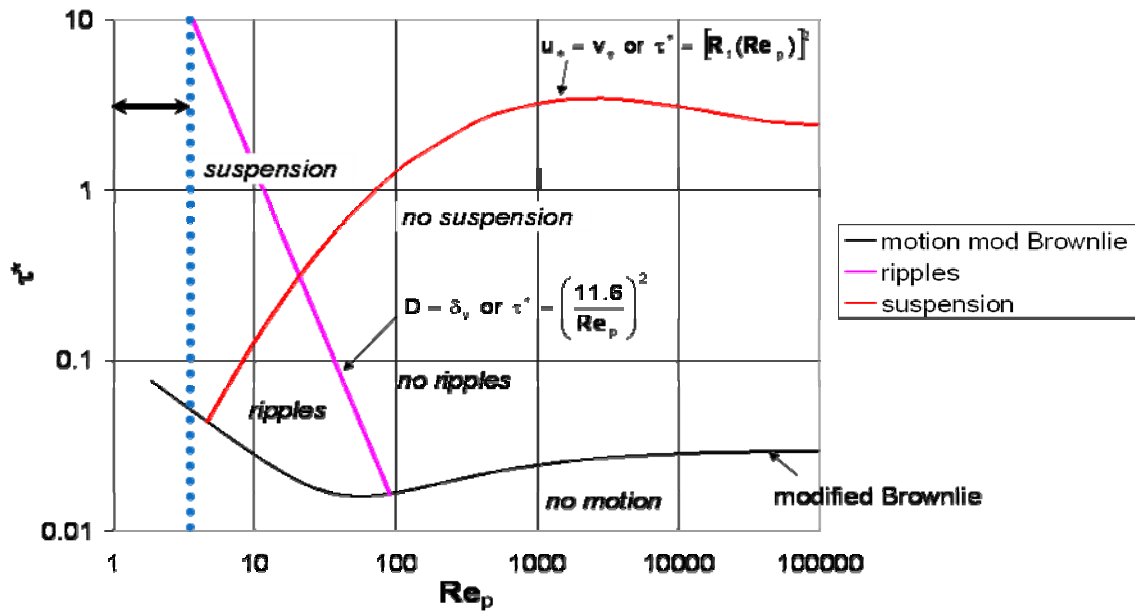


Fig. 26b. Results of the present unsteady experiments (blue dotted line) on the Shields diagram with the criterion for ripple formation (Parker, 2004)

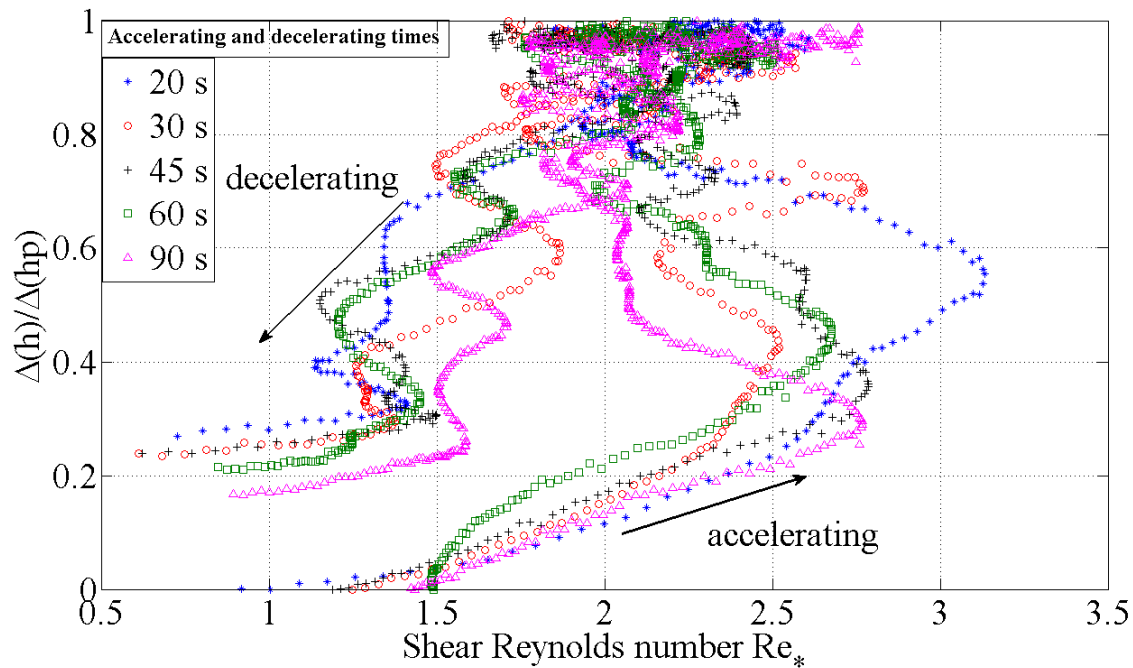


Fig. 27. Shear Reynolds number during the unsteady flow stages against depth variation for accelerating and decelerating times 20 s, 30 s, 45 s, 60 s and 90 s

4.3.4 SEDIMENT SUSPENSION STUDIES USING PTV

In this study, the PTV technique was used to calculate particle velocity and analyze the dynamics of suspended sediment in order to complement the ADV measurements discussed above. An example of velocity vectors calculated by PTV for the 60 s hydrograph are presented in Fig. 28, where two images that were taken at an 80 Hz frame rate during the early phase of the peak flow range are compared. The time interval between these two images is 0.05 s. As seen in Fig. 28a, suspension is nearly uniform in a shallow layer above the bed (about 2 cm high). Particle transport remained strong in this near bottom layer, in agreement with the ADV observations. Suspension into the water column above occurs in burst-like events. A sequence of bursts can be identified in Fig. 28a and bursts are strongest just behind the ripple crest that is on the right side of these images (see Fig. 31 for bed details). In Fig. 28b, the final burst on the right side has grown significantly in size and the shape of the others has changed. This rapid change in burst dynamics cannot be resolved with ADV measurements. Furthermore, the finite width of the ADV beam (between 7 mm and 10 mm) averages over much of the fine details seen in these images and the low particle density in the upper part of the images does not allow reliable ADV measurements, as discussed above. In these images, turbulence intensity and the strength of the burst events are not sufficient to suspend a significant number of particles over the full water depth.

In order to compare the results of PTV measurements with those obtained with the ADV, mean velocity calculations were carried out for the PTV data discussed above. For this purpose, the image was sliced in the vertical into 3 mm thick slices. This slice thickness is comparable to the height of the gates of the ADV. In the horizontal, the image was sliced into 10 mm wide strips. This width is close to the beam width of the ADV. Figure 28 shows the mean particle velocity profiles in six representative positions in the horizontal

direction of the images. The location of each position is indicated in Fig. 31. It can be seen in Fig. 31 that a ripple has developed on the right side of the image, followed in flow direction by a trough on the left side. These profiles are the average of over 2000 images. During this recording period, the bed shape did not change significantly. The profile form is comparable to the mean velocity profile measured by the ADV (Fig. 14) for E3. Velocity profiles are similar in all positions with a slight trend of increase from right (above the ripple) to left (in the trough). However, it should be recalled that the same averaging procedure that was used for the ADV measurements was also applied to the present analysis. Therefore, as indicated above, the velocities above the maximum of the profiles has to be interpreted with caution. This can be seen when comparing Figs. 28 and 29. In Fig. 28, velocity vectors in the upper part of the bursts are the strongest, as opposed to the mean profiles in this layer (Fig. 29). However, since fewer particles are elevated to this level, gaps will appear in the velocity time series. Thus, once again, averaging over all 2000 images results in biased mean values in these layers. As for the ADV data, the profiles presented here serve to indicate the layers of strong particle suspension. This example illustrates that the complementary application of the two different measurement methods can help in interpreting the results.

In Fig. 30, the sediment concentration profiles at the same positions, calculated from the averaged particle density for those positions are shown. The image was again split up as for the velocities indicated above. The highest concentration is found in the position where ripples are formed ($x = 10.2$ cm; Fig. 31) with a strong gradient towards the trough. This confirms the burst structure pattern seen in Fig. 28, with strongest bursts near the ripple crests. The mean backscattering profiles recorded with the ADV for the same section of the hydrograph are similar to the one at $x = 10.2$ cm. However, the ADV cannot reproduce the details seen in the analysis of the video images. Therefore, a combination of the two methods greatly enhances the understanding of the underlying processes.

In Fig. 32, velocity vector images that were taken at the beginning and at the end of the accelerating stage are compared, in order to demonstrate suspended sediment dynamics. Initially, suspension is nearly uniform in a shallow layer above the bed (about 2 cm high, Fig. 32a). Suspension into the water column above occurs in burst-like events in the final phase of the acceleration range and is strongest near the ripple crest (Fig. 32b). Particle transport remained strong in the near bottom layer; turbulence intensity and the strength of the burst events are not sufficient to suspend these particles over the full water depth.

Images were again segmented as described above. Figure 33 shows the mean particle velocity profiles in selected slices, averaged over 200 images for the initial (Fig. 33a) and the final (Fig. 33b) phase of the accelerating range. Profiles in individual slices are slightly different, indicating the turbulence structure of sediment transport and the effect of bedforms, as discussed above. Particle velocity profiles extend higher into the water column in the final phase (Fig. 33b).

In Fig. 34 are shown the corresponding sediment concentration profiles that were calculated from particle density. The highest concentration is found near the bottom. As for the mean particle velocities (Fig. 33), profiles for individual slices slightly vary, indicating the event structure of particle suspension and the effects of bedform. The height of the concentration profiles, and thus total suspension, increase in the final phase. This confirms the importance of burst structures, as seen in Fig. 33b, with the strongest bursts near the ripple crests. It also shows that the Rouse number distribution discussed above correctly indicates the increase in suspended sediment transport which is observed here.

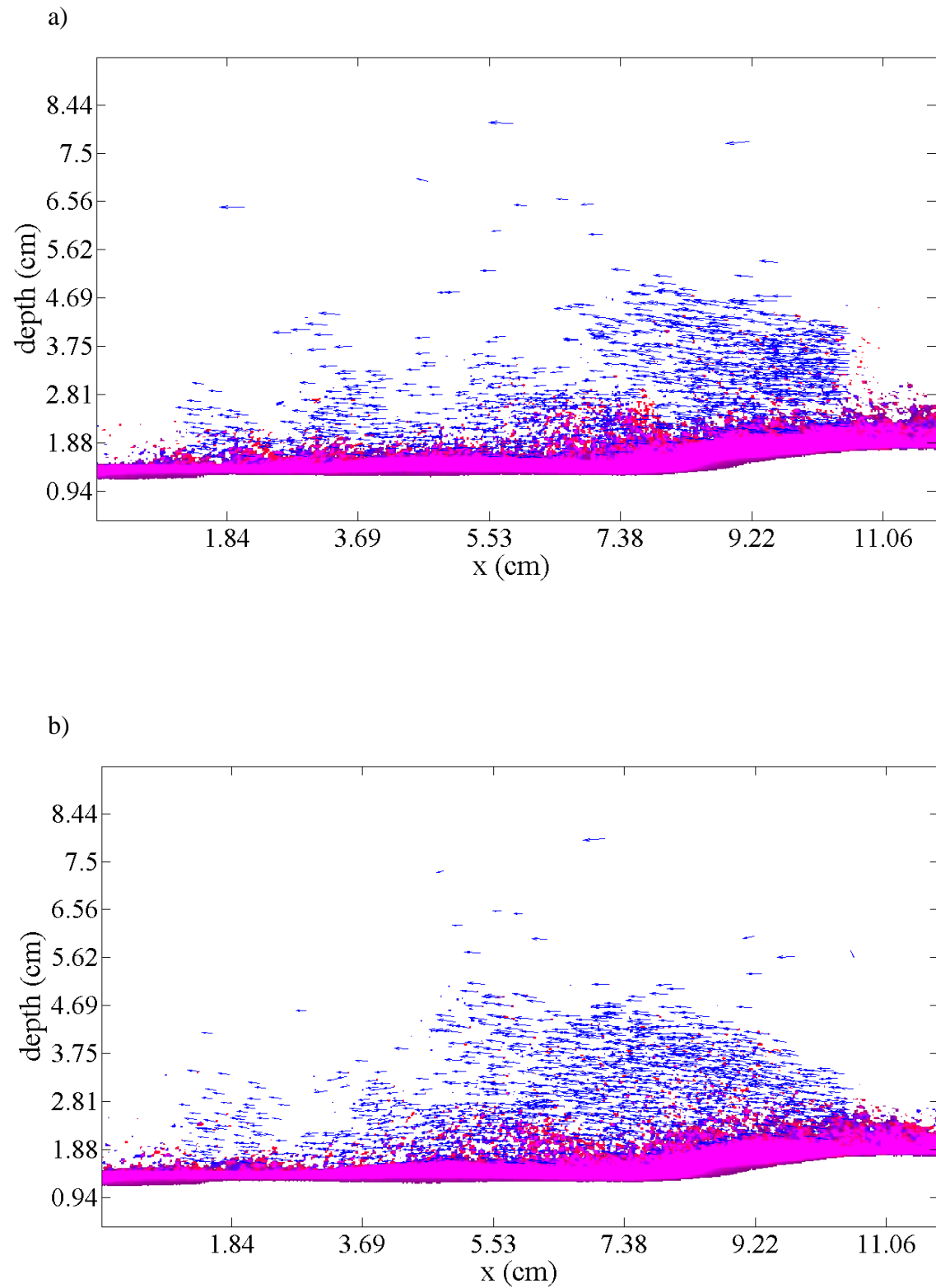


Fig. 28. Example of PTV results during the early phase of the steady peak flow range. Arrows indicate particle velocity vectors

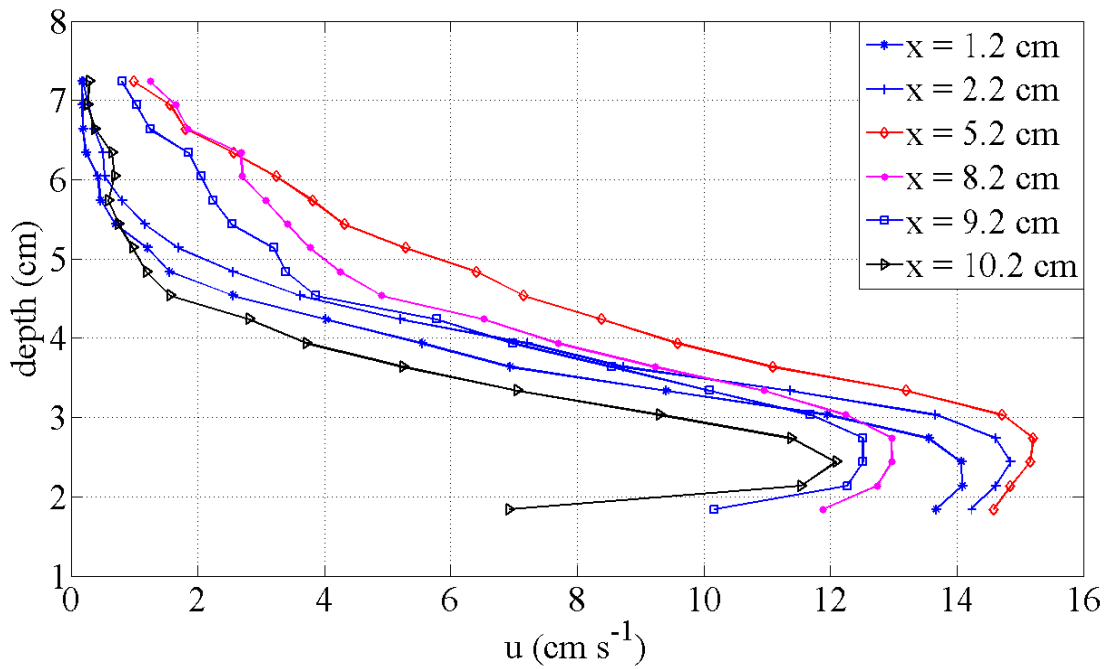


Fig. 29. Particle velocities in six positions of images. For positions, see Fig. 31.

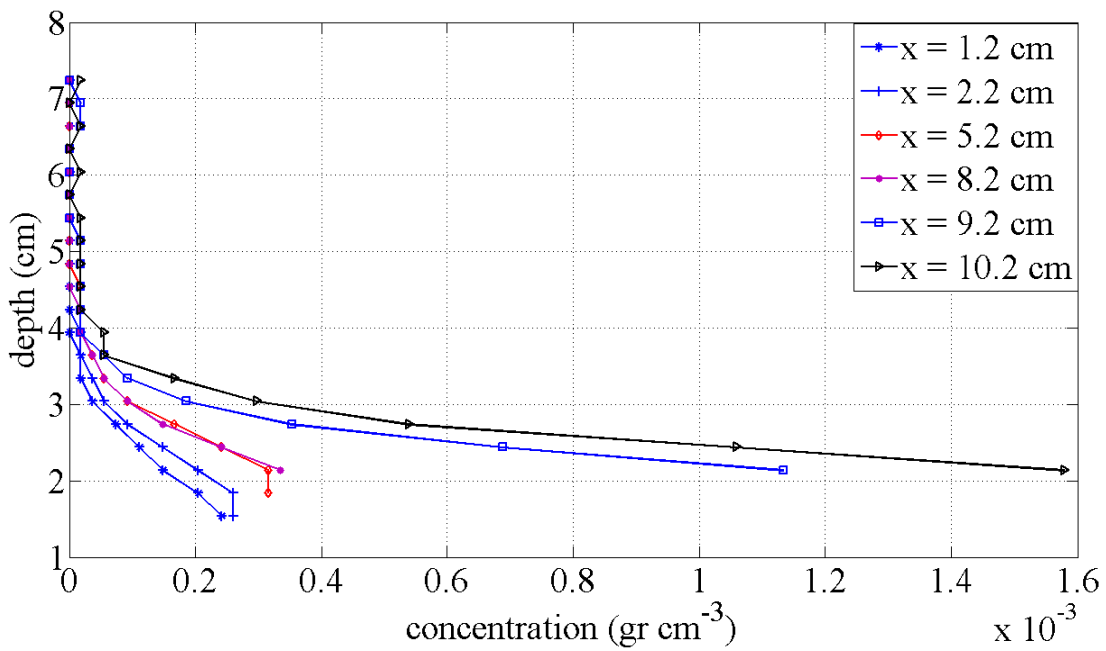


Fig. 30. Particle concentrations in the same position as Fig. 29. For positions, see Fig. 31.

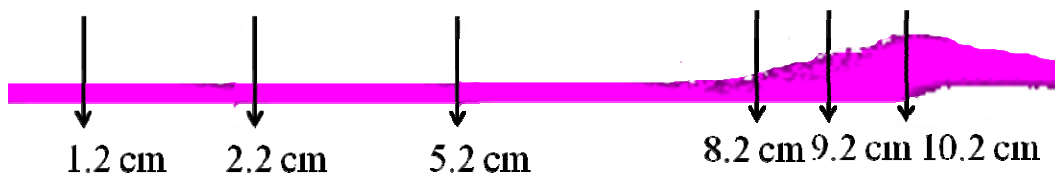


Fig. 31. Bed form formation during the early phase of the steady peak flow range indicating the positions shown in Figs. 29 and 30

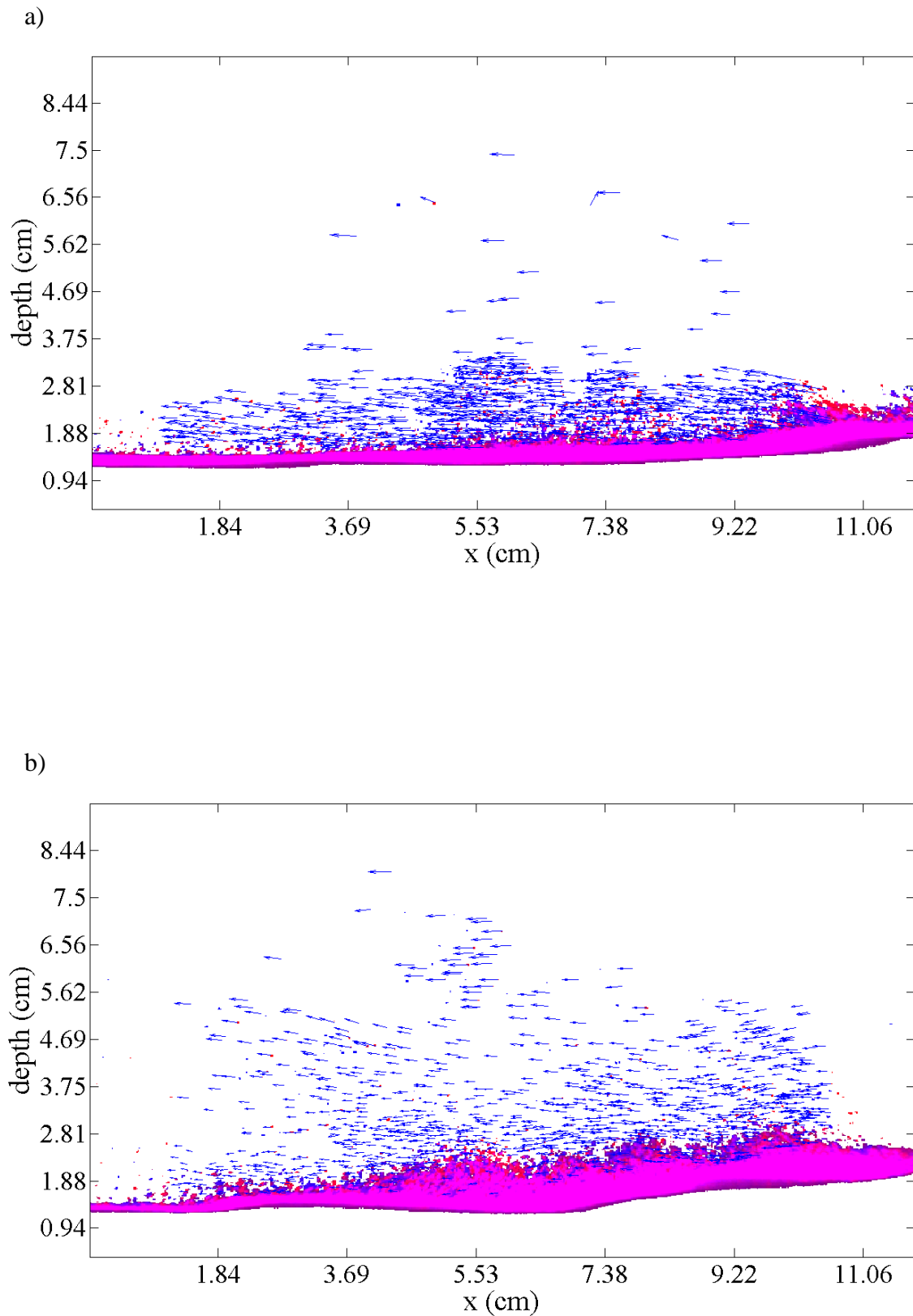


Fig. 32. PTV results during the (a) initial and (b) final phase of the accelerating range. Arrows indicate particle velocity vectors

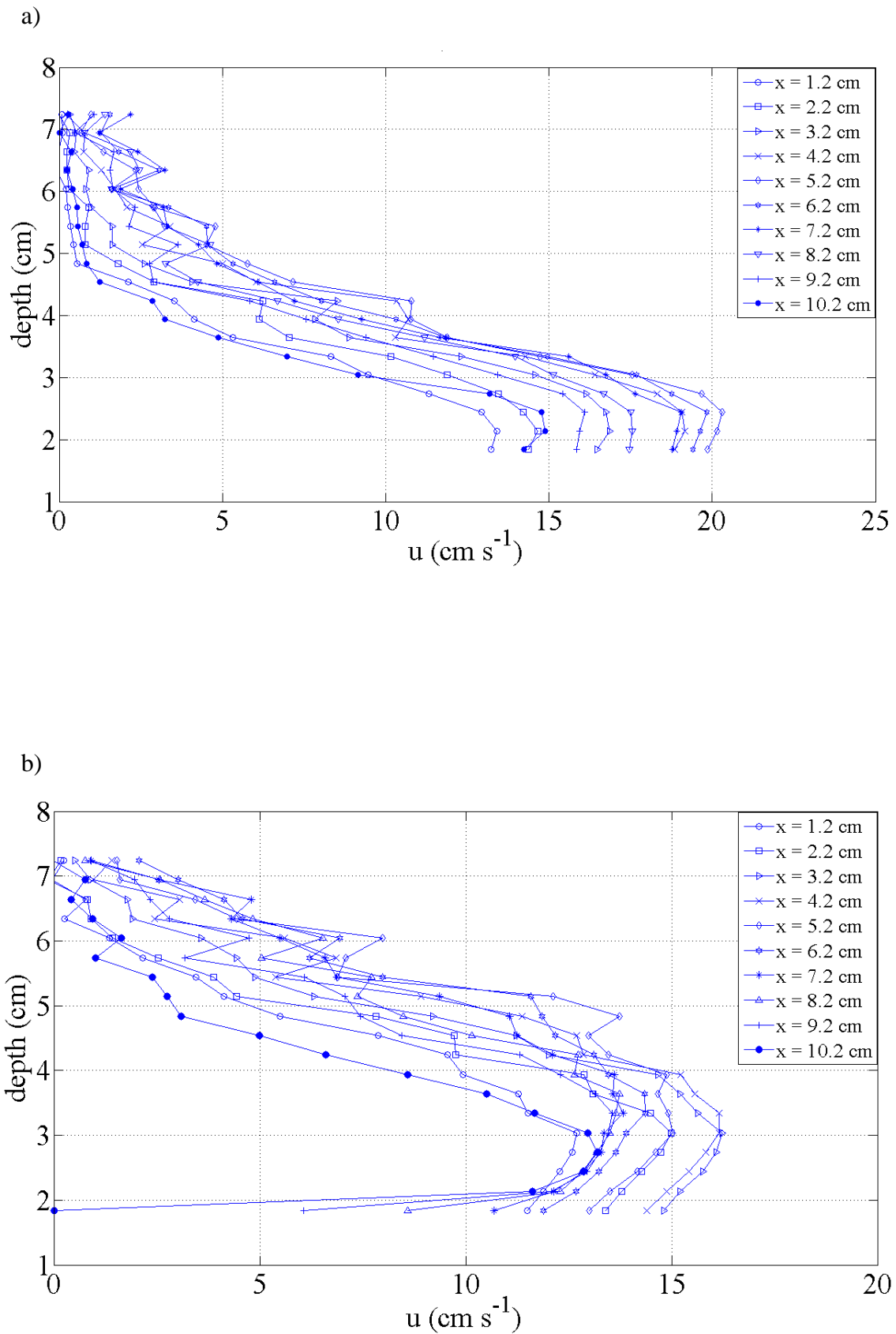


Fig. 33. Mean particle velocities in ten image slices for the (a) initial and (b) final phases of the accelerating range

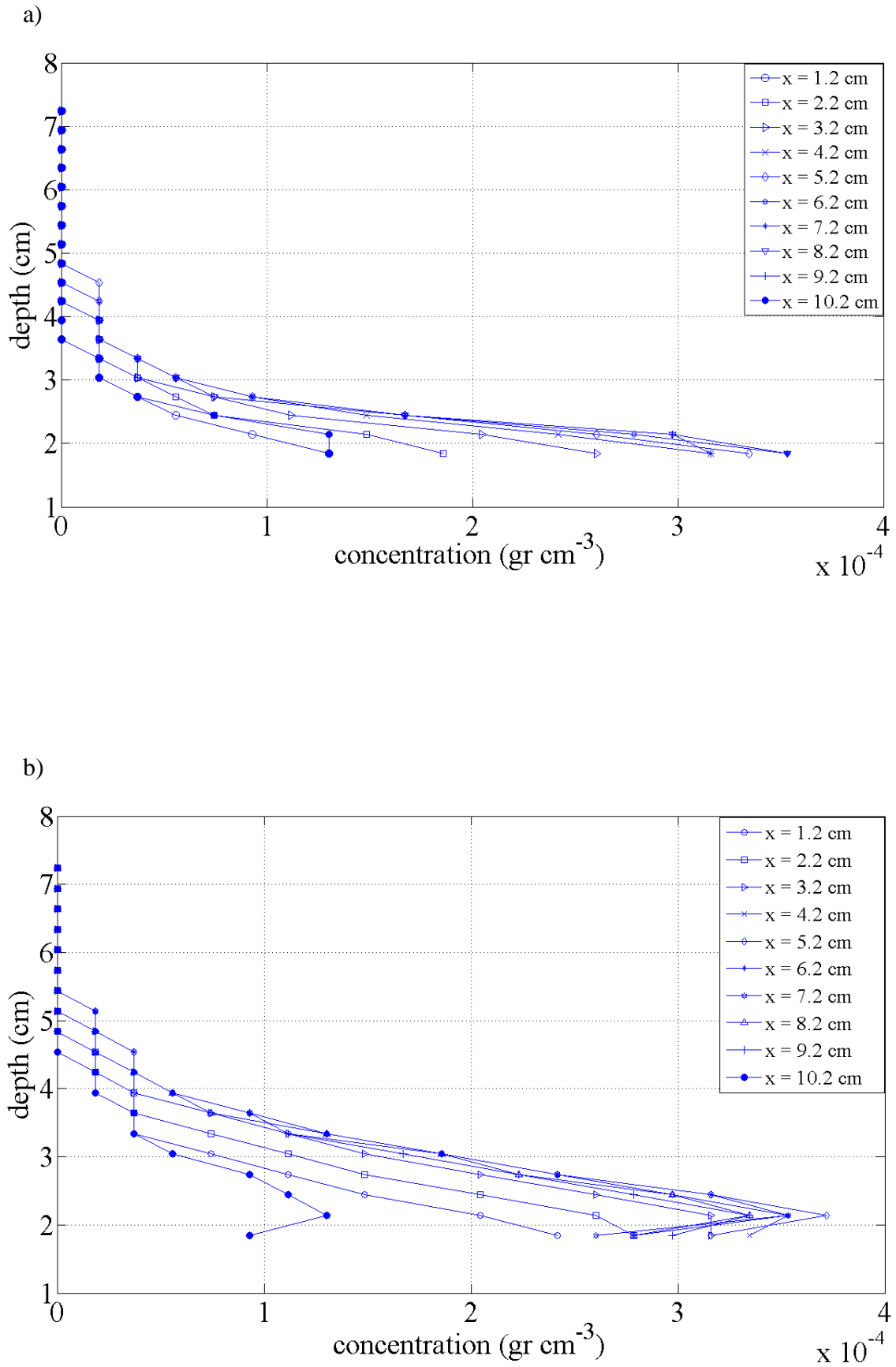


Fig. 34. Particle concentrations in the same image slices as in Fig. 33

Figures 35 and 36 show the particle numbers and concentration during the 31.24 s recording of the final phase of the accelerating range of the 60 s hydrograph respectively. Each image was again sliced into 3 mm high vertical layers. Averages were then made over 1 s periods (= 80 frames). For Fig. 35, averages were then taken over all vertical layers, whereas in Fig. 36, a sequence of profiles of the time slices is presented. In Fig. 35, a strong and rapid variability in the particle number is observed, resulting in a sequence of spikes. This pattern can be interpreted as a documentation of coherent structures with high particle numbers passing with periods of background turbulence with low particle numbers in between.

In Fig. 36, the sequence of profiles shows that most of the particles are concentrated in the near bed layer, confirming PTV and ADVP results discussed above. The distribution is dominated by many individual peaks, supporting the concept of particle suspension in coherent structures, as discussed above. Furthermore, concentration strongly increases with time, extending progressively into higher layers above the bed during this final phase of the acceleration range. This agrees with the results of other PTV recordings shown in Fig. 33, as well as to those obtained with the ADVP, as discussed above.

A sequence of the total velocity vectors, combining the horizontal, u , and the vertical, w , velocity vectors for the range 70 to 101.24 s is presented in Fig. 37. In each of these images, averages of the vector field were taken over one second periods. This corresponds to averages over 80 frames and is the same averaging as applied in Fig. 35. In the near bottom boundary layer, velocity vectors are often upwards oriented which can explain the suspension of fine sediment during this period. During the final phase of the unsteady flow, suspension events are more frequent. It is evident that sediment suspension occurs in individual events. In steady flow (Cellino and Lemmin 2004), it was demonstrated that these event structures are linked to coherent flow structures. A similar correlation can be expected in this case. Video images indicate that suspension sets in later in the unsteady flow than indicated by the Shields diagram and the velocity approach.

In the time interval from 80 s to 85 s in Figs. 35 and 36, in the range where video images indicate suspension by coherent structures, ejection events are seen in the images (Fig. 37 a6) and b6) to a8) and b8)).

These images show the passage of one coherent structure reaching up into the water column to about $0.4 h$, which is then followed by a second one, as seen in Figs. 37 a8) and 37 b8). In Fig. 37, suspension into the water column above occurs in burst-like events. In this flow, turbulence intensity and the strength of the burst events are not sufficient to suspend these particles over the full water depth. Particle transport remained strong in the near bottom layer, in agreement with the ADVP observations shown in Fig. 22.

During this time of the hydrograph, ripples formed rapidly on the bed. The ripples influenced sediment suspension dynamics (Fig. 37). These bedforms grew within a few seconds to a length of about 0.6 water depth and a height of about 5 to 10 mm. Sediment particles rolled up the ramp of the ripple and were ejected into the water column by vortex shedding from the ripple crest. They then propagated in the flow in the form of a burst, as seen in Fig. 37. Ripples remained in place when the flow was decelerated down to base flow. Thus, ripples control sediment suspension into the water column over an extended period of the hydrograph. This is evident from Fig. 23, where backscattering intensity increases towards the end, even though the flow is decelerating.

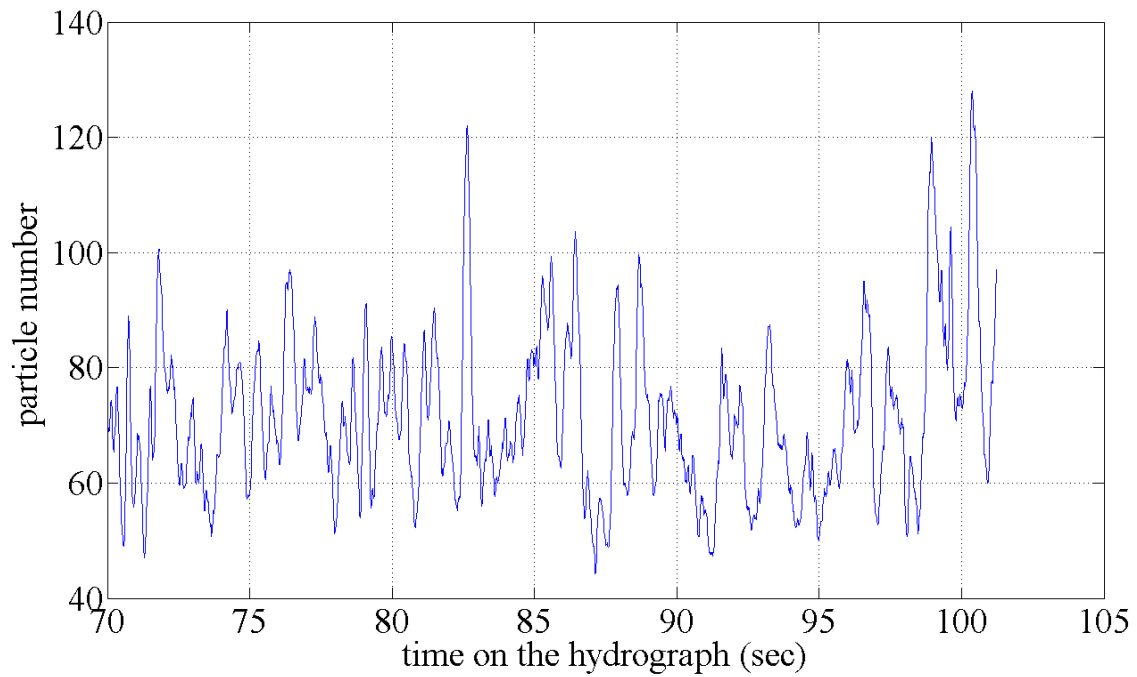


Fig. 35 Particle number for all images from the middle to the end of the accelerating range of the hydrograph (70 s to 101.24 s) for accelerating and decelerating time 60 s

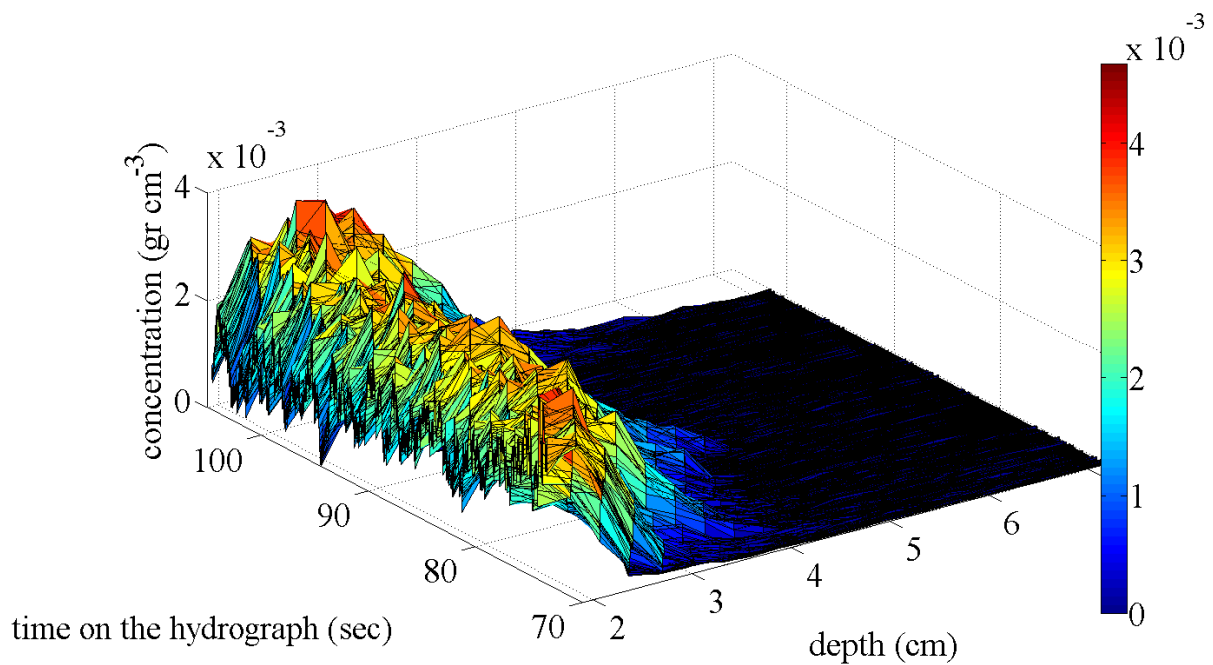
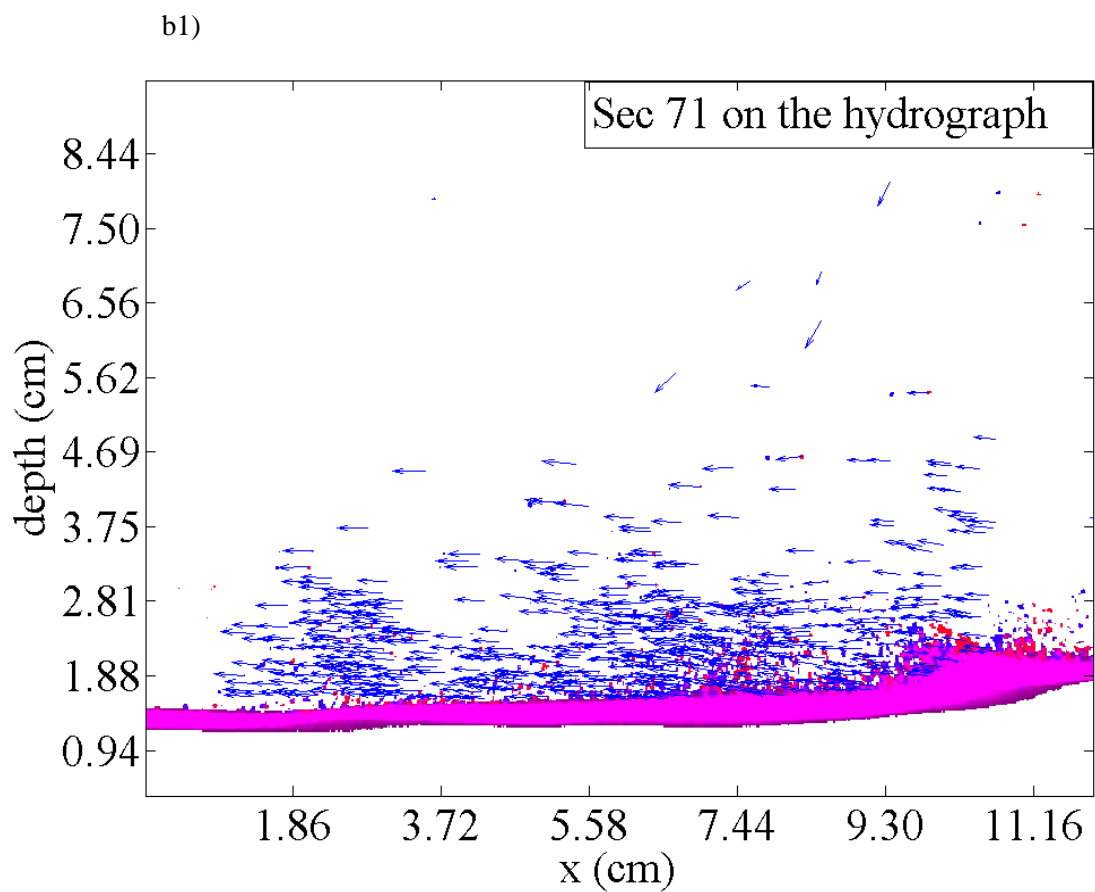
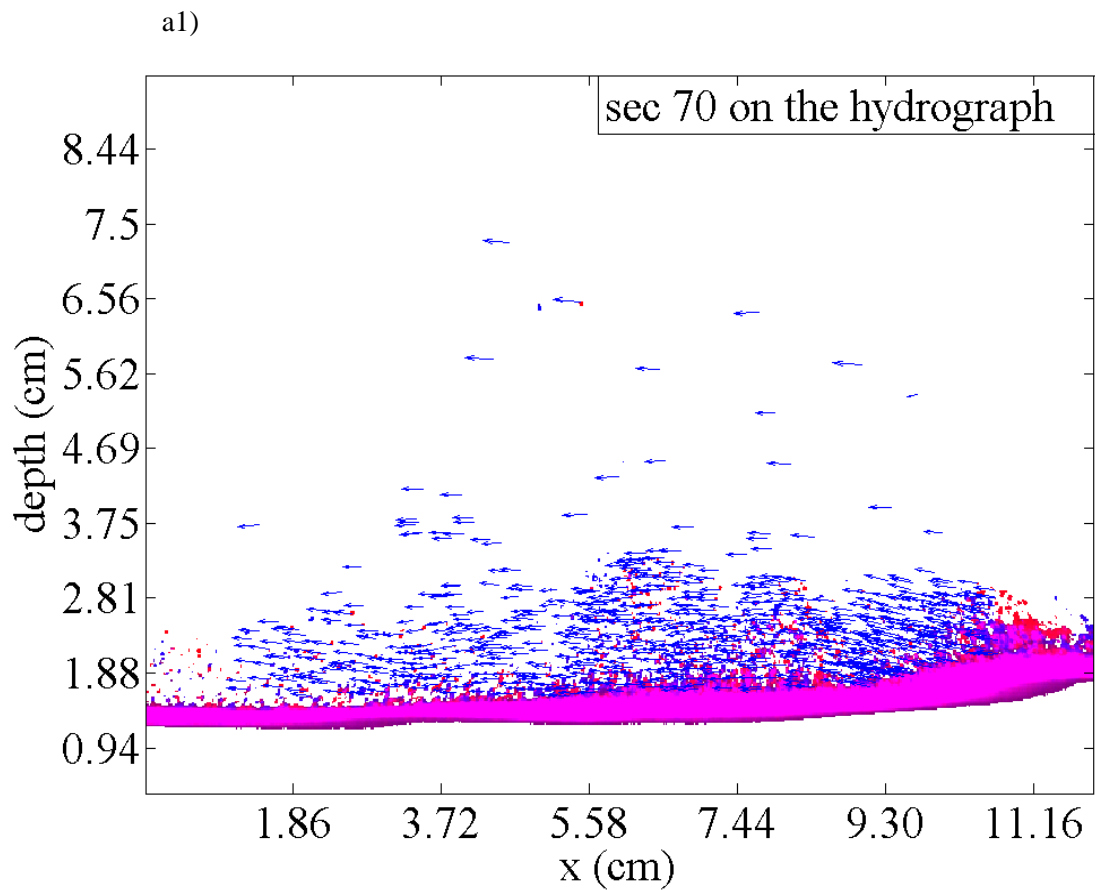
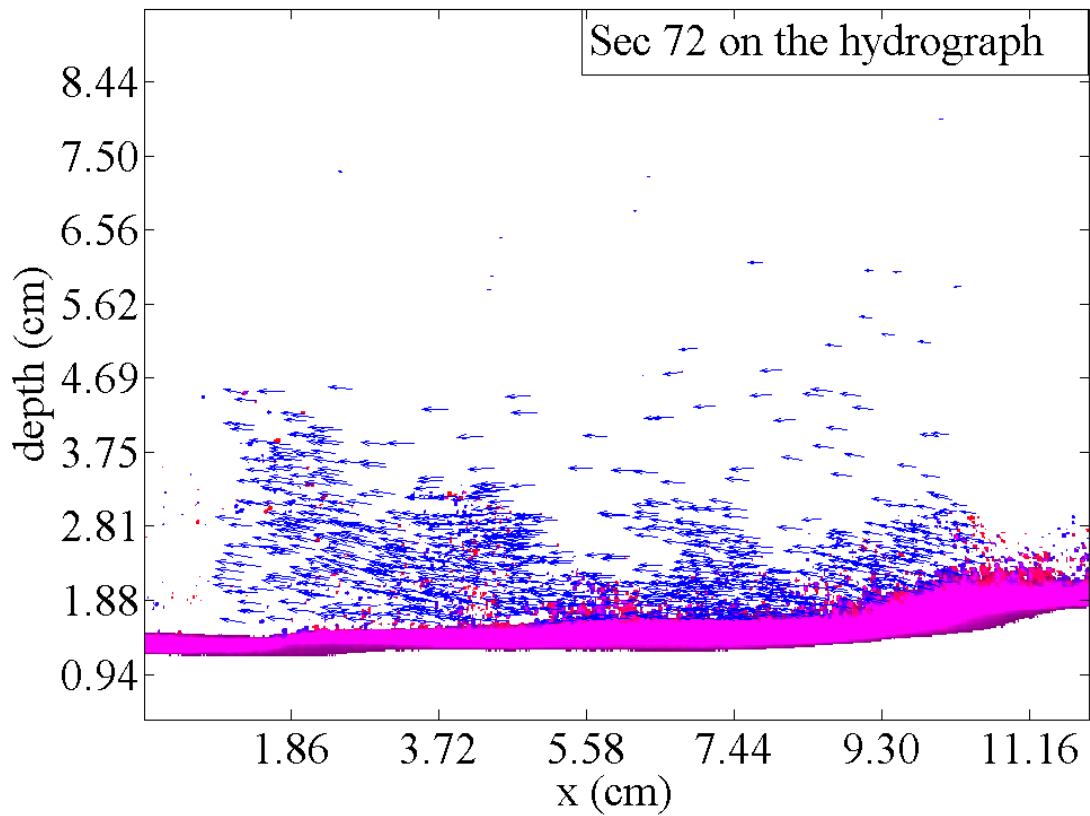


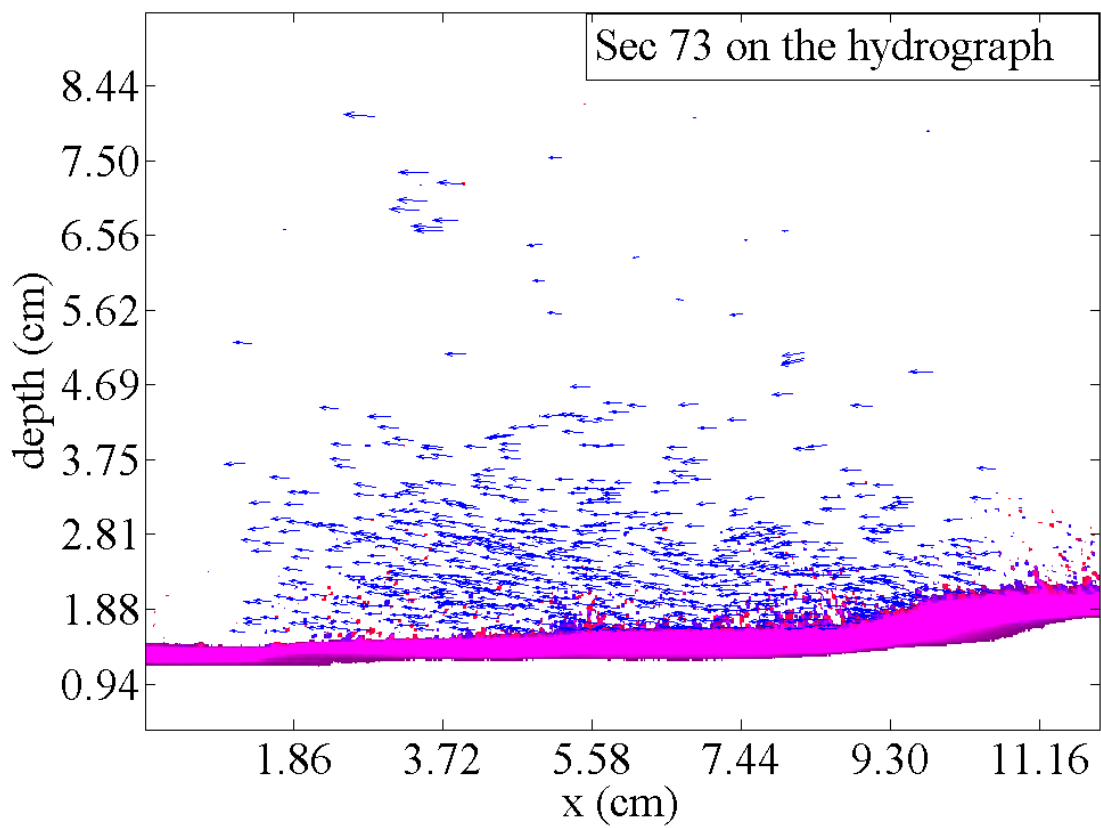
Fig. 36 Concentration from the middle to the end of the accelerating range of the hydrograph (70 s to 101.24 s) for accelerating and decelerating time 60 s



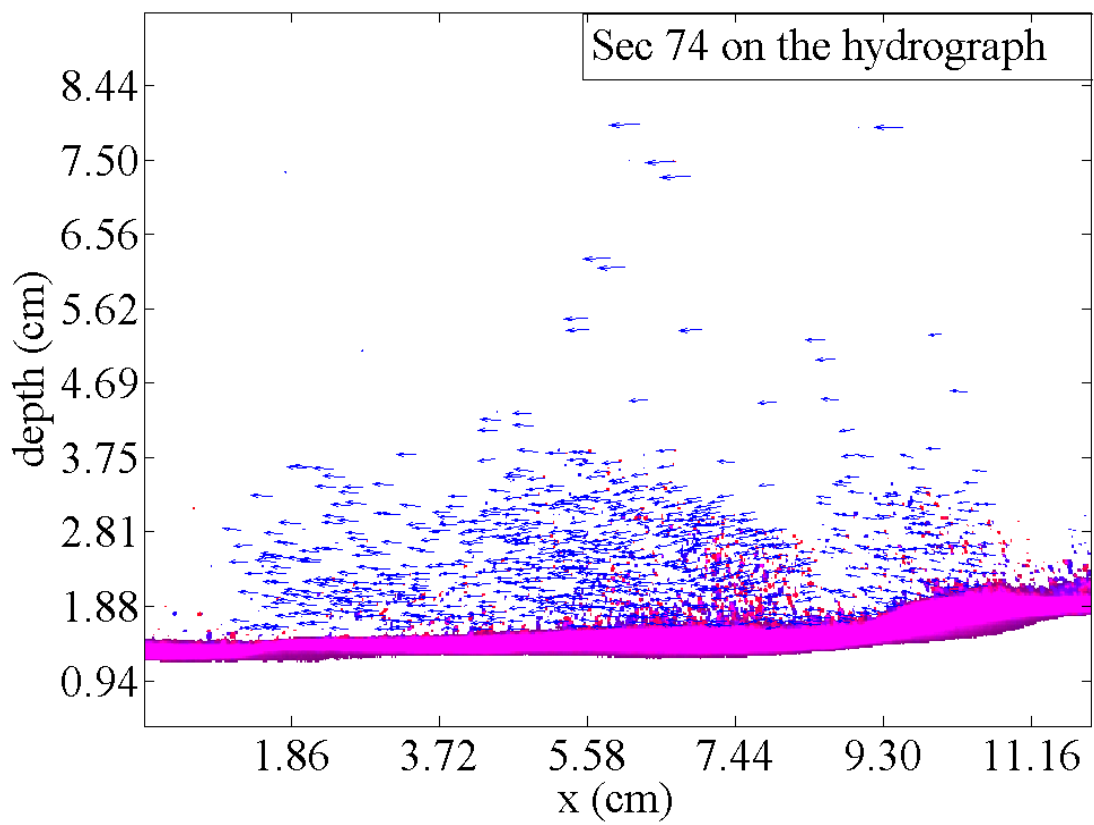
a2)



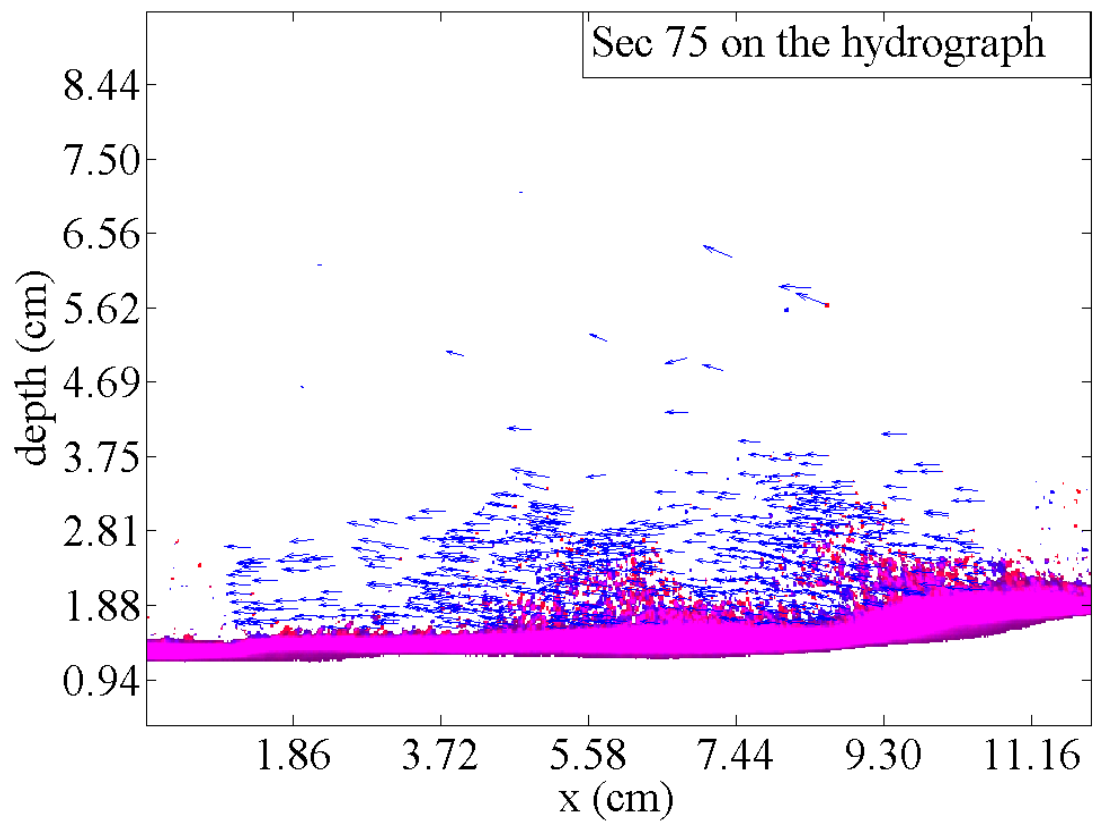
b2)

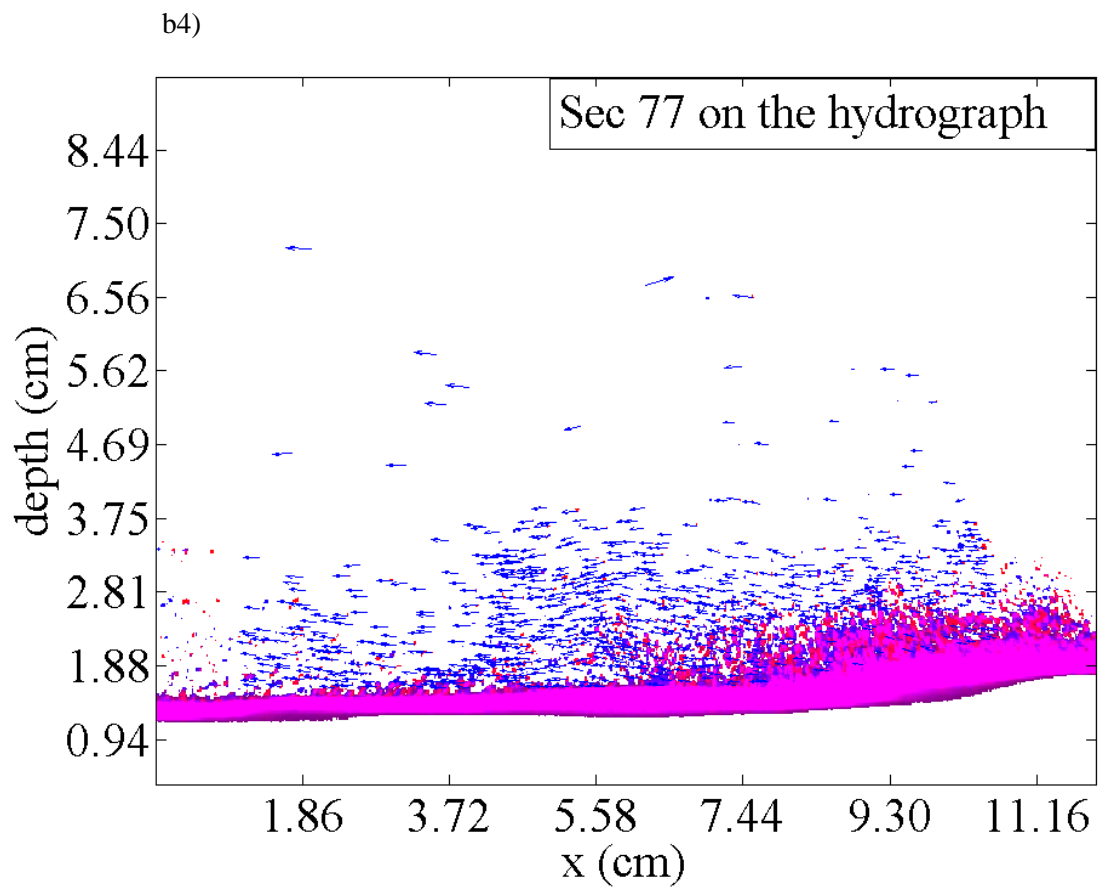
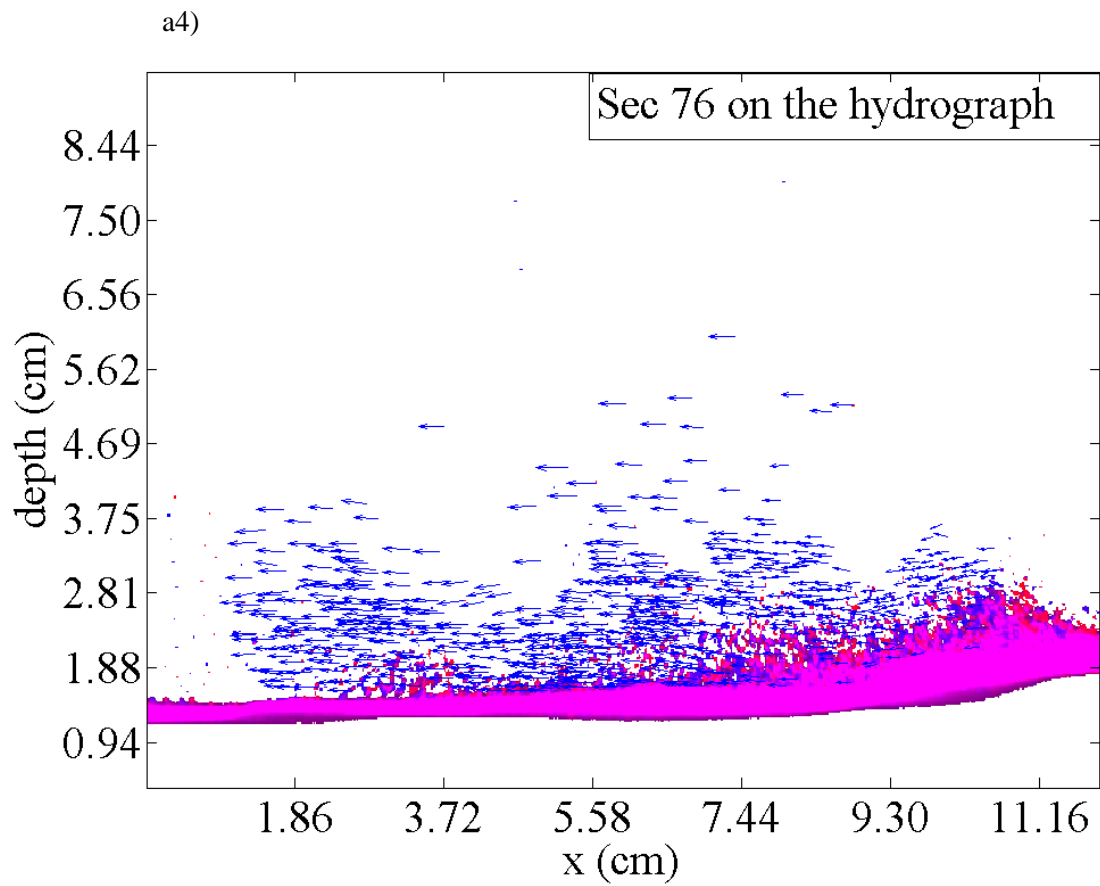


a3)

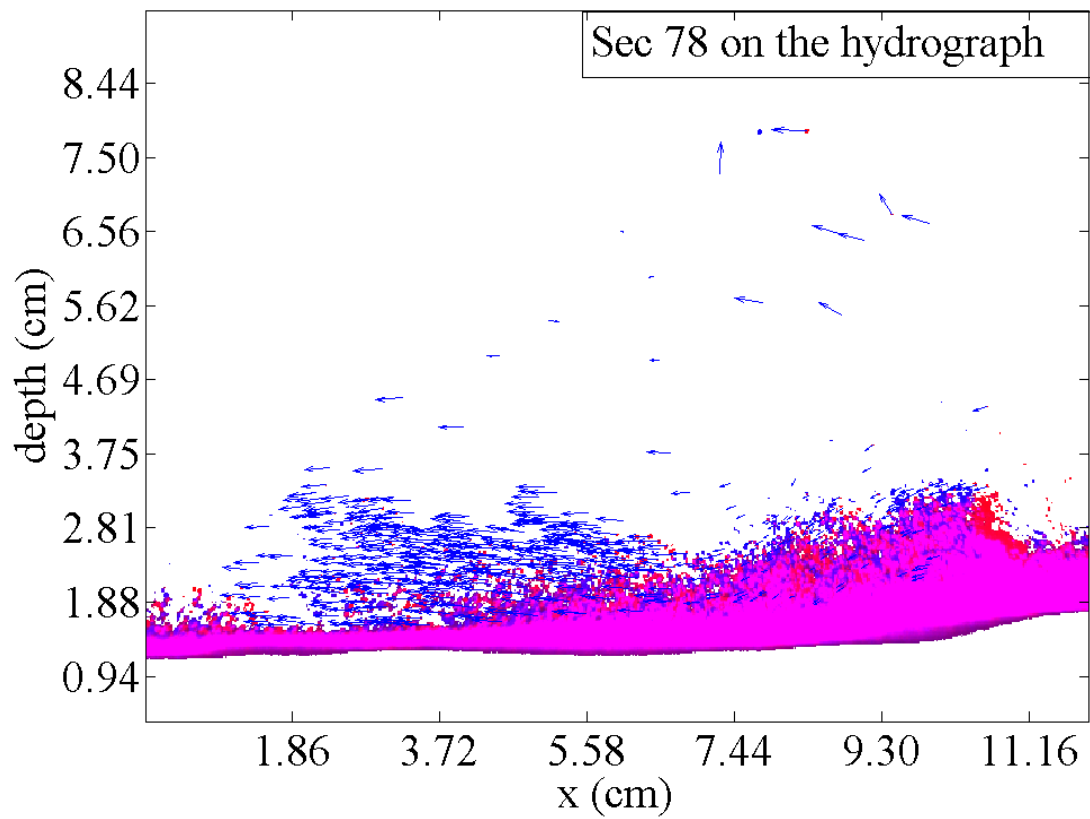


b3)

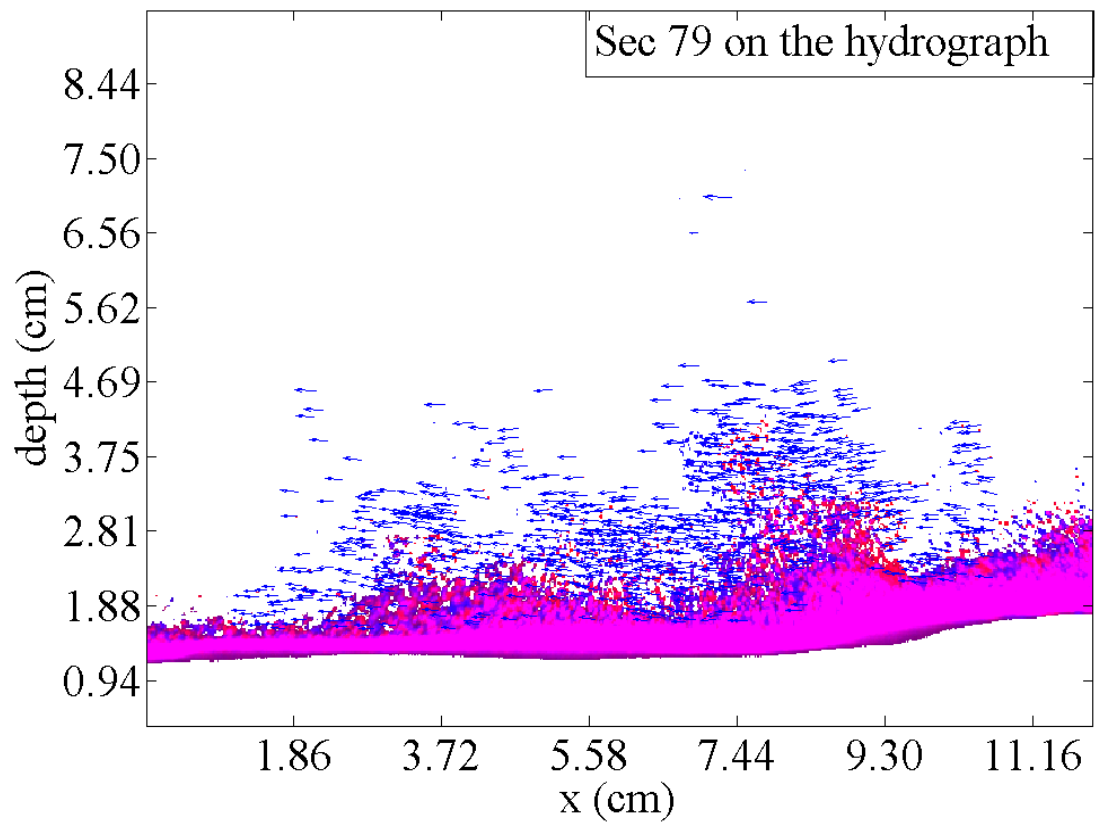




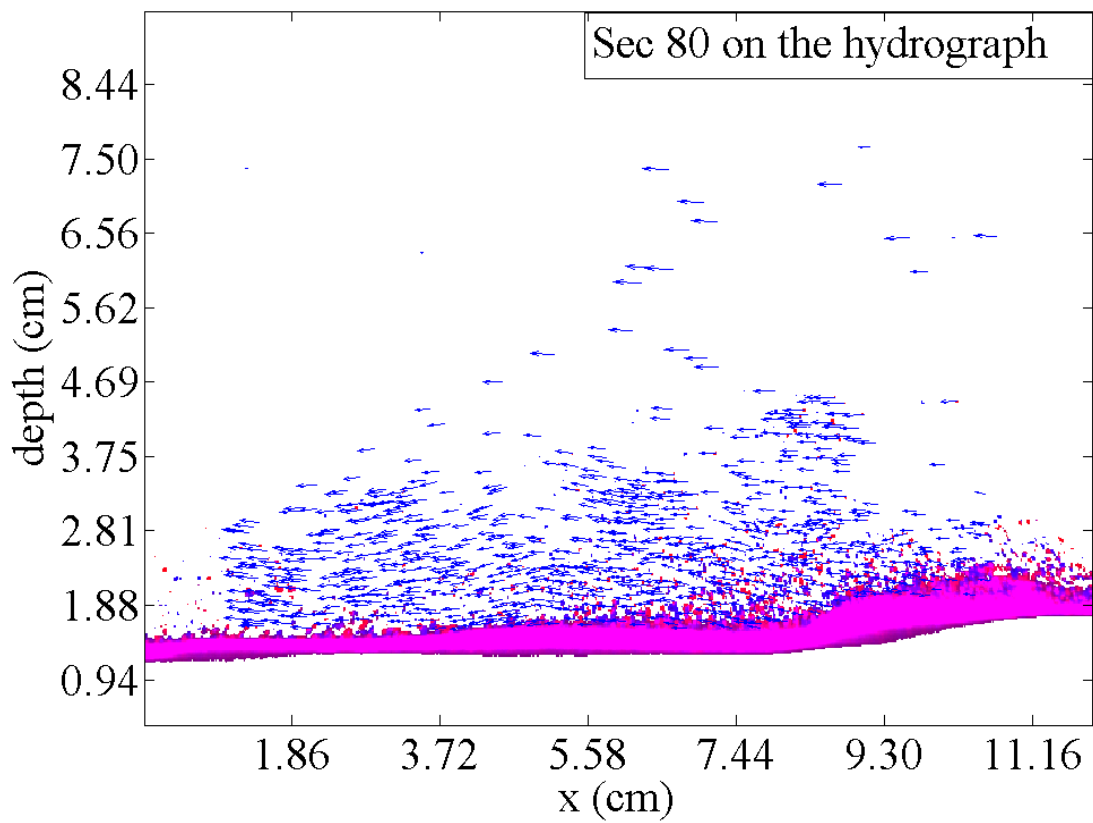
a5)



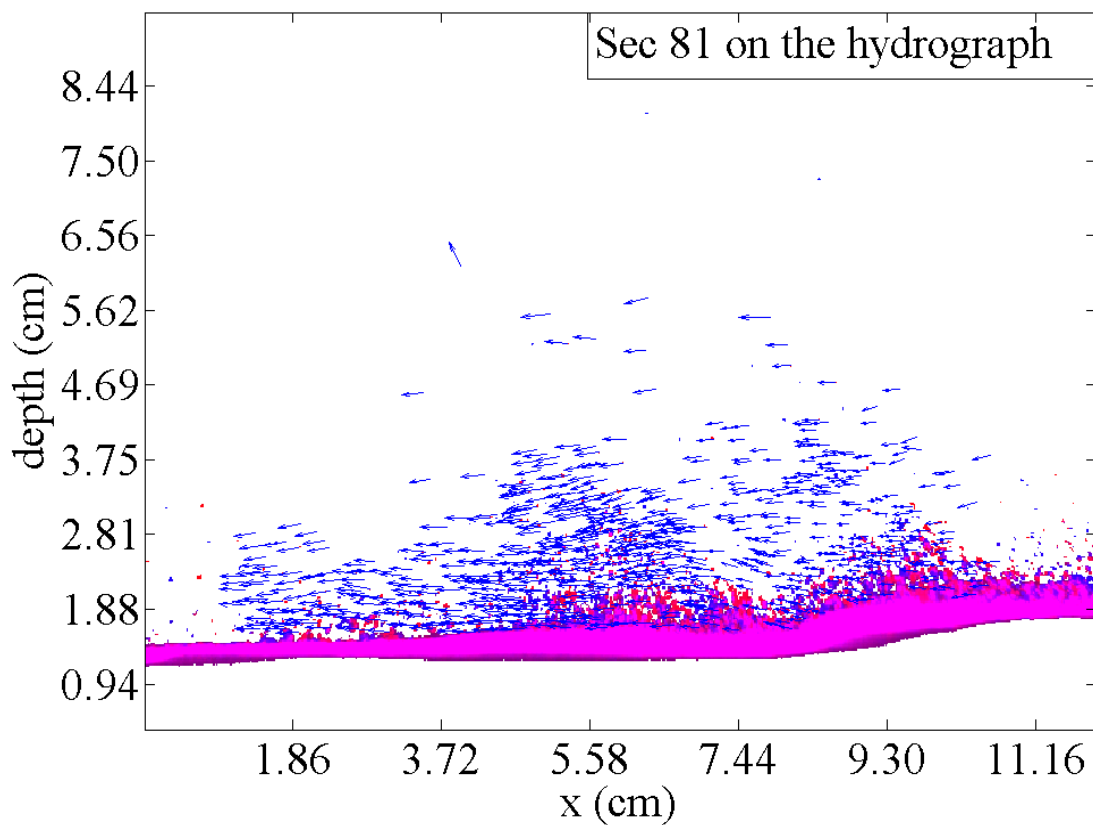
b5)



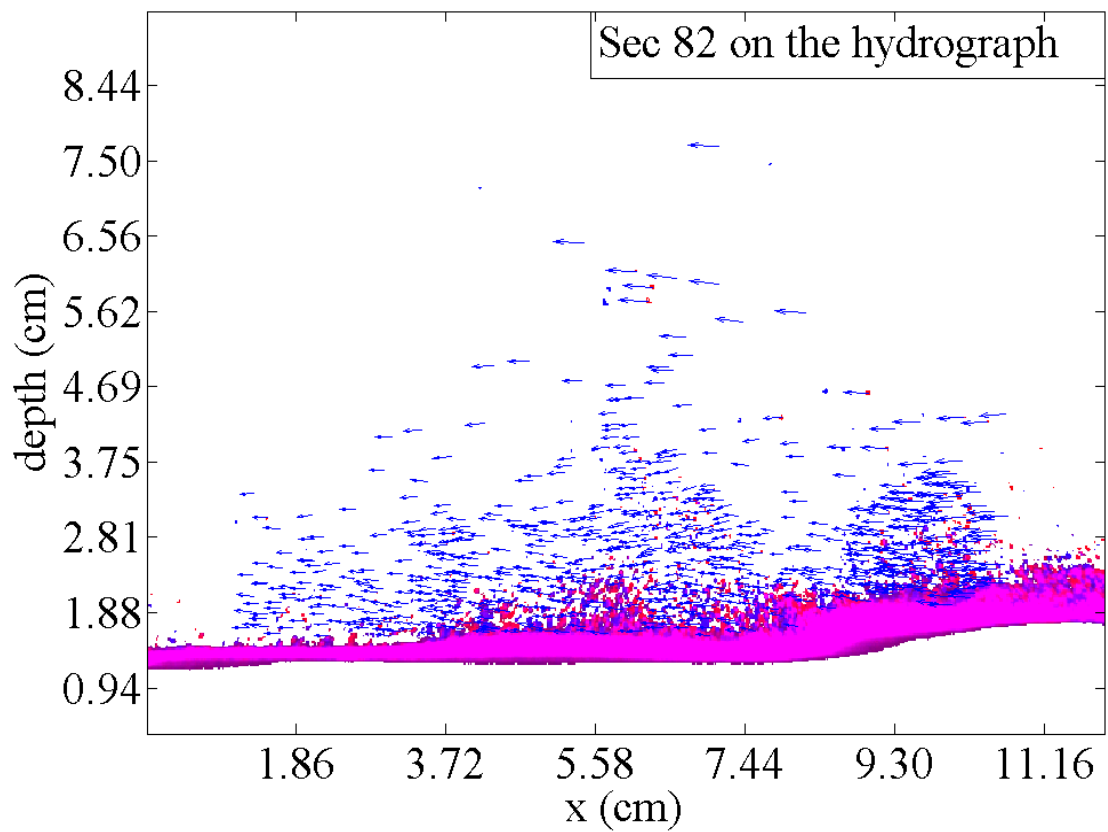
a6)



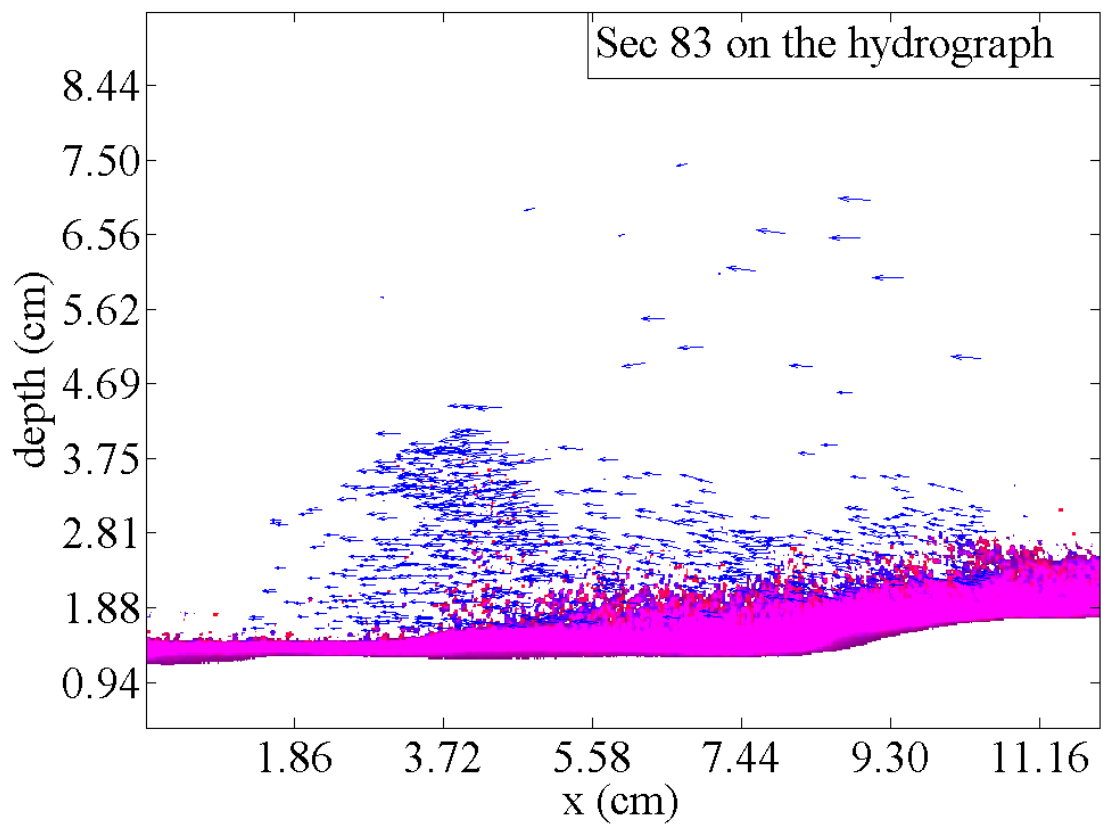
b6)



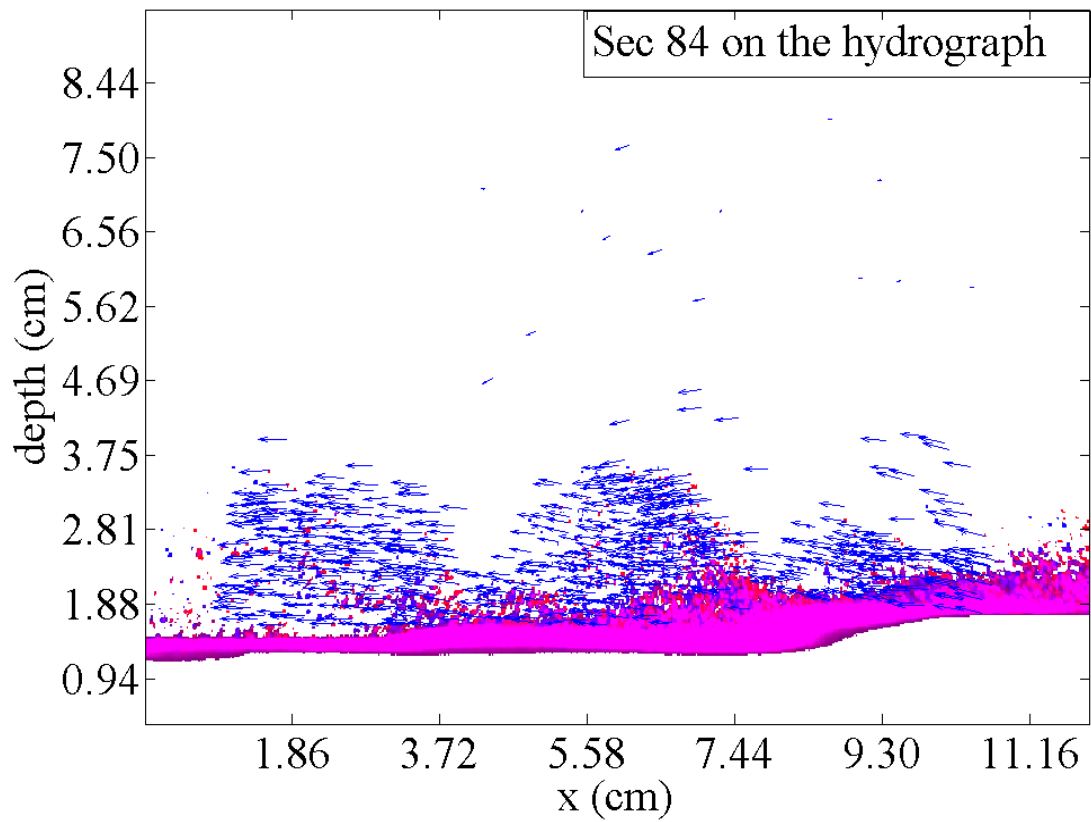
a7)



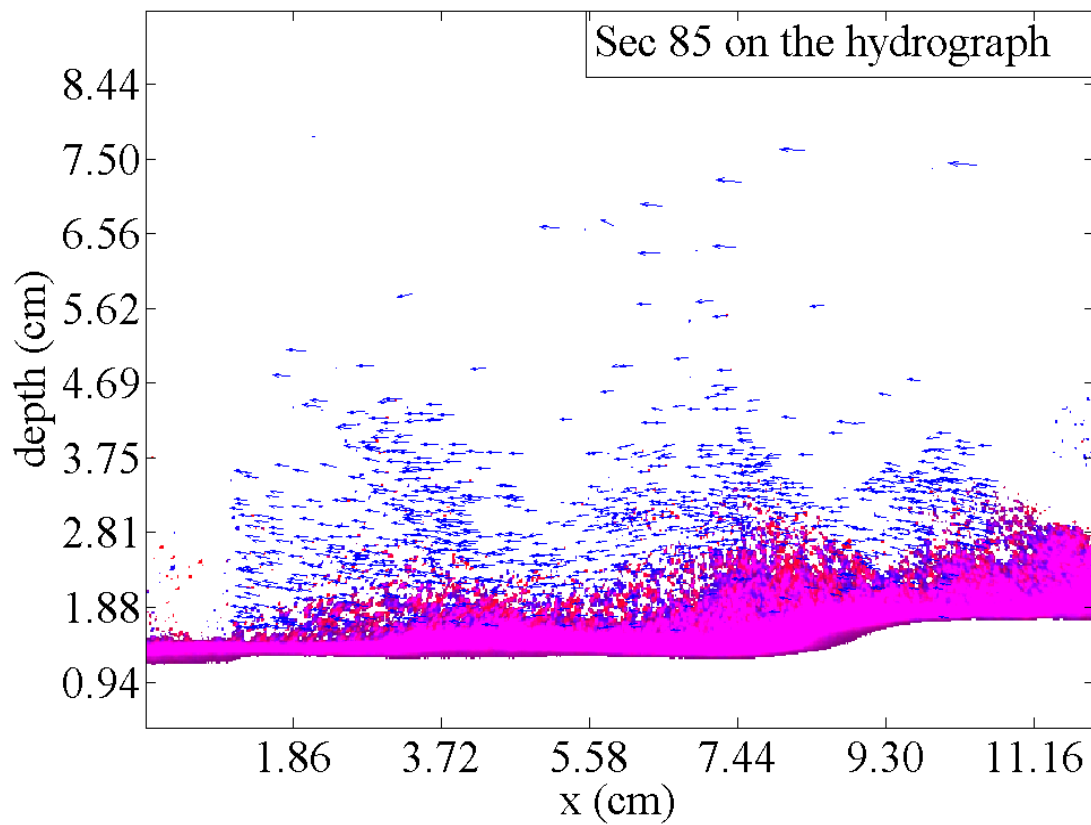
b7)



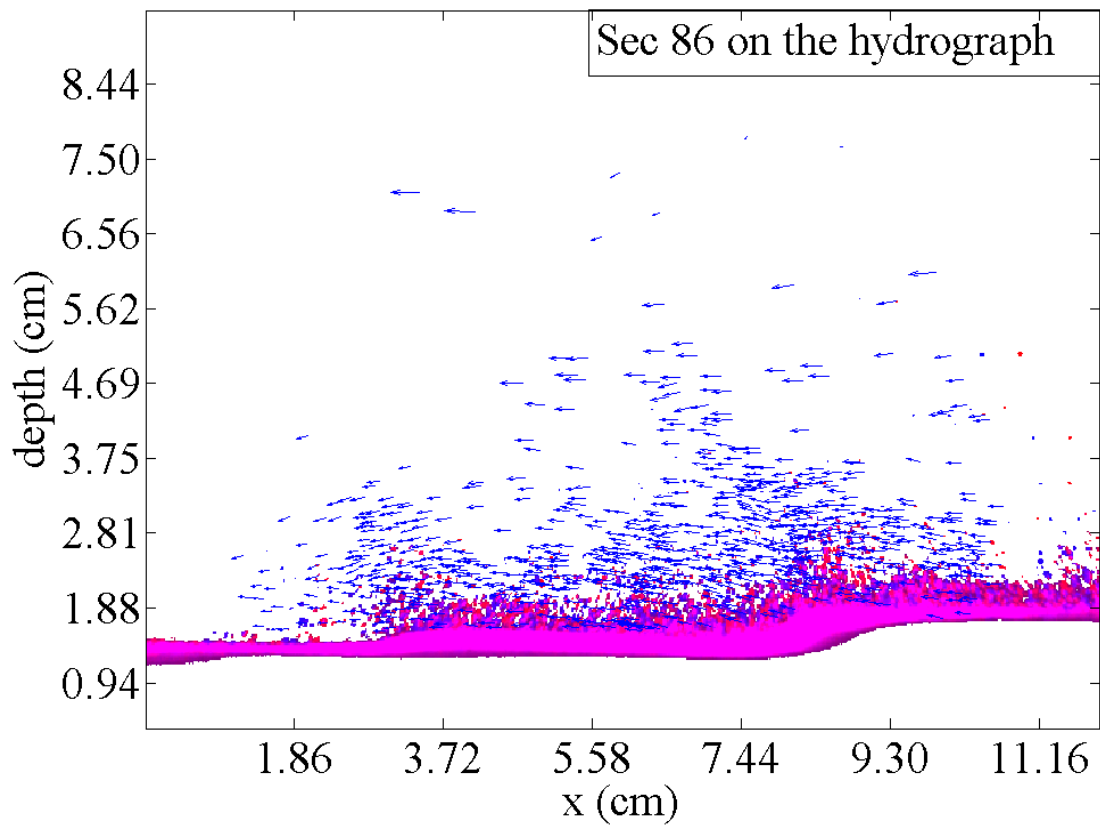
a8)



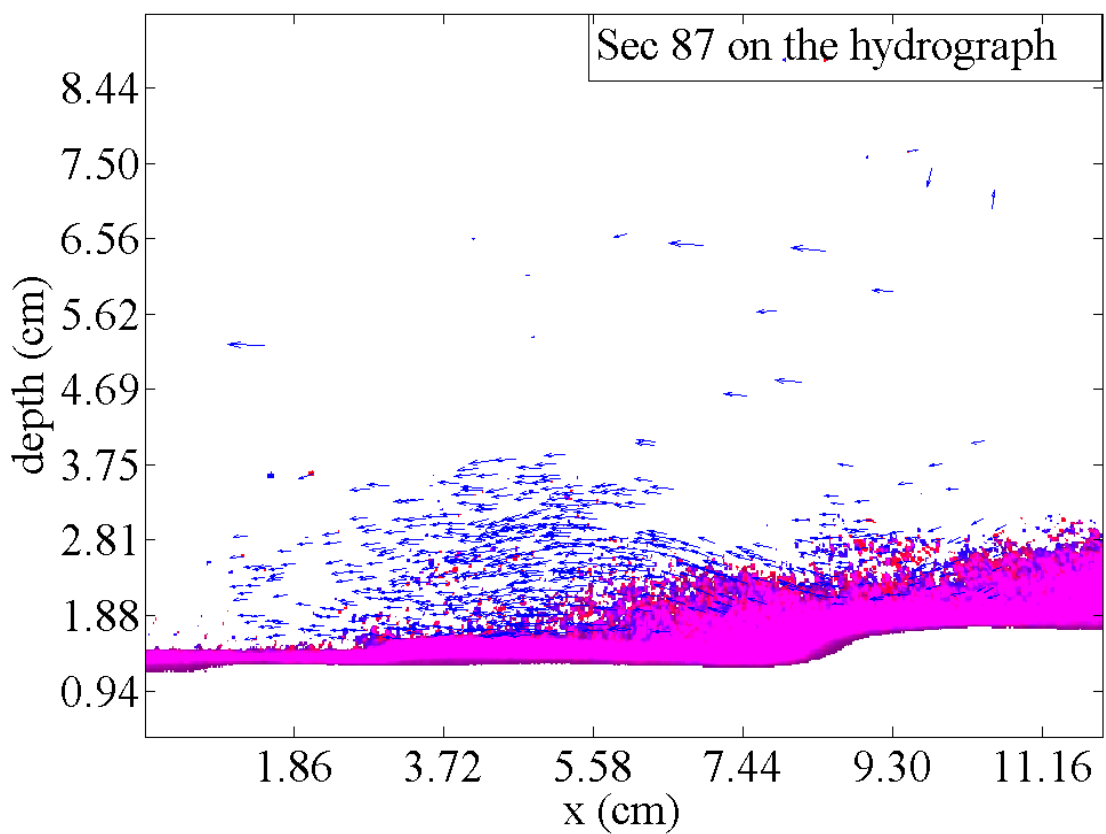
b8)



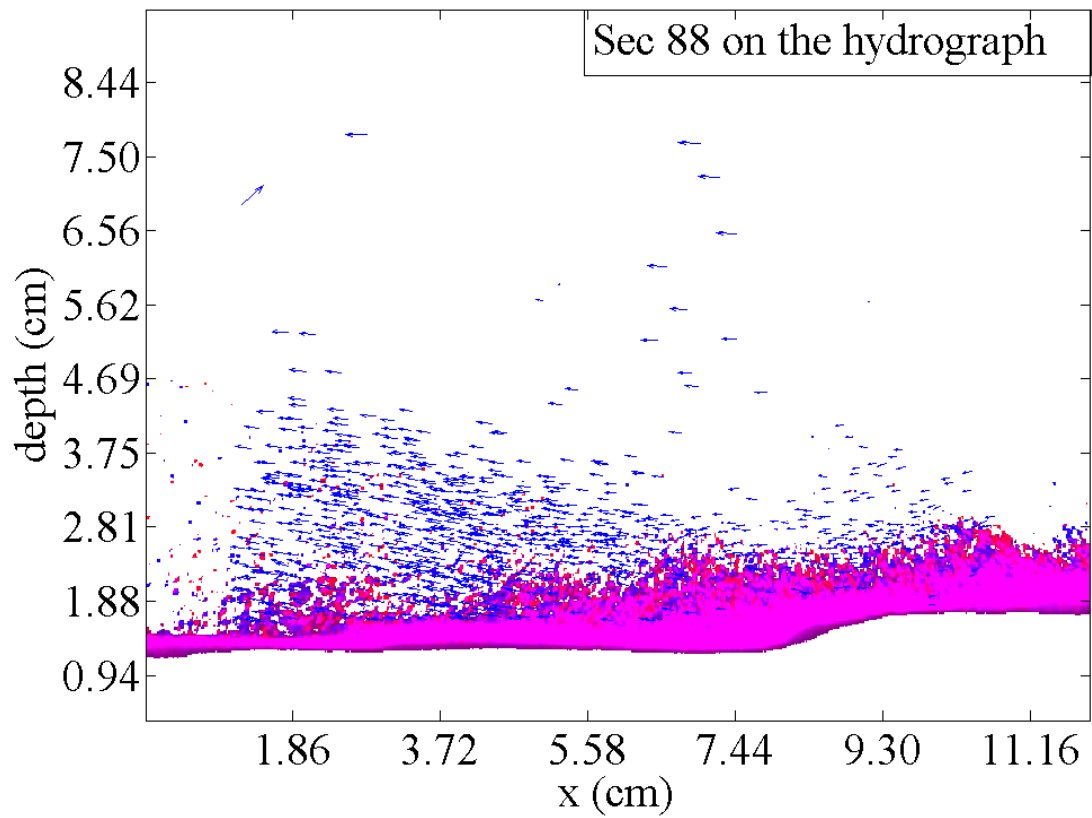
a9)



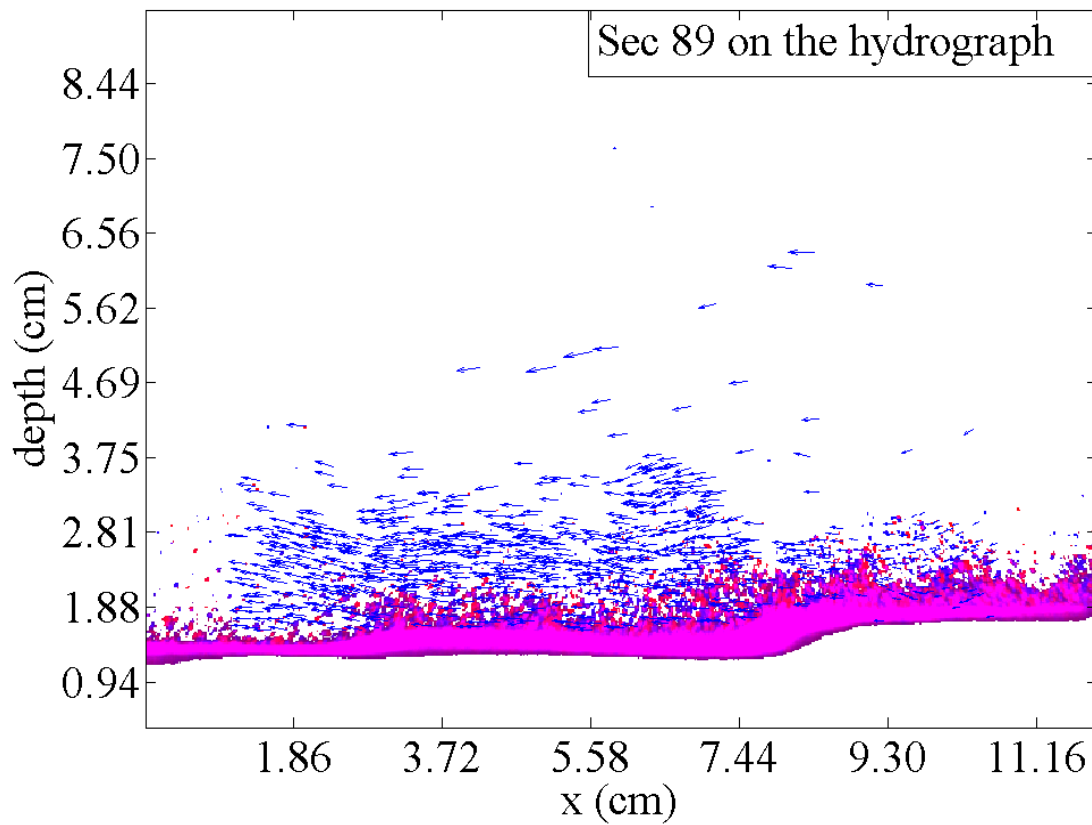
b9)



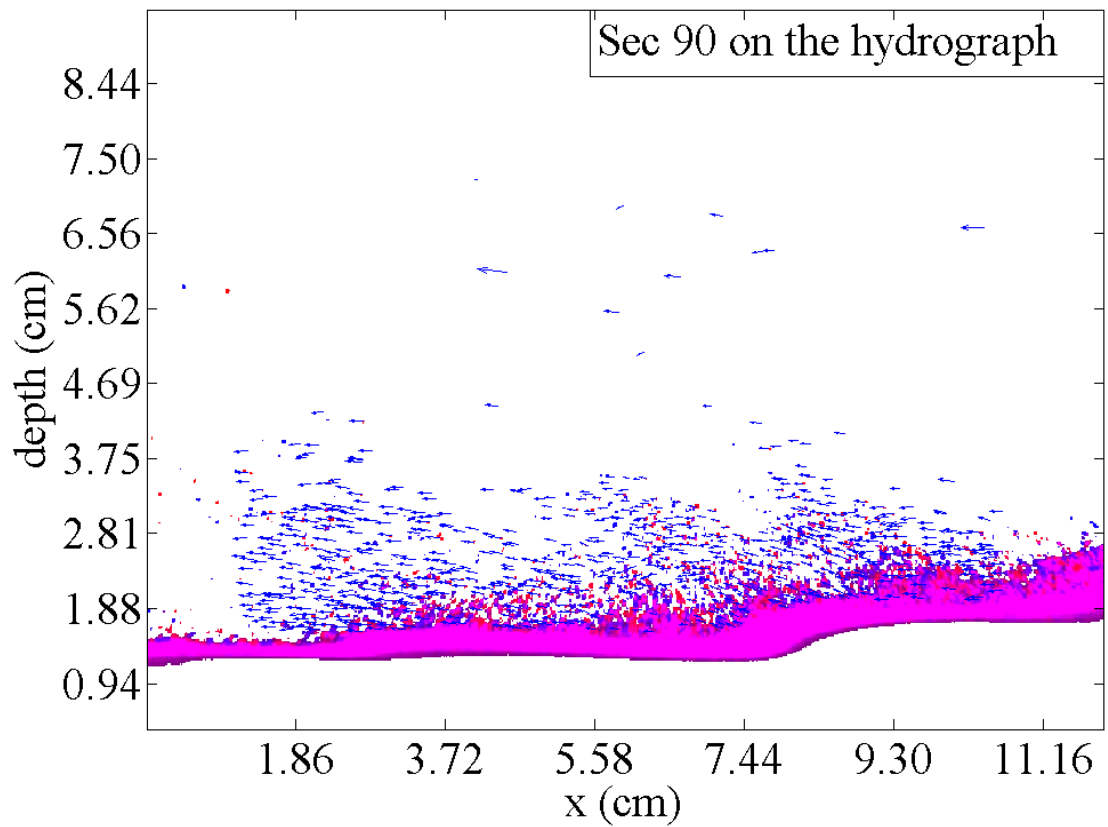
a10)



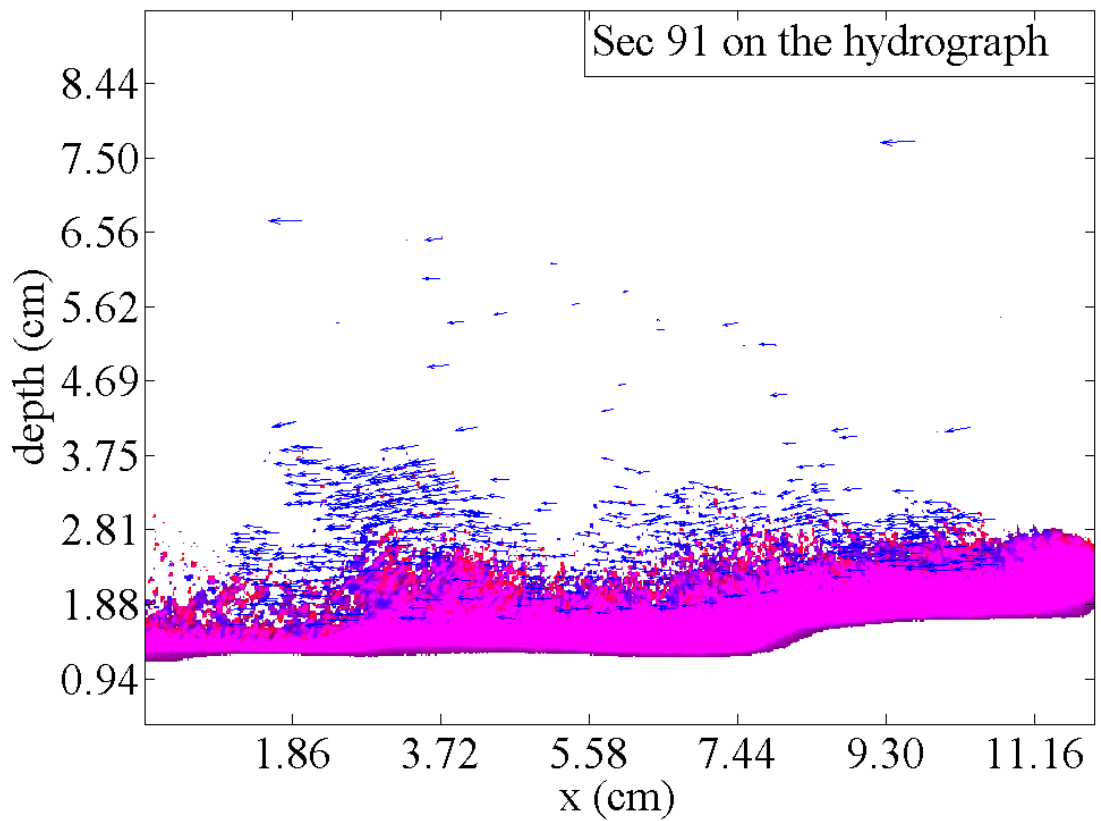
b10)



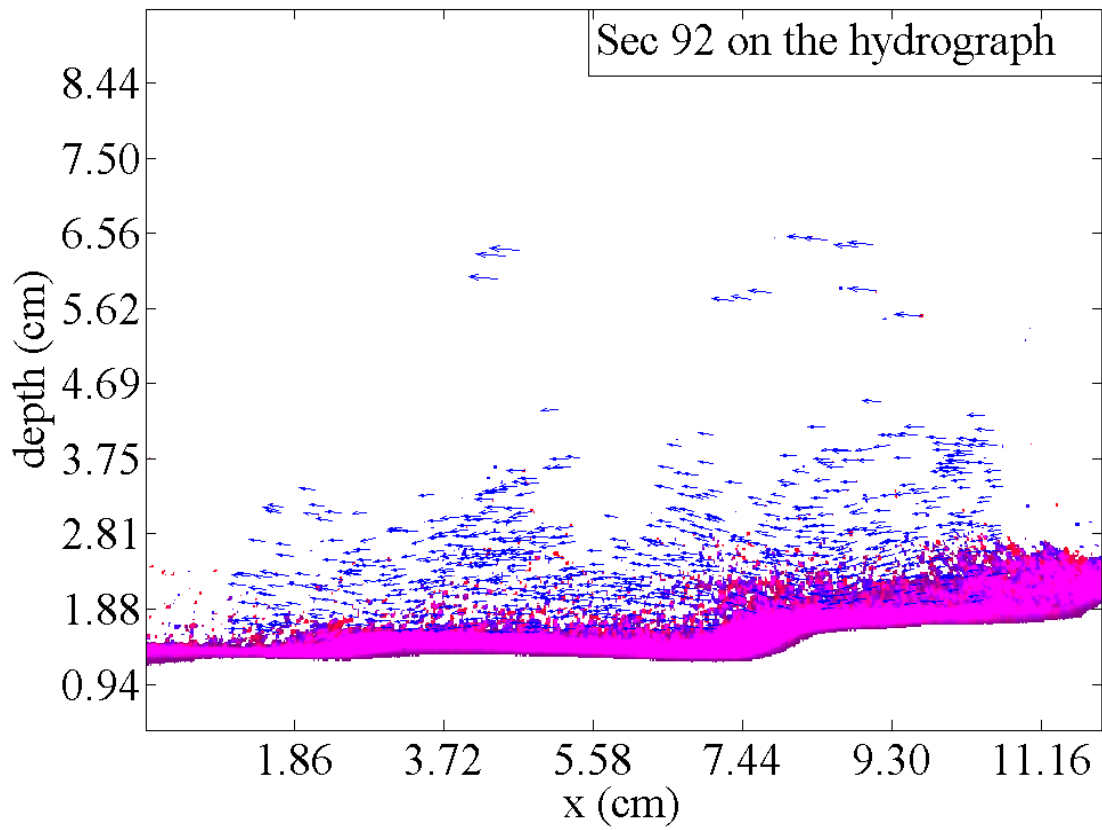
a11)



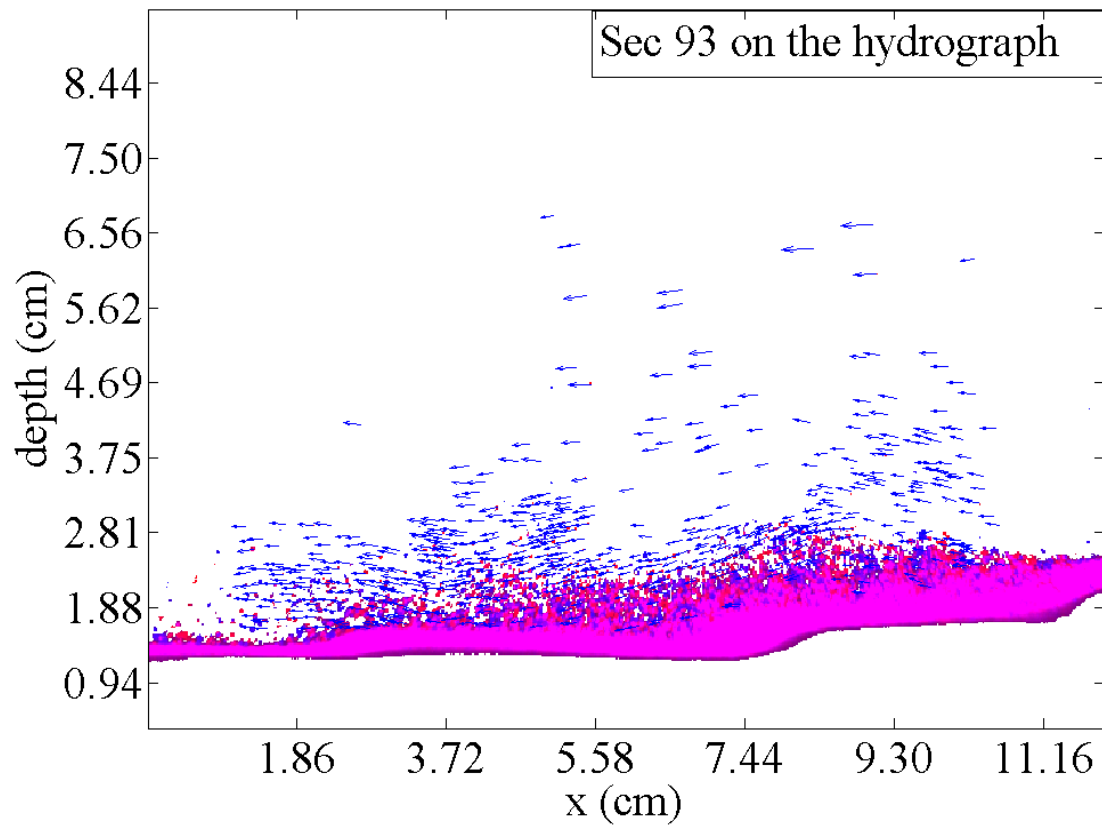
b11)



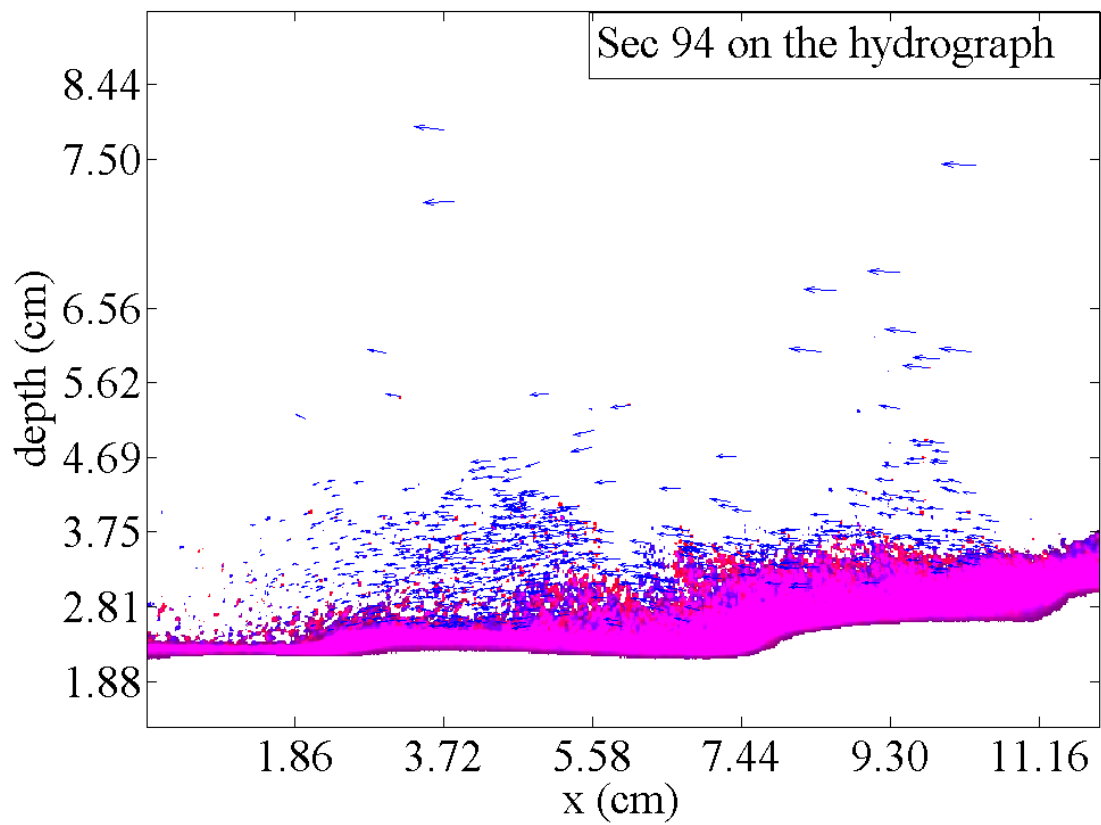
a12)



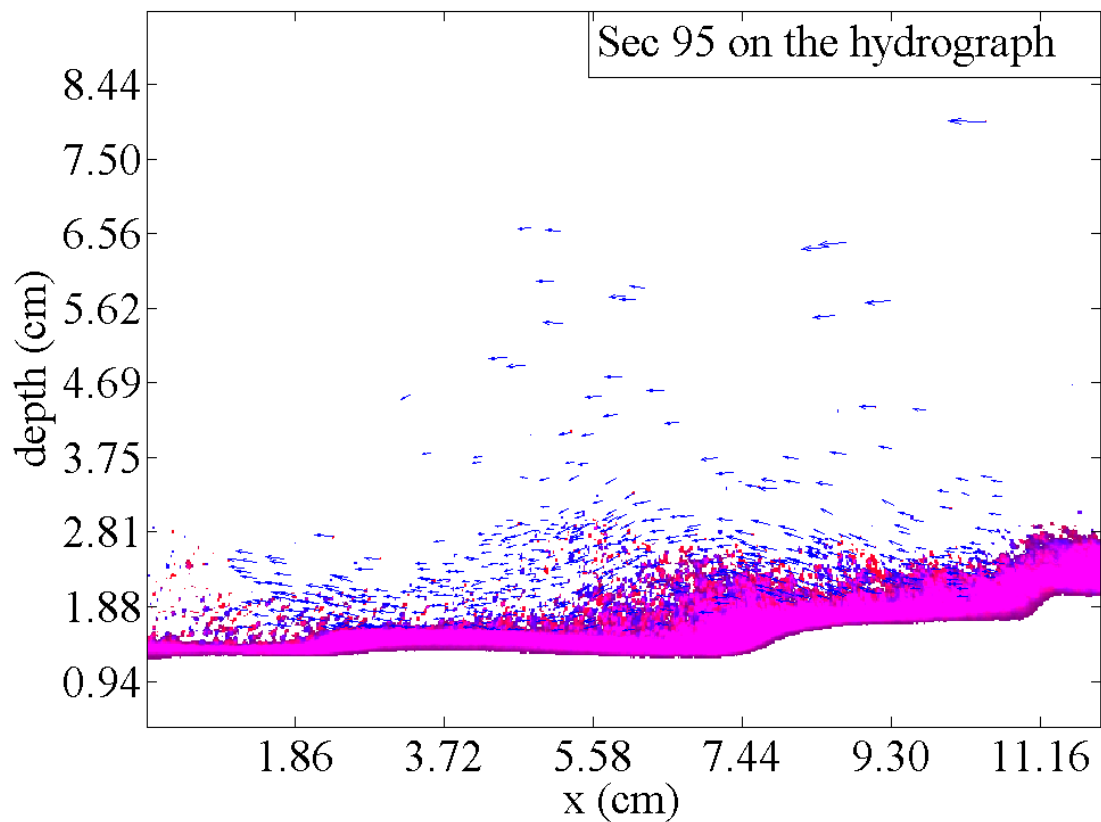
b12)



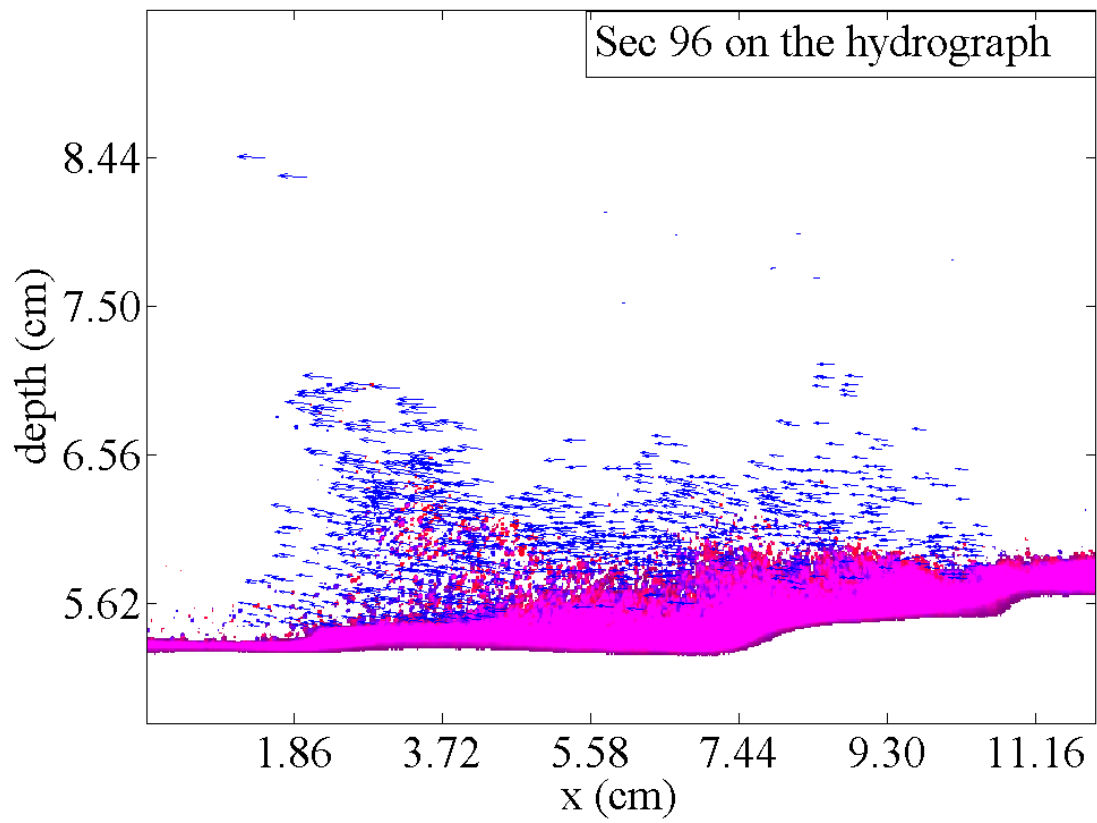
a13)



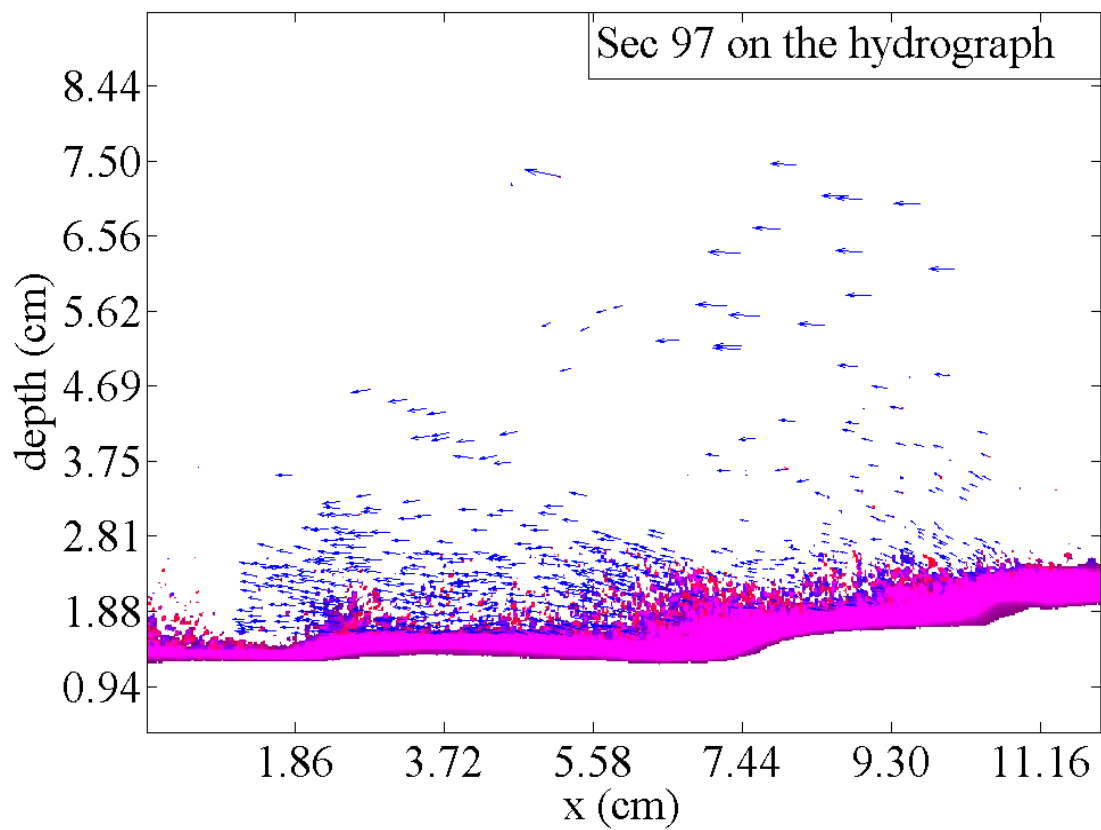
b13)



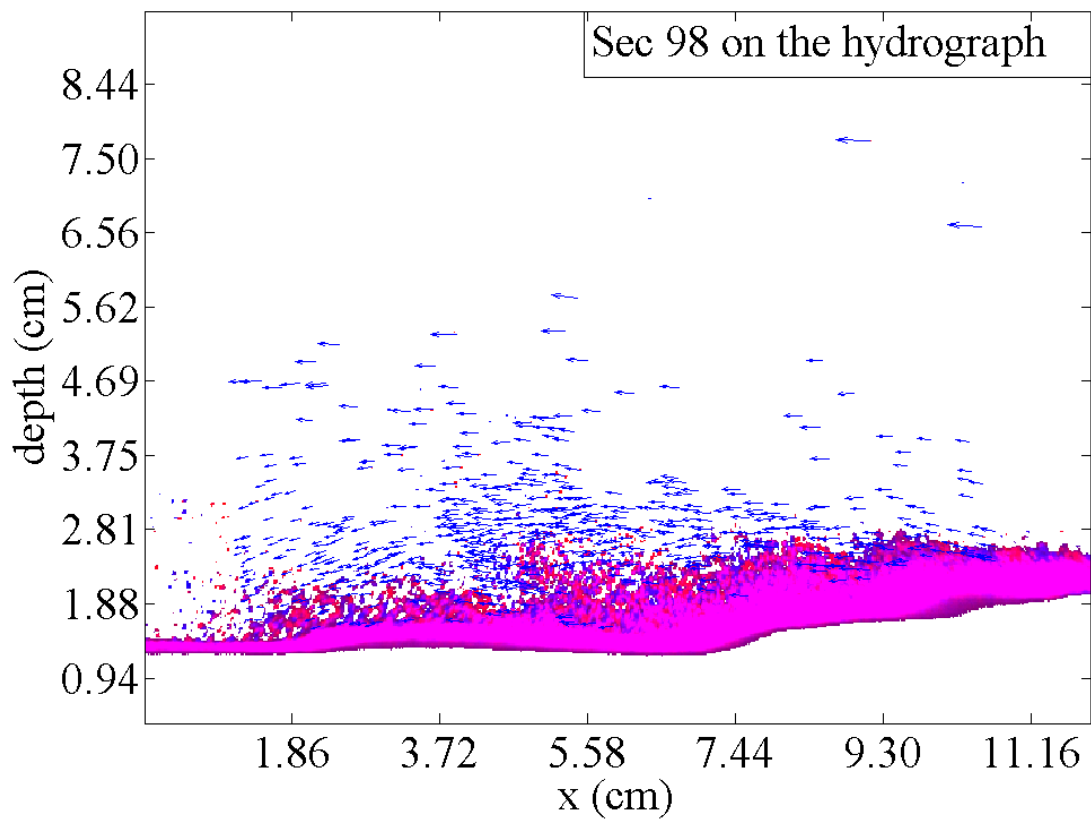
a14)



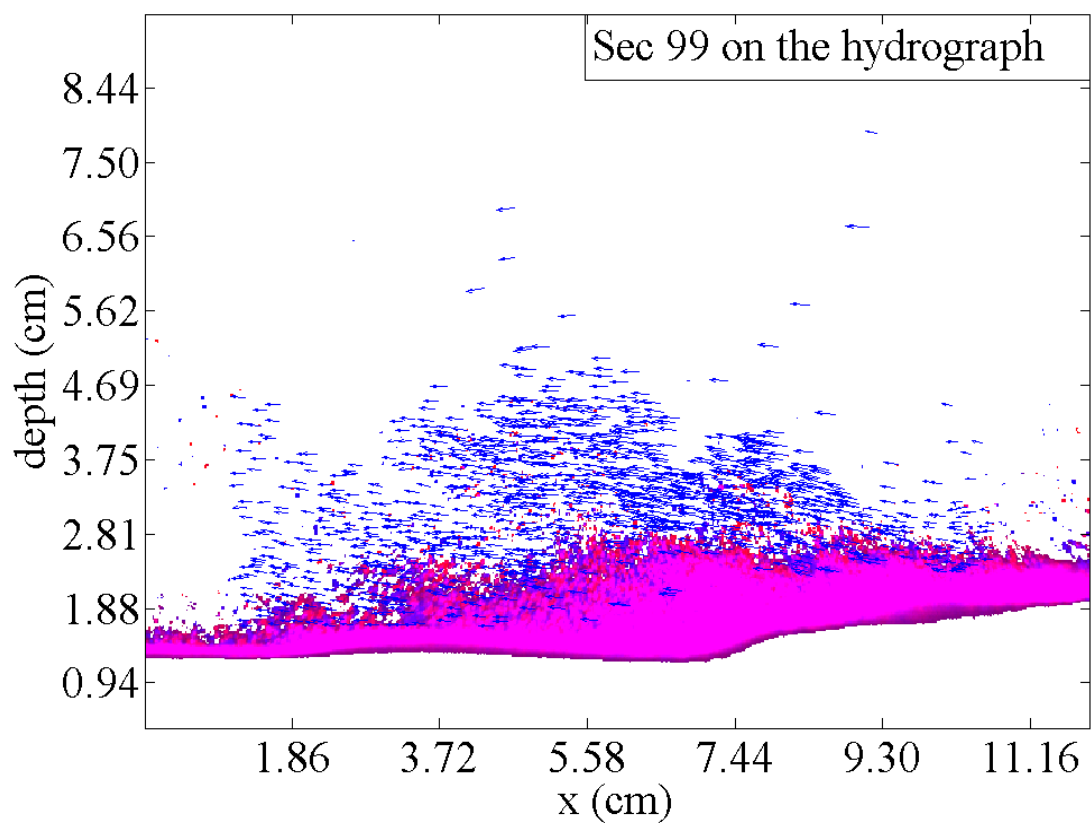
b14)

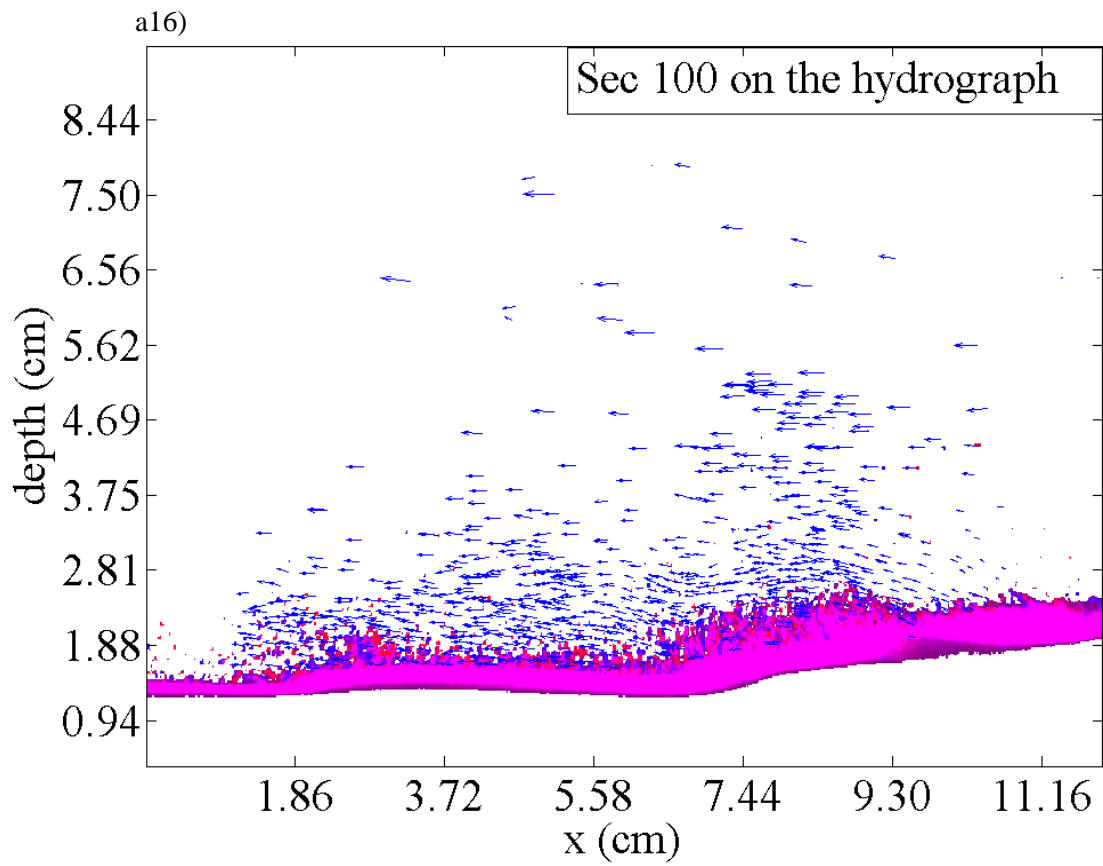


a15)

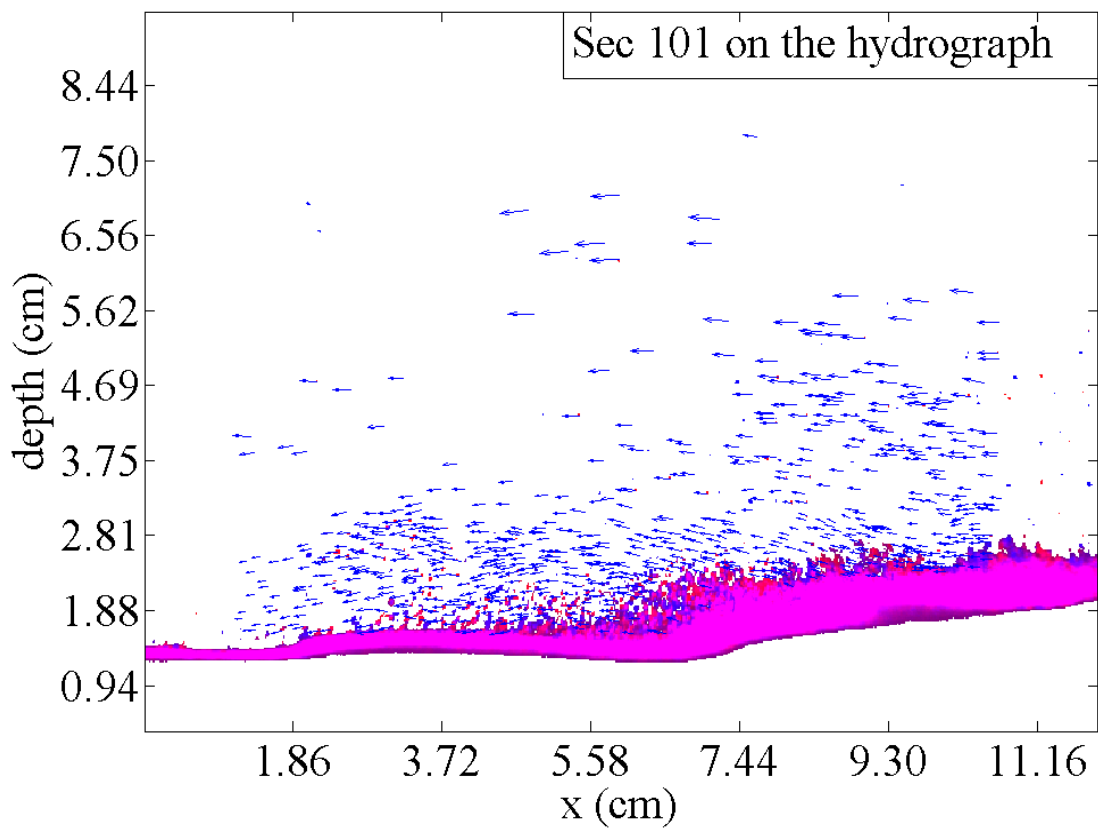


b15)





b16)



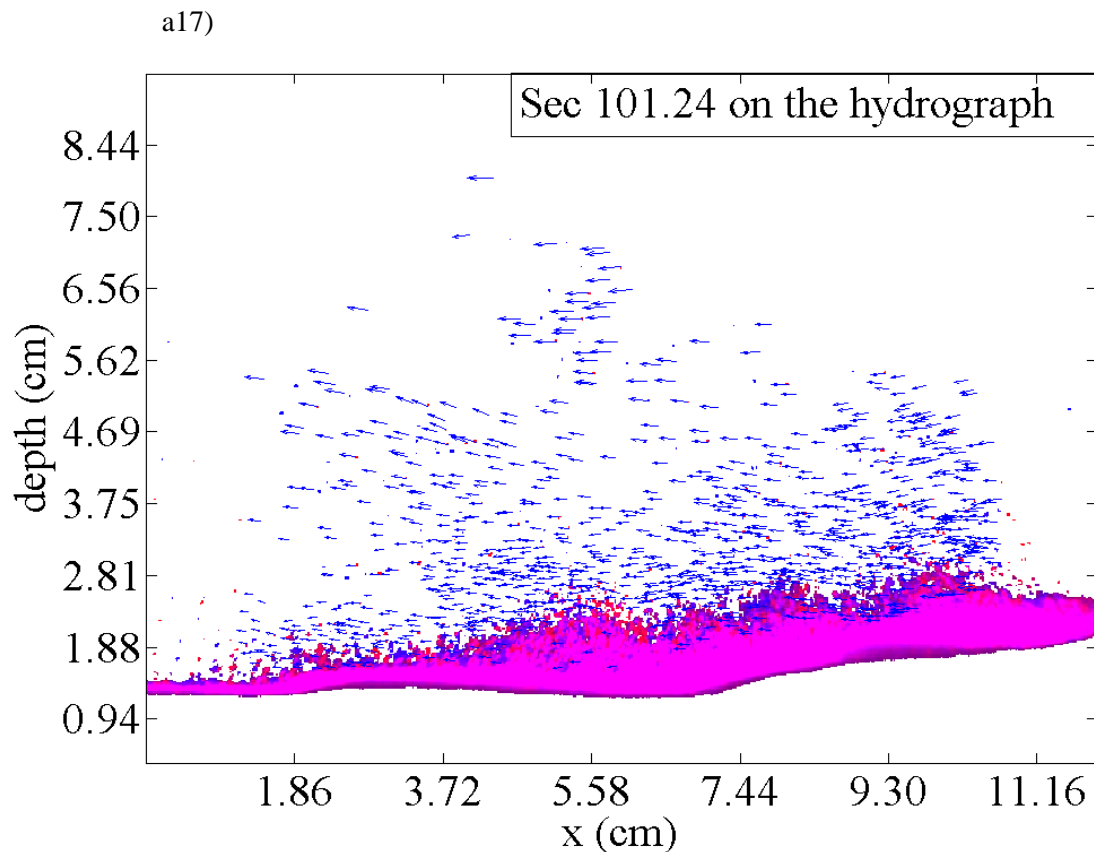


Fig 37. PTV results during the 31.27 s (correspond to Figs. 35 and 36) of the final phase of the accelerating range. Arrows indicate particle velocity vectors. Flow is from right to left

In Fig. 38 are shown the sediment concentrations that were calculated from particle density at different parts of the 20 s and 90 s hydrographs. It indicates that the highest concentration is found near the bottom for both hydrographs. When the results for highest unsteadiness (20 s) and lowest unsteadiness (90 s) are compared, the effect of the accelerating range is apparent: It shows that during the initial and final phase of the accelerating range of the hydrographs, the highest unsteadiness (20 s) has a higher concentration compared to the lowest unsteadiness (90 s). Thus higher suspension occurs for the hydrograph with 20 s accelerating time. Stronger unsteadiness produces particle suspension into higher depth levels that allows tracing the velocity distribution over a wider depth range. During the initial phase of the decelerating range of the hydrographs, they behave differently, and a higher concentration is seen for the 90 s than for the 20 s hydrograph.

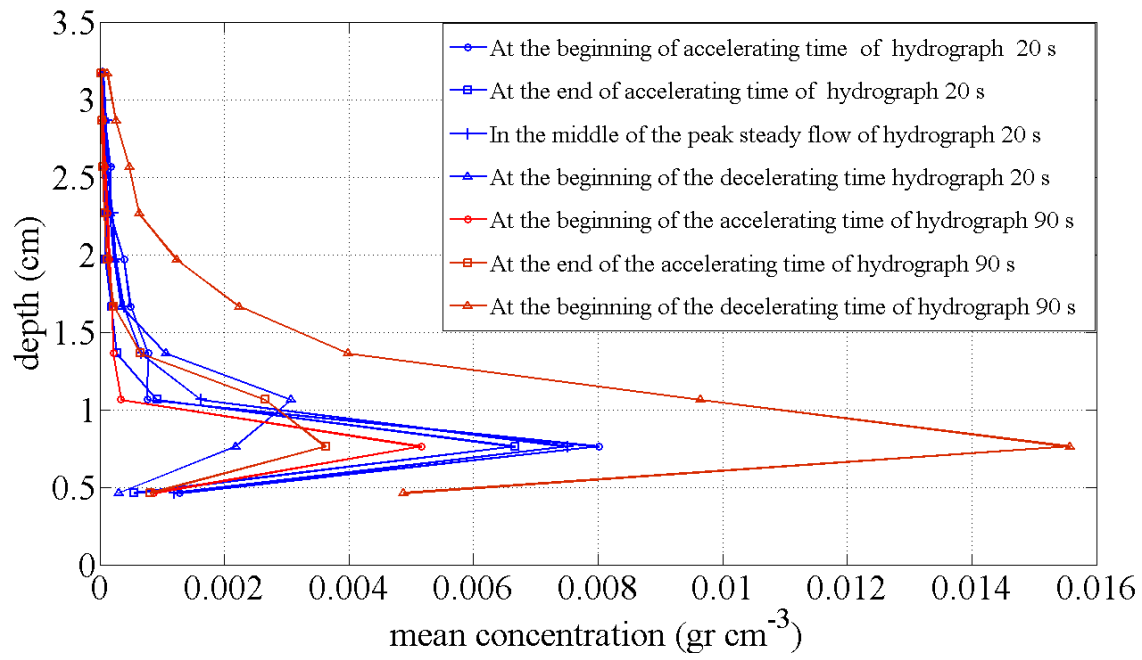


Fig. 38 Mean particle concentration for the different parts of the hydrographs for accelerating and decelerating times 20 s and 90 s

4.4 BEDFORMS AND PARTICLE–TURBULENCE INTERACTION IN UNSTEADY SUSPENDED SEDIMENT-LADEN OPEN-CHANNEL FLOW

To learn more about sediment suspension and ripple formation, two additional video studies were carried out. In the first one, the PTV camera was zoomed in the vicinity of the bed. Image size in this case was 1.7 cm high by 2.3 cm wide. A recording with a 40 Hz frame rate was made, covering the period from the beginning of the sediment motion on the bed during the acceleration range to the ripple movement during the steady peak flow range. Multiple exposures of individual particles were produced to show particle trajectories. Several images from this recording are presented to supplement the analysis above.

The videos showed that during the initial saltation of particles, the upper layer of the whole bed began to move (Fig. 39a). Particles may rise about 1 cm above the bed. Saltation above the bed level occurs in bursts. The ripple started forming 2.5 s after this image (Fig. 39b). Most particles roll along the ripple to the crest and then fall down the steep slope into the trough. However, other particles do not roll, but form curved trajectories when descending from the crest into the trough in the lee side of the crest. Curved trajectories and backward transport of particles indicate that a vortex is formed in the lee side of the crest. This type of particle motion becomes more evident as the ripple grows (Fig. 39c). Particles now also move higher into the water column and those well above the bed follow straight trajectories across the image. A strong event structure of the particle motion around the crest/trough area is evident. The origin of the particle ejections into the higher water column is found on the back of the ripple in an area known as the reattachment point (Best, 2005). Two examples are given in Figs. 39d and 39e. They demonstrate that particles are lifted off from a limited area of the bed and follow steep, curved trajectories. This indicates that a strong vertical velocity component exists in the near bottom layer. Once again, this process is strongly event structured. The curved trajectories that are repeatedly seen in Figs. 39d and 39e suggest that vortex motion in the water is controlling particle motion. Vortex motion in relation to coherent structures has been well documented (Nezu and Nakagawa, 1993). Therefore, it can be expected that coherent structures affect sediment suspension. These recordings indicate that the ejection phase of the coherent structures is focused on the reattachment point.

These video recordings were also taken at the end of the hydrograph when the flow was back to base flow. Images showed that ripples remained in place even though the flow had decelerated. Particle motion and saltation continued to occur, gradually advancing the ripple. This indicates that even though the friction velocity was well below the critical value for sediment motion under steady flat bed conditions at base flow (Fig. 11), form drag produced by the ripples was strong enough to maintain sediment motion. Considering that the light sheet was placed in the center of the channel and that PTV images and video images were taken at a distance of 35 cm from the channel center, it is evident that particle density in this flow was low. This is also confirmed by the images in Fig. 39, where individual particles can be followed in their trajectories without interference from other particles, even during burst events.

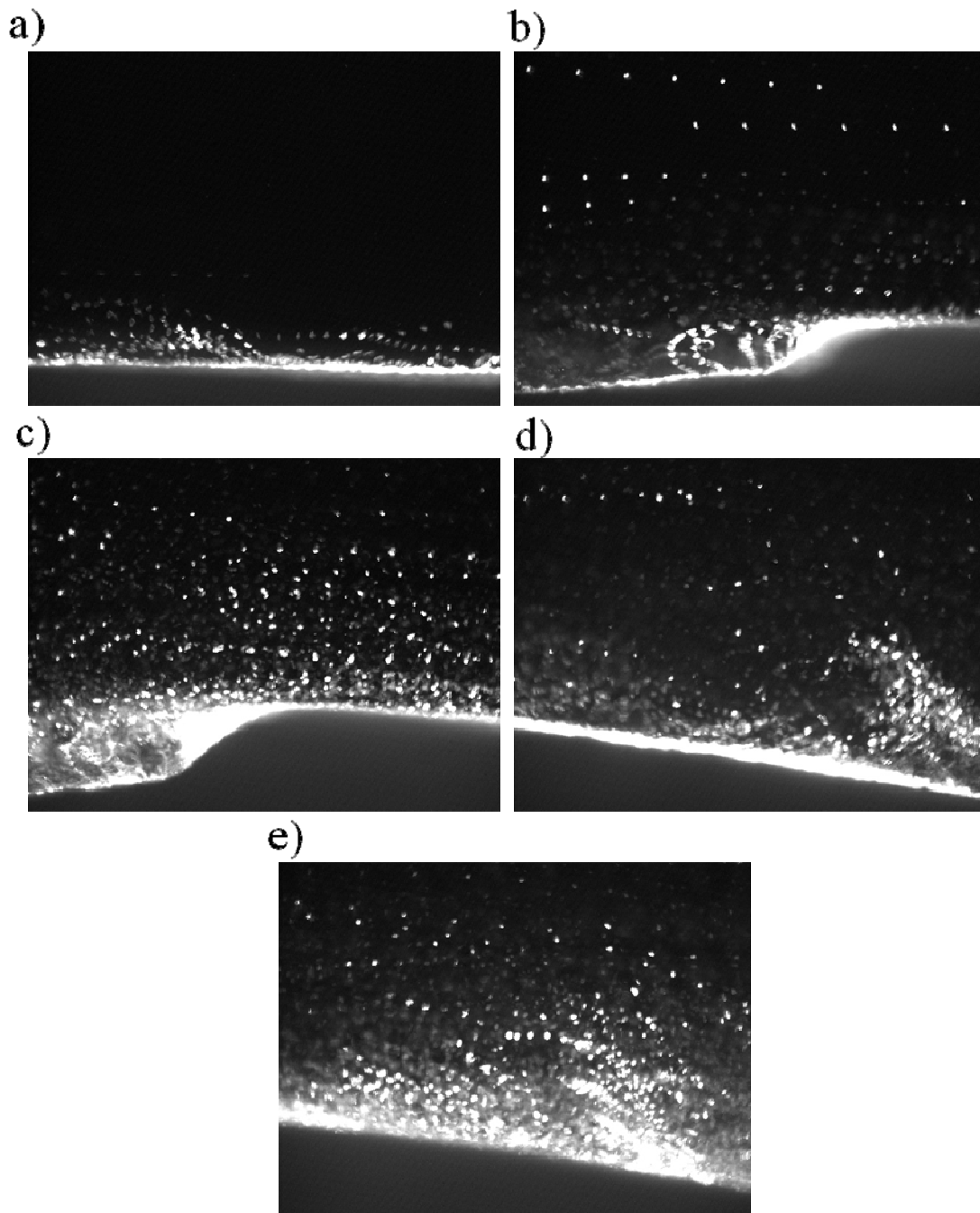


Fig. 39. Close-up view of sediment particle trajectories related to ripple formation

In a second video recording, large-scale images were taken over a wider section of the bed. The objective was to provide some information on the ripple formation. It is generally accepted in the literature (Best, 2005, Garcia, 2007) that ripples are formed from some instability on the bed. For this experiment, the whole 6 mm thick fine sediment bed was covered with a very thin layer of the same sediment particles that had been painted in black. Upon starting the hydrograph, it was observed that towards the end of the acceleration range, ripples occurred nearly simultaneously along the whole bed and quickly formed a pattern, as seen in the top view of the channel (Fig. 40). Each of the dark areas finishes on the left with a ripple crest and the steep slope at the angle of repose. This slope is only a few mm wide in the present image. The white areas cover the troughs in the

leeside of the crests. The whole pattern slowly moves in the direction of the flow, but the ripple distribution does not change significantly. Areas marked in red show “remains” of the initial reference bed level. This indicates that crests are rapidly piled up above the reference bed level with particles that have been moved horizontally from the present trough area onto this part of the downstream ripple, as seen in Fig. 39. Troughs are dug below that reference level. Over time during the steady peak flow of about 90 s, the color of the dark area changes little, indicating that not much of the material from the trough area is deposited onto the crest area. It appears that most of the material from the trough area is rolled up the slope and then suspended in bursts higher up in the water column and spread out over a wider area as described above.

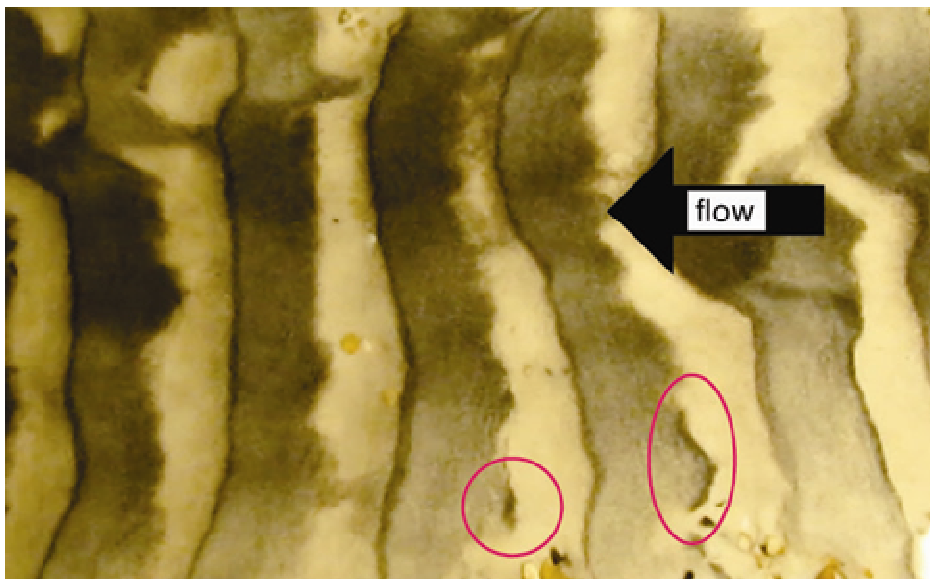


Fig. 40. Large scale image of ripple formation, seen from the top. Mean spacing of the ripples is about 6 cm. Red circles show remains of the initial reference bed level.

This experiment was repeated several times for the 20 s and 90 s hydrographs. All large scale recordings produced similar results with fairly regular ripples spanning the channel width, most often in almost linear bands. In order to verify the erosion-deposition pattern seen in these large scale videos, measurements with a laser gage described in Chapter 3, were carried out before and after each experiment. Results are shown in Fig. 41. In this figure, the red line shows the zero level at the beginning of the experiments when fine sediment covers the gravel bed and no bedforms were seen on the bed (flat bed). The other colors show the profiles of the ripples along the bed for the highest and lowest unsteadiness (20 s and 90 s, respectively). Figure 41 indicates that ripples are formed by erosion and deposition. It can be seen in this figure that for most ripples, no local equilibrium exists between erosion in the trough and the deposition on the following ripple.

Deposition often appears to be larger than erosion. Transport by suspended particle burst and vortex formation on the lee side of the crests may affect the pattern. The mean ripple length was 5 cm and the height of the ripples varies between 5 mm and 10 mm. Even though a zoom on the 2 ripples in Fig. 41 shows a small difference in the ripple height between the 20 s and 90 s hydrographs, no clear trend of unsteadiness with respect to

ripple shape can be determined. Therefore, the wavelength of the ripples appears not to depend on the unsteadiness. With the presence of ripples on the bed, unsteadiness appears to have less effect. Ripples did not change in appearance or dimension for the duration of the experiments.

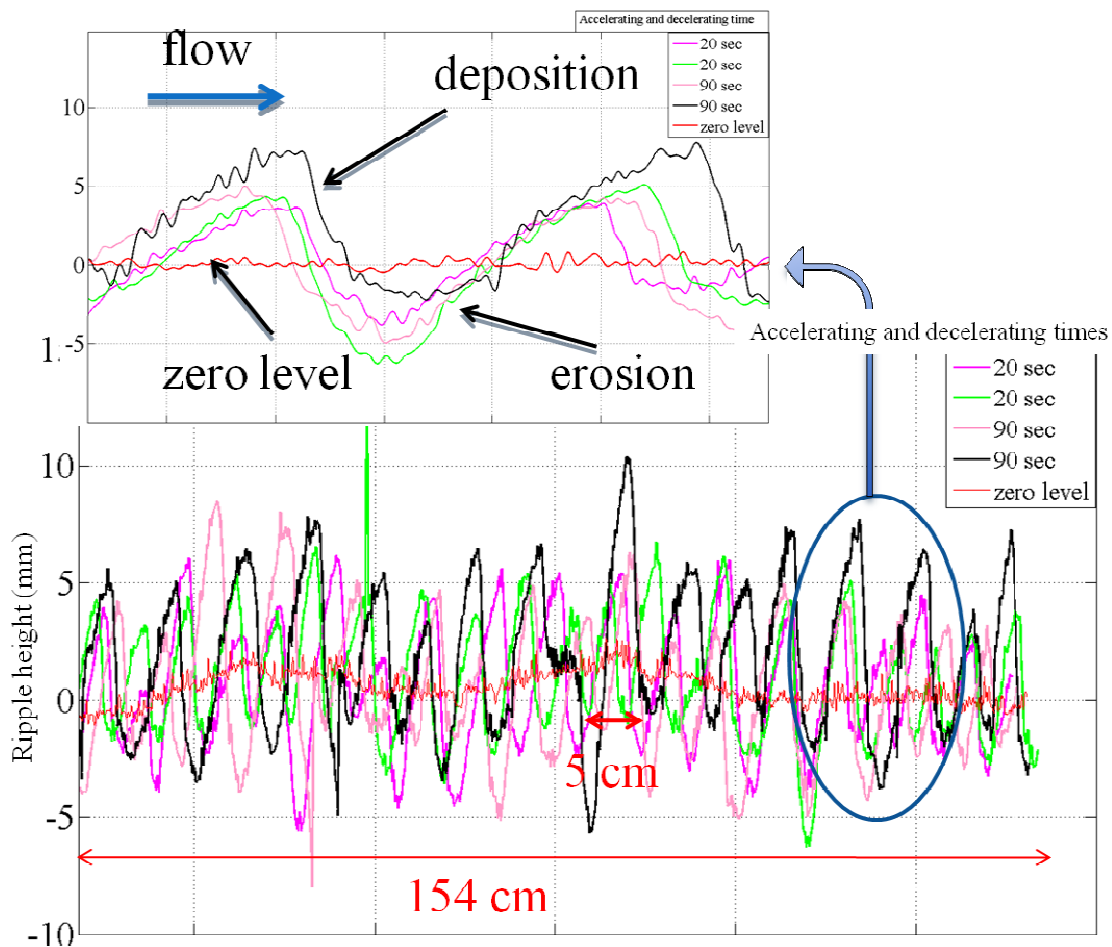


Fig. 41. Bed elevation and size of the ripples for accelerating and decelerating times 20 s and 90 s

The details of the processes related to hydrodynamics, sediment suspension and ripple formation made evident with optical methods in this study, cannot be obtained by only using ADV measurements. In field studies where these processes occur at larger scale, ADVs may resolve these scales. However, laboratory studies such as the present one have to be carried out before, in order to guide the field studies in data taking and the interpretation.

4.5 REFERENCES

- Best, J., 2005. The fluid dynamics of river dunes: a review and some future research directions. *J. Geophys. Res.* 110, F04S02, doi: 10.1029/2004JF000218.
- Bagherimiyab, F., Lemmin, U., 2010. Aspects of turbulence and fine sediment resuspension in accelerating and decelerating open-channel flow. In: *Proceedings of Riverflow 2010*, 8 – 10 September 2010, Braunschweig, Germany. 1, 121 – 127.
- Blanckaert, K., Lemmin, U., 2006. Means of noise reduction in acoustic turbulence measurements. *J. Hydr. Res.* 44, 3 – 17.
- Cellino, M., Lemmin, U. 2004. Influence of coherent flow structures on the dynamics of suspended sediment transport in open-channel flow. *J. Hydr. Eng.*, 130, 1077-1088.
- Garcia, M.H., 2007. Sediment transport and morphodynamics. In: M.H. Garcia (Ed.) *Sedimentation engineering*. ASCE Manuals and Reports on Engineering Practice No 110, pp. 21-146.
- Graf, W.H. (1971). *Hydraulics of sediment transport*. McGraw-Hill, NY.
- Lhermitte, R., Lemmin, U., 1993. Turbulent flow microstructures observed by sonar. *Geophys. Res. Letters* 20, 823 – 826.
- Nezu, I., Nakagawa, H., 1993. *Turbulence in open channel flows*. A.A. Balkema, Rotterdam, NL.
- Nezu, I., Kadota, A., Nakagawa, H., 1997. Turbulent structure in unsteady depth-varying open-channel flows. *J. Hydr. Eng.* 123, 752-763.
- Shen, C., Lemmin U., 1997. Ultrasonic scattering in highly turbulent clear water flow.
- Song, T., Lemmin, U., Graf, W.H., 1994. Uniform flow in open channels with mobile gravel bed. *J. Hydr. Res.* 32, 861-876.
- Yalin, C.T., da Silva, A.M. 2001. *Fluvial processes*. IAHR monogr., IAHR, Delft, NL.

CHAPTER 5

SUMMARY AND CONCLUSIONS

SUMMARY AND CONCLUSIONS

Despite the fact that flows in rivers and open channels are generally unsteady, few studies on turbulent structures in unsteady open-channel flows have been undertaken. The mechanism of sediment transport in rivers and open channels is governed by complicated interactions between unsteady accelerating and decelerating turbulent flow, particle motion and bed configuration. Understanding unsteady sediment-laden water flows, characterizing the velocity of suspended particles and their effect on water quality parameters is essential because of their impact on river dynamics, the environment and the ecological system.

In the present study, turbulent unsteady accelerating and decelerating open-channel flow over a movable (but not moving) coarse gravel bed ($D_{50} = 5.5$ mm) was investigated, with a discharge varying from 10 lit/s to 35 lit/s, resulting in a water depth variation from 103 mm to 164 mm and a Reynolds number ranging from 1.6×10^4 to 4.4×10^4 . Five symmetrical hydrographs with different unsteadiness (20 s, 30 s, 45 s, 60 s and 90 s) were investigated. Detailed, quasi-instantaneous velocity profiles were measured using a 3D Acoustic Doppler Velocity Profiler (ADVP). Profile measurements resolved turbulence scales, and for each hydrograph, they were repeated up to 20 times in order to establish a solid database. The unsteady flow was segmented into more than 400 time slices for the analysis.

In order to simulate fine sediment dynamics over an armored bed in a river during the passage of a flood wave, a layer of fine sediment of mean particle size about $120 \mu\text{m}$ was placed on the coarse gravel bed. The thickness of the fine sediment layer on the gravel bed was varied between 4 mm and 6 mm. Quasi-instantaneous profiles of velocity and sediment concentration were taken simultaneously and co-located by combining an acoustic Doppler and imaging method (ADVP) with an optical method (PTV) for suspended sediment particle tracking. Measurements resolved turbulence scales. The development of ripples was also investigated.

Even though the discharge was changed linearly at the same rate in both unsteady flow ranges, the change of relative submergence was not linear and it was different not only in the two flow ranges of each hydrograph, but also it was different in the five different unsteadiness, resulting in considerable differences in the flow dynamics. During the accelerating range, both mean velocity and friction velocity initially increased strongly and less thereafter. Unsteadiness effects are greatest in the accelerating range of the 20 s hydrograph and are the lowest in the 90 s one. Unsteadiness strongly affects the profile shape, particularly in the final phase of the accelerating range. During decelerating flow, only one slope and thus one relationship between bed shear velocity and mean flow velocity was found throughout the unsteady flow range. Furthermore, systematically higher friction velocities were observed in accelerating flow than in decelerating flow for comparable mean flow velocities. This indicates that the same change of relative submergence generates different flow dynamics during the accelerating and decelerating

flow ranges. The hysteresis loop found by Nezu et al. (1997) was confirmed. In order to determine when unsteady flow can be approximated by steady flow concepts and which simplifications are acceptable, experiments were carried out for six steady flows which covered the discharge ranges of unsteady experiments (base flow discharge, peak flow discharge and 4 discharges in between). Results showed that flow in decelerating range approaches steady flow.

A comparison of the results of shear velocity calculated by the logarithmic law method with Reynolds stress method showed that the assumption of a constant stress layer on which the calculation by $u_* = (-\overline{u'w'})^{1/2}$ is based, is not valid in this open-channel flow.

Fine sediment particles and hydrogen bubbles were used individually and combined as flow tracers in the acoustic measurements. When used individually, hydrogen bubbles provided full depth flow and backscattering information, whereas sediment particles traced only the lower layers of the flow, indicating sediment suspension. When both tracers were combined, hydrogen bubbles could only be distinguished from sediment particles, except when the acoustic frequency was changed. Therefore, in field studies where different acoustic tracers such as algae, gas bubbles and sediment particles may exist at the same time and where all of them may have a certain size range, the detection and quantification of an individual tracer based on acoustic measurements alone may be difficult. It has been shown that multi-frequency systems may help to solve this problem. However, transducer efficiency may limit the range that can be covered and therefore the potential of tracer separation.

The intermittency in sediment particle suspension was observed in the backscattering intensity of the acoustic system only when sediment particles were used as tracers. At the same time, velocities showed much less intermittence. Therefore, particle flux in this flow is controlled by particle dynamics. However, due to the low particle density, backscattering could not be translated into sediment concentration. Thus, in low particle environments, particle flux calculations cannot be carried out. Nevertheless, the ADV is sensitive enough to capture clean signals for the time history of sediment suspension in these low particle density conditions and valuable information about the sediment transport dynamics can be obtained.

The investigation of unsteady open-channel flow over a coarse bed with a fine sediment layer was limited to the observation of dynamics in velocities produced by suspended sediment particles serving as a tracer. No fine particle transport occurred during the initial phase of the unsteady flow, and particle suspension was progressively intensified during the unsteady flow range. Optical methods which were applied simultaneously helped to verify and to interpret the ADV data and to visualize the physical processes leading to suspension. The combination of acoustical and optical methods provides for an ideal approach to study suspension in unsteady flow. The event structure in fine sediment suspension is seen by the ADV and the PTV methods. PTV velocity vectors varied in speed and orientation, but were organized in large coherent packets, mainly in the near bed layers, but also extending well above the bed, supporting the concept that coherent structure events contribute to sediment suspension over ripples. The low particle number in the images confirmed the low particle density seen by the ADV. When the flow had sufficiently accelerated, fine sediment was suspended in bursts into the intermediate layers

of the water column and at the same time, rapidly created nearly stationary ripples during the final phase of the accelerating flow range. Sediment particles were not suspended into the upper 40% of the water column. Vortices shedding from the ripple crests produced most of the sediment suspension in the form of events, making suspension intermittent. High sediment suspension continued to occur during the decelerating flow even though the flow velocity decreased. This process cannot be parameterized by the critical Shields parameter. This phenomenon is attributed to the presence of ripples which remained in place during this phase of the hydrograph. The stronger unsteadiness produced stronger and higher suspension into the upper water column. Hydraulic parameters, such as water depth, mean velocity time development and profile form were not affected by the presence of fine sediment particles. The results indicate that sediment suspension in unsteady flow is controlled by the same large scale turbulence processes as in steady flow. Due to the presence of coherent structures in the water column and ripples on the bed, mean velocity concepts are difficult to apply in this flow case. Parameters such as the reference depth for Rouse profiles cannot be determined.

Ripples formed quickly, within about 3 sec after fine sediment particle saltation started. Ripples are generated by erosion and deposition with respect to the initial flat bed. Ripple troughs are the result of erosion, whereas crests are formed by deposition. A mass balance between a trough and the following crest cannot be established. The wavelength of the ripples appears not to depend on the unsteadiness. Ripples did not change in appearance or dimension for the duration of the experiments. No clear trend of unsteadiness with respect to ripple shape can be determined. Once established, the ripple pattern progressed slowly in the direction of the flow, mainly by sediment particles which rolled up the ramp of the ripple and dropped over the crest. No difference was found when the thickness of the fine sediment layer was changed from 4 to 6 mm.

The two methods provide complementary information, particularly when applied simultaneously. Optical methods helped to verify and to interpret the ADV data and to visualize the physical processes leading to suspension. New and detailed results made possible by combining the ADV and imaging techniques provide valuable insight into the dynamics of fine sediment suspension and ripple formation initiated by unsteady flow conditions that were previously not possible. ADV measurements allow long timeseries analysis, whereas the spatial details seen in the PTV results cannot be resolved in the ADV measurements. The characteristics of the ripples in the present study are too small to be resolved by the ADV. They are well traced by the PTV. In field studies, ripple dimensions may be large enough to be investigated by the ADV. However, laboratory studies such as the present one may help guide field measurement strategies and data interpretation. The combination of acoustic and optical methods provides for an ideal approach to study sediment dynamics in unsteady flow conditions, particularly ripple formation and suspension in low concentration flow.

A.APPENDICES

A.1	FINE SEDIMENT DYNAMICS IN TIDAL OPEN-CHANNEL FLOW STUDIES WITH ACOUSTIC AND OPTICAL SYSTEMS	151
A.2	SHEAR VELOCITY ESTIMATES IN ROUGH-BED OPEN CHANNEL FLOW	177
A.3	COHERENT STRUCTURES IN ROUGH-BED OPEN CHANNEL FLOW OBSERVED IN FLUCTUATIONS OF VELOCITY PROFILES, SHEAR VELOCITY AND PRESSURE	199
A.4	CURRICULUM VITAE	219

A.1 Fine sediment dynamics in tidal open-channel flow studied with acoustic and optical systems

Fereshteh Bagherimiyab¹ and Ulrich Lemmin²

¹ Ecole Polytechnique Fédérale de Lausanne (EPFL), ENAC, Station 18, CH-1015 Lausanne, Switzerland; email: fereshteh.bagheri-meyab@epfl.ch

² Ecole Polytechnique Fédérale de Lausanne (EPFL), ENAC, Station 18, CH-1015 Lausanne, Switzerland; email: ulrich.lemmin@epfl.ch

Abstract

In order to simulate fine sediment dynamics over an armored bed in a tidal river, unsteady accelerating, then steady open-channel flow over a movable (but not moving) coarse gravel bed ($D_{50} = 5.5$ mm) was studied. A layer of fine sediment of mean particle size of about 120 μm was placed on the coarse gravel bed. The thickness of the fine sediment layer on the gravel bed was varied between 4 mm and 6 mm, but it was found that the thickness of the layer had no effect on the results. Quasi-instantaneous profiles of velocity and sediment concentration were taken simultaneously and co-located. An acoustic Doppler and imaging method, using an Acoustic Doppler Velocity Profiler (ADVP) was combined with an optical method, using Particle Tracking Velocimetry (PTV) for suspended sediment particle tracking. Measurements resolved turbulence scales. During the final phase of the accelerating flow range, fine sediment suspension from the bed started in bursts and rapidly created a ripple pattern that remained nearly stationary. Thereafter, vortex shedding produced most of the sediment suspension into the water column in the form of events, making suspension intermittent. Simultaneously, sediment particles rolled along the bed following the ripple structure, thus slowly advancing the ripple pattern in the direction of the flow without altering ripple geometry. Fine sediment particles and hydrogen bubbles were used individually and combined as flow tracers in the acoustic measurements. When used individually, hydrogen bubbles provided full depth flow and backscattering information, whereas sediment particles traced only the lower layers of the flow, indicating sediment suspension. When both tracers were combined, hydrogen bubbles could not be distinguished from sediment particles. The intermittency was observed in the backscattering of the acoustic system. The event structure in fine sediment suspension is seen by the PTV method. PTV velocity vectors varied in speed and orientation, but were organized in large coherent packets, mainly in the near bed layers, but also extending well above the bed, supporting the concept that coherent structure events contribute to sediment suspension over ripples. The two methods provide complementary information. ADVP measurements allow long timeseries analysis, whereas the spatial details seen in the PTV results cannot be resolved in the ADVP measurements.

Keywords: *fine sediment, suspension, ripple formation, tidal open-channel flow, acoustic Doppler method, PTV (Particle Tracking Velocimetry).*

1. INTRODUCTION

Suspended sediment transport occurs in many geophysical flows and it directly impacts on physical and biogeochemical processes in the whole water column. In tidal channels, estuaries

and rivers, sediment erosion and deposition may lead to channel changes and relates to scour. It is therefore of great importance to understand suspended sediment transport dynamics and turbulent sediment fluxes, because geophysical flows are often turbulent. Most of these flows are unsteady and flow acceleration and deceleration during the unsteady phase may lead to the initiation or termination of sediment suspension, and generate or modify bed forms and change bed and channel topography. Initiation of sediment motion due to unsteady turbulent water flows is an important aspect of river and coastal engineering.

Although bed load transport in unsteady flow has been the subject of much research, less attention has been paid to the suspension of sediment under unsteady flow. In unsteady open-channel flows over a smooth wall, Nezu and Nakagawa (1993) found that the log law of the mean velocity is still valid. This was confirmed by Afzalimehr and Anctil (2000) who studied spatially accelerating shear velocity in gravel-bed channels. Nezu and Nakagawa (1993) estimated the friction velocity u_* and the wall shear stress ρu_*^2 as a function of time in unsteady flows. In oscillatory closed-channel flows, Jensen and Sumer (1989) and Akhavan et al. (1991) observed that the mean velocity obeyed the log law distribution, except at the very early stages of the acceleration phase and the late stages of the deceleration phase. By measuring the turbulence structure over a smooth wall in unsteady depth-varying open-channel flows, Nezu et al. (1997) established that in the rising stage, the wall shear stress attains its maximum ahead of the flow depth. They also detected hysteresis loop properties of velocity and turbulence profiles in unsteady open-channel flows.

Suspension of sediment particles occurs when the local bottom shear stress ρu_*^2 exceeds the critical value (Shields, 1936). Under steady flow conditions, suspension may also be caused by secondary currents (Nezu and Nakagawa, 1993) or coherent structures (Nezu and Nakagawa, 1993; Cellino and Lemmin, 2004; Nezu, 2005). Sediment transport studies in unsteady flow (Sutter et al., 2001) indicate a hysteresis loop in sediment concentration, similar to that observed in turbulence intensities by Nezu et al. (1997). All these studies demonstrate that determining the structure of turbulence in unsteady flow is important in order to advance the understanding of sediment flux development.

Ripples and dunes are the most prominent small-scale features in the low Froude number range among bed forms in loose bed conditions with fine sediments. A detailed description of the creation, geometry and movement of bedforms is given in DuBuat (1786). The triangular geometry of bedforms was recognized. According to DuBuat, sand grains move up a gentle slope, arrive at the summit and fall down a steep slope whose angle is close to the angle of repose of sand grains. The current erodes the upstream face and deposits the eroded material on the downstream face. By this process of sand grain movement, the whole bedform advances slowly in the direction of the flow. Their mode of advancement is similar to that of aeolian ripples.

More recently, it is recognized that due to the turbulent flow and particularly the presence of coherent structures in the flow, some of the sand grains are moved from the bed up into the water column and are then transported as suspended sediment. McLean et al. (1994) measured the turbulence structure over sand dunes and pointed out the importance of coherent eddies in lifting up sediment particles behind the dune crest. Flow over ripples is dominated by shear layer instability resulting from separation zones in the lee side of the ripple. Turbulent coherent structures are able to penetrate further into the outer flow and thus induce return flows that are able to exert greater shear stress as they impact on the bed (Best, 2005). The shear stress on the bed can be considered as the sum of flow-induced shear and form-induced shear by the ripples.

Ripples occur mainly in sands with diameters < 0.6 mm and are steeper and shorter than dunes. Their length depends on particle diameter. Best (2005) also indicated that differences in unsteady flow may affect the scales of bedforms. Dune length may scale with water depth (Yalin, 1977) and dunes often generate a corresponding deformation of the free water surface. Ripples have a larger height:length ratio than dunes (Allen, 1968). In most cases, ripples will develop first during unsteady accelerating flow, followed by dunes in the long term. Reviews by Best (2005) and Garcia (2007) summarize recent developments in bedform research. It is recognized that the characteristics of the flow over alluvial bedforms has many similarities to flow over tidal and oceanic bedforms as well as flow over aeolian dunes (Bagnold, 1941). Therefore, the results from an open-channel study carried out here, can also be applied to coastal ocean situations.

Most often the wavelength of ripple crests is given as an indicator characterizing ripples. Equations for equilibrium ripple dimensions are suggested by Baas (1999). However, in the present study we will focus on the initial development of ripples. As indicated by Baas, these dimensions are much smaller than the equilibrium dimensions.

In tidal rivers and the coastal ocean, tracers for acoustic and optical studies may include gas bubbles, algae, detritus or sediment particles. It is often difficult in field studies to determine a priori the nature of the scatterers in the flow field. Most often they occur as a mixture of several or all of them. However, transport of sediment particles is frequently of major interest because of its effect on bed and channel morphology. Therefore, the presence and concentration of individual tracers should be known in order to correctly quantify the contribution by sediment particles. Here we will study this effect under controlled conditions by selectively adding one or two tracers.

Most studies concerning the dynamics of ripple formation and sediment suspension reported in the literature have investigated steady flow situations. In the present study, ripple development in depth variable accelerating flow will be explored. We will cover a situation of a flat sediment bed at rest to quasi-steady flow with suspended sediments and ripple formation. This study focuses on some hydrodynamic aspects of open-channel flows without and with sediment transport in order to advance the understanding of sediment flux development and ripple formation. We will apply acoustic and optical methods providing high spatial and temporal resolution profile data in order to determine velocity profiles and particle dynamics and also consider the advantages of each method.

In particular, the situation of low sediment particle concentration suspended over only part of the water column will be addressed. In low sediment concentration flows which typically occur during the beginning of accelerating flow, acoustic methods may have difficulty determining the velocities and sediment particle concentration correctly, due to the relatively low number of particles inside the acoustic beam. Therefore, in this study, video images are recorded in parallel with the acoustic measurements in order to visualize the sediment suspension process during the hydrograph and thereby confirm the acoustic measurements.

First, the measurement techniques used and the experimental procedure will be described. The results will be discussed thereafter. It will be shown that a combination of acoustic and optical methods provides for the best results.

2. METHODOLOGY

In order to capture the dynamics of unsteady sediment-laden flow, instrumentation is required which can simultaneously measure hydrodynamics, sediment concentration in the whole water column and bed morphology with sufficient spatial and temporal resolution to resolve turbulent scales. Acoustic methods based on the backscattering of sound are well suited to fulfill these requirements. Acoustic Backscattering Systems (ABS) can capture the Doppler phase angle and the intensity of the backscattered signal from which flow velocity and sediment concentration, respectively, can be obtained. Thorne and Hanes (2002) have summarized the development of ABS techniques and instrumentation that allow extracting this information. At present, velocity and sediment concentration are most often obtained separately (Harris et al., 2003; VanderWeft et al., 2007; Thorne et al., 2009). By this approach, sediment flux can only be resolved for scales that are larger than the separation of the instruments.

In order to resolve sediment fluxes on smaller scales, velocities and sediment concentration have to be measured in the same scattering volume. An instrument that is capable of co-located measurements with resolution of turbulent scales was developed at our laboratory over the past twenty years. It is based on the development by Lhermitte (1983) which showed the feasibility of a pulse-to-pulse coherent system in resolving turbulence scales in tidal channel flows. Acoustic Doppler Velocity Profiler (ADVP) measurements are based on the backscattered echo produced when an ultrasonic signal is scattered by moving targets. The quality of the signal obtained with the ADVP measurement is closely related to the scattering targets and their capability to follow the fluid motion. In an ADVP, quasi-instantaneous velocity profiles resolving turbulence scales in space and time are obtained from the Doppler phase angle (Lhermitte and Lemmin, 1994) by the application of the pulse-pair algorithm (Lhermitte and Serafin, 1984). This system was extended to full 3D instruments (Rolland and Lemmin, 1997). These were further improved in the hardware (Hurther and Lemmin, 1998) and software (Hurther and Lemmin, 1998, 2008; Franca and Lemmin, 2006) domain in order to reduce noise contributions and are today flexible and reliable instruments used in the laboratory (Hurther et al., 2007a), in rivers (Franca et al., 2008), in lakes (Lemmin and Jiang, 1999) and in the shore zone of oceans (Hurther et al., 2007b). Smyth et al. (2002) also demonstrated the possibility of co-located velocity and concentration profiling using an ABS.

Backscattered intensity can be inverted into particle concentration after calibration (Thorne and Hanes, 2002). An iterative inversion method has been proposed by Thorne et al. (1993) and an explicit inversion method was proposed by Lee and Hanes (1993). However both methods suffer from errors propagating through the profile (Shen and Lemmin, 1998). Thus, even a small error at one point in the profile generates errors in all following points. This is particularly severe when an error is made at the first point where attenuation is assumed to be negligible, because it will cause errors over the entire profile. Therefore, these methods are not well suited for attenuating media found in highly turbulent benthic suspension flows.

This problem, however, was overcome by combining backscattered and forward scattered profile signals, thus providing attenuation compensation even in high particle concentrations as long as multiple scattering is avoided. Integrating this approach into the existing ADVP, an acoustic particle flux profiler was developed (Shen and Lemmin, 1996) which determined the 3D velocity field and the suspended particle concentration field co-located in the same scattering volumes of the full depth profile. It provided new insight into the dynamics of suspended particle transport (Hurther and Lemmin, 2001) and particularly demonstrated the

importance of coherent structures in sediment transport (Shen and Lemmin, 1999; Cellino and Lemmin, 2004).

The inconvenience of this solution for field applications of the system was overcome by a new approach based on the exploitation of backscattering intensity at two (or more) emitted frequencies (Hay and Sheng, 1992; Hurther et al., 2006; Bricault, 2006). The advantage of this solution is that two relatively close frequencies (such as 1.25 MHz and 2 MHz) completely resolve the concentration field of fine particles typically found in benthic boundary layer applications. This frequency range can be handled by a single emitter transducer. Therefore, a two-frequency backscattering intensity profiler can easily be integrated into the existing ADV that was initially conceived to work with pulse interleaving at different frequencies. This provides a particle flux profiler that is unlimited in its application in laboratory and field studies in rivers, estuaries, oceans and lakes, and, different from optical systems, it also functions well in high particle concentration. It has the important advantage that 3D velocity and particle concentration profile information is obtained simultaneously, co-located in the same scattering volumes within the profile and resolves turbulence scales in time and space. Although the velocity determined from the Doppler phase does not require any calibration, an initial calibration of the backscattering intensity for a given particle size distribution has to be established. This can be obtained by suction sampling or from ABS systems in the same flow (Thorne and Hanes, 2002). A description of the most recent software developments of this Acoustic Doppler Particle Flux Profiler, showing in particular the advantage of a multi-frequency approach and its application under breaking waves in the shore zone of a wave flume are given in Hurther et al. (2011).

In low suspended particle concentrations, the number of particles may not be sufficient to extract the velocity and backscattering information, unless there are other tracers in sufficient quantity in the water. If this is not the case, particles may only be tracked occasionally through two consecutive pulses to obtain a velocity estimate. The rest of the time, no velocity data will be available. Mean value estimates over a whole timeseries may then be wrong. We will investigate this situation in the present study. Such low particle density inside the scattering volume does not allow a calibration to obtain sediment concentration from backscattering intensity. Therefore, in this study no sediment flux estimates can be presented.

The location of the bed is easily extracted from ADV or particle flux profilers by the strong echo of the backscattering intensity or from the zero velocity in the Doppler phase. For coarse bed particles of the size discussed in this paper, it is found (Bagherimiyab et al., 2008) that the bed level detected from the velocity profiles is located at about $0.2 D_{50}$ of the bed particles which corresponds to the definition of reference bed level in rough flows.

In the present study, measurements by the Acoustic Particle Flux profiler were complemented by optical methods using Particle Tracking Velocimetry (PTV). Prandtl (Prandtl and Tietjens, 1929) already used particles to study fluid dynamics in a systematic manner. Later, Laser Doppler Velocimeters were developed using high particle concentrations. With the availability of fast, high-resolution digital cameras, Particle Image Velocimetry (PIV) and PTV became standard measurement methods using lower particle concentrations (Adrian, 2005). By the right choice of particle size and specific density it is assured that tracer particles accurately follow the flow. PTV of singly exposed multiple images tracks a particle through sequential images. PTV works well with low particle seeding which can avoid pairing ambiguities. Since the particle density is low and the particle distribution within a frame is rather inhomogeneous during the initial phase of sediment suspension and ripple formation in accelerating flow, this technique is well suited for the present study. PTV algorithms are generally more accurate than correlation-based PIV algorithms, because they are less affected

by displacement gradients (Cowen and Monismith, 1997). We will therefore apply PTV in this study.

Combining the two methods allows studying long-term developments in timeseries obtained with the ADV in a single profiler location and the details of the 2D velocity field by PTV in the vicinity of the ADV location over shorter periods. This provides for a better interpretation of the data and the underlying processes (Bagherimiyab and Lemmin, 2010).

3. EXPERIMENTAL SET-UP

The measurements were carried out in a glass-walled open-channel which is 17 m long and has a rectangular cross section 0.6 m wide and 0.8 m deep. The bottom is covered with a 0.1 m thick gravel layer (size range 3 to 8 mm; $D_{50} = 5.5$ mm). The channel is operated in closed circuit mode. Discharge is modified by changing the rotational speed of the pump by computer. A shallow weir at the end of the channel controls the water level. The water level in the channel is measured with four ultrasonic limnimeters spaced along the channel axis. The bed of the channel is horizontal.

The ADV, used in this study, measures full depth 2D quasi-instantaneous velocity profiles in the streamwise and the vertical direction. The instrument works optimally at an acoustic frequency of 1 MHz. The transducers still function correctly at 2 MHz, however with reduced efficiency. The spatio-temporal resolution of the full profiles (3.3 mm and 0.032 s, respectively) is sufficient to quantitatively estimate turbulence parameters in the productive and inertial ranges of the spectral space.

The emitter and the receivers of the ADV are placed in a water-filled housing which is installed above the water surface, and which slightly touches the flow. This is done to avoid measurements in the nearfield of the emitter transducer where acoustic wave fronts are perturbed and turbulence measurements cannot be carried out correctly (Lhermitte and Lemmin, 1994). The ADV follows the surface in the depth-varying region of the hydrograph (Fig. 1) by a computer-controlled system. ADV profiling was carried out on the centerline of the channel about 15 m from the entrance where turbulence is well developed. A 1 cm thick layer of the water column near the water surface was omitted from the analysis, because the flow in this layer is slightly perturbed by the instrument. This does not affect the present analysis that is focussed on the near bed layer.

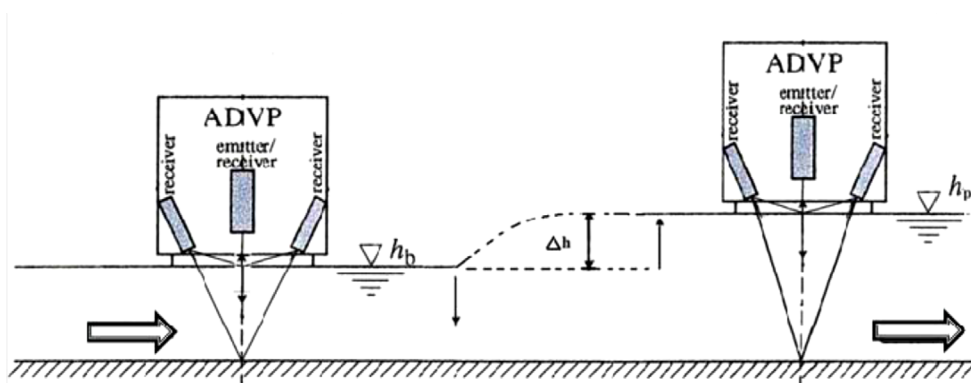


Fig. 1. Schematics of the ADV instrument in unsteady flow.

3.1. Experimental procedure

The hydrograph for the experiment consists of 5 parts. The flow is first maintained at the base discharge with $h = h_b$ for 60 s, followed by the rising stage of the unsteady flow (accelerating) where the discharge is linearly increased. Then the peak discharge is kept steady at $h = h_p$ for 180 s. Thereafter the discharge is linearly decreased during the falling stage of the unsteady flow (decelerating) to the initial base discharge. Two different accelerating and decelerating times, 30 s and 60 s, were investigated. The discharge, ADVP, and limnimeter data are simultaneously recorded during the hydrograph. Since the experiment is computer controlled, the deviations between individual experimental runs were less than 3%.

Table 1 gives the range of the discharge, water depth, and Reynolds number at the base and peak flow of the hydrograph investigated here.

Table 1

Range of variations of discharge, water depth and Reynolds number during unsteady flow

			Base	Peak
Pump discharge	Q	(l sec ⁻¹)	10	35
Water depth	h	(cm)	12	17
Mean velocity	u	(cms ⁻¹)		
Reynolds Number			1.5×10^4	5.3×10^4

In order to investigate the suspension of fine sediment particles, a layer of sand with $D_{50} = 0.12$ mm was spread on top of the coarse bed on a surface area of the channel extending about 1 m upstream from the location of the ADVP. For the present study, 4 mm and 6 mm thick layers were installed. They were carefully levelled by a carriage moving along the channel. This layer was thick enough to fully cover the coarse bed and it smoothed out gravel bed roughness in that area. The range of velocities and the diameter of the fine sand of the present study correspond well to the area of ripples designated in the bedform stability diagram of Southard and Boguchwal (1990).

The acoustic measurements are complemented by simultaneously taken high-speed videos in the center of the channel at the ADVP location. This allowed visualizing the dynamics of particle suspension during the unsteady flow and the formation of bedforms. A laser lightsheet spanning the water column was produced in the same plane as the acoustic transducer beams in the flow direction in the center of the channel by integrating the optical system into the ADVP housing described above (Fig. 1). Thus, ADVP and optical measurements were taken co-located and they were synchronized. A camera with 640 x 480 pixels was used with a frame rate of 80 Hz. Images 9 cm high by 11.5 cm wide were taken through the glass wall of the channel for flow visualization and PTV analysis. The fine sediment particles that serve as flow tracers are near the upper limit of particle size suitable for tracking the flow dynamics. The recording system of the camera did not allow recording images during the whole hydrograph. Therefore, the beginning of the images recording period was triggered by the ADVP recording system. The point of the trigger can be selected along the whole hydrograph. In the present experiments, image recording was started in the early part of the accelerating flow in order to cover the full period of sediment suspension and ripple formation.

The water in the recirculating installation of the channel was permanently filtered in order to minimize the number of floating particles in the water. In recirculating open-channel systems, gas bubbles are often produced by the pump and the water cascade from the weir at the end of

the channel. However, it was noticed that in the discharge range used in the present experiments almost no gas bubbles were entrained into the water during the duration of the experiments. Therefore, under conditions of no fine sediment suspension, the water in the channel was nearly free of any flow tracers for acoustic and optical flow measurements.

Nine sets of experiments were carried out. The experimental conditions for all experiments are summarized in Table 2. In order to investigate the performance of the ADV under these low particle concentration conditions, the acoustic frequency of the emitter was varied and hydrogen bubbles were used as additional flow tracers as described in Blanckaert and Lemmin (2006). It had previously been shown (Shen and Lemmin, 1997) that small gas bubbles or clusters of gas bubbles are ideal flow tracers, because they follow the fluid motion with negligible inertial lag. In fully turbulent flow, as in the present case, buoyancy forces of the small bubbles are sufficiently small in order not to affect the measurements. Hydrogen bubbles and sediment particles are two tracers with completely different backscattering characteristics. This will allow investigating whether one can distinguish between the contribution of the two tracers to the backscattering and the velocity distribution.

The rising time of the hydrograph was also changed in order to determine the effect of flow acceleration on the formation of ripples. For all experimental conditions, the experiments were repeated five times and combined for the analysis. All ADV data were de-aliased (Franca and Lemmin, 2006) and de-noised (Blanckaert and Lemmin, 2006) to improve data quality.

Table 2

Experimental conditions

	ADV frequency (MHz)	Hydrogen bubbles	Rising time (s)	Fine sediment layer thickness (mm)
E1	1	no	60	No
E2	1	yes	60	No
E3	1	no	60	4
E4	1	yes	60	4
E5	1	no	30	6
E6	1.66	no	60	6
E7	1.66	yes	60	6
E8	2	no	60	6
E9	2	yes	60	6

Figure 2 shows the depth variation $\Delta h = h_b - h_p$ near the ADV for four parts of the hydrograph. This curve is representative for all experiments discussed here. Even though the pump discharge is varied linearly in the course of the accelerating and decelerating stages, water depth changes non-linearly during parts of these periods. When the pump discharge was kept constant at peak flow, water depth still slowly increased and did not reach steady state. The discrepancy between the variation of the discharge and the observed water level over time indicates that along the channel, flow adjustment over the rough bed takes place. This behaviour is different from depth variation during comparable hydrographs reported in the literature (i.e. Nezu et al., 1997; Song et al., 1994). In the present experiments, the channel slope is zero and the velocities are smaller than in those studies.

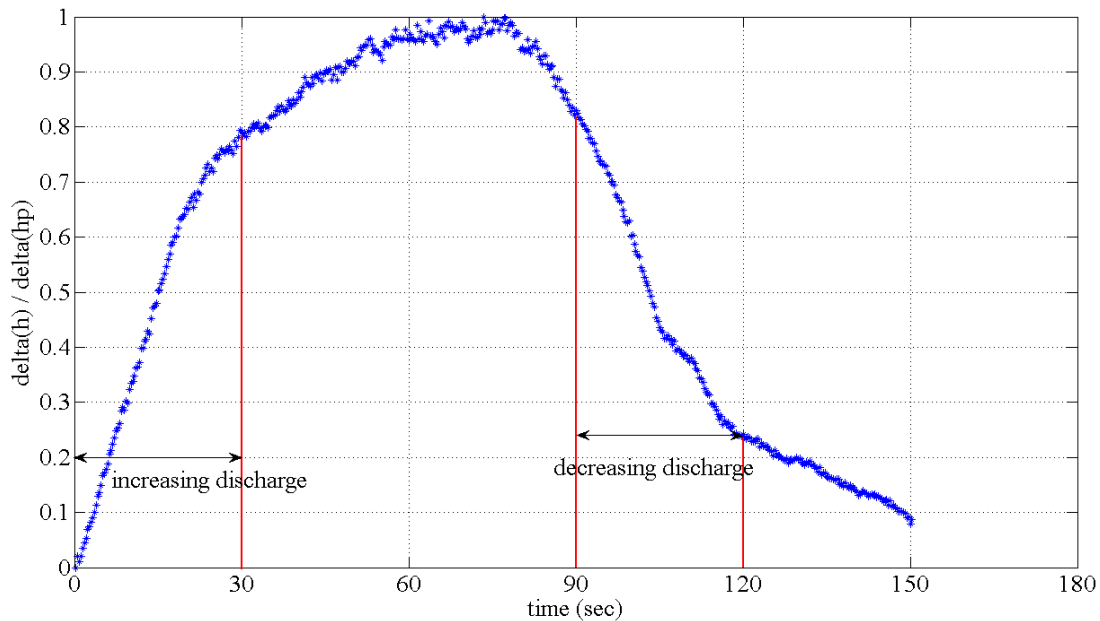


Fig. 2. Depth variation $\Delta h = h_b - h_p$ near the ADVP for 4 parts of the hydrograph.

4. RESULTS AND DISCUSSION

4.1. Flow and particle velocity measurements with the ADVP

In this paper the results of the steady peak flow range of the hydrograph for all experiments are compared. Figures 3 and 4 show the distribution of mean velocity and backscattering intensity, respectively, against the water depth that were obtained by averaging over the peak steady flow range. Starting with measurements at 1 MHz, it can be seen that there are hardly any background tracers in the water. The mean velocity profile for E1 is the result of averaging over mostly no velocity detection and some rare velocity data when occasional particles allowed velocity calculations during the recording. This indicates that it is useful to analyze the recorded timeseries in detail when nothing is known about the tracer concentration in the water in order to avoid a wrong interpretation of the data.

In E2, the hydrogen bubbles that were added are seen to be good tracers to obtain a correct open-channel flow profile over the whole water depth that corresponds to the measured discharge. No fine sediment was placed on the bed in this experiment. When a fine sediment layer is added to the bed in E3 and hydrogen bubbles are turned off, velocity data are only obtained in the lower half of the water depth due to the suspended sediment particles. In the upper half of the water depth, the backscattering situation corresponds to E1 and only the background velocity is recorded. A strong velocity gradient near the bed with maximum of the profile is found at around $0.25 h$ velocities then rapidly decrease and fall to zero at about $0.6 h$, this indicates that no sediment transport is detected by the ADVP above this level. It may be mentioned that during the initial phase of the acceleration range when no particle suspension occurred, no velocity data could be obtained with the ADVP. When this experiment is repeated with hydrogen bubbles added (E4), a full depth profile is once again obtained. The velocities are slightly higher than in E2, because bottom roughness is decreased by the presence of the fine sediment layer.

When unsteadiness is increased in E5, and all other conditions are kept constant, the velocity profile changes compared to E3. Strong velocities are now detected throughout the water column. However, except for the near bottom layer, these are not the velocities corresponding to the discharge, because the profile is significantly different from E4. Therefore, this profile is an indication that due to the higher unsteadiness, sediment particles are now transported higher into the water column when compared to experiment E3. The mean ripple length was measured in both experiments. For E3, a mean length of 7.4 cm was obtained and for E6 the mean length was 5.6 cm for a comparable ripple height. Therefore higher unsteadiness produces shorter ripples with a steeper slope. This may affect the development of burst events in the flow field and result in sediment transport higher up into the water column. The two experiments E3 and E5 were repeated by using the alternative sediment layer thickness. This did not affect the results. Therefore, the thickness of the sediment layer has no effect on the flow dynamics in our experiments, because during this early stage of the ripple development, the sediment layer is not eroded down to the gravel bed. If the steady peak flow was maintained for periods of hours, ripples eventually turned into dunes as reported in the literature.

In order to investigate whether the contribution of two different tracers made evident above is dependent on the acoustic characteristics of the instrument, the above experiments were repeated at different acoustic frequencies. The frequency dependence of backscattering has been demonstrated before (Lhermitte and Lemmin, 1993) and the resonance effect for gas bubbles had been pointed out. Therefore, the acoustic frequency was increased in two steps, first to 1.66 MHz and then to 2 MHz. The ADV hardware allows to work with frequencies up to 3 MHz. However, the drop in efficiency of the present transducer set with frequency increase was too strong to investigate even higher frequencies. At 1.66 MHz, the profile of E6 that corresponds to E3 at 1 MHz, is close to that of E3. Similarly, E7 and E4 correspond well for the lower half of the profile. The deviation of E7 from the expected profile is difficult to explain. One may consider that at that level E6 goes back to the background profile. In the upper half of the profile, hydrogen bubbles are the essential tracers and the deviation from the true profile is the effect of reduced backscatter from hydrogen bubbles with increased acoustic frequency. At 2 MHz, once again E8 is close to E3. E9 shows a continuation of the trend from E4 to E7 in that deviation from the true profile occurs already in the inner layer. The upper part of the E9 profile cannot be explained. It can be expected that a further increase of the acoustic frequency may suppress backscattering from hydrogen bubbles and thus produce a profile that corresponds to the one obtained only from sediment particles (E3), even in the presence of hydrogen bubbles.

All velocity profiles for experiments with fine sediment added have a similar gradient near the bed. This indicates that the profile form in this layer is determined by suspended sediment particle transport. By comparing E3 and E4, it appears that sediment does not affect the mean flow characteristics. During steady peak flow, it was found that mean flow velocity profiles for experiments E2, E4, E5 and E7 followed a logarithmic law in the inner layer. This allows calculating the friction velocity from these profiles. The results will be discussed below.

The corresponding backscattering intensity profiles are plotted in Fig. 4. For the two experiments with hydrogen bubbles (E2 and E4), backscattering intensity is clearly dominated by the presence of the bubbles and it shows the same profile values for both experiments. Therefore, from these backscattering profiles it cannot be determined whether suspended sediment particle transport occurred or not. All experiments, except in clean water with no flow tracers (E1), show that sediment transport is concentrated in the near bottom layer (Fig. 4). For E5, backscattering intensity greatly increases in the central layers of the water column,

mainly due to the shorter ripples which are formed on the bed and which influence sediment suspension, as discussed above. A comparison of the results of E3 in Figs. 3 and 4 shows that backscattering intensity decreases more rapidly than mean particle velocity with distance from the bed. This indicates that sediment transport above about 0.2 h is no longer a reliable tracer for mean velocity determination. Therefore, the upper part of the velocity profile above $z = 2$ cm for E3 in Fig. 3 should be interpreted with caution. From the backscattering intensity profile, it has to be expected that particle presence in this layer is strongly intermittent. This affects the mean velocity calculation as discussed above. Actual velocities in this layer may be higher and the mean value over the whole profile shown here is not representative, even though the profile is smooth. This indicates that more sophisticated techniques than long-term averaging should be applied for determining the actual velocity profile. This example shows that only the simultaneous analysis of velocity and backscattering allows determining the correct interpretation. The higher acoustic frequency data are also included in this figure. However, these profiles do not provide realistic information. This is due to the low transducer efficiency at these acoustic frequencies.

In order to relate backscattering intensity to particle density in the water column, the number of particles in the water was determined from PTV images taken in parallel. Two different tendencies can be observed when comparing the backscattering intensity which was measured by the ADV (Fig. 4) and particle numbers which were calculated by the PTV technique (Fig. 5). First, hydrogen bubbles do not contribute to the particle numbers indicated in Fig. 5. This shows that hydrogen bubbles cannot be detected by the camera system used in this study. Therefore, hydrogen bubbles are much smaller than the fine sediment particles. Secondly, in the layer just above the bed, particle numbers are similar for E3 and E4 and are higher for E5. In E5, the layer of high particle numbers is also extended upward into the water column. This confirms the ADV results discussed above. However, it also shows that mean particle numbers and mean backscattering decrease more sharply than mean velocity. The low particle numbers found in the PTV analysis confirm that the present experiments are carried out in a low particle density environment. No attenuation compensation is needed in this situation.

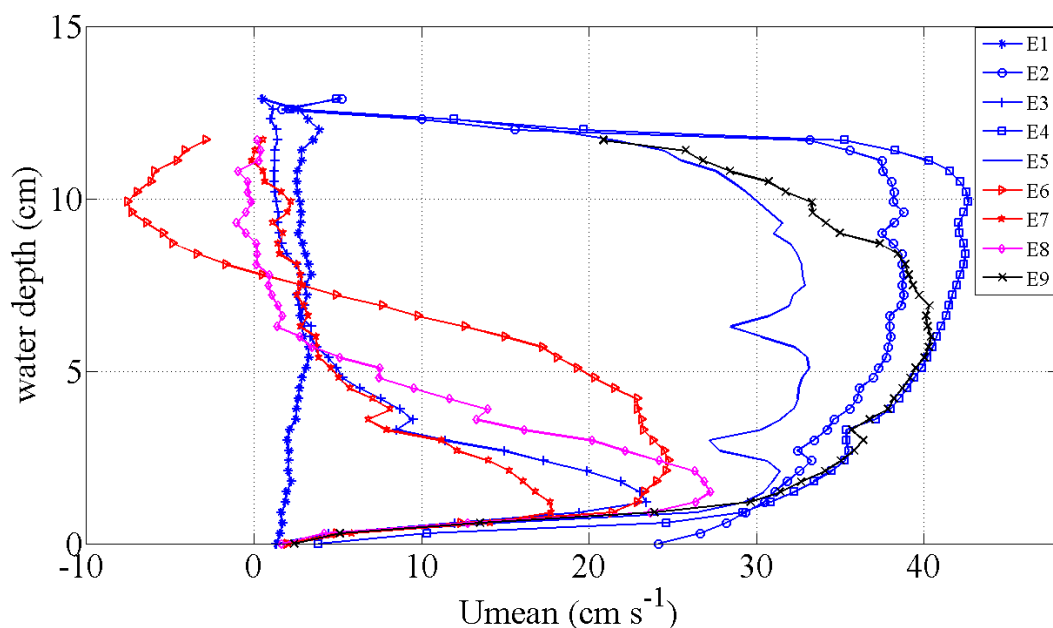


Fig. 3. Mean velocity profiles during steady peak flow for all experiments. For details on the legend see Table 2.

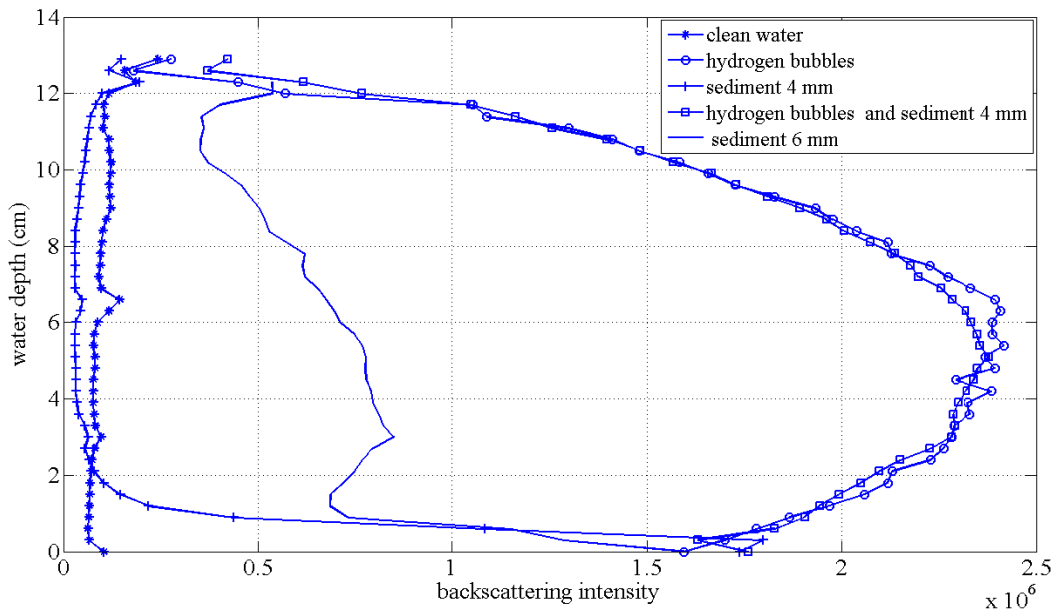


Fig. 4. Backscattering intensity profiles during steady peak flow for all experiments. For details on the legend see Table 2.

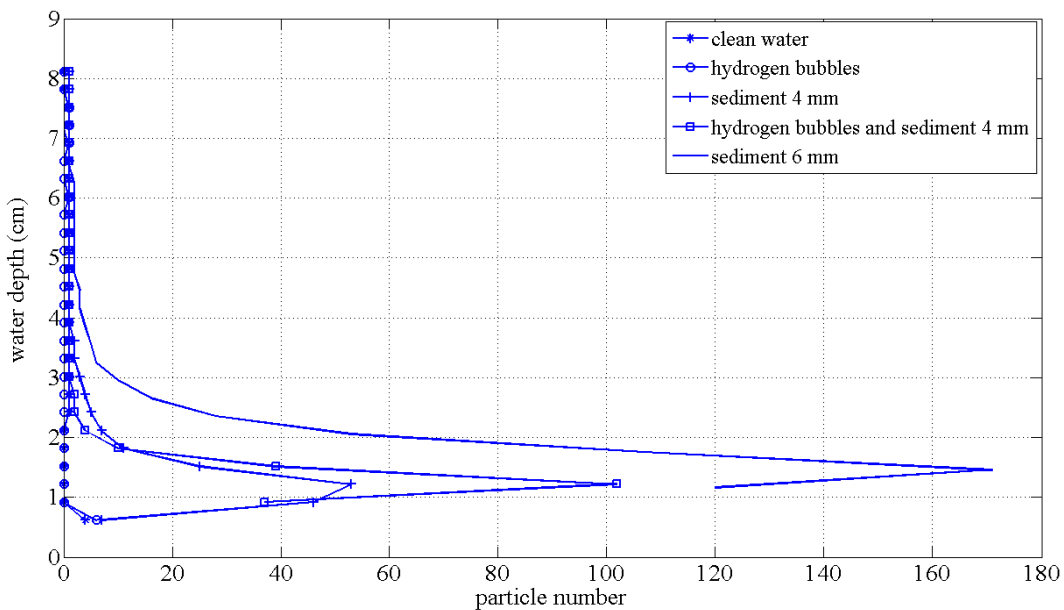


Fig. 5. Mean particle number for 1MHz experiments obtained from PTV images.

In order to further investigate the time stability of velocity and backscattering profiles, mean profiles over ten consecutive profiles were calculated for both data sets. This corresponds to a 3 Hz resolution that is indicative of coherent structure scales. Results for E3, E4 and E5 are presented in Figs. 6, 7 and 8, respectively. In each case, velocity and backscattering data are presented. All three velocity profile timeseries show a rapid increase in the velocity profile in the layers near the bottom all along this section of the hydrograph. Over time, velocity profiles change little from the bottom to a depth of 2 cm. In all three experiments, velocities vary little between individual time slices, indicating that sufficient tracer particles are present at all times. Above this level, differences between the experiments can be seen. In E3 (Fig. 6a), velocity rapidly falls to zero in the upper part of the water column, because no sediment is

suspended into this part of the water column. For E4 (Fig. 7a), smooth velocity profile timeseries over the whole water column are seen. In E5 (Fig. 8a), strong, but variable velocity profiles are observed for the different time slices in the upper layers. Variability occurs along the profiles and also between profiles.

The backscattering timeseries explain the observed differences in the velocity distribution. For E3 (Fig. 6b), significant backscattering only occurs directly above the bed. Although the velocity timeseries was rather smooth, strong variability in time is seen in the backscattering intensity in the near bottom layer. This indicates that backscattering and thus sediment suspension is strongly event-structured. As expected, backscattering in E4 (Fig. 7b) is more homogeneous in time. The maximum of the backscattering intensity is found in the mid-depth range of the profile. In the case of strong unsteadiness, E5 (Fig. 8b), the near bottom backscattering time development is similar to that observed in E3. However, significant backscattering, once again organized in events, also occurs in the remaining water column. When sediment particles are the only flow tracers, individual peaks in the backscattering intensity document a strong temporal and spatial variability and an event structure of the particle suspension process. When the results for E3 (Fig. 6) and E5 are compared (Fig. 8), the effect of unsteadiness of the accelerating flow is apparent: stronger unsteadiness produces particle suspension into higher depth levels that allows tracing the velocity distribution over a wider depth range. From these results, it appears that sediment flux timeseries calculation will be strongly variable due to the variability of the particle density and not because of variability of the velocities.

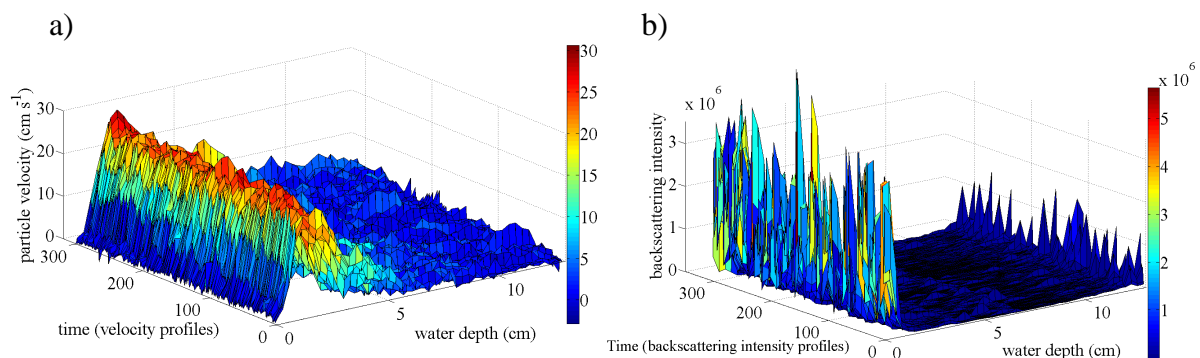


Fig. 6. Particle velocity and backscattering intensity during steady peak flow range for E3.

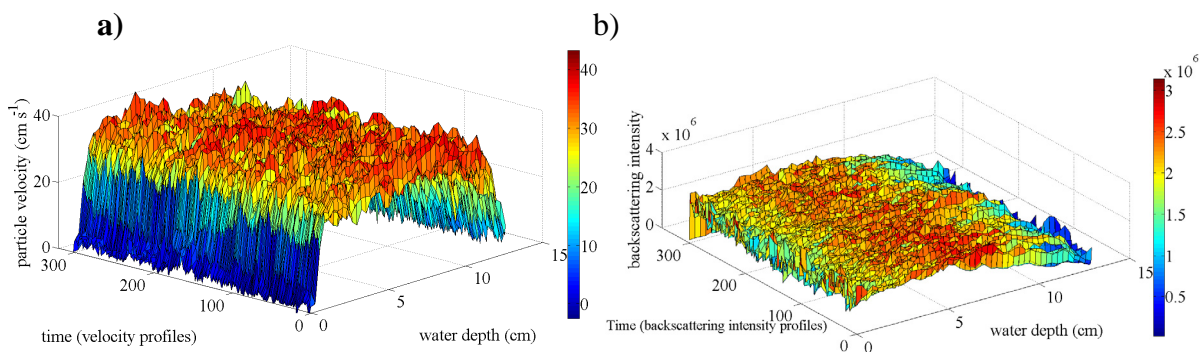


Fig. 7. Velocity and backscattering intensity profiles during steady peak flow for E4.

a)

b)

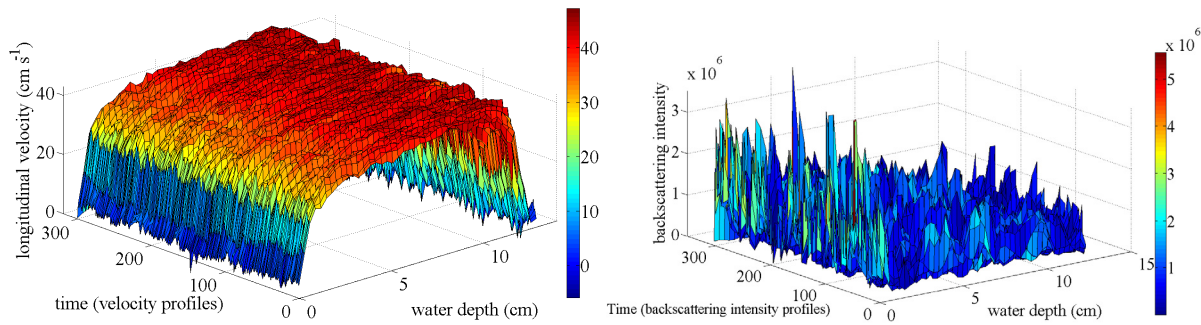


Fig. 8. Particle velocity and backscattering intensity during steady peak flow range for E5.

Friction velocity was determined using the logarithmic mean velocity profile method for Experiments 2, 4, 5 and 7, using profile data in the inner layer. In the remaining experiments, the profile range was not sufficiently long to apply the method, or the profiles did not follow the logarithmic law. These calculations do not take into consideration the contribution of form drag caused by the presence of ripples. Calculations were again carried out over subsequent time slices of ten profiles each. The results are presented in Fig. 9. Friction velocity u_* in all experiments falls into the same range, but it shows some time variability. For E5, time adjustment to steady peak flow appears to be slower than for the less unsteady cases E2 and E4. However, the final level for E5 is similar to that of the less unsteady experiment. The level of friction velocity for E7 is systematically higher. This may be caused by a different position of the ADVP along the ripple length in this case. It has to be recalled that the formation of ripples is random in the different experiments and the position of measurement with respect to the ripple profile cannot be controlled, as will be discussed below.

Figure 10 shows friction velocity for all time slices against the depth variation $\Delta h = h_b - h_p$. In this case, the friction velocity in the accelerating flow range has been included in order to show the effect of the unsteadiness. In the accelerating range, the peak of the friction velocity is attained before the maximum of the water level, as found by Nezu et al. (1997). During the steady peak flow range above $\Delta h = 0.8$, friction velocity varies as was detailed in Fig. 9. Friction velocity forms a loop over the whole hydrograph and changes differently in the accelerating and decelerating flow ranges. Friction velocity u_* does not return to the initial value of the base flow after the decelerating ranges, because water depth continues to slowly decrease past the end of the decelerating ranges and reaches base flow depth much later (Fig. 10) as seen in Fig. 2. It decreased linearly in the decelerating flow range and is similar for 30 s (E5) and 60 s (E4). However, it shows a more complex relationship in the accelerating flow range, which is of importance for the present analysis. It is noticed that during the initial phase of the acceleration, both curves closely follow each other. The large difference between the two hydrographs in the later phase of the unsteady accelerating ranges illustrates the effect of the difference in unsteadiness. For comparable mean velocities in the accelerating and decelerating flow ranges, friction velocities are different. During this later phase, the value of the friction velocity for the 60 s hydrograph attains the value it has during the following steady peak flow. Thus, for the 60 s hydrograph, acceleration only affects the initial phase of the friction velocity. Even though flow velocities come to the same value at the peak flow end of the unsteady flow ranges, friction velocities of the unsteady flow ranges in the 30 s hydrograph are larger than those in the 60 s one. For the 30 s hydrograph, friction velocities strongly increase during the last two-thirds of the accelerating range, and the maximum values are significantly larger than those during the steady peak flow. This shows that mean flow adjustment during the peak flow phase is different in the two hydrographs. Friction velocity u_*

which affects sediment suspension is significantly different during acceleration in the two cases and the length of the ripples are shorter in the 30 s hydrograph than in the 60 s.

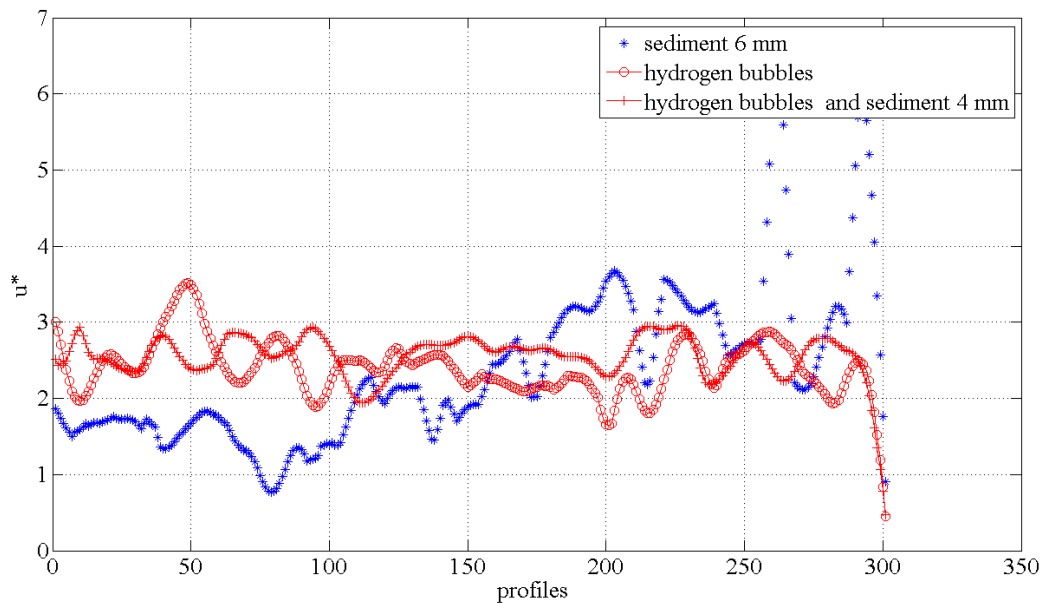


Fig. 9. Friction velocity u_* distribution for peak steady flow for 3 sets of experiments.

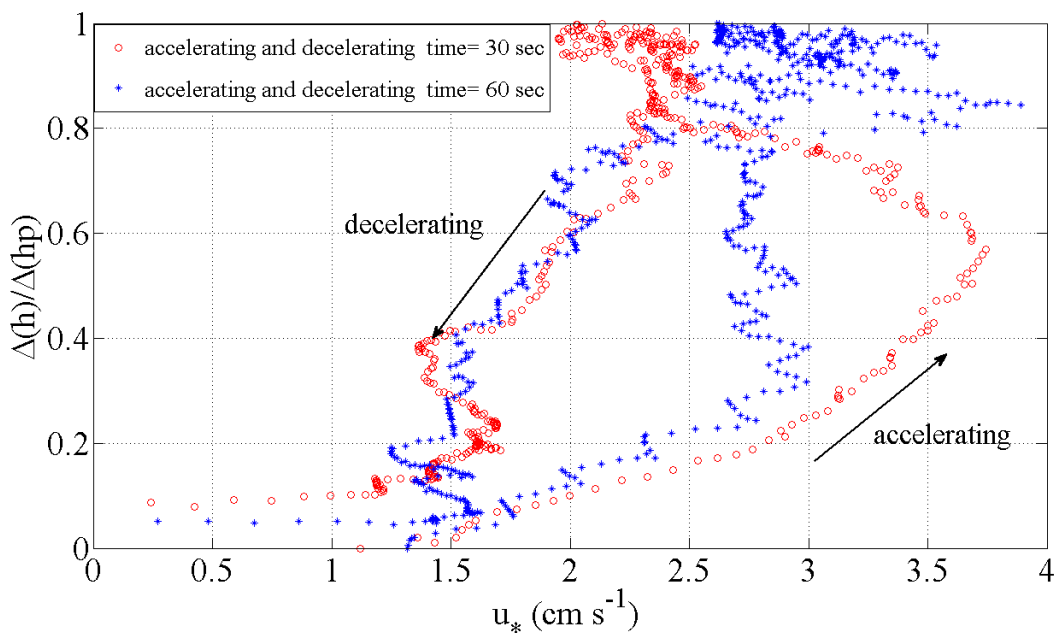


Fig. 10. Friction velocity u_* distribution for the unsteady ranges of 30 s and 60 s.

3.2 Video imaging

In this study, the PTV technique was used to calculate particle velocity and analyze the dynamics of suspended sediment in order to complement the ADV measurements discussed above. An example of velocity vectors calculated by PTV is presented in Fig. 11, where two images that were taken at an 80 Hz frame rate during the early phase of the peak flow range are compared. The time interval between these two images is 0.05 s. As seen in Fig. 11, suspension is nearly uniform in a shallow layer above the bed (about 2 cm high). Particle transport remained strong in this near bottom layer, in agreement with the ADV observations. Suspension into the water column above occurs in burst-like events. A sequence

of bursts can be identified in Fig. 11a and bursts are strongest just behind the ripple crest that is on the right side of these images (see Fig. 14 for bed details). In Fig. 11 b, the final burst on the right side has grown significantly in size and the shape of the others has changed. This rapid change in burst dynamics cannot be recorded with ADV measurements. Furthermore, the finite width of the ADV beam (between 7 mm and 10 mm) averages over much of the fine details seen in these images and the low particle density in the upper part of the images does not allow reliable ADV measurements as discussed above. In these images, turbulence intensity and the strength of the burst events are not sufficient to suspend a significant number of particles over the full water depth.

In order to compare the results of PTV measurements with those obtained with the ADV, mean velocity calculations were carried out. For this purpose, the image was sliced in the vertical into 3 mm thick slices. This slice thickness is comparable to the height of the gates of the ADV. In the horizontal, the image was sliced into 10 mm wide strips. This width is close to the beam width of the ADV. Figure 12 shows the mean particle velocity profiles in six representative positions in the horizontal direction of the images. The positions are indicated in Fig. 14. These profiles are the average of over 2000 images. The profile form is similar to the mean velocity profile measured by the ADV (Fig. 3) for E3. Velocity profiles are similar in all positions with a slight trend of increase from right (above the ripple) to left (in the trough). However, it has to be recalled that the same averaging procedure that was used for the ADV measurements was also applied to the present analysis. Therefore, as indicated above, the velocities above the maximum of the profiles has to be interpreted with caution. This can be seen when comparing Figs. 11 and 12. In Fig. 11, velocity vectors in the upper part of the bursts are the strongest, as opposed to the mean profiles in this layer (Fig. 12). This illustrates that the complementary application of the two different methods can help in interpreting the results.

In Fig. 13 are shown the sediment concentration profiles at the same positions, calculated from the averaged particle density for those positions. The image was again split up as for the velocities indicated above. The highest concentration is found in the position where ripples are formed ($x = 10.2$ cm; Fig. 14) with a strong gradient towards the trough. This confirms the burst structure pattern seen in Fig. 11 with strongest bursts near the ripple crests. The mean backscattering profiles recorded with the ADV for the same section of the hydrograph are similar to the one at $x = 10.2$ cm. However, the ADV cannot reproduce the details seen in the analysis of the video images. Therefore, a combination of the two methods greatly enhances the understanding of the underlying processes.

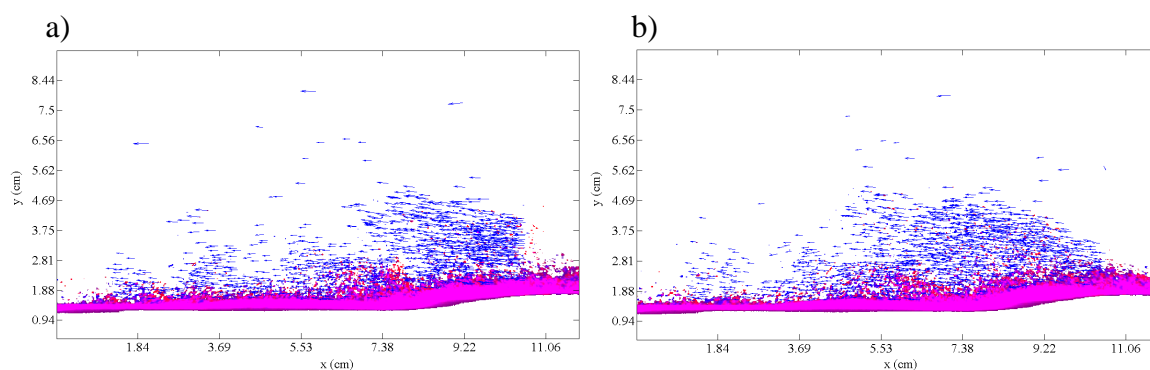


Fig. 11. Example of PTV results during the early phase of the steady peak flow range. Arrows indicate particle velocity vectors.

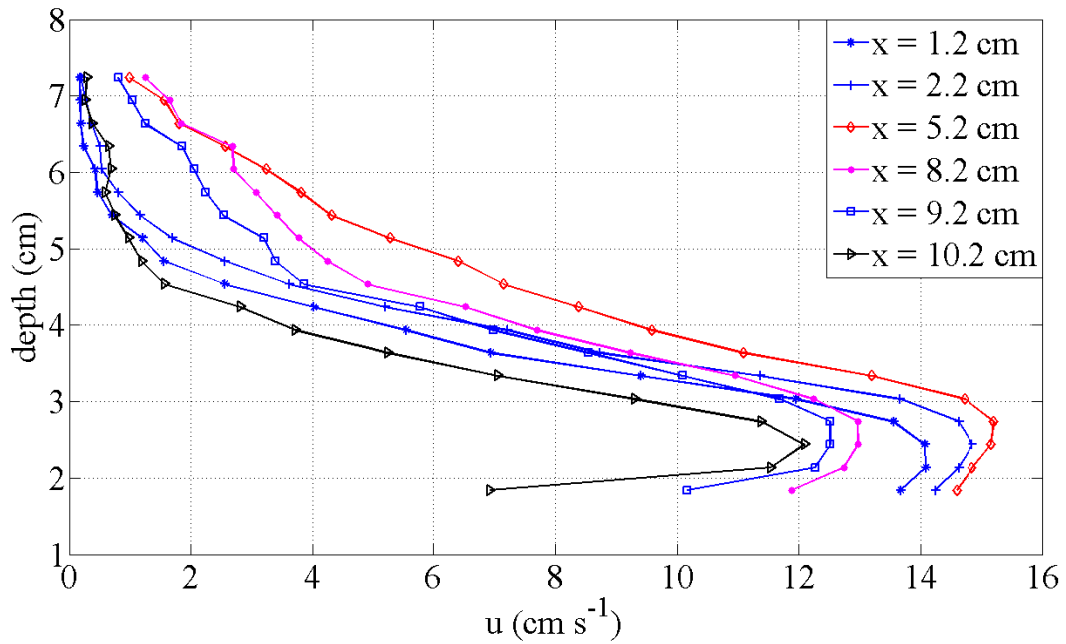


Fig. 12. Particle velocities in six positions of images. For position see Fig. 14; for details see text.

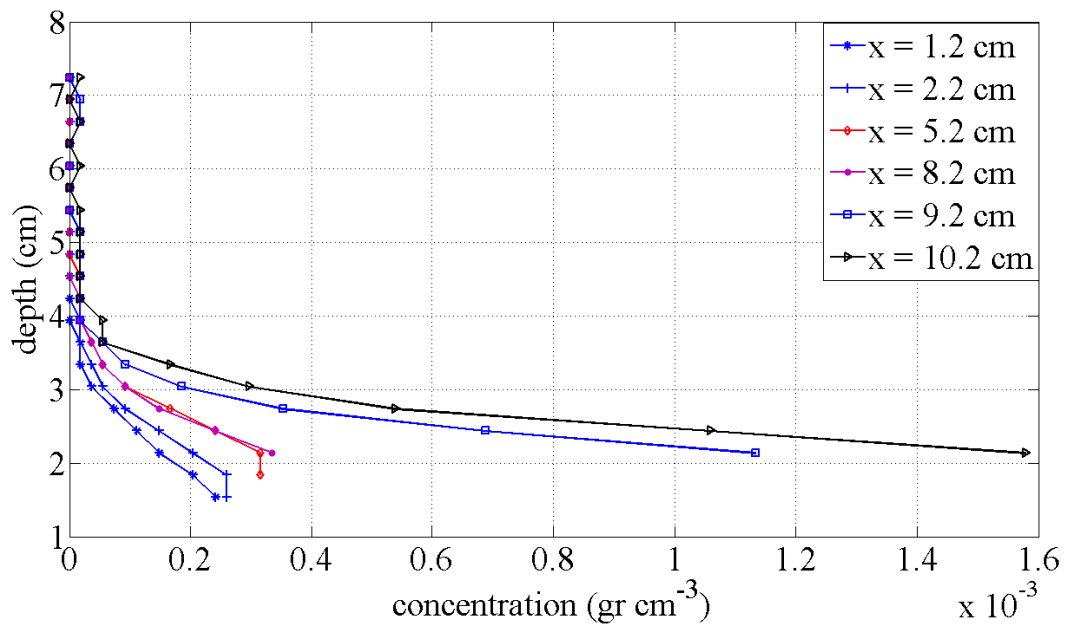


Fig. 13. Particle concentrations in the same position as Fig. 12. For position see Fig. 14; for details see text.

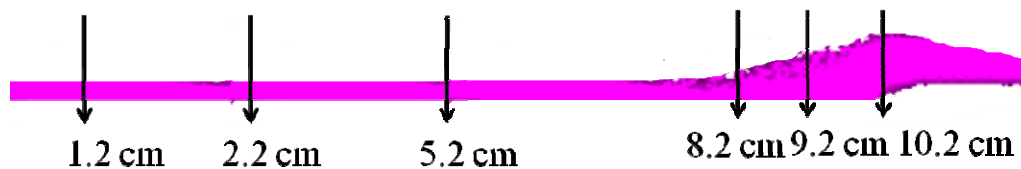


Fig. 14. Bed form formation during the early phase of the steady peak flow range indicating the positions shown in Figs. 12 and 13.

In order to learn more about sediment suspension and ripple formation, two additional video recordings were carried out. In the first one, the PTV camera was zoomed in the vicinity of the bed. Image size in this case was 1.7 cm high by 2.3 cm wide. A recording with a 40 Hz frame rate was made, covering the period from the beginning of the sediment motion on the bed during acceleration range to the ripple movement during the steady peak flow range. Multiple exposure of individual particles was produced in order to show particle trajectories. Several images from this recording are presented to supplement the analysis above.

The videos showed that during the initial saltation of particles, the upper layer of the whole bed began to move (Fig. 15a). Particles may rise about 1 cm above the bed. Saltation above the bed level occurs in bursts. The ripple started forming 2.5 s after this image (Fig. 15b). Most particles roll along the ripple to the crest and then fall down the steep slope into the trough. However, other particles do not roll, but form curved trajectories when descending from the crest into the trough in the lee side of the crest. Curved trajectories and backward transport of particles indicate that a vortex is formed in the lee side of the crest. This type of particle motion becomes more evident as the ripple grows (Fig. 15c). Particles now also move higher into the water column and those well above the bed follow straight trajectories across the image. A strong event structure of the particle motion around the crest/trough area is evident (but unfortunately cannot be shown here). The origin of the particle ejections into the higher water column is found on the back of the ripple in an area known as the reattachment point (Best, 2005). Two examples are given in Figs. 15d and 15e. They demonstrate that particles are lifted off along steep, curved trajectories from a limited area of the bed. Therefore, the vertical velocity component is strong in the near bottom layer. Once again, this process is strongly event structured. The curved trajectories that are repeatedly seen in Figs. 15d and 15e suggest that vortex motion in the water is controlling particle motion. Vortex motion in relation to coherent structures has been well documented (Nezu and Nakagawa, 1993). Therefore, it can be expected that coherent structures affect sediment suspension. These recordings indicate that the ejection phase of the coherent structures is focussed on the reattachment point. Once again, these details cannot be obtained with only ADV measurements in the present study. In field studies where these processes occur at larger scale, ADVs may resolve these scales. However, laboratory studies such as the present one have to be carried out before, in order to guide the field studies in data taking and the interpretation.

These video recordings were also taken at the end of the hydrograph when the flow was back to base flow. Images showed that ripples remained in place even though the flow had decelerated. Particle motion and saltation continued to occur, gradually advancing the ripple. This indicates that even though the friction velocity was well below the critical value for sediment motion at base flow (Fig. 10), form drag produced by the ripples was strong enough to maintain sediment motion. Considering that the light sheet was placed in the center of the channel and that PTV images and video images were taken at a distance of 35 cm from the channel center, it is evident that particle density in this flow was low. This is also confirmed by the images in Fig. 15 where individual particles can be followed in their trajectories without interference from other particles, even during burst events.

In a second video recording, large-scale images were taken over a wider section of the bed. The objective was to provide some information on the ripple formation. It is generally accepted in the literature (Best, 2005, Garcia, 2007) that ripples are formed from some instability on the bed. For this experiment, the whole 6 mm thick fine sediment bed was covered with a very thin layer of the same sediment particles that had been painted in black. Starting the hydrograph, it was observed that towards the end of the acceleration range, ripples occurred nearly simultaneously along the whole bed and quickly formed a pattern as

seen in the top view of the channel (Fig. 16). Each of the dark areas finishes on the left with a ripple crest and the steep slope at the angle of repose. This slope is only a few mm wide in the present image. The white areas cover the trough in the leeside of the crest. The whole pattern slowly moves in the direction of the flow, but the distribution does not change significantly. Areas marked in red show “remains” of the initial reference bed level. This indicates that crests are rapidly piled up above the reference bed level with particles that have been moved horizontally from the present trough area onto this part of the downstream ripple. Troughs are dug below that reference level. Over time during the steady peak flow of about three minutes, the colour of the dark area changes little, indicating that not much of the material from the trough area is deposited onto the crest area. It appears that most of the material from the trough area is suspended in bursts higher up in the water column and spread out over a wider area as described above.

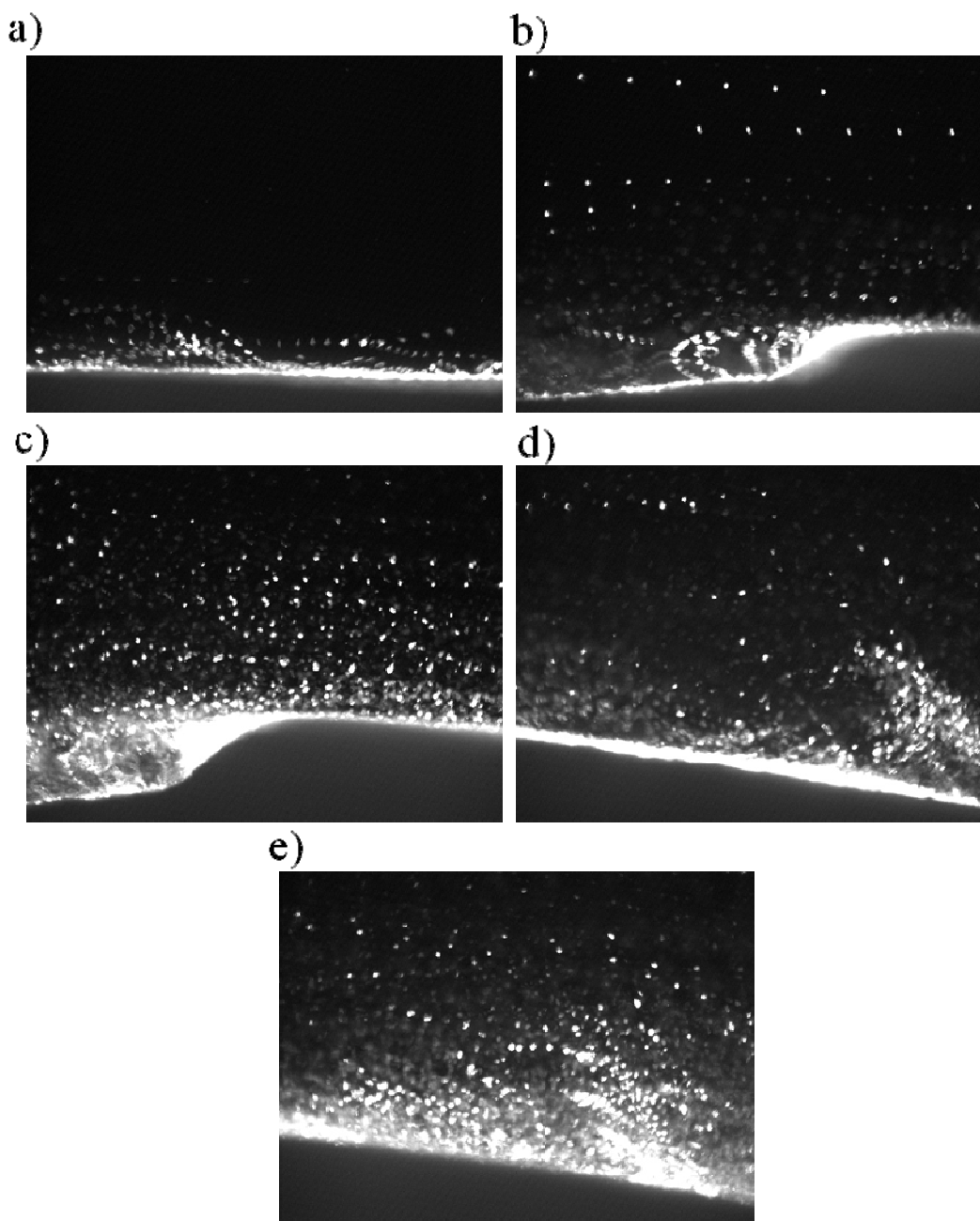


Fig. 15. Close-up view of sediment particle trajectories related to ripple formation. For details, see text.

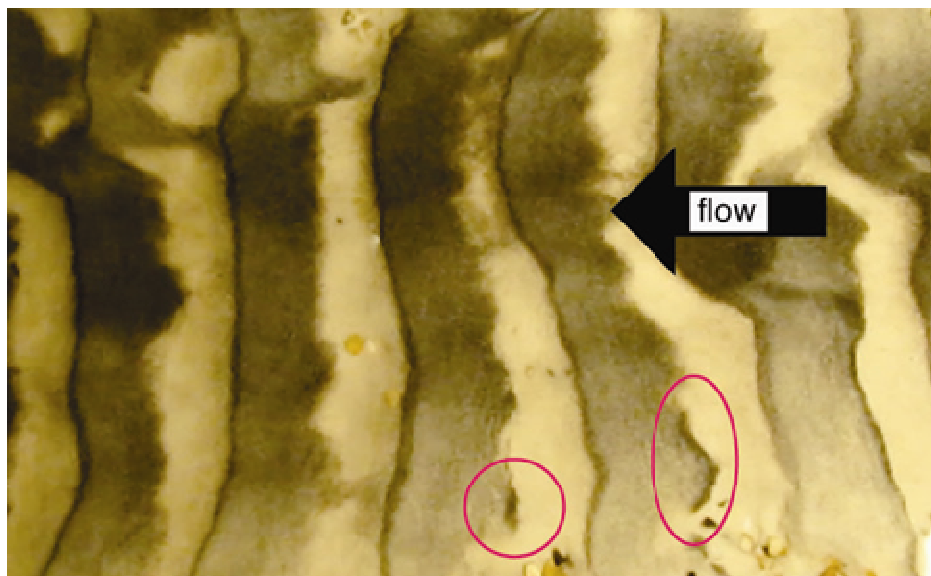


Fig. 16. Large scale image of ripple formation, seen from the top. Mean spacing of the ripples is about 6 cm. For details, see text.

5. CONCLUSION

In this study, the onset of fine sediment transport and the development of ripples were investigated by first accelerating the flow and then holding it steady. Ripples formed quickly, within about 3 sec after fine sediment particle saltation started. The wavelength of the ripples depended on the rate of acceleration. Faster acceleration produced shorter ripples due to a much stronger friction velocity. Sediment suspension occurred in bursts and extended up into the intermediate layers of the water column. The height and the intensity of the upward suspension related to the ripple length. The shorter ripples produced stronger and higher suspension. Once established, the ripple pattern progressed slowly in the direction of the flow, mainly by sediment particles rolled up the ramp of the ripple and dropped over the crest. Ripples did not change in appearance or dimension for the duration of the experiments. No difference was found when the thickness of the fine sediment layer was changed from 4 to 6 mm.

Fine sediment particles and hydrogen bubbles were used individually and combined as flow tracers in the acoustic measurements. When used individually, hydrogen bubbles provided full depth flow and backscattering information, whereas sediment particles traced only the lower layers of the flow, indicating sediment suspension. When both tracers were combined, hydrogen bubbles could only be distinguished from sediment particles, except when the acoustic frequency was changed. Therefore, in field studies where different acoustic tracers such as algae, gas bubbles and sediment particles may exist at the same time and where all of them may have a certain size range, the detection and quantification of an individual tracer based on acoustic measurements alone may be difficult. It has been shown that multi-frequency systems may help to solve this problem. However, transducer efficiency may limit the range that can be covered and therefore the potential of tracer separation.

The intermittency in sediment suspension was observed in the backscattering intensity of the acoustic system only when sediment particles were used as tracers. At the same time, velocities showed much less intermittence. Therefore, particle flux in this flow is controlled by particle dynamics. However, due to the low particle density, backscattering could not be

translated into sediment concentration. Thus, in low particle environments, particle flux calculations cannot be carried out. Nevertheless, the ADV is sensitive enough to capture clean signals for the time history of sediment suspension in these low particle density conditions and valuable information about the sediment transport dynamics can be obtained.

The event structure in fine sediment suspension is seen by the PTV method. PTV velocity vectors varied in speed and orientation, but were organized in large coherent packets, mainly in the near bed layers, but also extending well above the bed, supporting the concept that coherent structure events contribute to sediment suspension over ripples. The results indicate that sediment suspension in the final phase of unsteady flow and the following steady flow is controlled by the same large scale turbulence processes as indicated for steady flow in the literature. The low particle number in the images confirmed the low particle density seen by the ADV.

The two methods provide complementary information, particularly when applied simultaneously. Optical methods helped to verify and to interpret the ADV data and to visualize the physical processes leading to suspension. New and detailed results made possible by combining the ADV and imaging techniques provide valuable insight into the dynamics of fine sediment suspension and ripple formation initiated by unsteady flow conditions that were previously not possible. ADV measurements allow long timeseries analysis, whereas the spatial details seen in the PTV results cannot be resolved in the ADV measurements. The characteristics of the ripple in the present study are too small to be resolved by the ADV. They are well traced by the PTV. In field studies, ripple dimensions may be large enough to be investigated by ADV. However, laboratory studies such as the present one may guide in the field measurement strategies and data interpretation. The combination of acoustical and optical methods provides for an ideal approach to study sediment dynamics in tidal flow conditions, particularly ripple formation and suspension in low concentration flow.

6. ACKNOWLEDGMENTS

This study is supported by the European Commission (FP6; RII3; Contract no. 022441) HYDRALAB III-SANDS. We sincerely thank Navid Borhani for providing the optical system and his assistance. The technical support of Claude Perrinjaquet is greatly appreciated.

7. REFERENCES

- Adrian, R.J., 2005. Twenty years of particle image velocimetry. *Exp. in Fluids* 39, 159-169.
- Afzalimehr, H., Anctil, F., 2000. Accelerating shear velocity in gravel-bed channels. *J. Hydrol. Sci.* 45, 113- 123.
- Akhavan, R., Kamm, R. D., Shapiro, A. H., 1991. An investigation of transition to turbulence in bounded oscillatory Stokes flows. I: Experiments. *J. Fluid Mech.* 225, 395-422.
- Allen, J.R.L., 1968. *Current ripples: their relation to patterns of water and sediment motion.* Elsevier, New York.
- Baas, J.H., 1999. An empirical model for the development and equilibrium morphology of current ripples in fine sand. *Sedimentology* 46, 123-138.
- Bagherimiyab, F., Lemmin, U., 2010. Aspects of turbulence and fine sediment resuspension in accelerating and decelerating open-channel flow. In: *Proceedings of Riverflow 2010*, 8-10 September 2010, Braunschweig, Germany.
- Bagherimiyab, F., Albayrak, I., Lemmin, U., 2008. Bed shear velocity estimates in rough open-channel flow obtained from Acoustic Doppler Velocity Profiler data and direct bed

- shear stress measurements. In: Proceedings of Riverflow 2008, Izmir, Turkey. Vol 2., 151-159.
- Bagnold, R.A., 1941. The physics of blown sand and desert dunes. Methuen, New York.
- Best, J., 2005. The fluid dynamics of river dunes: a review and some future research directions. *J. Geophys. Res.* 110, F04S02, doi: 10.1029/2004JF000218.
- Blanckaert, K., Lemmin, U., 2006. Means of noise reduction in acoustic turbulence measurements. *J. Hydr. Res.* 44, 3-17.
- Bricault, M., 2006. Rétrodiffusion acoustique par une suspension en milieu turbulent: application à la mesure de concentration pour l'étude de processus hydro-sédimentaires. PhD thesis, Grenoble Institut National Polytechnique, Grenoble.
- Cellino, M., Lemmin, U., 2004. Influence of coherent flow structures on the dynamics of suspended sediment transport in open-channel flow. *J. Hydr. Eng.* 130, 1077-1088.
- Cowen, E.A., Monismith, S.G., 1997. A hybrid particle tracking velocimetry technique. *Exp. in Fluids* 22 199-211.
- DuBuat, P., 1786. Principes d'hydraulique. L'imprimerie de monsieur, Paris, France.
- Franca, M.J., Lemmin, U., 2006. Eliminating velocity aliasing in acoustic Doppler velocity profiler data. *Meas. Sci. Technol.* 17, 313-322.
- Franca, M.J., Ferreira, R.M.L., Lemmin, U., 2008. Parameterization of the logarithmic layer of double-averaged streamwise velocity profiles in gravel-bed river flows. *Advances in Water Resources* 31, 915-925.
- Garcia, M.H., 2007. Sediment transport and morphodynamics. In: M.H. Garcia (Ed.) *Sedimentation engineering. ASCE Manuals and Reports on Engineering Practice No 110*, pp. 21-146.
- Harris, K., Butman B., Traykovski P., 2003. Winter-time circulation and sediment transport in the Hudson Shelf Valley. *Cont. Shelf Res.* 23, 801-820.
- Hay, A.E., Sheng, J., 1992. Vertical profiles of suspended sand concentration and size from multifrequency acoustic back-scatter. *J. Geophys. Res.* 97, 15661-15677.
- Hurther, D., Lemmin, U., 1998. A constant beam width transducer for 3D acoustic Doppler profile measurements in open channels. *Meas. Sci. Tech.* 9, 1706-1714.
- Hurther, D., Lemmin, U., 2001. Equilibrium near-bed concentration of suspended sediment, *J. Hydraul. Eng.* 16, 430 - 433.
- Hurther, D., Lemmin U., 2008. Improved turbulence profiling with field adapted acoustic Doppler velocimeters using a bi-frequency Doppler noise suppression method. *J. Atmos. Oceanic Technol.* 25, 452-463.
- Hurther, D., Lemmin, U., Bricault, M., 2006. Multistatic acoustic Doppler profilers for fine-scale studies of velocity and particle flux processes. In: Proceedings UAM07, Heraklion, Greece.
- Hurther, D., Lemmin, U., Terray, E.A., 2007a. Turbulent transport in the outer region of rough-wall open-channel flows: the contribution of Large Coherent Shear Stress Structures (LC3S). *J. Fluid Mech.* 574, 465-493.
- Hurther, D., Michallet, H., Gondran, X., 2007b. Turbulent measurements in the surf zone suspension. *J. Coast. Res.* S150, 297-301.
- Hurther D., Thorne, P.D., Bricault, M., Lemmin, U., Barnoud, J.M., 2011. A multi-frequency acoustic concentration and velocity profiler for boundary layer measurements of fine-scale flow and sediment transport processes. *Coastal Engineering* in press.
- Jensen, B.L., Sumer, B. M., 1989. Turbulent oscillatory boundary layers at high Reynolds numbers. *J. Fluid Mech.* 206, 265-297.
- Lee, T.H., Hanes, D.M., 1995. Direct inversion method to measure the concentration profile of suspended particles using backscattered sound. *J. Geophys. Res.* 100, 2649-2657.
- Lemmin, U., Jiang, R., 1999. Vertical velocity structure and eddy scale distribution in the water column of the stratified Lake of Geneva. In: P.A. Davies (Ed.), *Mixing and dispersion in stratified flows*. Oxford University Press, Oxford, pp. 123-144.
- Lhermitte, R., 1983. Doppler sonar observation of tidal flow. *J. Geophys. Res.* 88, 725-742.
- Lhermitte, R., Serafin, R., 1984. Pulse-to-pulse coherent Doppler signal processing techniques. *J. Atmos. Oceanic Technol.* 20, 429-442.
- Lhermitte, R., Lemmin, U., 1993. Turbulent flow microstructures observed by sonar. *Geophys. Res. Letters* 20, 823-826.
- Lhermitte, R., Lemmin, U., 1994. Open channel flow and turbulence measurement by high-resolution Doppler sonar. *J. Atm. and Ocean. Tech.* 11, 1295-1308.
- McLean, S.R., Nelson, J.M., Wolfe, S.R., 1994. Turbulence structure over two dimensional bedforms: implications for sediment transport. *J. Geophys. Res.* 99, 12729-124747. doi: 10.1029/94JC00571.

- Nezu, I., 2005. Open-channel flow turbulence and its research prospect in the 21st century. *J. Hydr. Eng.* 131, 229-246.
- Nezu, I., Nakagawa, H., 1993. *Turbulence in open channel flows*. Balkema, Rotterdam, NL.
- Nezu, I., Kadata, A., Nakagawa, H., 1997. Turbulent structure in unsteady depth-varying open-channel flows. *J. Hydr. Eng.* 123, 752-763.
- Prandtl, L., Tietjens, O., 1929 and 1931. *Hydro- und Aerodynamik* (2 vol.), Berlin.
- Rolland, T., Lemmin, U., 1997. A two-component acoustic velocity profiler for use in turbulent open-channel flow. *J. Hyd. Res.* 35, 545-561.
- Shen, C., Lemmin, U., 1996. Ultrasonic measurements of suspended sediments: A concentration profiling system with attenuation compensation. *Meas. Sci. Tech.* 9, 1191-1194.
- Shen, C., Lemmin U., 1997. Ultrasonic scattering in highly turbulent clear water flow. *Ultrasonics* 35, 57-64.
- Shen, C., Lemmin, U., 1998. Improvements in acoustic sediment concentration profiling using an LMS compensation algorithm. *IEEE J. Oceanic Eng.* 23, 96-104.
- Shen, C., Lemmin, U., 1999. Application of an acoustic particle flux profiler in particle-laden open-channel flow. *J. Hydraul. Res.* 37, 407-419.
- Shields, A., 1936. Anwendung der Aehnlichkeitsmechanik und der Turbulenzforschung auf die Geschiebebewegung. *Mitt. Preuss. Versuchsanstalt für Wasserbau, Berlin, Heft 26*.
- Smyth, C.E., Zedel, L., Hay, A.E., 2002. Coherent Doppler profiler measurements of near-bed suspended sediment fluxes and the influence of bedforms. *J. Geophys. Res.* 107, C8, 19.1-19.20.
- Song, T., Lemmin, U., Graf, W.H., 1994. Uniform flow in open channels with mobile gravel bed. *J. Hydr. Res.* 32, 861-876.
- Southard, J.B., Boguchwal, L.A., 1990. Bed configuration in steady unidirectional water flows. *J. Sedim. Petrol.*, 60, 658-679.
- Sutter de, R., Verhoeven, R., Krein, A., 2001. Simulation of sediment transport during flood events: laboratory work and field experiments. *Hydrol. Sci.* 46, 599-610.
- Thorne, P.D., Hanes, D.M., 2002. A review of acoustic measurement of small-scale sediment processes. *Cont. Shelf Res.* 22, 603-632.
- Thorne, P.D., Davies, J.S., Bell, P.S., 2009. Observations and analysis of sediment diffusivity profiles over sandy rippled beds under waves. *J. Geophys. Res.* 114, C02023, doi:10.1029/2008JC004944.
- Thorne, P.D., Hardcastle, P.J., Soulsby, R.L., 1993. Analysis of acoustic measurements of suspended sediments. *J. Geophys. Res.* 98, 899-910.
- VanderWeft, J.J., Doucette, J.S., O'Donoghue, T., Ribberink, J.S., 2007. Detailed measurements of velocity and suspended sand concentration over full-scale ripples in regular oscillatory flow. *J. Geophys. Res.* 112, F02012.
- Yalin, M.S., 1977. *Mechanics of sediment transport*. Elsevier, New York.

Figure captions:

Fig. 1. Schematics of the ADV instrument in unsteady flow.

Fig. 2. Depth variation $\Delta h = h_b - h_p$ near the ADV for 4 parts of the hydrograph.

Fig. 3. Mean velocity profiles during steady peak flow for all experiments. For details on the legend see Table 2.

Fig. 4. Backscattering intensity profiles during steady peak flow for all experiments. For details on the legend see Table 2.

Fig. 5. Mean particle number for 1MHz experiments obtained from PTV images.

Fig. 6. Mean particle velocity and backscattering intensity during steady peak flow range for E3.

Fig. 7. a: Mean velocity and backscattering intensity profiles during steady peak flow for E4.

Fig. 8. Mean particle velocity and backscattering intensity during steady peak flow range for E5.

Fig. 9. Friction velocity u_* distribution for peak steady flow for 3 sets of experiments.

Fig. 10. Friction velocity u_* distribution for the unsteady ranges of 30 s and 60 s.

Fig. 11. Example of PTV results during the early phase of the steady peak flow range. Arrows indicate particle velocity vectors.

Fig. 12. Particle velocities in six positions of images. For position see Fig. 14; for details see text.

Fig. 13. Particle concentrations in the same position as Fig. 12. For position see Fig. 14; for details see text.

Fig. 14. Bed form formation during the early phase of the steady peak flow range indicating the positions shown in Figs. 12 and 13.

Fig. 15. Close-up view of sediment particle trajectories related to ripple formation. For details, see text.

Fig. 16. Large scale image of ripple formation, seen from the top. Mean spacing of the ripples is about 6 cm. For details, see text.

Highlights:

- > We simulated fine sediment dynamics in tidal rivers in a laboratory open-channel flow
- > Ripples are formed rapidly after bed-load movement started
- > Fine sediment is suspended into the water column in bursts
- > Most bursts originate on the reattachment point of ripples
- > Acoustic and optical measurement systems complement each other
- > The combination provides new detailed results for sediment dynamics in tidal rivers.

A.2 Shear velocity estimates in rough-bed open-channel flow

F. Bagherimiyab, I. Albayrak* and U. Lemmin

ENAC, Ecole Polytechnique Fédérale de Lausanne (EPFL), Station 18, CH-1015

Lausanne, Switzerland

fereshteh.bagheri-meyab@epfl.ch ismail.albayrak@abdn.ac.uk

ulrich.lemmin@epfl.ch

*present address :

Dept of Engineering, University of Aberdeen, Aberdeen, AB24 3UE, U.K.

ABSTRACT

Shear velocity u_* was determined using the logarithmic mean velocity profile, the Reynolds stress profile, the turbulent kinetic energy (TKE) profile and spectral methods in an open channel with a non-moving bed of loose mixed gravel ($D_{50} = 1.5$ cm) with Reynolds numbers ranging from 3.24×10^4 to 1.07×10^5 . This analysis is based on quasi-instantaneous 3D velocity profiles with high spatial and temporal resolution which were measured with an Acoustic Doppler Velocity Profiler (ADVP). Results from all methods fall into a range of $\pm 15\%$ variability. The logarithmic mean velocity profile method allows determining the height of the roughness layer and the height of the logarithmic layer ($\approx 0.2 z/h$). From the Reynolds stress method, the two-dimensionality (2D) of the flow was confirmed. Estimates from TKE and Reynolds stress closely agree. Spectral energy of the vertical velocity component strongly increased with distance from the bed in the inner layer, making the choice of the reference level and thus the application of this method difficult. The results of the analysis confirm the importance of detailed velocity profile measurements for the determination of shear velocity in rough-bed flows.

Keywords: rough-bed open-channel flow, shear stress, Reynolds stress, TKE, turbulence spectra, ADVP.

1. Introduction

Bed shear stress τ is an important parameter in many geophysical and environmental engineering applications. It is a fundamental variable and turbulence scaling parameter in river and oceanographic studies, because it relates to scour, determines particle erosion and deposition, and may be an important parameter for channel changes. The estimate of critical erosion and deposition thresholds and of erosion and deposition rates requires the determination of hydrodynamic forces applied to sediment as bed shear stress. The accuracy of sediment transport rate calculations is strongly affected by shear stress estimates due to the non-linear, rapid increase in transport rates with shear stress.

Bed shear stress τ is related to shear velocity u_* by $\tau = \rho u_*^2$, where ρ is water density. Shear velocity is linked to turbulent flow structures close to the bed and as such, is of major importance for the basic understanding of the development of near-

bed turbulence. In most loose gravel-bed flows, shear stress cannot be measured directly. Values of local shear stress are therefore most often indirectly determined through u_* from characteristics of the water flow. Due to the quadratic relationship between τ and u_* , high-quality estimates of u_* are required in order to obtain reliable shear stress estimates.

The water column in open-channel flow can be divided into an outer layer ($h/z > 0.2$; h = water depth) and an inner layer ($h/z < 0.2$) (Monin and Yaglom [19]; Nezu and Nakagawa [20]). In the inner layer, profiles of the flow parameters are controlled by the conditions at the bottom of the channel. Inner layer scaling can be based on u_* and a length scale characterizing the surface texture of the wall (Monin and Yaglom [19]). In smooth bed flows, the length scale is the viscous length scale ν/u_* defining a viscous layer above the flat wall. In rough bed flows, the length scale is the sum of the viscous length and additional lengths that characterize the bed roughness. For densely packed, homogeneously distributed geometrically regular protrusions (equivalent sand roughness, Nikuradse [26]; ‘k’ roughness, Townsend [37] and Jiménez [13]), the diameter, D , of the roughness element is the representative roughness parameter and is taken as additional length scale. If the mean diameter of the elements is large compared to the viscous length scale, the viscous length scale can be ignored. For movable roughness elements with a range of diameters, D , and a bed thickness of several mean element diameters (here taken as D_{50}), bed roughness becomes irregular, and the size, form, relative position and spacing of the elements also enter in the length scale. In rivers, it is therefore not always easy to define a length scale that is representative for a larger bed surface area and it becomes even more difficult as the range of diameters of the roughness elements increases.

In movable gravel bed flows, there exists a layer immediately above the bed that has been termed the ‘roughness layer’ (Raupach [28]; Nikora and Smart [22]) and whose flow dynamics are directly influenced by the length scales associated with bed roughness elements. The flow in this layer is often 3D and Nikora et al. [24] suggested that the roughness layer can be further subdivided into an interfacial sublayer close to and partially within the roughness elements and a form induced sublayer above it. No universal concept for the determination of the height of this layer exists. A wide range of propositions for the layer height is found in the literature: 50 roughness lengths z_0 , Townsend [37]; 2 to 5 diameters D , Raupach et al. [29]; 3 diameters D , Wilcock [38]; σ_D (σ_D = standard deviation of the bed elevations), Nikora and Goring [23] and $0.05 h$, Smart [33].

Above the roughness layer, concepts of smooth boundary layer flow may be applied to characterize the flow in the water column. The applicability of smooth bed concepts in boundary layer flows over hydraulically rough beds also depends on the relative roughness D/h . If the relative roughness increases, the height of the water column may not be sufficient for the boundary layer profiles to develop according to known smooth bed flow distribution laws. Katul et al. [15] suggest that these laws may fail for $h < 10D$.

In order to determine representative flow parameter estimates in irregular rough-bed flows, temporal and spatial averaging over a representative area (double averaging method) were suggested by Raupach et al. [29] for atmospheric flows and by Nikora et al. [24] for gravel bed flows. Spatial averaging yields additional, physically meaningful terms in the momentum equation, in particular form drag and form

induced stresses. The latter may be significant in irregular roughness layers (Nikora et al. [25]).

In this study, local mean shear velocity estimates will be calculated. Different methods of calculating shear velocity have been proposed for flows over hydraulically smooth beds and have been verified over smooth and transitionally rough beds. We will first summarize methods to determine shear velocity. We will then investigate the possibility of applying them to turbulent flow over a fully rough bed using Acoustic Doppler Velocity Profiler (ADVP) data that was obtained under controlled laboratory conditions in a movable gravel-bed open-channel flow. The results obtained by the different methods will be compared.

2. Techniques for estimating shear velocity

Shear velocity was initially defined within concepts of boundary layer flow. Commonly employed techniques are based on the assumption of the presence of a constant shear layer. However, in open-channel flow, a constant shear layer does not exist and therefore those concepts should not be used in open-channel flow. Nevertheless, as will be shown below, they have been applied in some open-channel flow studies. For open-channel flow over rough beds, Nezu and Nakagawa [20] suggest four methods to calculate shear velocity and bed shear stress: (1) the logarithmic law method, (2) the Reynolds stress method, (3) a bulk method using the channel slope, also called the reach average method, and (4) direct measurements.

In order to compare the methods presented below, a bulk shear stress or shear velocity estimate based on a force balance over a control section of the open-channel is often used as a reference. The shear velocity can be expressed as

$$u_* = \sqrt{g R I}$$

where g is the gravitational acceleration, R the hydraulic radius and I the bed slope of the channel. However, in fully rough flows, local estimates of the shear velocity may strongly deviate from this section mean, because of the significant bed irregularity. As will be discussed below, this method cannot be applied in the present case, since the bed slope is zero. Direct measurements can also be made using a hot-film sensor. However, for rough-bed flows, an in situ calibration is necessary (Albayrak et al. [2]; Albayrak [1]). Therefore, this is not an independent method and it was not included in the present analysis.

2.1 Logarithmic velocity profile method

Shear velocity can be calculated by assuming an equation for the vertical profile of streamwise velocity. In rough bed flows, Katul et al. [15] suggest that if $h > 10D$, a logarithmic velocity profile may exist in the inner layer of the flow, covering the lowest 20% of the water depth. The logarithmic velocity distribution is described by the von Karman-Prandtl equation with the following form (Schlichting [31]):

$$\frac{u}{u_*} = \frac{1}{\kappa} \ln \left(\frac{z}{z_0} \right) \quad (1)$$

where z_0 describes the characteristic hydraulic roughness length (or roughness), and u is the mean longitudinal velocity at height z above the bed. Monin and Yaglom [19] define z_0 as the height at which the mean velocity of the flow would become zero, if the logarithmic law would be applicable down to this height. For 2D uniform flow without sediment transport, it is well established that the constant κ is von Karman's constant ($\kappa = 0.4$). In rough bed flows, the relative magnitude of z_0 and a representative length scale for the roughness elements are important for the determination of the lower limit of the validity of the log-law. For homogeneous sand roughness, Monin and Yaglom [19] established $z_0/D_{50} = 1/30$ between the roughness length z_0 and bed roughness parameter D_{50} . For irregular roughness, the proportionality coefficient may vary and is often larger: $z_0/D_{50} \approx 1/10$ or even $z_0/D_{50} \approx 1/5$ (Monin and Yaglom [19]; Townsend [37]). These authors stress that this coefficient may not strictly be a constant for a set of irregularities, since it also depends on the form of the roughness element.

The logarithmic velocity profile method is widely used in open-channel flow and river studies (Nezu and Nakagawa [20]). In order to provide estimates for z_0 and u_* , measured data $u = f(z)$ are plotted in semi-logarithmic form. The procedure involves fitting a straight line by ordinary least-square regression to the profile and calculating the values of u_* and z_0 from the slope and intercept of the computed regression equation. This procedure requires that the level of the profile origin ($z = 0$) is known. In rough bed flows, a logarithmic profile will develop above the roughness layer. Townsend [37] indicated that the log law can only be valid at heights of $z/z_0 > 50$. According to Wilcock [38], a logarithmic profile is found between $3 D_p < z < h/5$ (D_p being the grain size for which p percent are finer; often taken as D_{84}), but it may actually extend higher into the outer region. Smart [33] suggested a range of $0.05 h < z < h/2$.

2.2 Reynolds stress method

When turbulence measurements are available, local mean shear velocity can be determined from the measured Reynolds stress distribution in the constant stress layer that is found at the lower end of the logarithmic profile layer. It can be expressed as

$$u_* = \sqrt{-\overline{u'w'}} \quad (2)$$

where u' and w' are the velocity fluctuations of the longitudinal (streamwise) and vertical components, respectively. The overbar denotes time mean values. Recently, instruments that can measure the two components of turbulent velocity fluctuations with sufficient temporal resolution have become available, allowing the calculation of shear velocity in rough bed flows by this method when it may be difficult to apply the logarithmic profile method. However, this method is sensitive to any deviation from 2D uniform flow (Nezu and Nakagawa [20]; Kim et al. [16]; Nikora and Goring [23]; Albayrak [1]) and a precise sensor alignment is required in order to obtain reliable data for the two velocity components.

The shear velocity u_* can be calculated from turbulence measurements at a single depth within the constant stress layer at the bottom of the logarithmic profile layer, if the thickness of the roughness layer and the level of the constant stress layer are known. However, acoustic Doppler instrument measurements are less reliable in

strong velocity gradient layers such as the one close to the bed due to internal shear within the measuring volume (Lhermitte and Lemmin [17], Dombroski and Crimaldi [5]). Kim et al. [16] measured with an ADV at 14 cm above a silt bed and estimated the height of the logarithmic layer as 44 cm.

In rough-bed open-channel flow, Reynolds stress varies linearly from the bed to the free surface (Nezu and Nakagawa [20]). Therefore, Nezu and Nakagawa [20] and Nikora and Goring [23] suggested using the extrapolation of the Reynolds stress profile to the bed,

$$u_* = \sqrt{\left(-\overline{u'w'}\right)_{z \rightarrow 0}} \quad (3)$$

We will apply this method in the present analysis. In addition, this method allows verifying the 2D flow conditions by a linear distribution of the Reynolds stress above the maximum. Nezu and Nakagawa [20] favor this method.

2.3 Turbulent Kinetic Energy (TKE) method

Bed stress can also be obtained from turbulent velocity fluctuations through turbulent kinetic energy (TKE) calculations. TKE is defined as

$$TKE = \frac{1}{2} \left(\overline{u'^2} + \overline{v'^2} + \overline{w'^2} \right) \quad (4)$$

where v' is the fluctuating transversal velocity component. Linear relationships between TKE and shear stress have been formulated (Townsend [37]). Soulsby [34] found that the average ratio of bottom shear stress to TKE is constant

$$|\tau| = C_1 \rho TKE \quad (5)$$

Therefore,

$$|u_*| = \sqrt{C_1 TKE} \quad (6)$$

where C_1 is a proportionality constant. For oceanic conditions, Soulsby [34] suggested $C_1 \approx 0.2$, while Stapleton and Huntley [35] applied $C_1 \approx 0.19$, which is the same value as for the atmospheric boundary layer. The value $C_1 \approx 0.19$ was used by MacVicar and Roy [18] in a gravel bed river, by Rowinski et al. [30] in a rough-bed open channel and by Pope et al. [27] in river and laboratory studies. Wolf [40] proposed values $C_1 < 0.19$ from his coastal ocean studies. Kim et al. [16] used $C_1 \approx 0.21$ in an estuary.

Kim et al. [16] suggested that bed shear stress may be related to the vertical variance component,

$$|\tau| = C_2 \rho \overline{w'^2} \quad (7)$$

$$|u_*| = \sqrt{C_2 \overline{w'^2}} \quad (8)$$

with $C_2 \approx 0.9$, assuming a linear relationship between TKE and the variance.

As with the Reynolds stress method, the TKE method depends on second moment statistics. In the constant stress layer, it is not subject to errors related to sensor height z , but the roughness height and the thickness of the constant stress layer have to be known. For open-channel flow, Biron et al. [3] proposed taking the maximum value of

the TKE profile at $z/h \approx 0.1$. However, it has to be recalled that a constant stress layer does not exist in open-channel flow.

Nezu and Nakagawa [20] have shown that Reynolds stress and TKE are correlated in open-channel flow. In the inner layer, the correlation coefficient $R = (-\overline{uw} / 2 TKE)$ has a value close to 0.1 that results in $-\overline{uw} \approx 0.2 TKE$. As for the Reynolds stress method, by extrapolation of the TKE profile to the bed, we obtain $u_* \approx \sqrt{0.2 TKE}_{z \rightarrow 0}$.

2.4 Spectral method

In the equilibrium layer, a balance exists between shear production p and energy dissipation ε that is given by (Tennekes and Lumley [36]; Townsend [37])

$$-p + \varepsilon = \overline{u' w'} \left(\partial u / \partial z \right) + \varepsilon = 0 \quad (9)$$

In the log-law region, the range of shear production is well separated from the range of energy dissipation. In this case, an inertial subrange is established between the two ranges. If there are no sources or sinks of energy in the inertial subrange, the spectrum of a velocity component in the inertial subrange has the following form:

$$\phi_{ii}(k) = \alpha_i \varepsilon^{2/3} k^{-5/3} \quad (10)$$

where $\phi_{ii}(k)$ is the spectral density of the i th velocity component at wave number k , and α_i is the 1D Kolmogorov constant (Kim et al. [16]). For locally isotropic turbulence, $\alpha_1 \approx 0.51$ (Kaimal et al. [14]) and $\alpha_2 \approx \alpha_3 = 4/3 \alpha_1 \approx 0.69$ (Tennekes and Lumley [36]). These values were used by Huntley [10], Stapelton and Huntley [35] and Green [9] in the ocean and by Kim et al. [16] in the estuary. Grant et al. [8] suggested $\alpha_3 \approx 0.50$ in their continental shelf study. For velocity data obtained in the time domain, frequency spectra have to be transferred into wave-number spectra. Under the condition of $k \phi_{ii}(k) / u^2 \ll 1$, Taylor's "frozen turbulence" hypothesis can be applied by assuming $k \phi_{ii}(k) = f \phi_{ii}(f)$, where f is the frequency (Huntley [10]).

For a logarithmic profile with a constant stress layer, one can obtain u_* from eq. (9) as

$$u_* = (\varepsilon \kappa z)^{1/3} \quad (11)$$

By combining equations 10 and 11, we obtain for the vertical velocity component

$$u_* = \left(\frac{2 \pi \kappa z}{u} \right)^{1/3} \left(\frac{\phi_{ww}(f) f^{5/3}}{\alpha_3} \right)^{1/2} \quad (12)$$

The inertial subrange is defined as the frequency range where $\phi_{ii}(f) f^{5/3}$ is constant. This method of estimating the shear velocity u_* has mainly been used in oceanography. It is less sensitive to errors in sensor alignment than the Reynolds stress method. We will investigate the suitability of this method in open-channel flow, even though eq. 11 is not strictly valid in this flow. Its advantage is that it can provide estimates based on measurements at a single depth.

The methods discussed in this section have been developed and verified in flows over smooth and transitionally rough beds. Here we will investigate the possibility of

applying them to turbulent flow over a fully rough bed using ADVP data that was obtained under controlled laboratory conditions.

3. Experiments

3.1 *Experimental set-up*

Experiments were carried out in a 2.4 m wide by 27 m long open-channel with a 10 cm thick bed of loose mixed gravel with $D_{50} = 1.5$ cm (Fig. 1a; Table 1). Measurements were made 12 m from the channel entrance where the flow is well developed for two flow depths ($h = 19$ and 20 cm, respectively) and with Reynolds numbers ranging from 3.24×10^4 to 1.07×10^5 . The rough permeable bed did not move during the experiments. The channel has a zero slope angle.

3.2 *Acoustic Doppler Velocity Profiler (ADVP)*

The ADVP measures quasi-instantaneous profiles of all three velocity components over most of the water depth of an open-channel flow (Shen and Lemmin [32]). This instrument consists of a central emitter and four wide-angle receiver transducers placed symmetrically around the center (Fig. 1b). The transducers are arranged in two perpendicular planes, each of which allows resolving profiles of one horizontal component and the vertical velocity component. Thus, two simultaneous profiles of the vertical component are taken in the same measuring volumes. The redundancy of the vertical component profiles allows controlling the quality of the geometrical alignment of the transducers, both in the horizontal and the vertical plane. This is important for the application of the Reynolds stress and the TKE methods. The transducer arrangement provides velocity profiles along a single straight vertical line of consecutive scattering volumes (Fig. 1b). Thus, all points in the profiles were nearly simultaneously measured during a single recording.

All velocity components are evaluated from phase information coming from the same scattering volume, because sound is only emitted from the central transducer. Complete 3D Doppler phase profiles are sampled at 1000 Hz. Velocity profiles are obtained from these data by the pulse-pair method (Lhermitte and Lemmin [17]) averaged over 32 pairs. The resulting spatio-temporal resolution (3.2 mm and 0.032 s, respectively) is sufficient to quantitatively estimate turbulence parameters in the productive and inertial ranges of the spectral space.

3.3 *Procedure*

In this study, a series of nine experiments at different Reynolds numbers for two slightly different flow depths was conducted (Table 1). Due to the zero bed slope, the flow is in a state which Yaglom [41] called “moving equilibrium,” where water depth and shear velocity vary sufficiently slowly in the downstream direction so that their variation in that direction can be ignored. In this case, u_* can be considered as a local value for a given location. Both flow depths have approximately the same relative roughness ($D_{50}/h \approx 0.075$) and the effect of relative roughness will not be

investigated. Shallower water depths were studied in Albayrak [1] where no disturbing effect of relative roughness was found down to $D_{50}/h \approx 0.125$, and profiles of all parameters had the same profile shape as those presented here. Results for $D_{50}/h \approx 0.075$ are discussed, because ADV measurements resulted in profiles with approximately 50 sampling volumes in the water column, thus allowing for a detailed profile analysis. Data were collected for three minutes in the center of the channel. For each experiment, three-minute recordings were repeated several times and the mean profiles of the streamwise velocity for each run were compared during the experiment in order to assure that the mean velocity profiles were constant and that the data set chosen for the analysis was representative for the experiment.

Since ADV measurements are made from above the water surface (Hurther et al. [12]), the Mylar sheet of the instrument housing which touches the water surface slightly perturbs the flow and creates a boundary layer in the near surface water layer (Fig. 1b). Therefore, measured profiles were cut at $z/h = 0.9$ (Hurther et al. [12]) which had no effect on the present analysis. Measuring from above the water surface also allows determining the local water depth. In each experiment, the bottom level was identified from the velocity information ($u = 0$), and confirmed by the corresponding change of backscatter intensity at that level. Backscattering intensity is obtained from a sampling volume of height $\Delta z = 3.2 \text{ mm}$. The origin of the coordinate system was placed at $1/2 \Delta z$ of the lowest sampling volume where $1/2 \Delta z$ is equal to about $0.1 D_{50}$. Water depth was measured as the distance between this level and the Mylar sheet at the surface. The stability of the mean water depth during the experiment was controlled by a limnimeter.

The bed level was controlled and the bed was spray-painted black before each experiment. It was observed after the experiments that even though the bed was not moving, the painted surface was often disturbed in small patches, indicating water working of the bed during the experiment.

To optimize data quality, the collected data were first de-aliased (Franca and Lemmin [6]) to remove spikes and subsequently de-noised using the redundant information of the vertical velocity in the two planes (Hurther and Lemmin [11]). Measured velocities have an error of the order $O(2 \div 3 \text{ mms}^{-1})$ (Hurther et al. [12], Blanckaert and Lemmin [4]). For the present analysis, the vertical velocity which was measured in the longitudinal plane was used. The measured velocities were decomposed into a mean (u for streamwise, w for vertical) and a fluctuating component (u' for streamwise, w' for vertical) by Reynolds decomposition.

The methods for calculating shear velocity presented above assume 2D flow. However, streamwise secondary current cells develop in wide channels such as the one used here and in rivers, thus making the flow in the whole water column 3D. These cells also produce corresponding bottom shear stress deviations from the mean across the channel (Nezu and Nakagawa [20], Albayrak [1]). The distribution of these cells depends on the ratio of water depth to channel width. We found that in the center of the channel, where the present measurements were taken, the effect of these cells was small and the flow was most often 2D.

4. Results

Using ADV measurements, shear velocities u_* were determined by the methods detailed above. We will first briefly describe the application of the different methods. Thereafter we will compare the results of all the experiments.

4.1 Logarithmic profile method

Representative profiles for the lower $0.4 z/h$ are given in Fig. 2 in semi-logarithmic form. The linear least-square fit of eq.1 to these data is shown as a solid line and it can be seen that the fit closely follows the measured mean longitudinal velocity profiles. Very close to the bed, typically for the lowest two or three points in the profile, a deviation from the logarithmic law is observed due to the presence of the roughness layer. In the roughness layer, individual roughness elements may affect the flow structure and the flow may become 3D (Nikora and Goring [23]; Albayrak [1]). The thickness of the roughness layer of three profile points corresponds to $0.05 h$, as was suggested by Smart [33]. However, it is about $0.7D$ which is much smaller than 2 to 5 D proposed by Raupach et al. [29] or 3 D proposed by Wilcock [38].

In order to investigate the stability of the linear least-square fitting procedure to the profile data, a fitting loop was carried out, starting from the first data point above the roughness layer. In each fitting step, the next higher data point was added to the fitting procedure, and u_* as well as the regression coefficient were determined. With each new data point added, u_* increases. Over the range 0.05 to 0.4 z/h , the increase in u_* is of the order $O(10\%)$. However, over the same depth range, the regression coefficient R^2 , which in all experiments is relatively high (> 0.99), goes to a maximum between $z/h = 0.25$ and $z/h = 0.3$. Near the maximum of R^2 , u_* values have a slight plateau and the rate of change of u_* slightly decreases above $z/h = 0.35$. Even though a logarithmic fit still appears reasonable beyond $0.3 z/h$, the regression coefficient analysis indicates that the height of the logarithmic layer is limited to $z/h \approx 0.25$. This value is larger than the value of $z/h = 0.2$ given for the validity of the logarithmic law (Monin and Yaglom [19]; Nezu and Nakagawa [20]), but smaller than $z/h = 0.5$ suggested by Smart [33]. For the determination of u_* and z_0 , the layer height corresponding to the maximum of R^2 was taken.

The roughness height z_0 is defined as the height at which the mean velocity of the flow would become zero, if eq. 1 were applicable down to this height (Monin and Yaglom [19]). Smart [33] had already indicated that a wide range of z_0 can be expected in rough-bed flows. In these flows, not only the dimension of the bed material at the base of the profile and the different forms of roughness element composition will affect the roughness length, but also the bed conditions upstream of the velocity profile location. The present results vary by an order of magnitude, grouped into two subgroups. A trend of z_0 increasing with u_* as observed by Smart [33] in rough-bed river flows can be observed in each subgroup. The ratio between the physical roughness height z_0 and D_{50} is smaller than $z_0/D_{50} \approx 1/10$ for flows over irregular rough surfaces (Monin and Yaglom [19]; Townsend [37]), but it falls into the range suggested by Smart [33].

Using the estimates for u_* (Table 1), we calculated the mean velocity profile in the log-law layer by the equation $u/u_* = 1/\kappa \ln(z/D_{50}) + A$ (Nezu and Nakagawa [20]). Monin and Yaglom [19] suggested $A \approx 8.5$ for fully rough flow. The calculated profiles closely followed the measured ones (Fig. 2). The difference was below 10% in all cases and calculated velocities were larger than the measured ones, indicating that a value close to $A \approx 8.5$ applies in this rough bed flow.

Since the ADV takes full depth velocity profiles in one recording, no relative errors in z occur, thus rendering the profile fitting more robust than point-by-point measurements. Furthermore, in all experiments, the range of the profile which is fitted to eq. 1 is composed of at least 10 points. This large number of points significantly reduces the error (Wilkinson [39]).

4.2 Reynolds stress method

The Reynolds stress profile was calculated for all points in the profile up to $0.9 z/h$. Typical Reynolds stress profiles which are shown in Fig. 3 closely follow a linear distribution above the maximum, indicating that the flow is 2D. In order to determine u_* , the profile above the maximum was approximated by a linear fit that is extrapolated to level $z = 0$ (Nezu and Nakagawa [20]; Nikora and Goring [23]). A maximum in the Reynolds stress distribution is observed at around $0.2 z/h$ in all experiments, except experiment 6 (Fig. 3), where it is slightly shifted upwards. This shift may be due to longitudinal secondary current cells mentioned above (Nezu and Nakagawa [20]; Albayrak [1]) which may cause a deviation from the 2D profile. The non-2D effect results in a higher u_* value compared to estimates by other methods (Table 1). Below the maximum, the form of the decreasing profile is determined by the bottom roughness.

4.3 TKE method

The TKE and the variance of the vertical component (hereinafter labeled TKE W') were calculated for all points and the profile was again limited to $0.9 z/h$. Figure 3 shows typical TKE profiles which in their linear form above the maximum closely follow the Reynolds stress profiles. TKE profiles peak at around $0.1 z/h$ as has previously been observed (Biron et al. [3], Nicholas [21]). Compared to the Reynolds stress profile for exp. 6 (Fig. 3), it appears that the TKE method is less sensitive to non-2D conditions. For all experiments, the form of the TKE W' profile is different from that of the TKE method; experiment 8 is given as an example in Fig. 3. The short range above the maximum is not suited for linear fitting. Therefore, the estimates based on TKE W' fitting have to be considered less reliable than full TKE estimates. Kim et al. [16] applied the TKE W' method to single point measurements.

4.4 Spectral method

Energy density spectra were calculated for all sampling volumes of the profiles. In all spectra, except for those very close to the bed ($z/h \leq 0.054$), a production and an inertial range were well developed, thus allowing the application of this method.

Shear velocity was calculated for the longitudinal and the vertical components, as explained in Section 2. It was found that this method often gives poor results for the longitudinal component, because spectral curves of this component have a shorter inertial subrange and large amplitude fluctuations in the inertial subrange (Fig. 4), thus making it difficult to determine reliable values for $\phi_{ii}(f) f^{5/3}$. Therefore, these results were omitted from the analysis. In order to determine the reference depth for a representative u_* obtained from the spectra of the vertical velocity component, u_* was calculated by this method for all measurement volumes in each profile. Results for the lower 0.4 z/h in Fig. 5 show that u_* continuously increases with height above the bed throughout the logarithmic layer which corresponds to a rise in the spectral energy level with height above the bed. The overall pattern is similar for all experiments. Kim et al. [16] made estimates for heights of 14 and 44 cm above bed, and observed a 25% increase in u_* for the higher of the two points which corresponds to our observations.

In order to determine the height of representative u_* values, one may compare u_* values obtained from the spectral method at different heights above the bed within the log layer to those obtained by the methods discussed above (Table 1). For experiment 1, a u_* value at 0.2 z/h is closest to the values given in Table 1. In the remaining experiments, best agreement is found for the u_* value near 0.1 z/h . These values were included in Table 1. Townsend [37] had indicated that in shear flows over a solid boundary layer, an equilibrium layer of wall turbulence exists near the solid wall. The equilibrium layer is characterized by exceptionally high rates of generation and dissipation of turbulent energy when compared with the outer layer. Furthermore, local conditions determine the motion field in this layer. Hurther et al. [12] had shown for the same flow conditions in the same channel investigated here that in the near-wall layer an equilibrium layer exists. Near the wall, generation and dissipation are about 6 times higher than in the outer layer. Furthermore, TKE flux has a maximum at around 0.1 z/h . Therefore a reference level near 0.1 z/h fulfils the conditions for the validity of this approach. However, this method does not provide objective, universal results in rough-bed open-channel flow and is rather sensitive to the profile resolution.

4.5 A Comparison of the results

Table 1 presents the shear velocity values obtained using the different methods for all the experiments. The results cover a wide range of Reynolds numbers and thus flow velocities. As can be expected for such rough bed flow, different shear velocity estimates for a given flow case rarely coincide and no systematic trend between the results of the different methods is obvious. However, some tendencies can be observed in the results.

Nezu and Nakagawa [20] suggested that the extrapolated Reynolds stress method that we use here, gives the most reliable results. Taking these values as reference (except for exp. 6; see above), the logarithmic profile method often comes close to it. In 4 of the 9 experiments, logarithmic profile method estimates are higher, but in the remaining cases they are lower than the Reynolds stress method estimates. Rowinski et al. [30] observed systematically higher values for the logarithmic method and they concluded that this method was not applicable to their flow. In our case, the relative roughness is $D_{50}/h \approx 0.075$ and thus $h \approx 13.3 D_{50}$ which should allow using the

logarithmic profile method (Katul et al. [15]). The high regression coefficients in the fitting to the logarithmic profile also suggest that the results are valid estimates.

The differences between the TKE method and the Reynolds stress method are less than those discussed above, except for the slowest flow case (exp. 5), where the estimate is affected by a noisy TKE profile. The coefficient $C_1 \approx 0.19$ in the TKE method was taken from the literature and applied to this rough bed flow. Rowinski et al. [30] using the same coefficient also found good agreement between these two methods. In Fig. 3, we plotted profiles of Reynolds stress and 0.19 TKE. We found good agreement between the two profiles over most of the water depth, thus confirming the observations by Townsend [37] of a constant ratio between Reynolds stress and TKE. This also indicates that $C_1 \approx 0.19$ is a suitable constant. Due to the short range over which the profile is linear, we cannot recommend the TKE W' method from our experience even though we found reasonable estimates.

For the spectral method, robust data for the vertical velocity component were found at all levels in the inertial subrange. Assuming that a level at around $0.1 z/h$ is best suited for estimates in our roughness conditions, the flow may be non-isotropic (Fig. 4), thus deviating from the isotropic conditions assumed in the derivation of eq. 12. Further investigations should be carried out before this method can be recommended as a universal tool for estimating shear velocity in rough-bed open-channel flow. Longer records of velocity profiles may help to reduce the degrees of freedom of the spectral estimates and thus reduce the variability within the inertial subrange.

Ninety-six percent of all u_* estimates in this study fall into a range of $\pm 15\%$. A similar range of variability was observed by Kim et al. [16] over a silt bottom in tidal flows. Nezu and Nakagawa [20] mention a range of $\pm 30\%$ when comparing results from the logarithmic profile method and the Reynolds stress method with the bulk method. They indicate that this range increased with increasing roughness size, whereas we found a smaller range with our detailed profile measurements.

For each experiment, shear stress was calculated from the mean u_* values (Table 1), and the results are plotted in Fig. 6 against the corresponding mean streamwise velocities. A quadratic relationship with $\tau \approx 4.59 u^2$ has been fitted to the points. Pope et al. [27] found $\tau \approx 2 u^2$ for fine sediments over the same velocity range and suggested that steeper curves can be expected with increasing roughness. This calculation was repeated separately for each of the different methods. The following regression coefficients were determined: $R^2 = 0.68$ for the log-law method, $R^2 = 0.83$ for the Reynolds stress method and $R^2 = 0.79$ for the TKE method. The latter two methods have a higher reliability.

5. Summary and conclusion

The ADV provides quasi-instantaneous velocity profiles with high temporal and spatial resolution. Due to the consecutive segmenting of the water column into gates, there are more points in individual profiles than are normally taken with traditional instrumentation. The high temporal resolution resolves turbulent scales and therefore allows applying different analysis methods for the estimation of shear velocity. These profile data were used in the present study to determine shear velocity by four different methods in flows over significant irregular roughness, where relative roughness is $D_{50}/h \approx 0.075$. In order to apply these methods in rough bed flow, it is

necessary to know the structure of the bed, the thickness of the roughness layer, the relative roughness, the extent of the logarithmic profile layer and the profile origin, as well as the two-dimensionality of the mean flow. It was shown here that for irregular roughness and the given relative roughness in controlled laboratory experiments, the above parameters and conditions could be specified from the ADVP profile data using the logarithmic profile and the Reynolds stress methods. We found a roughness layer height of $\approx 0.05 h$ that agrees with the prediction by Smart [33]. However, this roughness layer height correspond to about $0.7 D_{84}$, which is less than that suggested in the literature.

All methods provide comparable results for the shear velocity. Nevertheless, some questions about the validity of the different methods in rough-bed flows remain. The logarithmic profile method is appreciated, because it is based on the mean velocity profile, which usually has less uncertainty than the other methods, and regression coefficients were high in our curve fitting. However, for comparable flow conditions, we found significant variability in the shear velocity estimates (Table 1). Since the measurement conditions did not change in the experiments, local, temporal variation in bed roughness may contribute to the variability between experiments. The Reynolds stress method gave consistent results except when deviation from 2D flow occurred. Nezu and Nakagawa [20] considered this method well suited for rough-bed flows. For the TKE method, we used the coefficient $C_1 = 0.19$ as given in the literature (Pope et al. [27]). The TKE method seems to be less sensitive to the mean 2D condition and TKE profiles were smoother than Reynolds stress profiles. For the spectral method applied to the vertical velocity component, we were unable to objectively identify the proper level at which the method should be applied. Kim et al. [16] had similar difficulties. In rough-bed flows it is best to analyze velocity profile data by different methods. As indicated in this study, in addition to the friction velocity estimate, each method provides supplementary information about the flow characteristics, which may in turn contribute to better evaluate the flow field in question.

When shear stress is calculated from u_* values and plotted against the mean streamwise velocity of all experiments, the logarithmic profile method has the lowest regression coefficient ($R^2 = 0.68$). Reynolds stress and TKE method estimates have higher values and are close to each other ($R^2 \approx 0.8$). Therefore, it appears that the latter two methods are better suited. Reynolds stress profiles and TKE profiles coincided over most of the water column. The constant ratio between the two profiles (Townsend [37]) allows replacing one method by the other. Since the TKE method is less sensitive to deviations from the 2D flow conditions and TKE profiles are smoother, it may be of interest to explore the TKE method further for rough-bed flow studies.

In this study, we found reasonable agreement between the different shear velocity estimates for one fixed location in the channel. In rough-bed flows the spatial roughness distribution is irregular, and single location profiling may not provide shear stress estimates representative for a section, in particular for higher values of mean roughness and relative roughness. Double averaging (in time and space) analysis for rough bed flows was suggested by Nikora et al. [24] as a way to determine section mean parameters. However, for this analysis high-resolution profile measurements have to be repeated at a sufficiently large number of statistically independent positions. In field measurements this may require a great effort with the risk that discharge conditions do not remain stable for a sufficiently long time. Spatially

distributed high resolution ADV profiling combined with double averaging analysis has given new insight into flow dynamics and has shown that the double averaged profile is close to the logarithmic profile in irregular rough-bed flows (Franca et al. [7]). On the other hand, sediment dynamics is strongly influenced by the local shear stress conditions and section mean values are not of great value. Form and mutual spacing of roughness elements may play a key role in the local friction velocity dynamics (Monin and Yaglom [19]).

Acknowledgement

This study was sponsored by European Commission contract no. 022441 (RII3) HYDRALAB-III and by the Swiss National Science Foundation, grant 200020-100383. We are grateful for the support. The technical assistance by Claude Perrinjaquet is greatly appreciated.

REFERENCES

- [1] Albayrak I. An experimental study of coherent structures, secondary currents and surface boils and their interrelation in open-channel flow. *Ph.D. Thesis, No 4112, Ecole Polytechnique Fédérale (EPFL), Lausanne;2008*
- [2] Albayrak I, Hopfinger EJ, Lemmin U. Near-field flow structure of a confined wall jet on flat and concave rough walls. *J Fluid Mech* 2008; 606: 27-49.
- [3] Biron PM, Robson C, Lapointe MF, Gaskin SJ. Comparing different bed shear stress estimates in simple and complex flow fields. *Earth Surf Process Landforms* 2004; 29: 1403-1415.
- [4] Blanckaert K, Lemmin U. Means of noise reduction in acoustic turbulence measurements. *J Hydraul Res* 2006; 44: 1-37.
- [5] Dombroski DE, Crimaldi JP. The accuracy of acoustic Doppler velocimetry measurements in turbulent boundary layer flows over a smooth bed. *Limnol Oceanogr Methods* 2007; 5: 23-33.
- [6] Franca M, Lemmin U. Eliminating velocity aliasing in acoustic Doppler velocity profiler data. *Meas Sci Technol* 2006; 17: 313 – 322.
- [7] Franca MJ, Ferrera RML, Lemmin U. Parameterization of the logarithmic layer of double-averaged streamwise velocity profiles in gravel-bed river flows. *Adv Water Resources* 2008; 31: 915-925.
- [8] Grant WD, Williams III AJ, Glenn SM. Bottom stress estimates and their prediction on the northern California continental shelf during CODE-1: the importance of wave-current interaction. *J Phys Oceanogr* 1984; 14: 506-527.
- [9] Green MO. Spectral estimates of bed shear stress at subcritical Reynolds numbers in a tidal boundary layer. *J Phys Oceanogr* 1992; 22: 903-917.
- [10] Huntley DA. A modified inertial dissipation method for estimating seabed stresses at low Reynolds numbers, with application to wave/current boundary layer measurements. *J Phys Oceanogr* 1988; 18: 339-346.
- [11] Hurther D, Lemmin U. A correction method of mean turbulence measurements with a 3D acoustic Doppler velocity profiler. *J Atm Ocean Tech* 2001; 18: 446-458.

- [12] Hurther D, Lemmin U, Terray EA. Turbulent transport in the outer region of rough-wall open-channel flows: the contribution of large coherent shear stress structures (LC3S). *J Fluid Mech* 2007; 574: 465-493.
- [13] Jiménez J. Turbulent flows over rough walls. *Ann Rev Fluid Mech* 2004; 36: 173-196.
- [14] Kaimal JC, Wyngaard JC, Izumi Y, Cote OR. Spectral characteristics of surface-layer turbulence. *Quart J Roy Meteor Soc* 1972; 98: 563-589.
- [15] Katul G, Wiberg P, Albertson J, Hornberger G. A mixed layer theory for flow resistance in shallow streams. *Water Resour Res* 2002; 38: 1250, doi: 10.1029/2001WR000817.
- [16] Kim SC, Friedrichs CT, Maa JPY, Wright LD. Estimating bottom stress in a tidal boundary layer from acoustic Doppler velocimeter data. *J Hydraulic Engineering, ASCE* 2000; 126: 399-406.
- [17] Lhermitte R, Lemmin U. Open channel flow and turbulence measurement by high resolution Doppler sonar. *J Atm Ocean. Tech* 1994; 11: 1295-1308.
- [18] MacVicar BJ, Roy AG. Hydrodynamics of a forced riffle pool in a gravel bed river: 1. Mean velocity and turbulence intensity. *Water Resour Res* 2007; 43: W12401, doi:10.1029/2006WR005272.
- [19] Monin AS, Yaglom AM. *Statistical fluid mechanics*. Vol. 1, Cambridge: MIT Press; 1971.
- [20] Nezu I, Nakagawa H. *Turbulence in open-channel flows*. Rotterdam: A.A. Balkema; 1993.
- [21] Nicholas, AP. Computational fluid dynamics modeling of boundary roughness in gravel bed rivers: an investigation of the effects of random variability of bed elevation. *Earth Surf Process Landforms* 2001; 26: 345-362.
- [22] Nikora VI, Smart GM. Turbulence characteristics of New Zealand gravel-bed rivers. *J Hydraulic Engineering, ASCE* 1997; 123: 764-773.
- [23] Nikora VI, Goring D. Flow turbulence over fixed and weakly mobile gravel beds. *J Hydraulic Engineering, ASCE* 2000; 126: 679-690.
- [24] Nikora VI, Goring D, McEwan I, Griffiths G. Spatially averaged open-channel flow over rough bed. *J Hydraulic Engineering, ASCE* 2001; 127: 123-133.
- [25] Nikora VI, McEwan I, McLean S, Coleman S, Potkrajac D, Walters R. Double-averaging concept for rough-bed open-channel and overland flows: theoretical background. *J Hydraulic Engineering, ASCE* 2007; 133: 873-883.
- [26] Nikuradse J. *Laws of flow in rough pipes*. NACA Tech. Memo 1292 Washington: Natl. Advis. Comm. for Aeron 1933
- [27] Pope ND, Widdows J, Brinsley MD. Estimation of bed shear stress using the turbulent kinetic energy approach – a comparison of annular flume and field data. *Continental Shelf Research* 2006; 26: 959-970.
- [28] Raupach MR. Conditional statistics of Reynolds shear stress in rough-wall and smooth-wall turbulent boundary layers. *J Fluid Mech* 1981; 108: 363-382.
- [29] Raupach MR, Antonias RA, Rajagopalan S. Rough-wall turbulent boundary layers. *Appl Mech Rev* 1991; 44: 1-25.
- [30] Rowinski PM, Aberle J, Mazurczyk A. Shear velocity estimation in hydraulic research. *Acta Geophys Pol* 2005; 53: 567-583.
- [31] Schlichting H. *Boundary-layer theory*. New York: McGraw-Hill; 1987
- [32] Shen C, Lemmin U. A two-dimensional acoustic sediment flux profiler. *Meas Sci Technol* 1997; 8: 880-884.
- [33] Smart GM. Turbulent velocity profiles and boundary shear in gravel bed rivers. *J Hydraulic Engineering, ASCE* 1999; 125: 106-116.
- [34] Soulsby RL. Measurements of the Reynolds stress components close to a marine sand bank. *Marine Geology* 1980; 42: 35-47.
- [35] Stapleton KR, Huntley DA. Seabed stress determination using the inertial dissipation method and the turbulent kinetic energy method. *J Earth Surf Process Landforms* 1995; 20: 807 – 815.
- [36] Tennekes H, Lumley JL. *A first course in turbulence*. Cambridge: MIT press; 1972

- [37] Townsend AA. The structure of turbulent shear flow. New York: Cambridge Univ Press; 1976
- [38] Wilcock PR. Estimating local bed shear stress from velocity observations. *Water Resour Res* 1996; 32: 3361-3366.
- [39] Wilkinson RH. A method for evaluating statistical errors associated with logarithmic velocity profiles. *Geo-marine Letters* 1983; 3: 49-52.
- [40] Wolf J. The estimation of shear stresses from near-bed turbulent velocities for combined wave-current flows. *Coastal Engineering* 1999; 37: 529-543.
- [41] Yaglom AM. Similarity laws for constant-pressure and pressure-gradient turbulent wall flows. *Ann Rev Fluid Mech* 1979; 11: 505-540.

Notation

- D_p = grain size for which the percentage of sample of bed material is finer (cm);
- D_{50} = grain size for which 50% of sample of bed material is finer (cm);
- h = water depth (cm);
- κ = von Karman's constant;
- p = shear production;
- u, v, w = local mean longitudinal, transverse and vertical velocity (cm s^{-1});
- u_* = shear velocity (cm s^{-1});
- u', v', w' = local fluctuating longitudinal, transverse and vertical velocity (cm s^{-1}); overbar = time mean values
- $\bar{U} = 0.75 U_{\max}$ (cm s^{-1});
- U_{\max} = maximum velocity in the profile (cm s^{-1});
- z_0 = characteristic hydraulic friction length (cm);
- z = vertical axis (cm);
- f = frequency (s^{-1});
- ρ = water density (kg m^{-3});
- τ = bed shear stress (kg s^{-2});
- $\phi_{ii}(k)$ = the spectral density of the i th velocity component at wave number k ;
- α_i = the 1D Kolmogorov constant;
- \mathcal{E} = energy dissipation;
- σ_D = standard deviation of the bed roughness elements.

Table 1. Experimental conditions and estimates of u_* by different methods

Exp.	Water depth h cm	\bar{U} cms ⁻¹	Reynolds Number	z_0 cm	Methods for u_* (cms ⁻¹) calculations						
					Logarithmic	Reynolds	TKE $C_1=0.19$	TKE W' $C_2=0.9$	Spectral	Mean	Standard deviation
1	19	36.63	6.93×10^4	0.029	2.92	2.64	2.37	2.45	2.65	2.61	0.21
2	20	45.79	9.12×10^4	0.002	2.26	2.94	3.16	2.48	3.20	2.81	0.42
3	20	50.2	1.00×10^5	0.0025	2.72	3.32	3.32	2.98	3.30	3.13	0.27
4	20	53.21	1.06×10^5	0.005	3.57	3.66	3.62	2.99	4.19	3.61	0.42
5	19	17.12	3.24×10^4	0.061	1.18	1.58	2.30	1.18	2.44	1.74	0.60
6	19	34.82	6.59×10^4	0.025	2.65	3.04	2.57	2.67	2.70	2.73	0.18
7	19	41.38	7.83×10^4	0.04	3.23	2.71	2.77	2.32	3.45	2.90	0.45
8	19	49.09	9.29×10^4	0.06	3.98	3.24	3.24	2.73	3.54	3.35	0.46
9	19	56.54	1.07×10^5	0.03	4.37	3.79	3.79	3.37	4.41	3.95	0.44

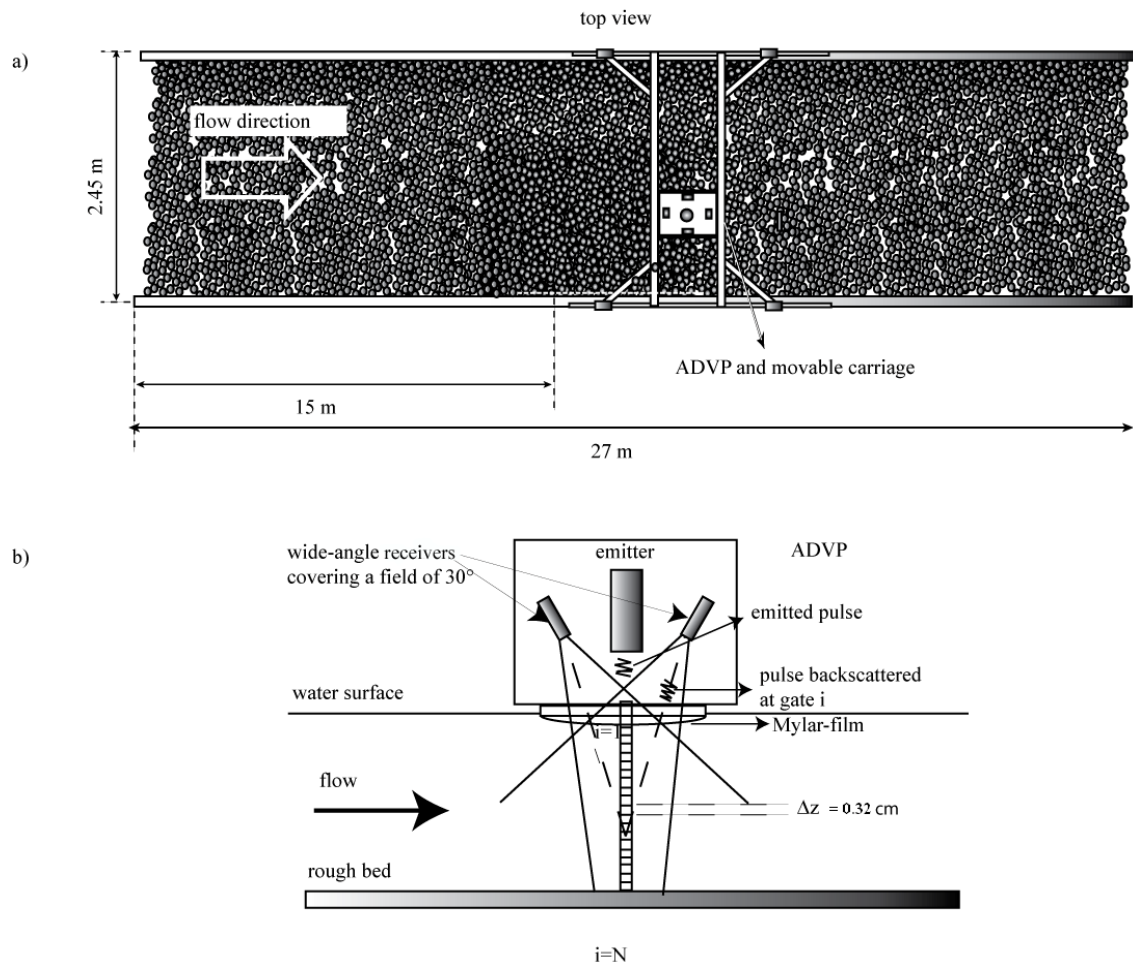


Fig. 1. Schematics of a) the hydraulic open channel, and b) the ADVP instrument

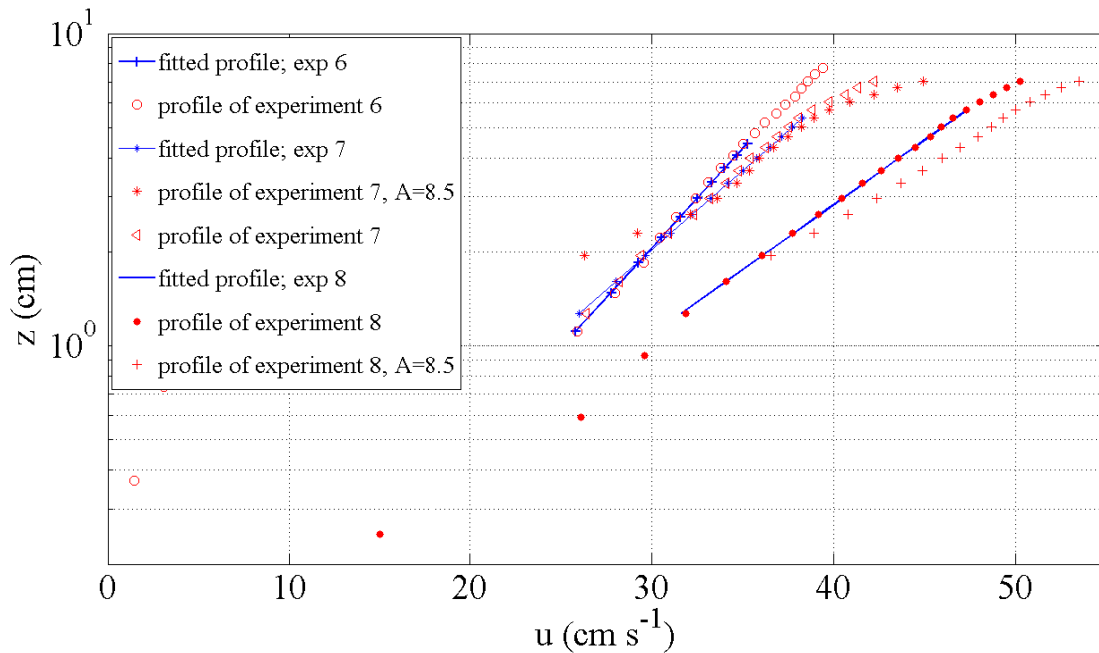


Fig. 2. Logarithmic profile method for different experiments with water depth $h = 19$ cm. Also plotted is the profile calculated with the log-law using the additive constant $A = 8.5$.

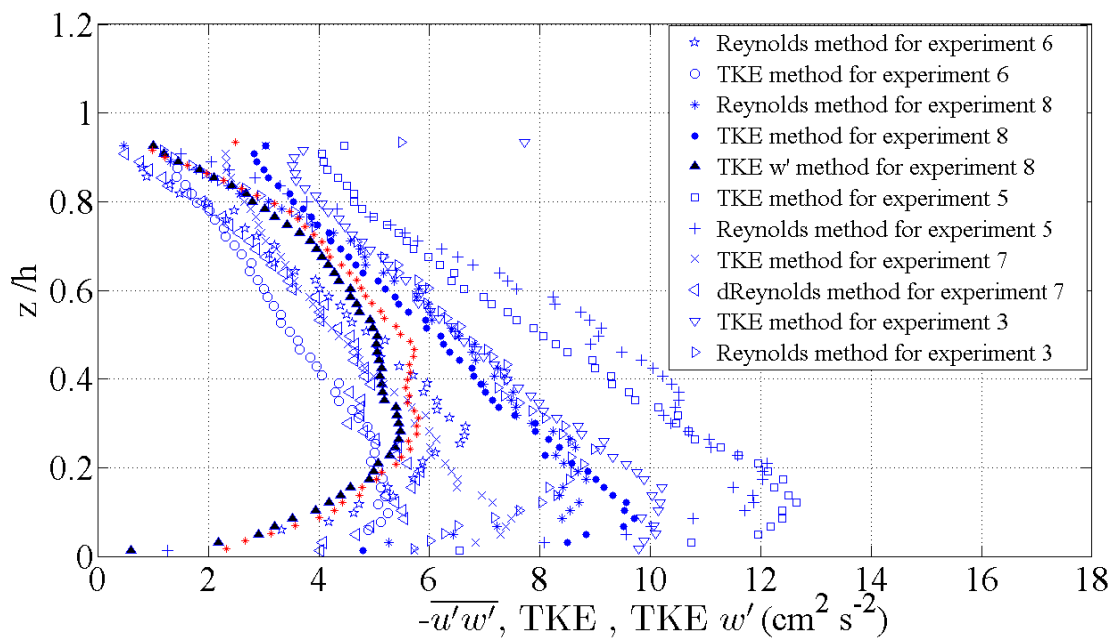


Fig. 3. Reynolds stress and TKE profiles for ADVP data with water depth $h = 19$ cm for different experiments.

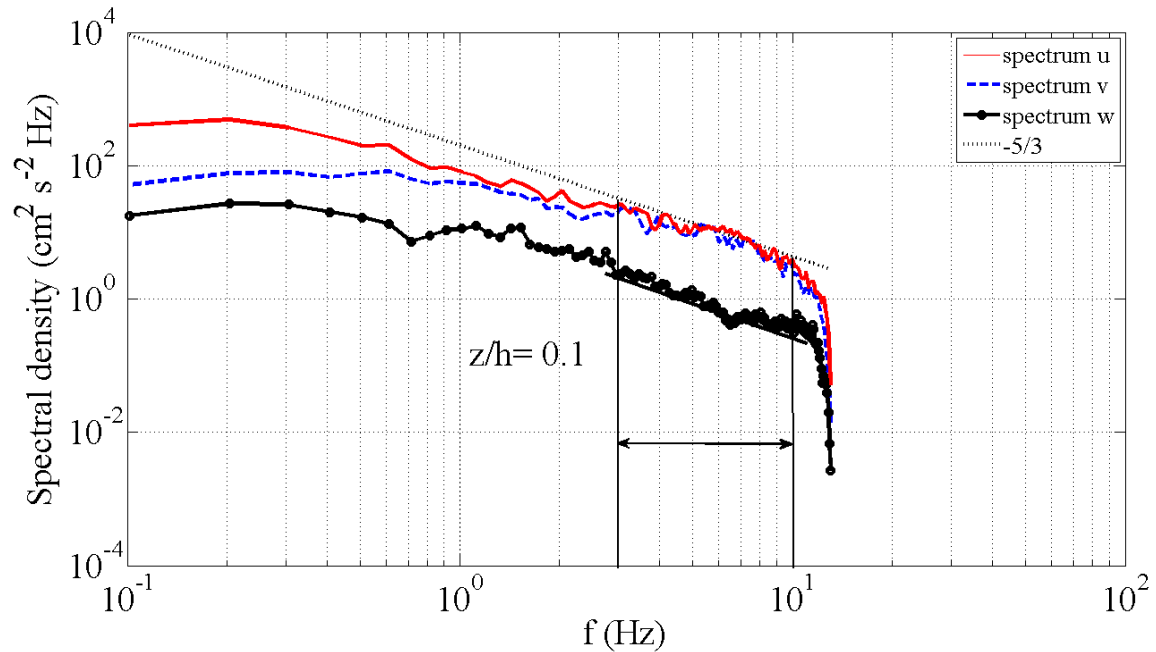


Fig. 4. Typical energy spectra for all velocity components at $z/h = 0.1$ (experiment 6). The inertial subrange is indicated by the arrows.

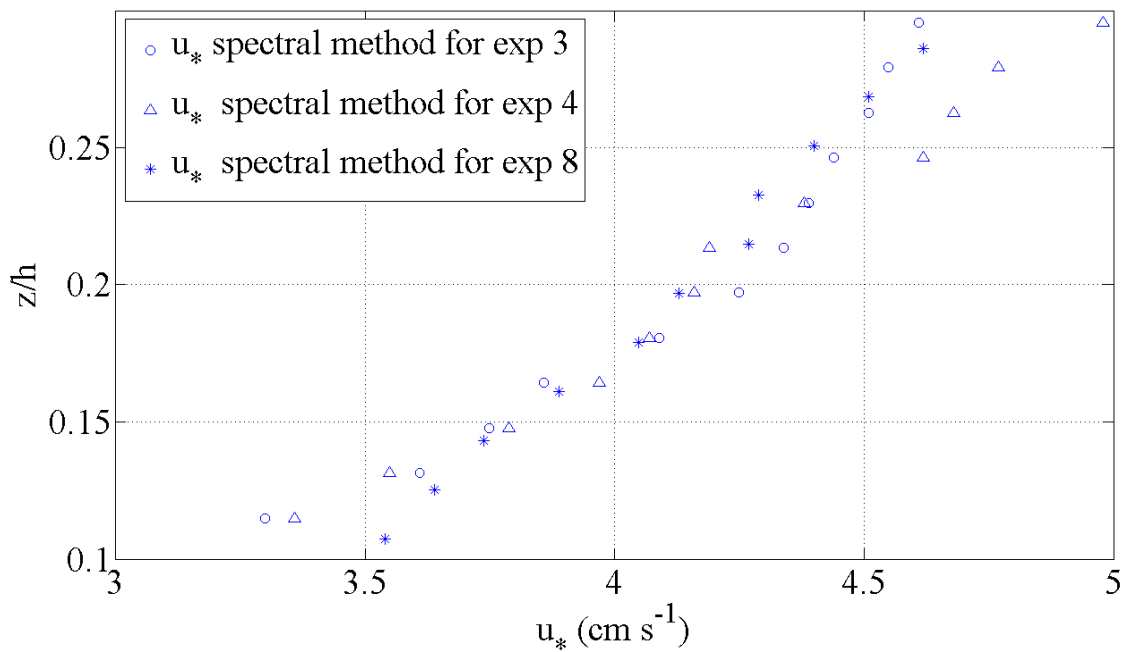


Fig. 5. Shear velocity u_* obtained from spectra of the vertical velocity component for different experiments in the range $0.1 < z/h < 0.3$.

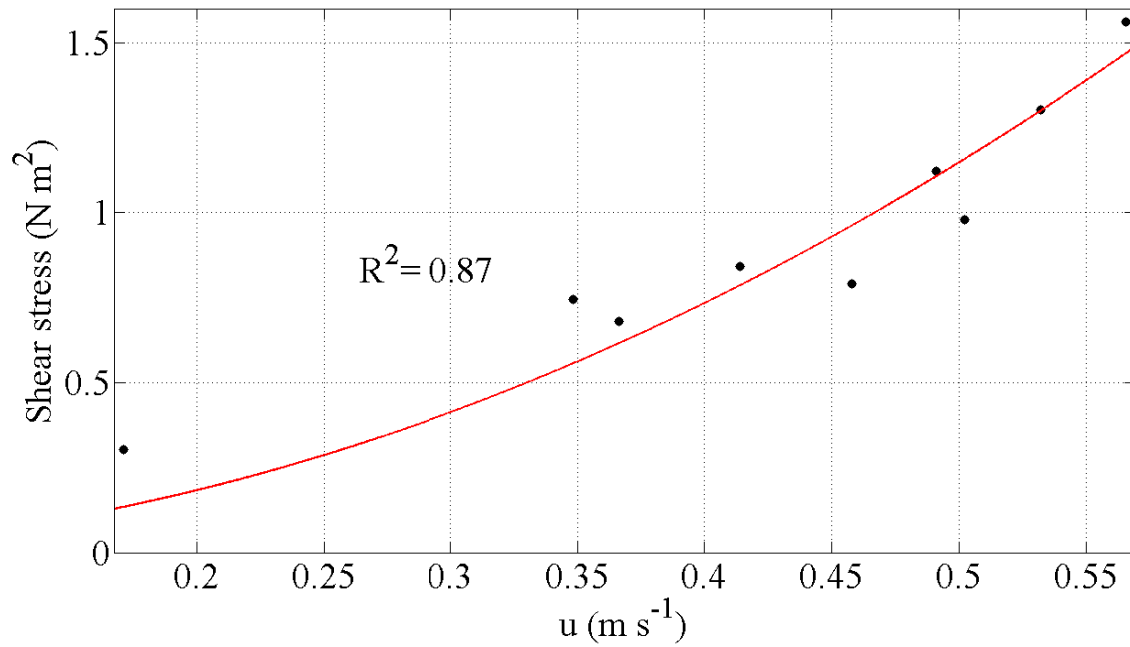


Fig. 6. Relationship between shear stress averaged over all methods and mean streamwise velocity.

A.3 Coherent structures in rough-bed open-channel flow observed in fluctuations of velocity profiles, shear velocity and pressure

F. Bagherimiyab and U. Lemmin

Ecole Polytechnique Fédérale de Lausanne (EPFL), ENAC, Station 18, CH-1015 Lausanne, Switzerland

fereshteh.bagheri-meyab@epfl.ch ulrich.lemmin@epfl.ch

ABSTRACT

In order to study the dynamics of bed shear velocity u_* , quasi-instantaneous 3D velocity profiles with high spatial and temporal resolution were measured with an Acoustic Doppler Velocity Profiler (ADVP) in an open channel with a non-moving bed of loose mixed gravel ($D_{50} = 1.5$ cm) with Reynolds numbers ranging from 3.24×10^4 to 1.07×10^5 . A mean u_* was first determined using logarithmic mean velocity profiles and Reynolds stress profiles which were then compared to u_* measured on the bed simultaneously by a flush-mounted hot-film sensor. All methods yield similar estimates of u_* . The fluctuating component of flow velocity was analyzed together with the fluctuating signals of the hot-film sensor and a Piezoresistive pressure transducer mounted in the top layer of the bed, in order to determine the correlation between the different signals. A quadrant analysis of the velocity fluctuation data in the inner layer shows that down to the bed, ejections and sweeps clearly dominate the shear stress distribution. The quadrant distribution of the data obtained with the hot-film sensor and the pressure transducer is similar to that of the velocities in the water column. A correlation between coherent structure dynamics of the velocity in the water column and the sensors on the bed is made evident. Sweep events in the water column lead to an increase in bottom pressure and shear velocity. An increase in bottom pressure correlates with an increase in shear velocity.

Keywords: open-channel flow, bed shear stress, Reynolds stress, coherent structures, ADVP, hot-film sensor, Piezoresistive pressure transducer

1 INTRODUCTION

Despite long efforts, turbulence continues to persist as one of the least resolved fields in geophysical flows. Even though it is recognized that turbulence is an important contributor to the dynamics of most natural flows, mean value concepts are still applied, instead of turbulence based approaches for many practical applications governed by turbulence, such as sediment suspension in rivers and open-channel flow. Coherent structures are part of the turbulence field and are considered highly interesting features of turbulent shear flows. It is often argued that their dynamical significance has been overemphasized. Coherent structures are predominantly found in regions adjacent to a wall in turbulent boundary layers. In these fully developed turbulent shear flows, incoherent turbulence is also important and cannot be ignored, but contributions from coherent Reynolds stress, vorticity, and production are comparable to those of their time-averaged counterparts (Hussain 1983).

Using an Acoustic Doppler Velocity Profiler (ADVP) which provides quasi-instantaneous 3D velocity profiles with resolution of turbulence scales, Shen and Lemmin (1999) made evident the full depth extension of coherent structure cells with alternating ejection and sweep events.. In rivers and sediment-laden open-channel flows, mean shear, turbulent fluctuations and coherent structures contribute to sediment suspension and transport (Cellino and Lemmin 2004, Hurther and Lemmin 2000). It was demonstrated that coherent structures may carry nearly one-half of the suspended load (Hurther and Lemmin 2001). Reynolds shear stresses, velocity spectra, and coherence functions obtained from measurements in a gravel-bed river indicated a dominance of longitudinal-vertical shedding vortices in the wake of a cluster (Lacey et al. 2008). Quadrant analysis of their flow field revealed that coherent structure events contributed 80% of the local longitudinal-vertical component Reynolds shear stress, with ejection events prevailing in the wake of clusters. Grass (1982), Rashidi et al. (1990) and Kaftori and Hetsroni (1998) suggested that the initiation of sediment motion may be caused by sweeps.

In turbulent gravel-bed flows, particle lift and form drag forces result from pressure differences across the bed particles. Smart (2005) indicated that pressure fluctuations advected from upstream produce lift forces that exceed the submerged weight of bed surface stones. In rivers and open channels, rapid pressure fluctuations can be caused by flow separating behind particles or bed forms, by eddies advected by flow and or by surface waves. There is a link between the mean shear stress approach to entrainment, as proposed by Shields (1936) and turbulent pressure fluctuations. Over the years, experiments have shown that time-averaged bed shear stress parameters such as Shield's θ , are a reasonable indicator for predicting particle entrainment, because shear stress is an indicator of the pressure fluctuation intensity. Investigations by Smart and Habersack (2007) in gravel bed rivers showed that advected pressure fluctuations can create a vertical pressure differential on the bed surface layer that is sufficient to entrain gravel particles. Under low-mobility conditions, turbulence fluctuations of velocity and pressure are a key factor in the entrainment of bed particles, since mean forces alone are not strong enough to displace particles (Kleinhans and van Rijn 2002). Hofland et al. (2005) measured fluctuating pressures on coarse bed material. Their measurements showed that the magnitude of the fluctuating pressure at a point on their measurement cube is a function of the cube exposure relative to the stones upstream. They also showed through quadrant analysis that the drag force is not only directly dependent on the horizontal near-bed velocity, but also on the vertical velocity. Thomas and Bull (1983) and Bernard et al. (1993) observed that pressure peaks are related to sweep events in the near-wall shear layer.

The temporal and spatial shear velocity distribution is related to turbulent flow structures close to the bed and is as such of major importance for the basic understanding of the development of near-bed turbulence. From direct simulation of fully turbulent channel flow, Kravchenko et al. (1993) found that high values of skin friction are closely related to sweep motion. Experimental work in duct flow by Grosse and Schröder (2009) demonstrated that wall shear stress fluctuations correlate with near-wall coherent structures.

In this paper, ADVP velocity profile data are analyzed together with measurements of a hot-film sensor mounted flush on the bed and differential pressure measurements in the bed surface layer. First, mean shear velocity estimates by different methods are compared. Thereafter, the relation between coherent structures in the near-bed water column and fluctuations of shear velocity and bed surface pressure are investigated. It will be shown that

turbulent fluctuations of velocity, shear velocity and bed pressure are correlated in the form of coherent structures.

2 TECHNIQUES FOR DETERMINING SHEAR VELOCITY

Over time, different methods of calculating mean bed shear velocity have been proposed. We will briefly summarize the concepts of two of those methods below:

Logarithmic law method

Shear velocity can be calculated by assuming an equation for the vertical profile of velocity. However, reliable formulas for the vertical distribution of longitudinal time-averaged velocities are still a problem in river mechanics, even for 2D flows (Nikora and Smart 1997). For the inner logarithmic region of the flow covering the lowest 20% of the water depth, the velocity profile is shown to have the following form (Schlichting 1987):

$$\frac{u}{u_*} = \frac{1}{k} \ln \left(\frac{z}{z_0} \right) \quad (1)$$

For 2D uniform flow, it is well established that the constant k is von Karman's constant ($k = 0.4$). This equation can be plotted in semi-logarithmic form in order to provide values for z_0 and u_* . The procedure involves fitting a straight line by ordinary least square regression to the profile and calculating the values of u_* and z_0 from the slope and intercept of the computed regression equation, as will be done in this paper.

Reynolds stress method

When turbulence measurements are available, local shear velocity can be determined from the measured Reynolds stress distribution as

$$u_* = \sqrt{-\overline{u'w'}} \quad (2)$$

In this equation, u' and w' are the velocity fluctuations of the longitudinal (streamwise) and vertical components. The development of instruments which can measure the three components of turbulent velocity fluctuations has prompted the use of this method to calculate bed shear velocity in rivers, where it may otherwise be difficult to apply the logarithmic profile method. However, this method is fairly sensitive to any deviation from 2D uniform flow (Nezu and Nakagawa 1993).

In this paper, bed shear velocity will be calculated with the methods described above for the ADVP experimental data, and will then be compared with hot-film shear velocity measurements.

3 QUADRANT ANALYSIS

The quadrant analysis method is used to study the relationship between temporal fluctuations of velocity components, u' and w' , in particular their distribution in the four quadrants.

Outward interactions are found in quadrant $Q1$ ($u' > 0, w' > 0$), the correlation between $u' < 0, w' > 0$ indicates ejection events in quadrant $Q2$, inward interaction occur in quadrant $Q3$ ($u' < 0, w' < 0$) and sweep events are present in quadrant $Q4$ ($u' > 0, w' < 0$). An ejection event is characterized by an upward movement of low speed fluid, because the instantaneous local velocity u is lower than the time-averaged local velocity. By the same definition, a sweep is a downward movement of high speed fluid towards the bed. It is possible to distinguish events falling into the different quadrants by analyzing the direction of the instantaneous fluctuating components. Lu and Willmarth (1973) proposed the u' - w' quadrant threshold technique which combines the local instantaneous velocity fluctuations in two perpendicular directions. Correlation between u' and w' established in this manner reveals the presence of turbulent coherent structures (Lu and Willmarth 1973; Nezu and Nakagawa 1993) and their importance in flow dynamics using

$$|u'w'| = H \sqrt{u'^2} \sqrt{w'^2} \quad (3)$$

where H is the hole size representing a threshold level, as explained in Nezu and Nakagawa (1993). The quadrants, excluding the hole area, are the regions contributing to events. From eq. 3, the first order moments as a function of threshold level H will be calculated. By increasing the level of H , progressively stronger fractional events will be selected and their distribution over the different quadrants will be investigated. In turbulent open-channel flow, it is observed that ejections ($Q2$) and sweeps ($Q4$) dominate the quadrant distribution (Nezu and Nakagawa 1993) of the velocity components. The present analysis applies this concept to the ADVP velocity data and it is also used to relate coherent structures in the velocity field to the separately, but simultaneously measured hot-film bed shear stress and pressure variations.

4 EXPERIMENTAL SET-UP

The experiments were carried out in a 2.4 m wide and 27 m long open-channel with a 10 cm thick bed of loose mixed gravel with $D_{50} = 1.5$ cm (Figure 1a). Measurements were made 12 m from the channel entrance where the flow is well developed for the two different flow depths ($h = 19$ and 20 cm, respectively) and with Reynolds numbers ranging from 3.24×10^4 to 1.07×10^5 . The bed was not moving during the experiments.

Acoustic Doppler Velocity Profiler (ADVP)

The ADVP instrument which was developed in our laboratory measures quasi instantaneous profiles of 3D velocity components over the entire water depth of open-channel flow (Shen and Lemmin 1997, Hurther 2001). This instrument consists of a central emitter and four wide-angle receiver transducers placed symmetrically around the center (Figure 1b). The transducers are arranged in two perpendicular planes, each of which allows resolving profiles of one horizontal and the vertical velocity component. The redundancy of the vertical component allows controlling the quality of the geometrical alignment of the transducers (Hurther and Lemmin 2000). This transducer arrangement provides velocities along a single straight vertical line of consecutive scattering volumes (Figure 1b). All velocity components are evaluated from phase information coming from the same scattering volume, because sound is only emitted from the central transducer. The typical spatio-temporal resolution (4

mm and 0.032 s, respectively) is sufficient to quantitatively estimate turbulence parameters in the productive and inertial ranges of the spectral space. The instrument provides quasi-instantaneous 3D velocity profiles from which time-averaged profiles of mean and turbulent quantities are calculated by Reynolds decomposition for the present analysis. Thus, all points in the profiles shown in this paper were nearly simultaneously measured.

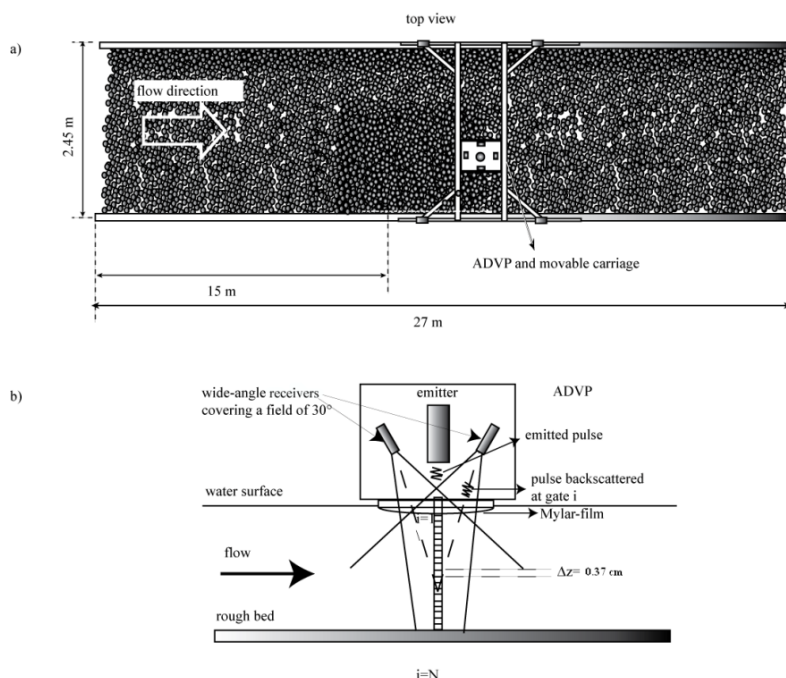


Figure 1. Schematics of a) the hydraulic open channel and b) the ADVP instrument

Hot-film sensor

Bed shear velocity was measured with a sensor based on the hot-film principle. It has constant sensitivity in variable temperature flow. A specially designed temperature compensation bridge contains two sub-bridges for flow and temperature sensors (Shen et al. 1998). Hot-film elements, one operating as a hot-film and one as a cold film, were mounted flush with the bed below the velocity profile point (Figure 2). Bottom shear stress sensors have been successfully used in smooth bottom flows (Hanratty and Campbell 1983, Chandrasekaran et al. 2005). In the present study, it is applied on a rough wall and form drag effects may be present. In order to minimize the variability of form drag, gravel stones were glued in place on a 15 cm x 15 cm square surrounding the sensor. The porosity of the bed was not affected. The sensor was calibrated in place for a range of flow velocities, as described in Albayrak et al. (2008). Data were recorded at a frequency of 100 Hz.

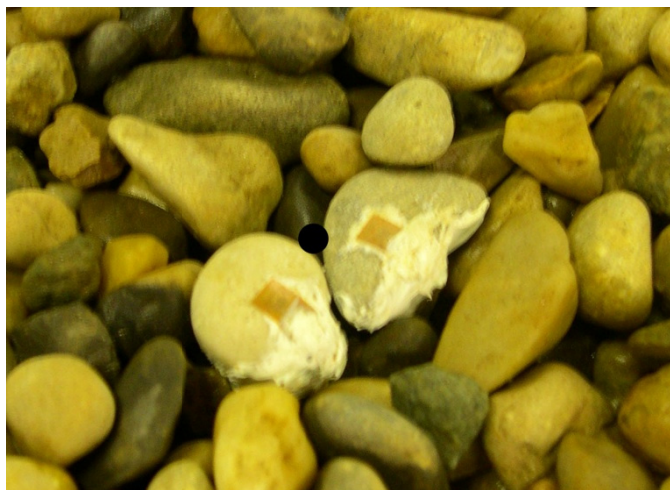


Figure 2. Hot-film sensor on the bed of the open channel. Active surfaces of the hot-film elements (brown squares) measure 2 x 2.5 mm. Black dot: position of the pressure tube which ended at one-half stone height below the hot-film sensor level.

Piezoresistive pressure transducer

Figure 3 shows the schematic of the piezoresistive differential pressure transducer arrangement. In order to capture the pressure fluctuations on the gravel bed, the transducer was installed under the gravel bed. A rigid tube was connected to the transducer and ended at one-half the mean gravel diameter below the mean bed level, as shown in Figure 3. The end of this tube was placed near the hot-film elements (Figure 2). Another rigid tube connected the transducer to the bottom of a cylinder which acted as a stilling basin at mean water level. The transducer was calibrated in situ for a range of water depth. Data were recorded at 100Hz.

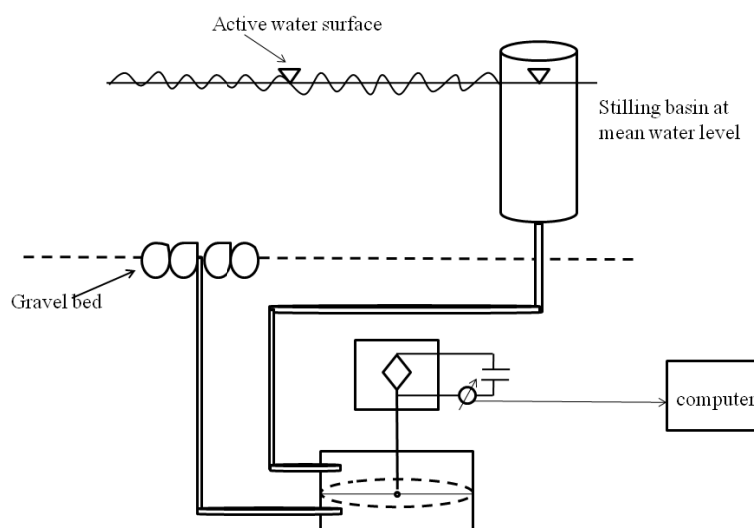


Figure 3. Schematic of the piezoresistive differential pressure transducer on the bed of the open channel.

5 PROCEDURE

In this study, three series of experiments at different Reynolds numbers for two different flow depths were conducted. With all three instruments, data were simultaneously collected for three minutes in the center of the channel. Quasi-instantaneous 3D velocity profiles with high spatial and temporal resolution were measured with the ADV, using a PRF = 1000 Hz and 714 Hz. ADV measurements were made from above the water surface (Hurther et al. 2007) by placing the transducers into a water filled housing which touched the water surface by a Mylar sheet. The water column was divided into layers of about 4 mm thickness and in each layer, the three velocity components were measured. Therefore, quasi-instantaneous 3D velocity profiles with up to 50 points in the vertical were obtained. Since the instrument perturbs the flow near the water surface (Figure 1b), this layer was omitted in the analysis; and profiles were cut at $z/h = 0.9$. From the data, profiles of mean values of the three velocity components, the velocity variance and the shear velocity were calculated. Bed shear velocities were measured with the hot-film sensor placed below the ADV profile line and pressure fluctuations were measured with the piezoresistive pressure transducer placed near the hot-film element at one-half mean gravel bed diameter below the surface. The beginning of the recording of the hot-film sensor, the differential piezoresistive pressure transducer and the ADV data was synchronized.

6 RESULTS OF BED SHEAR VELOCITY ESTIMATES

From the instantaneous velocity profile data measured by the ADV instrument, bed shear velocities u_* were determined using the logarithmic mean velocity profile and the Reynolds stress profile. The large number of simultaneously measured points in each profile allowed for a detailed analysis. The results were compared with the bed shear velocities which were measured by the hot-film sensor. We will first briefly describe the application of the methods, and thereafter, we will compare the results of all of the experiments.

Logarithmic profile method

A typical profile is given in Figure 4. It can be seen that for the lower 20% of the water column, the mean longitudinal velocity profile closely follows the logarithmic profile. Very close to the bed, typically for the lowest two points in the profile, a deviation is observed. This is due to the effect of the relatively large bed roughness. In this layer, individual roughness elements determine the flow structure and the flow becomes 3D (Albayrak 2008). By using the procedure proposed in the literature (Smart 1999), the profile was slightly shifted up or down in the vertical in order to find the optimal fit. This compensates for the difficulty in determining the profile origin reference level under such rough bed flow conditions.

Reynolds stress method

The Reynolds stress was calculated for all points in the profile. In order to avoid the disturbing effects of the instrument at the surface, the profiles were limited to $0.9 z/h$. A typical Reynolds stress profile is shown in Figure 5. A maximum in the Reynolds stress

distribution is observed at around $0.25 z/h$. Below the maximum, the form of the profile is determined by the bottom roughness. The profile above the maximum was well approximated by a linear fit which is extrapolated to the bed.

A comparison of the results

Table 1 presents the shear stress values obtained with the methods which were explained above for all experiments at different water depths. The results cover a wide range of Reynolds numbers and thus flow velocities. The results of the hot-film measurements can be compared to the bed shear velocities obtained with the other methods. For such rough bed flow, calculated and measured bed shear velocities rarely coincide and no systematic trend is obvious. Most of the calculated bed shear velocities fall to within $\pm 15\%$ of the measured ones. The logarithmic mean velocity profile method allows determining the height of the roughness layer and the height of the logarithmic layer ($\approx 0.2 z/h$). From the Reynolds stress method, the two-dimensionality (2D) of the flow was confirmed.

Table 1. Estimates of u_* by two different methods and hot-film measurements

Methods Experiments	Water depth h (cm)	u_* (cms ⁻¹)			
		Logarithmic	Reynolds	Hot-film	Reynolds number
1	19	2.82	2.68	2.93	6.93×10^4
2	20	2.26	2.94	3.21	9.12×10^4
3	20	2.72	3.32	2.98	1.00×10^5
4	20	3.57	3.66	3.85	1.06×10^5
5	19	1.14	1.58	1.67	3.24×10^4
6	19	2.60	3.04	2.75	6.59×10^4
7	19	3.50	2.71	3.51	7.83×10^4
8	19	3.98	3.23	3.84	9.29×10^4
9	19	4.30	3.74	4.51	1.07×10^5

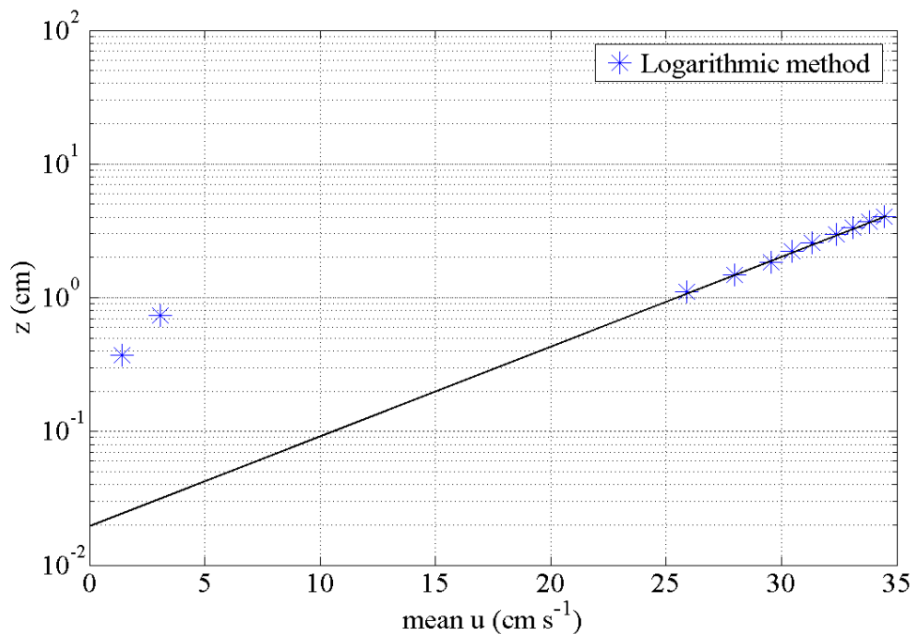


Figure 4. Logarithmic profile method for ADVP data with water depth $h = 19$ cm (experiment 6).

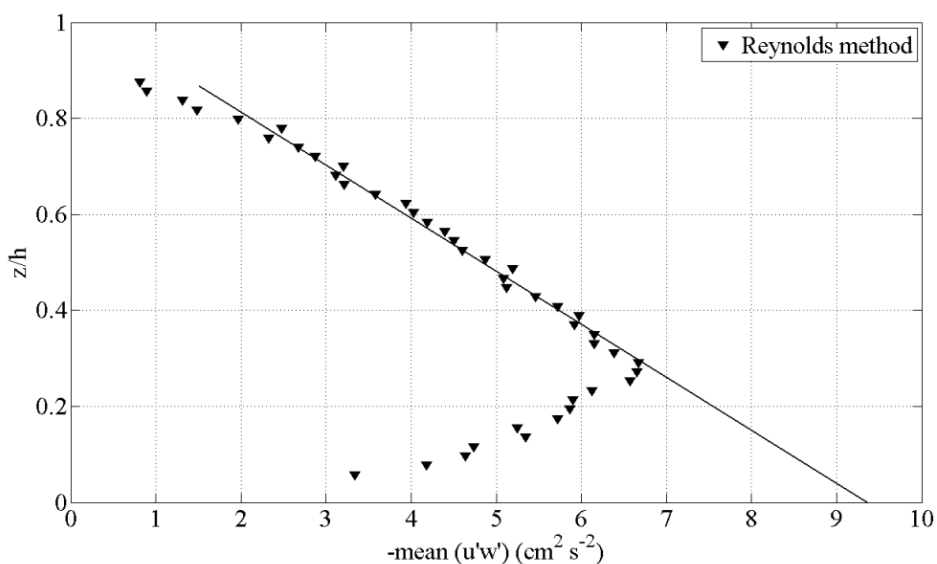


Figure 5. Reynolds stress and TKE profiles for ADVP data with water depth $h = 19$ cm (experiment 6).

7 RESULTS OF THE COHERENT STRUCTURE ANALYSIS

In the present analysis, we will compare the event dynamics in the near-bed logarithmic layer recorded by the ADVP with the one obtained from the hot-film bed shear velocity measurements and with the pressure fluctuation measurements which were acquired with a piezoresistive differential pressure transducer.

The conditional quadrant method involves studying the relationship between the turbulence fluctuations of the velocity components, u' and w' , and in particular, the distribution of the related Reynolds shear stress into four quadrants, as explained above. In order to demonstrate the coherent structure dynamics in the water column, a short timeseries of the instantaneous Reynolds shear stress $-u'w'$ in the near bed logarithmic layer at $z/h = 0.1$ is shown in Figure

6. The event structure of the Reynolds stress is obvious from this example. It can also be seen that the events are randomly distributed and that most events occur with small amplitude. A probability of large amplitude events exists with both positive and negative signs. In the quadrant analysis, the contribution of these events will be documented for large hole size H . Figure 7 presents the Reynolds stress contours and the corresponding instantaneous fluctuation profiles of the 2D velocity (arrows) for most of the water column. From a visual inspection of this sample, it can be seen that turbulent fluctuations and Reynolds shear stress are organized in event structures that are particularly strong in the inner region, but often extend over most of the water column. Furthermore, coherent structures are quite evident in large parts of the water column. A similar large scale pattern of event structures was already observed by Shen and Lemmin (1999) in smooth bed flow.

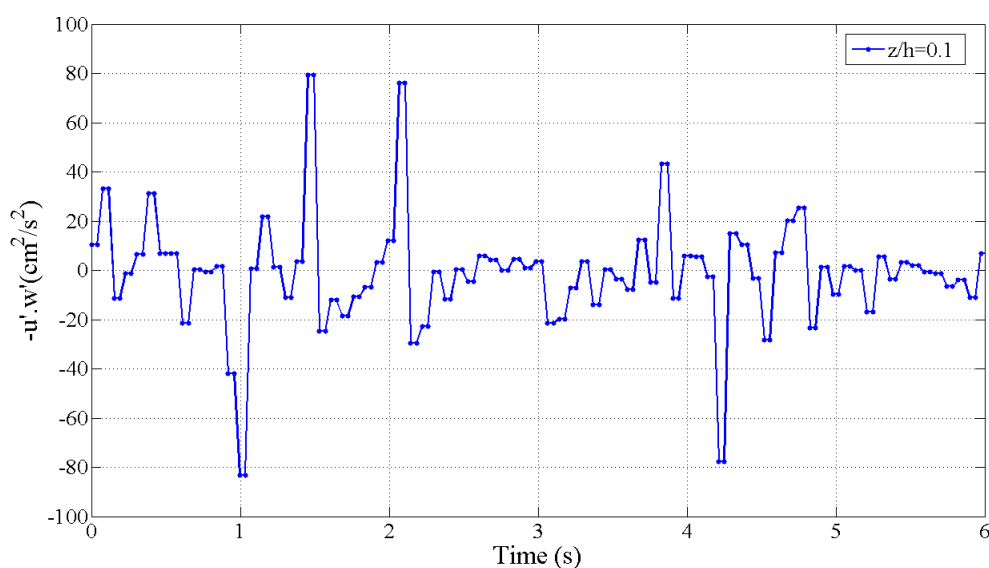


Figure 6. Instantaneous Reynolds shear stress versus time at $z/h = 0.1$ (experiment 6).

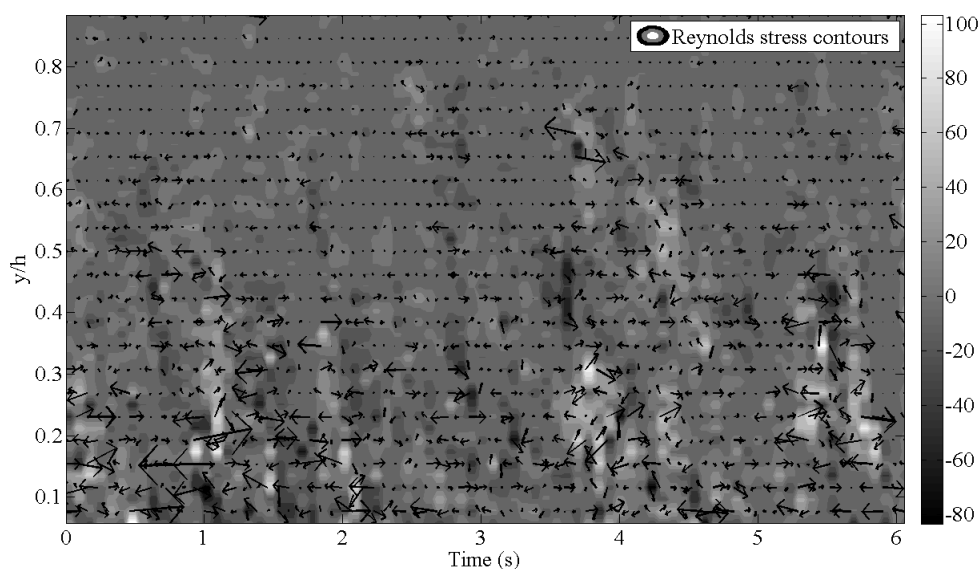


Figure 7. The Reynolds stress contours and the instantaneous fluctuation profiles of 2D velocity (arrows) demonstrate the coherent structures of the turbulence field (experiment 6).

In order to investigate the event dynamics in the near-bed logarithmic layer by quadrant analysis, we shall quantify the contributions of the relative shear stress for the cross-product

term $e1 = u'w'/\overline{u'w'}$ in the water column as a function of the hole size $H1$. The hole size represents the threshold level used in the analysis, as explained in Nezu and Nakagawa (1993). In the same way, by combining hot-film fluctuations u_* , pressure fluctuations p' , and ADV data u' and w' , we calculate $e2 = u_*'u'/\overline{u_*'u'}$ and $e2 = p'u'/\overline{p'u'}$ with threshold $H2$, $e3 = u_*'w'/\overline{u_*'w'}$ and $e3 = p'w'/\overline{p'w'}$ with threshold $H3$ and $e4 = u_*'p'/\overline{u_*'p'}$ with threshold $H4$. The quadrant structure of $e1$ at $z/h = 0.1$ in the lower part of the logarithmic region, is presented in Figure 8 where the dominance of ejection and sweep events is evident. This is a typical result for open channel flow in accordance with the literature (Nezu and Nakagawa 1993, Hurther and Lemmin 2003). In Figure 9, the quadrant structure of $e1$ at one-half the water depth $z/h = 0.5$ is plotted and shows the same coherence pattern as in Figure 8. This means that coherent structures extend over most of the water column, as was already obvious from the event patterns in Figure 7.

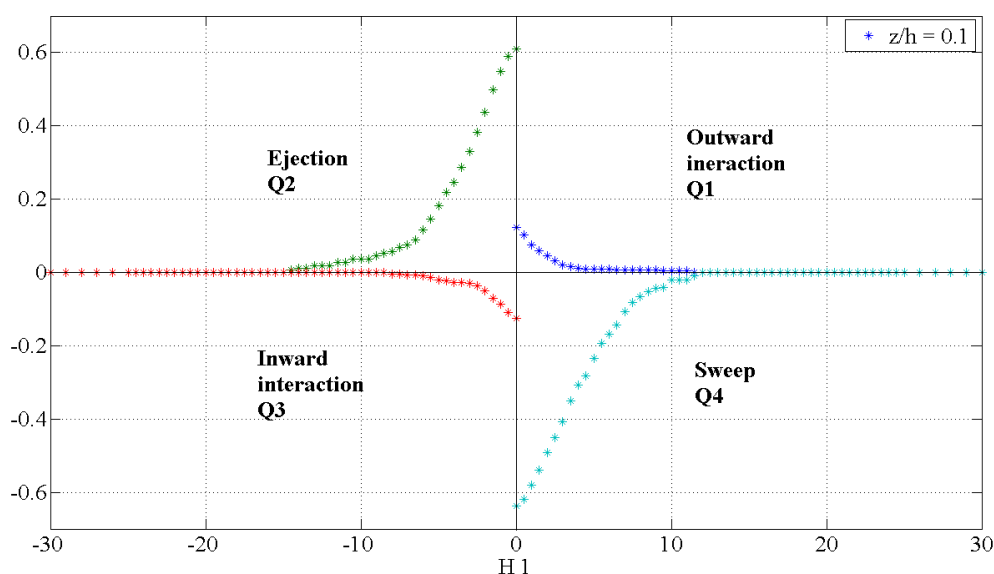


Figure 8. Fractional contribution of relative covariance $e1 = u'w'/\overline{u'w'}$ versus threshold level $H1$ for ADVP data at $z/h = 0.1$ (experiment 6).

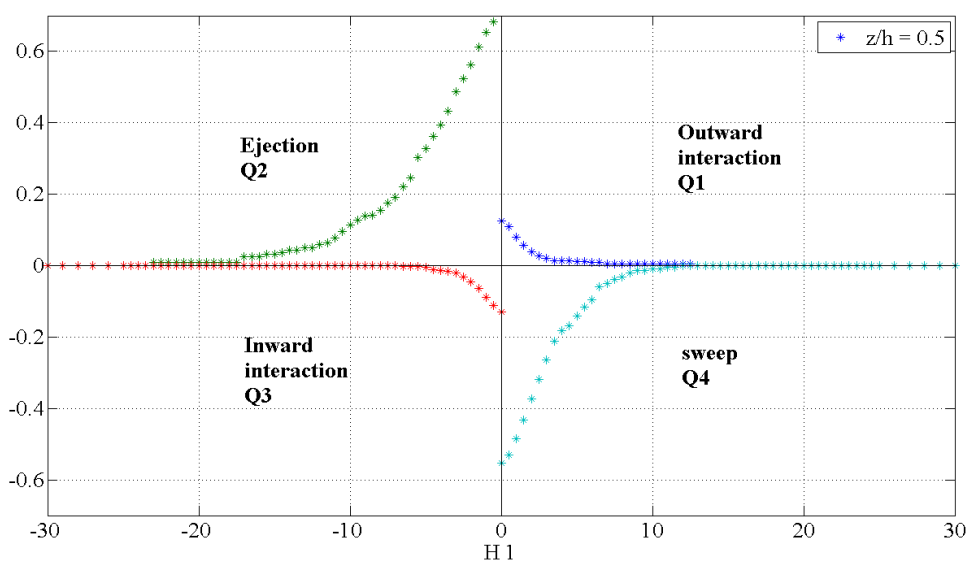


Figure 9. Fractional contribution of relative covariance $e1 = u'w'/\overline{u'w'}$ versus threshold level $H1$ for ADVP data at $z/h = 0.5$ (experiment 6).

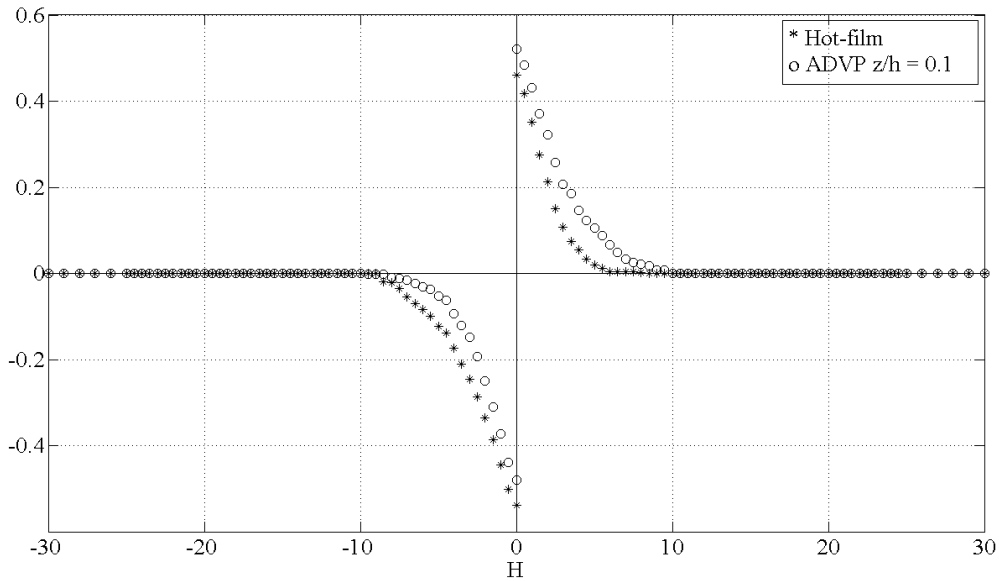


Figure 10. Fractional contribution of relative covariance

$e = u'u'/\overline{u'u'}$ versus threshold level H for ADVP data at $z/h = 0.1$ and $e = u_*'u_*'/\overline{u_*'u_*'}$ for hot-film data (experiment 6).

Event dynamics of hot-film $e = u_*'u_*'/\overline{u_*'u_*'}$ and ADVP data, $e = u'u'/\overline{u'u'}$ and $e = U_*'U_*'/\overline{U_*'U_*'}$, and of pressure transducer $e = p'p'/\overline{p'p'}$ and ADVP data, $e = u'u'/\overline{u'u'}$ are compared in Figures 10 and 11, respectively. From the similarity of the fall-off of the curves for the two data sets in each of the two figures, it appears that the dynamics of bed shear velocity fluctuation and pressure fluctuation events are comparable to that of the turbulence in the water column. Similar results were obtained using the vertical component of the ADVP velocity data.

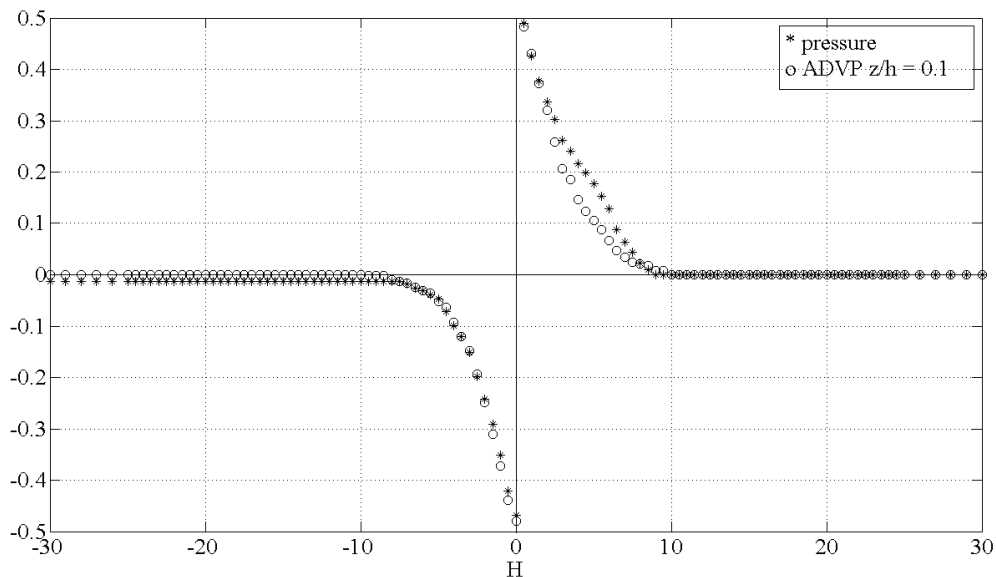


Figure 11. Fractional contribution of relative covariance

$e = u'u'/\overline{u'u'}$ versus threshold level H for ADVP data at $z/h = 0.1$ and $e = p'p'/\overline{p'p'}$ for pressure fluctuations (experiment 6).

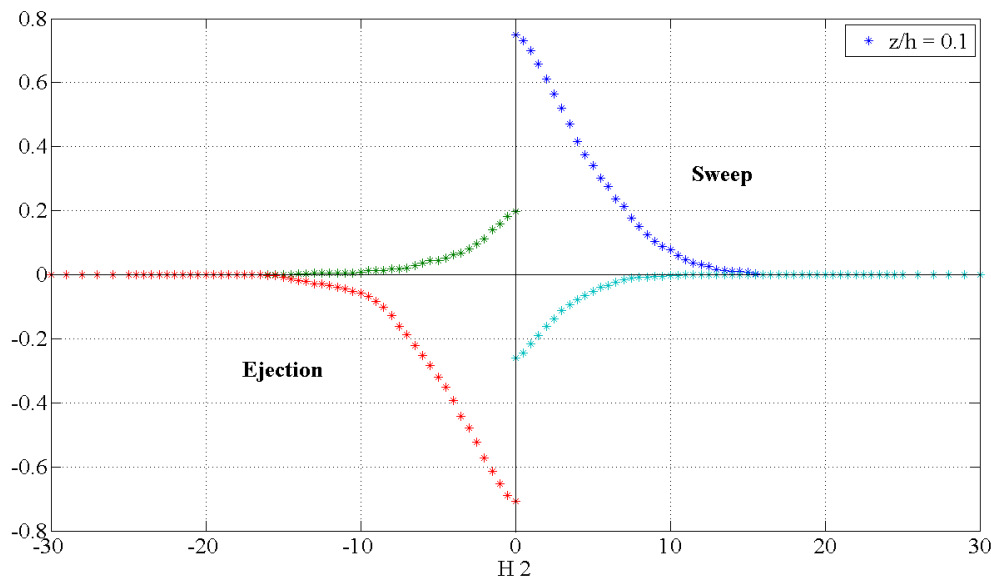


Figure 12. Fractional contribution of relative covariance

$e2 = u_*'u'/\overline{u_*'u'}$ versus threshold level H2 for ADVP data at $z/h = 0.1$ and hot-film data (experiment 6).

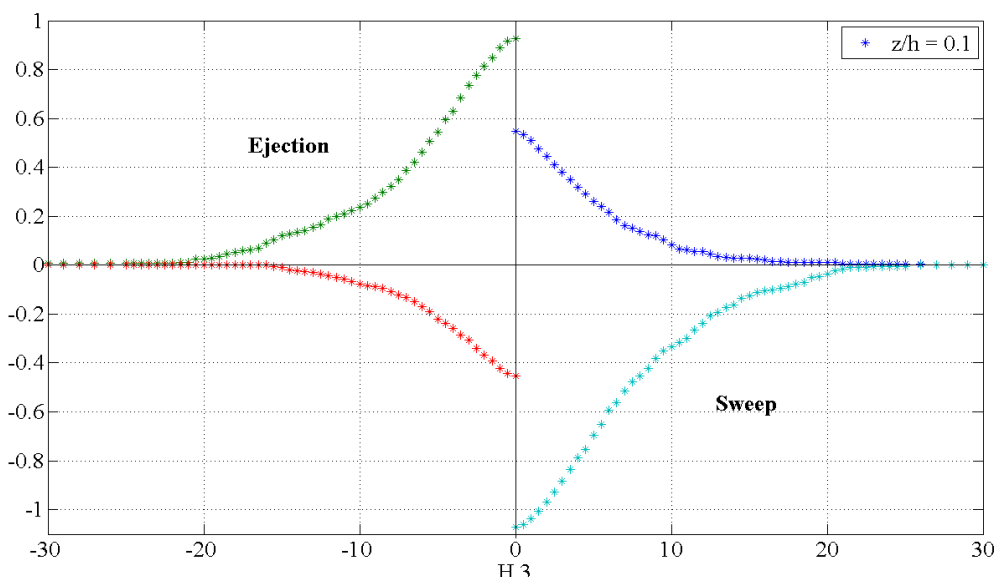


Figure 13. Fractional contribution of relative covariance

$e3 = u_*'w'/\overline{u_*'w'}$ versus threshold level H3 for ADVP data at $z/h = 0.1$ and hot-film data (experiment 6).

The relationship between the coherent structures in the water column and bottom shear stress is evident from the quadrant analysis which combines hot-film data on the bed and ADVP data at $z/h = 0.1$. Results are shown for $e2 = u_*'u'/\overline{u_*'u'}$ in Figure 12 and for $e3 = u_*'w'/\overline{u_*'w'}$ in Figure 13. In Figure 12, quadrants of u' and u_* having the same sign show higher values than those of opposite sign. Sweeps in the velocity field which are marked by positive u' are associated with increases in bed shear values. Ejections correlate with a decrease of bed shear stress. The results are confirmed by the quadrant analysis which combines the vertical velocity component w' and bed shear stress u_* . When compared with the results of the ADVP velocity data in Figure 8, it can be seen that ejections and sweeps again dominate the quadrant distribution in the present analysis. Therefore, coherent structures in the water column directly influence the shear velocity dynamics on the bed. It

should be noted, however, that inward and outward interactions more strongly contribute to the correlation between water flow and bed shear than they do to the flow field above the bed.

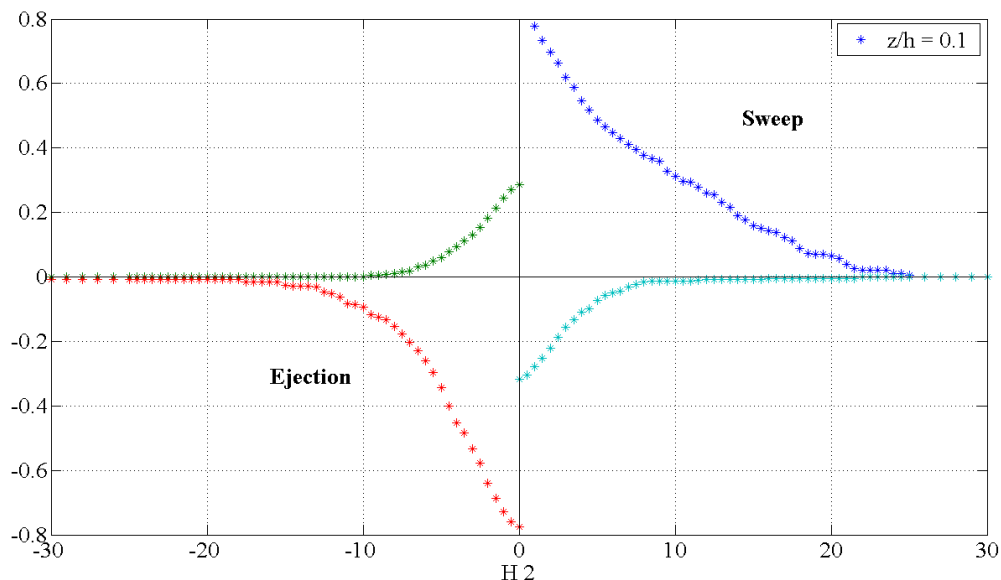


Figure 14. Fractional contribution of relative covariance

$e3 = p'u'/\overline{p'u'}$ versus threshold level $H2$ for ADVP data at $z/h = 0.1$ and pressure fluctuations (experiment 6).

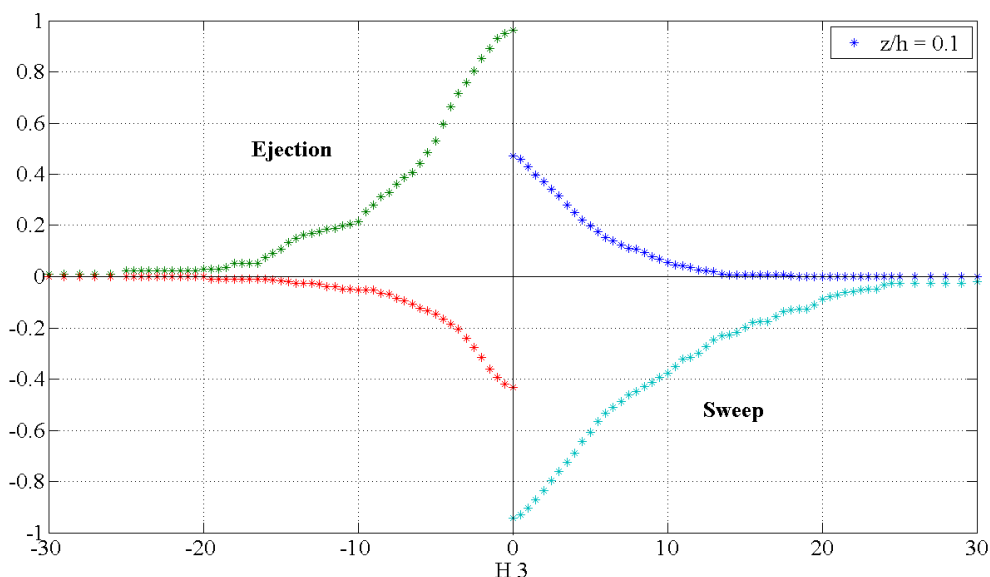


Figure 15. Fractional contribution of relative covariance

$e3 = p'w'/\overline{p'w'}$ versus threshold level $H3$ for ADVP data at $z/h = 0.1$ and pressure fluctuations (experiment 6).

The results of a quadrant analysis combining pressure transducer data and ADVP data are shown in Figures 14 and 15. The dominance of opposite quadrant pairs in Figures 13 and 14, when compared with the results in Figure 8, shows that pressure fluctuations increase for sweeps when highspeed water masses are transported towards the wall and decrease for ejections. This confirms the results for shear velocity above. Therefore coherent structures in

the water column influence the shear velocity dynamics on the bed. It should be noted, however, that inward and outward interactions more strongly contribute to the correlation between water flow and bed shear than they do to the flow field above the bed. Furthermore, the quadrant distributions in Figures 12, 13, 14 and 15 have longer tails than those in water flow (Figure 8). This implies that events with higher intermittency contribute more to the correlation between flow and bed shear and the correlation between flow and pressure.

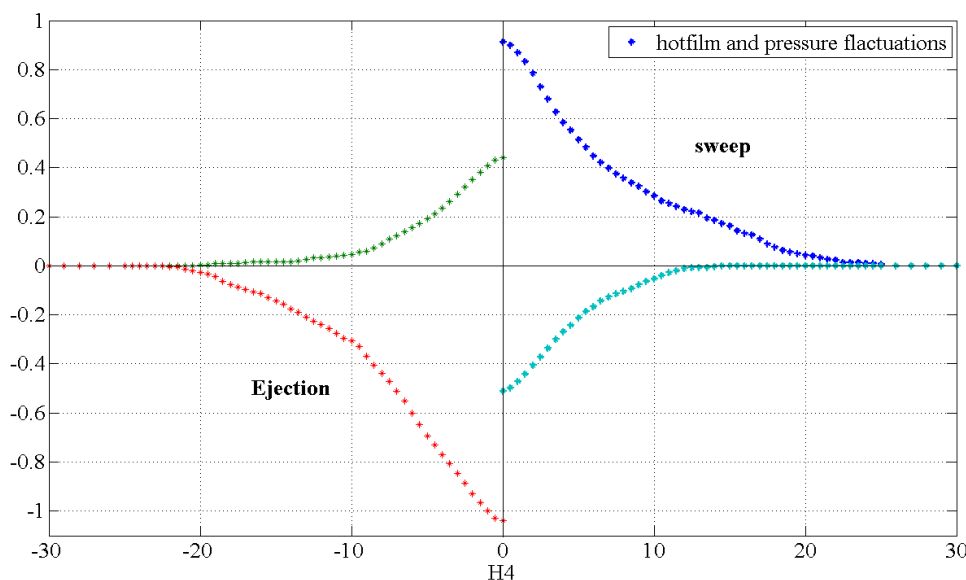


Figure 16. Fractional contribution of relative covariance

$e4 = \overline{u_*' p' / u_*' p'}$ versus threshold level $H4$ for hot-film and pressure fluctuations (experiment 6).

In Figure 16, event dynamics between hot-film and pressure fluctuations shows that bed shear velocity and pressure fluctuations increase for sweeps where high-speed water masses are transported towards the wall and decrease for ejections. Again, the quadrant distribution in Figure 16 has larger tails in comparison with Figure 8, and the dominance of quadrants is the same as in Figures 12 and 13, with larger tails in the quadrant distribution.

8 CONCLUSIONS

Logarithmic and Reynolds methods for the calculation of bed shear velocity have been applied in this study. The results were also compared with measurements of bed shear velocity taken by a hot-film sensor. All methods are based on certain assumptions and have certain advantages and disadvantages. It is generally assumed that the logarithmic profile method provides the most reliable results (Pope 2000). However, in flows over significant roughness as in the present case where $D_{50}/h \approx 0.075$, this method is difficult to apply, because it can be difficult to determine the profile origin. Thom (1975) had already shown that this problem may affect shear stress values. The procedure proposed by Smart (1999) helps to alleviate the problem, but cannot eliminate it. Furthermore, under rough-bed conditions, the flow near the bed can be expected to be 3D (Franca and Lemmin 2007), which may invalidate 2D concepts in this layer. In our experiments, the lowest two points in the profile were often affected. The Reynolds stress method avoids this problem, since it is not referenced to profile origin. In the present study, we observed that it provides results that are

often close to the hot-film values. It has a slight tendency towards values that are below the logarithmic profile and the hot-film results. This method is sensitive to the quality of the approximation of the profile points. A large number of profile points, such as we measured in the detailed instantaneous velocity profiles with the ADV, is important for a good estimate.

Bed shear velocities may be calculated by using both methods simultaneously in order to obtain reliable estimates. This may also help to identify likely sources of error. Modern instrumentation such as the ADV and Particle Image Velocimetry (PIV) facilitates this approach. However, the majority of the estimates fall into a band less than $\pm 15\%$. For most practical applications, this variability is still acceptable considering that these are mean values that may not be relevant for such processes as sediment suspension. The hot-film measurements also fall into this band indicating that bottom roughness effects are minor.

An analysis of synchronized ADV, hot-film and pressure fluctuation measurements was carried out. It showed that coherent structures in the water column are well developed. They are dominated by ejections and sweeps. A comparison between the results at different water depth indicates that they spread well into the outer region. The relationship between the coherent structures in the water column and bottom shear stress was investigated by a quadrant analysis which combined hot-film, pressure transducer and ADV data. The coherent structures in the water column are correlated with fluctuations of shear stress on the bed and pressure in the bed. It was documented that sweep events in the water column, where high-speed fluid is projected downwards to the bed, produce an increase in bed shear stress and in pressure in the bed. This confirms the observation by Kravchenko et al. (1993) that high values of skin friction are closely related to sweep motions. The opposite correlation is found for ejections. Furthermore, a correlation between positive shear stress fluctuations and positive pressure fluctuations was established. However, tails in the correlations between different sensors are longer than those found in the water column. This indicates that greater intermittency is important in this correlation. Thus, hydrodynamics processes on the bed are linked with coherent structures in the water column. These observations have implications for sediment suspension dynamics from the bed. Several authors (Grass 1982, Rashidi et al. 1990, Kaftori and Hetsroni 1998) had suggested that initiation of sediment motion may be caused by sweeps. The three-dimensional (3D) roughness layer above the bed which was identified by the shear stress analysis did not affect this correlation.

Acknowledgements

This study was sponsored by the European Commission contract No. 022441 (RII3) HYDRALAB-III and by the Swiss National Science Foundation, grant 200020-100383. We are grateful for the support.

9 REFERENCES

- Albayrak, I. (2008). An experimental study of coherent structures, secondary currents and surface boils and their interrelation in open-channel flow. *Ph.D. Thesis, No 4112, Ecole Polytechnique Fédérale (EPFL), Lausanne, Switzerland.*
- Bernard, J., M., Thomas, M. and Handler, R.A. (1993). Vortex dynamics in near-wall turbulence. In *Near-wall turbulent flows* (R.M.S.C. So, C.G. Speziale and B.E. Launder, eds.) Elsevier, New York, 43-52.

- Chandrasekaran, V., Cain, A., Nishida, T., Cattafesta, L.N., and Sheplak, M. (2005). Dynamic calibration technique for thermal shear stress sensors with mean flow. *Exp. in fluids*, 39, 56-65.
- Cellino, M., and Lemmin, U. (2004). Influence of coherent flow structures on the dynamics of suspended sediment transport in open-channel flow. *Journal of Hydraulic Engineering*, ASCE, 130, 1077-1088.
- Diplas, P., Dancey, C.L., Celik, A.O., Valyrakis, M., Greer, K., and Akar, T. (2008). The role of impulse on the initiation of particle movement under turbulent flow conditions. *Science*, 322, 717-720.
- Franca, M.J., and Lemmin, U. (2007). Discussion of, "Unobstructed and obstructed turbulent flows in gravel bed rivers," by H.M. Tritico and R.H. Hotchkiss. *Journal of Hydraulic Engineering*, ASCE, 133, 116-117.
- Franca, M.J., and Lemmin, U. (2006). Detection and reconstruction of coherent structures based on wavelet multiresolution analysis. *River Flow 2006*, 1, 181-188.
- Grass, A.J. (1982). The influence of boundary layer turbulence on the mechanics of sediment transport. (B.M. Sumer and A. Müller eds.), Balkema, Rotterdam, 3-17.
- Grosse, S. and Schröder, W. (2009). Wall-shear stress patterns of coherent structures in turbulent duct flow. *J. Fluid Mech.*, 633, 147-1258.
- Hanratty, T.J., and Campbell, J.A. (1983). Measurements of wall shear stress. *In: Fluid mechanics measurements (Ed. R.J. Goldstein), Hemisphere.*
- Hofland, B., Battjes, J. A. and Booij, R. (2005). Measurement of fluctuating pressures on coarse bed material. *Journal of Hydraulic Engineering*, ASCE, 131, 770-781.
- Hurther, D. (2001). 3D Acoustic Doppler velocimetry and turbulence in open-channel flow. *Ph.D. thesis, No. 2395, Ecole Polytechnique Fédérale (EPFL), Lausanne, Switzerland.*
- Hurther, D., and Lemmin, U. (2000). Shear stress statistics and wall similarity analysis in turbulent boundary layers using a high resolution 3D ADVP. *Journal of Oceanic Engineering*, IEEE, 25, 446-457.
- Hurther, D., and Lemmin, U. (2001). A discussion of equilibrium near-bed concentration of suspended sediment, *J. Hydraul. Eng.* 16, 430-433.
- Hurther, D., and Lemmin, U. (2003). Turbulent particle flux and momentum flux statistics in suspension flow. *Journal of water resources research*, Vol. 39, No.5, 1139.
- Hurther, D., Lemmin, U., and Terray, E.A., (2007). Turbulent transport in the outer region of rough-wall open-channel flows: the contribution of Large Coherent Shear Stress Structures (LC3S), *J. Fluid Mech.* 574, 465-493.
- Hussain, A. K. M. F. (1983). Coherent structures-reality and myth., *Journal of Physics Fluids*, vol. 26, No. 10.
- Kaftori, D. and Hetsroni, G. (1998). The effect of particles on wall turbulence. *Int. J. Multiphase Flow*, 24, 395-381.
- Kleinhans, M. G., and Van Rijn, L. C. (2002). Stochastic prediction of sediment transport in gravel bed rivers. *Journal of Hydraulic Engineering* ASCE, 128, 412-425.
- Kravchenko, A.G., Choi, H. and Moin, P. (1993). On the relation of near-wall streamwise vortices to wall skin friction in turbulent boundary layers. *Phys. Fluids A*, 5, 3307-3309.
- Lacey, R., Jay, W. and Roy, A.G. (2008). Fine-scale characterization of the turbulent shear layer of an instream pebble cluster. *Journal of Hydraulic Engineering*, ASCE, 134, 925-936.
- Lu, S.S., and Willmarth, W.W. (1973). Measurements of the structure of the Reynolds stress in a turbulent boundary layer. *Journal of Fluid Mechanics*, 60, 481-511.
- Nezu, I., and Nakagawa, H. (1993). *Turbulence in open-channel flows*. A.A. Balkema, Rotterdam, IAHR, Monograph series.
- Nikora, V.I., and Smart, G.M. (1997). Turbulence characteristics of New Zealand gravel-bed rivers. *Journal of Hydraulic Engineering*, ASCE, 123, 764-773.
- Pope, S.B. (2000). *Turbulent flows*. Cambridge University Press, Cambridge, United Kingdom.
- Radice, A., and Ballio, A. (2008). Double-average characteristics of sediment motion in one-dimensional bed load. *Acta Geophysica*, 56, 654-668.
- Rashidi, M., Hetsrone, G. and Banerjee, S. (1990). Particle-turbulence interaction in a boundary layer. *Int. J. Multiphase Flow*, 16, 935-949.

- Schlichting, H. (1987). *Boundary-layer theory*. McGraw-Hill, New York.
- Shen, C., and Lemmin, U. (1997). A two-dimensional acoustic sediment flux profiler. *Meas. Sci. Technol.*, Vol.8, 880-884.
- Shen, C. and Lemmin. (1999). Application of an acoustic particle flux profiler in particle-laden open-channel flow. *J. Hydraul. Res.* 37, 407-419.
- Shen, C., Song, T., and Lemmin, U. (1998). Skin friction measurements in a variable temperature flow. *Instrumentation and Measurement Technology Conference*, IEEE, Brussels, 523-526.
- Shields, I.A. (1936). Anwendung der Aehnlichkeitsmechanik und der Turbulenzforschung auf die Geschiebebewegung. *Mitt. Preuss. Versuchsanstalt für Wasserbau, Berlin*, Heft 26.
- Smart, G.M. (1999). Turbulent velocity profiles and boundary shear in gravel bed rivers. *Journal of Hydraulic Engineering*, ASCE, 125, 106-116.
- Smart, G. M. (2005). A novel gravel entrainment investigation. *River Coastal and Estuarine Morphodynamics 2005, Balkema*, 65-70.
- Smart, G. M., and Habersack, H. M. (2007). Pressure fluctuations and gravel entrainment in rivers. *Journal of Hydraulic Research*, 45, No. 5, 661-673.
- Song, T., and Graf, W.H. (1996). Velocity and turbulence distribution in unsteady open-channel flows. *Journal of Hydraulic Engineering*, ASCE, 122, 141-154.
- Thom, A.S. (1975). Momentum, mass and heat exchange of plant communities. *Vegetation and the atmosphere*. J.L. Monteith, ed., Academic Press, San Diego, 57-109.

CURRICULUM VITAE



Last Name : Bagherimiyab
First Name : Fereshteh
E-Mail : fereshteh.bagheri-meyab@epfl.ch, febagheri@yahoo.com
Work Phone : +41 21 693 23 78
Mobile Phone : +41 78 773 75 35
Fax : +41 21 693 67 67

RESEARCH INTEREST

- Sediment transport and river morphodynamics
- Turbulence in open-channel flow
- Unsteady open-channel flow

EDUCATION

- **Ph.D. Candidate**, Ecole Polytechnique Fédérale de Lausanne (EPFL), Environmental Fluid Mechanics Laboratory (EFLUM), Switzerland, (2007 - present)
Supervisor: Prof. Dr. Ulrich Lemmin (ulrich.lemmin@epfl.ch).
Title of Ph.D. Thesis: Sediment flux dynamics in turbulent unsteady, depth-varying open-channel flow over a gravel bed.
- **M.Sc. in Irrigation Structures**, Department of Irrigation & Reclamation Engineering, Faculty of Agricultural Engineering and Technology, College of Agriculture & Natural Resources, University of Tehran, Iran, (2005).
Supervisor: Prof. Salah Kouchakzadeh (skzadeh@ut.ac.ir).
Title of Master thesis: Studying the Hydraulic Characteristics of Corrugated PVC Pipes and Determining their Carrying Capacity based on the Free Surface Spatially Varied Flow Equation.
- **B.Sc. in Irrigation and Reclamation Engineering**, Department of Irrigation & Reclamation Engineering, Faculty of Agricultural Engineering and Technology, College of Agriculture & Natural Resources, University of Tehran, Iran. (2001)

ACADEMIC POSITIONS

- Research and Teaching Assistant & PhD Student, Ecole Polytechnique Fédérale de Lausanne (EPFL), Switzerland, (2007– present).

- Research and Teaching Assistant, Tehran University, Tehran, Iran. (2001-2006).

TEACHING EXPERIENCE

- Teaching Assistant, Ecole Polytechnique Fédérale de Lausanne (EPFL), LHE, Switzerland, (2007-2009). Fluids Mechanics I & II.
- Teaching Assistant, Tehran University, Faculty of water and irrigation Engineering, (2001-2006). Open-channel hydraulics.

AWARDS AND SCHOLARSHIPS

- First Prize in J.F. Kennedy Student Paper Competition organized by the International Association of Hydraulic Engineering and Research (IAHR), for the paper entitled, “Coherent structure and particle turbulence interaction in suspended sediment-laden laboratory open-channel flows” at the 34th IAHR World Congress, Brisbane, Australia (2011).
- Doctoral school scholarship, by the European Commission (FP6; RII3; Contract no. 022441) HYDRALAB III–SANDS. (2007).

HOBBIES AND INTERESTS

Sports, Swimming, Reading, Learning languages, Music, Traveling.

LANGUAGES

- Persian (mother tongue)
- English (fluent)
- French (good)
- Arabic (good in writing and reading)

PUBLICATIONS

Journals

- Bagherimiyab, F. and U. Lemmin (2011), Fine sediment dynamics in tidal open-channel flow studied with acoustic and optical systems, submitted to the Journal of Continental Shelf Research.
- Kouchakzadeh, S., E. Bayat, R. Azimi, and F. Bagherimiyab (2011), Spatially varied flow impact on resistance in corrugated pipes. Journal of Water Management Vol.164, p. 1-10.
- Doroudian, B., F. Bagherimiyab, and U. Lemmin (2010), Improving the accuracy of four-receiver acoustic Doppler velocimeter (ADV) measurements in turbulent boundary layer flows. Journal of Limnol. Oceanogr: Methods 8, 575–591.
- Kouchakzadeh, S. and F. Bagherimiyab (2006), Investigation of the hydraulic performance of corrugated pipes and developing applied conveyance relations for corrugated pipes based on their hydraulic performance. Iranian Journal of agricultural techniques and engineering Vol. 7, No. 27.
- Kouchakzadeh, S. and F. Bagherimiyab (2004), Carrying capacity of corrugated drainage pipes: uniform or non-uniform flow formula? Iranian Journal of Agricultural Sciences, Vol. 35, No. 2.
- Kouchakzadeh, S. and F. Bagherimiyab (2003), Determination of the roughness coefficient for corrugated drainage pipes based on real flow conditions. Iranian Journal of Agricultural Sciences, Vol. 34, No. 3.
- Kouchakzadeh, S., F. Bagherimiyab, and A. Mahdavi (2003), Application assessment of the conventional drainage diameter design formula based on actual free surface spatially varied flow condition. Scientific Journal of Agriculture, University of Tabriz, Vol. 14, No. 1.

Conferences

Proceedings

- Bagherimiyab, F. (2011), Coherent structure and particle-turbulence interaction in suspended sediment-laden laboratory open-channel flows. Proceedings of the 34th IAHR World Congress. Fluvial hydraulics, 3354. 26 June –1 July 2011. Brisbane, Australia.
- Bagherimiyab, F. and U. Lemmin (2011), Turbulence and fine sediment suspension in accelerating and decelerating open-channel flow. Proceedings of the 34th IAHR World Congress, 3362. 26 June –1 July 2011. Brisbane, Australia.
- Bagherimiyab, F. and U., Lemmin (2011), Effects of bedform structure on particle-turbulence interaction in unsteady suspended sediment-laden laboratory open-channel flows. Geophysical Research Abstracts Vol. 13, EGU 2011-6871, EGU General Assembly, Vienna, Austria 2011.
- Bagherimiyab, F. and U. Lemmin (2010), Aspects of turbulence and fine sediment resuspension in accelerating and decelerating open-channel flow.

- International Conference on Fluvial Hydraulics (River Flow, September 2010). Braunschweig, Germany.
- Bagherimiyab, F. and U. Lemmin (2010), Sediment flux dynamics in turbulent unsteady open-channel flow over a gravel bed. 6th International Symposium on Environmental Hydraulics, Athens, Greece.
- Bagherimiyab, F. and U. Lemmin (2010), An experimental investigation of the relationship between aspects of turbulence and fine sediment resuspension in accelerating open-channel flow. 17th Congress of the Asia and Pacific Division of the International Association of Hydraulic Engineering and Research, Auckland, New Zealand.
- Bagherimiyab, F. and U. Lemmin (2010), Interaction between turbulence and fine sediment resuspension in accelerating and decelerating open-channel flow. Latsis symposium, October 17-20, 2010, Lausanne, EPFL, Switzerland.
- Bagherimiyab, F. and U. Lemmin, (2009), Experimental study on fine sediment resuspension in accelerating rough-bed open-channel flow. International Workshop on Environmental Hydraulics IWEH09, 29 - 30 October 2009, Valencia, Spain.
- Bagherimiyab, F., U. Lemmin, D. Hurther, and P. D. Thorne (2009), On using acoustic profiling to study bottom boundary layer dynamics in unsteady sediment-laden open-channel flow. 3rd International Conference on Underwater Acoustic Measurements: Technologies & Results (UAM), p.104, 21 -26 June 2009, Nafplion, Greece.
- Bagherimiyab, F. (2009), Fine sediment resuspension in accelerating rough-bed open-channel flow. 33rd IAHR Congress, August 9 – 14, 2009, Vancouver, British Columbia, Canada.
- Bagherimiyab, F. and U. Lemmin, (2009), Velocity and turbulence distribution in Unsteady rough-bed open-channel flow. 33rd IAHR Congress, 9 – 14 August 2009, Vancouver, British Columbia, Canada.
- Bagherimiyab, F., U. Lemmin, D. Hurther, and P. D., Thorne, (2009), A study of bottom boundary layer dynamics in unsteady sediment-laden open-channel Flow Using Acoustic Profiling. 33rd IAHR Congress, 9 – 14 August 2009, Vancouver, British Columbia, Canada (CD).
- Bagherimiyab, F., I. Albayrak and U. Lemmin (2008), Bed shear velocity estimates in rough open-channel flow obtained from acoustic Doppler velocity profiler data and direct bed shear stress measurements. The River Flow Conference, Vol. 1, p.151-159, 3-5 September 2008, Izmir, Turkey.
- Bagherimiyab, F. and S. Kouchakzadeh (2005), Determination of hydraulic characteristics for corrugated drainage pipes. The 5th Iranian Hydraulics Conference, Kerman, Iran.
- Bagherimiyab, F. and S. Kouchakzadeh (2003), Application of the spatially varied flow equation in drainage pipes and compared with common equations. The 4th Iranian Hydraulics Conference, Shiraz, Iran.

Posters

- Bagherimiyab, F. and U. Lemmin (2011), Turbulence and fine sediment suspension in accelerating and decelerating open-channel flow. Proceedings of

the 34th IAHR World Congress, 3362. 26 June–1 July 2011. Brisbane, Australia.

Bagherimiyab, F. and U. Lemmin (2010), Interaction between turbulence and fine sediment resuspension in accelerating and decelerating open-channel flow. Latsis symposium, October 17-20, 2010, Lausanne, EPFL, Switzerland.

Bagherimiyab, F. (2009), Fine sediment resuspension in accelerating rough-bed open-channel flow. 33rd IAHR Congress, August 9 – 14, 2009, Vancouver, British Columbia, Canada.

TECHNICAL REPORTS

Bagherimiyab, F. (2007), Numerical simulation of the advection equation using flux-limited methods, Presented in the PhD Seminar on Numerical Methods for Environmental Fluids Course, EPFL, Lausanne.

Bagherimiyab, F. (2005), Particle densimetric Froude number for estimating sediment transport, Presented in MSc. Seminar of Sediment Hydraulics Course, University of Tehran

Bagherimiyab, F. (2005), Rehabilitation of dam foundations, Presented in MSc. Seminar II Course, University of Tehran.

Bagherimiyab, F. (2005), Brink depth-discharge relationship for spatially-varied flows in pipes, Presented MSc. Seminar I Course, University of Tehran.

Bagherimiyab, F. (2004), New investigations on two-phase chute flow, Presented in MSc. Seminar of Physical and Hydraulic Models Course, University of Tehran.

Bagherimiyab, F. (2004), Roller compacted concrete in dams, Presented in MSc. Seminar of Soil Dams Course, University of Tehran.

Bagherimiyab, F. (2004), Soil improvement by preloading, Presented in MSc. Seminar of Geotactic Course, University of Tehran.

RESEARCH PROJECTS

Backwater effects on drainage pipe design using the spatially varied flow equation, (Research assistant), Tehran University, (2003)

Determination of the hydraulic characteristics of corrugated pipes (Research assistant), Tehran University, (2003)

Design criteria for drainage pipes based on the spatially varied flow equation (Research assistant), Tehran University, (2002)

PARTICIPATION IN WORKSHOPS AND SUMMER SCHOOLS

International short course on Sediment Transport and GSTARS Computer Modeling, given by Prof. Chih Ted Yang, International Doctoral program Environmental Water, University of Stuttgart, Germany, 8 - 12 November 2010.

Summer School on Biogeodynamics and Earth System Sciences (BESS), Venice, Italy, 11 - 19 June 2010.

Young researchers workshop in HYDRALAB III, Barcelona, Spain, June 2009.

Course on Sediment Transport: Measurement, Modelling and Management, CTFC Forestry and Technology Center of Catalonia, Solsona, Spain, 31 March - 2 April 2009.

International Summer School on Complex flows, Turbulence, Morphodynamics and Ecology in Rivers, Delft University of Technology, 25 - 29 August 2008.

HYDRALAB III First Young Persons meeting on PIV and ADV techniques, International Conference Center of Meteo-France, in Toulouse, France, May 19 - 22, 2008.

REFERENCES

- Prof. Ulrich LEMMIN, Professor, Environmental Hydraulics Laboratory LHE, Ecole Polytechnique Fédérale de Lausanne (EPFL), ENAC ICARE LHE GC A1 375 (Bâtiment GC) 1015 Lausanne Station 18, Switzerland, Tel. +41 21 693 23 79, Fax. +41 21 693 67 67, e-mail: ulrich.lemmin@epfl.ch
- Prof. Marc Parlange, Dean School of Architecture, Civil and Environmental Engineering, Ecole Polytechnique Fédérale de Lausanne (EPFL), ENAC IIE EFLUM GR A0 412 (Bâtiment GR) Station 2, CH-1015 Lausanne, Switzerland, Tel. +41 36391, 36392, Fax. +41 (0) 21 693 63 90, e-mail: marc.parlange@epfl.ch
- Prof. Gary Parker, Professor, Department of Civil and Environmental Engineering, University of Illinois 2527c Hydrosystems Laboratory , 301 N. Mathews Ave., Urbana, IL 61801, U.S.A., Tel: (217) 244-5159, Fax: (217) 333-0687, Email: parkerg@illinois.edu
- Prof. Salah Kouchakzadeh, Professor in Hydraulics, Department of Irrigation & Reclamation Engineering, Faculty of Agricultural Engineering and Technology, College of Agriculture & Natural Resources, University of Tehran, Iran. Phone: +98 261 2241119 Ext. 111, Fax: +98 261 2241119 Ext. 201, Email: skzadeh@ut.ac.ir, URL: <http://utcan.ut.ac.ir/member/kouchakzadeh.aspx>.